

From Nuclei to Compact Stars

Contents

1	Topics	1115
2	Participants	1119
2.1	ICRANet	1119
2.2	External on going collaborations	1119
2.3	Postdocs	1120
2.4	Graduate Students	1120
3	Publications 2018	1123
3.1	Refereed Journals	1123
3.1.1	Printed	1123
3.1.2	Accepted for publication or in press	1127
3.1.3	Submitted for publication	1128
3.2	Conference Proceedings	1130

1 Topics

The study of compact objects such as white dwarfs, neutron stars and black holes requires the interplay between nuclear and atomic physics together with relativistic field theories, e.g., general relativity, quantum electrodynamics, quantum chromodynamics, as well as particle physics. In addition to the theoretical physics aspects, the study of astrophysical scenarios characterized by the presence of at least one of the above compact object is focus of extensive research within our group. The research of our group can be divided into the following topics:

- **Nuclear and Atomic Astrophysics.** We study the properties and processes occurring in compact stars in which nuclear and atomic physics have to be necessarily applied. We focus on the properties of nuclear matter under extreme conditions of density, pressure and temperature in the compact star interiors. The matter equation of state is studied in detail taking into account all the interactions between the constituents within a full relativistic framework.
- **White Dwarfs Physics and Structure.** The aim of this part of our research is the construction of the white dwarf structure within a self-consistent description of the equation of state of the interior together with the solution of the hydrostatic equilibrium equations in general relativity. Non-magnetized, magnetized, non-rotating and rotating white dwarfs are studied. The interaction and evolution of a central white dwarf with a surrounding disk, as occurred in the aftermath of white dwarf binary mergers, is also a subject of study.
- **White Dwarfs Astrophysics.** We are interested in the astrophysics of white dwarfs both isolated and in binaries. Magnetized white dwarfs, soft gamma repeaters, anomalous X-ray pulsars, white dwarf pulsars, cataclysmic variables, binary white dwarf mergers, and type Ia supernovae are studied. The role of a realistic white dwarf interior structure is particularly emphasized.

- **Neutron Stars Physics and Structure.** We calculate the properties of the interior structure of neutron stars using realistic models of the nuclear matter equation of state within the general relativistic equations of equilibrium. Strong, weak, electromagnetic and gravitational interactions have to be jointly taken into due account within a self-consistent fully relativistic framework. Non-magnetized, magnetized, non-rotating and rotating neutron stars are studied.
- **Neutron Stars Astrophysics.** We study astrophysical systems harboring neutron stars such as isolated and binary pulsars, low and intermediate X-ray binaries, inspiraling and merging double neutron stars. Most extreme cataclysmic events involving neutron stars and their role in the explanation of extraordinarily energetic astrophysical events such as gamma-ray bursts are analyzed in detail.
- **Radiation Mechanisms of White Dwarfs and Neutron Stars.** We here study the possible emission mechanisms of white dwarfs and neutron stars. We are thus interested in the electromagnetic, neutrino and gravitational wave emission at work in astrophysical systems such as compact star magnetospheres, accretion disks surrounding them and inspiraling and merging relativistic binaries such as double neutron stars, neutron star-white dwarfs, white dwarf-white dwarf and neutron star-black hole.
- **Exact and Numerical Solutions of the Einstein and Einstein-Maxwell Equations in Astrophysics.** We analyze the ability of analytic exact solutions of the Einstein and Einstein-Maxwell equations to describe the exterior spacetime of compact stars such as white dwarfs and neutron stars. For this we compare and contrast exact analytic with numerical solutions of the stationary axisymmetric Einstein equations. The problem of matching between interior and exterior spacetime is addressed in detail. The effect of the quadrupole moment on the properties of the spacetime is also investigated. Particular attention is given to the application of exact solutions in astrophysics, e.g. the dynamics of particles around compact stars and its relevance in astrophysical systems such as X-ray binaries and gamma-ray bursts.
- **Critical Fields and Non-linear Electrodynamics Effects in Astrophysics.** We study the conditions under which ultrastrong electromagnetic fields

can develop in astrophysical systems such as neutron stars and in the process of gravitational collapse to a black hole. The effects of non-linear electrodynamics minimally coupled to gravity are investigated. New analytic and numeric solutions to the Einstein-Maxwell equations representing black holes or the exterior field of a compact star are obtained and analyzed. The consequences on extreme astrophysical systems, for instance gamma-ray bursts, are studied.

2 Participants

2.1 ICRANet

- C. L. Bianco (ICRANet, Italy)
- J. A. Rueda (ICRANet, Italy)
- R. Ruffini (ICRANet, Italy)
- N. Sahakyan (ICRANet, Armenia)
- G. Vereschagin (ICRANet, Italy)
- S.-S. Xue (ICRANet, Italy)

2.2 External on going collaborations

- L. Becerra (Universidad Industrial de Santander, Colombia)
- K. Boshkayev (Al-Farabi Kazakh National University, Kazakhstan)
- R. Camargo (Universidade do Estado de Santa Catarina, Florianópolis, Brazil)
- C. Cherubini (Università Campus Biomedico, Rome, Italy)
- J. G. Coelho (Universidade Tecnológica Federal do Paraná, Brazil)
- S. Filippi (Università Campus Biomedico, Rome, Italy)
- C. L. Fryer (University of Arizona; Los Alamos National Laboratory, USA)
- E. Gacía-Berro (Universitat Politècnica de Catalunya, Spain)

- G. A. González (Universidad Industrial de Santander, Colombia)
- M. M. Guzzo (Universidade Estadual de Campinas, Brazil)
- F. D. Lora-Clavijo (Universidad Industrial de Santander, Colombia)
- P. Lorén Aguilar (University of Exeter, United Kingdom)
- S. O. Kepler (Universidade Federal do Rio Grande do Sul, Brazil)
- M. Malheiro (Instituto Tecnológico de Aeronáutica, Brazil)
- R. M. Jr. Marinho (Instituto Tecnológico de Aeronáutica, Brazil)
- G. Mathews (University of Notre Dame, USA)
- D. P. Menezes (Universidade Federal de Santa Catarina, Brazil)
- L. A. Nuñez (Universidad Industrial de Santander, Colombia)
- C. V. Rodrigues (Instituto Nacional de Pesquisas Espaciais, Brazil)
- F. Rossi-Torres (Universidade Estadual de Campinas, Brazil)
- J. I. Zuluaga (Universidad de Antioquia, Colombia)

2.3 Postdocs

- C. L. Ellinger (Los Alamos National Laboratory, USA)
- J. P. Pereira (Universidade Federal do ABC, Brazil)
- Y. Wang (ICRANet, Italy)

2.4 Graduate Students

- E. Becerra (ICRANet; Sapienza University of Rome, Italy)
- J. M. Blanco-Iglesias (Universitat Politècnica de Catalunya)
- S. V. Borges (Instituto Tecnológico de Aeronáutica, Brazil)

- S. Campion (ICRANet; Sapienza University of Rome, Italy)
- G. A. Carvalho (Instituto Tecnológico de Aeronáutica, Brazil)
- R. V. Lobato (ICRANet; Sapienza University of Rome, Italy; Instituto Tecnológico de Aeronáutica, Brazil)
- R. Moradi (ICRANet; Sapienza University of Rome, Italy)
- R. Riahi (Isfahan University of Technology, Iran)
- J. F. Rodriguez (ICRANet; Sapienza University of Rome, Italy)
- J. D. Uribe (ICRANet; Sapienza University of Rome, Italy)

3 Publications 2018

3.1 Refereed Journals

3.1.1 Printed

1. Rodríguez, J. F.; Rueda, J. A.; Ruffini, R., *On the Final Gravitational Wave Burst from Binary Black Holes Mergers*, *Astronomy Reports* 62, 940, 2018.

We use perturbation theory in the strong-field regime to study the inspiral-to-plunge transition of a test particle into a Kerr black hole. We found a smooth transition, without burst, and with lower energy and angular momentum radiated in gravitational waves with respect to previous treatments in the literature. Besides their theoretical interest, our results are relevant for the waveform templates of binary black hole mergers used for gravitational waves detection which are constructed on the basis of a inspiral-to-plunge transition with a high energetic burst.

2. Rueda, J. A.; Ruffini, R.; Becerra, L. M.; Fryer, C. L., *Simulating the induced gravitational collapse scenario of long gamma-ray bursts*, *International Journal of Modern Physics A* 33, 1844031, 2018.

We present the state-of-the-art of the numerical simulations of the supernova (SN) explosion of a carbon-oxygen core (CO_{core}) that forms a compact binary with a neutron star (NS) companion, following the induced gravitational collapse (IGC) scenario of long gamma-ray bursts (GRBs) associated with type Ic supernovae (SNe). We focus on the consequences of the hypercritical accretion of the SN ejecta onto the NS companion which either becomes a more massive NS or gravitationally collapses forming a black hole (BH). We summarize the series of results on this topic starting from the first analytic estimates in 2012 all the way up to the most recent three-dimensional (3D) smoothed-particle-hydrodynamics (SPH) numerical simulations in 2018. We present a new SN ejecta morphology, highly asymmetric, acquired by binary interac-

tion and leading to well-defined, observable signatures in the gamma- and X-rays emission of long GRBs.

3. Rueda, J. A.; Ruffini, R.; Wang, Y.; Aimuratov, Y.; Barres de Almeida, U.; Bianco, C. L.; Chen, Y. C.; Lobato, R. V.; Maia, C.; Primorac, D.; Moradi, R.; Rodriguez, J. F., *GRB 170817A-GW170817-AT 2017gfo and the observations of NS-NS, NS-WD and WD-WD mergers*, Journal of Cosmology and Astroparticle Physics, Issue 10, 006, 2018.

The LIGO-Virgo Collaboration has announced the detection of GW170817 and has associated it with GRB 170817A . These signals have been followed after 11 hours by the optical and infrared emission of AT 2017gfo. The origin of this complex phenomenon has been attributed to a neutron star-neutron star (NS-NS) merger. In order to probe this association we confront our current understanding of the gravitational waves and associated electromagnetic radiation with four observed GRBs originating in binaries composed of different combinations NSs and white dwarfs (WDs). We consider 1) GRB 090510 the prototype of NS-NS merger leading to a black hole (BH); 2) GRB 130603B the prototype of a NS-NS merger leading to massive NS (MNS) with an associated kilonova; 3) GRB 060614 the prototype of a NS-WD merger leading to a MNS with an associated kilonova candidate; 4) GRB 170817A the prototype of a WD-WD merger leading to massive WD with an associated AT 2017gfo-like emission. None of these systems support the above mentioned association. The clear association between GRB 170817A and AT 2017gfo has led to introduce a new model based on a new subfamily of GRBs originating from WD-WD mergers. We show how this novel model is in agreement with the exceptional observations in the optical, infrared, X- and gamma-rays of GRB 170817A-AT 2017gfo.

4. Ruffini, R.; Rodriguez, J.; Muccino, M.; Rueda, J. A.; Aimuratov, Y.; Barres de Almeida, U.; Becerra, L.; Bianco, C. L.; Cherubini, C.; Filippi, S.; Gizzi, D.; Kovacevic, M.; Moradi, R.; Oliveira, F. G.; Pisani, G. B.; Wang, Y., *On the Rate and on the Gravitational Wave Emission of Short and Long GRBs*, The Astrophysical Journal 859, 30, 2018.

On the ground of the large number of gamma-ray bursts (GRBs) detected with cosmological redshift, we classified GRBs in seven subclasses, all with binary progenitors which emit gravitational waves (GWs). Each binary is composed of combinations of carbon-oxygen cores (COcore),

neutron stars (NSs), black holes (BHs), and white dwarfs (WDs). The long bursts, traditionally assumed to originate from a BH with an ultra-relativistic jetted emission, not emitting GWs, have been subclassified as (I) X-ray flashes (XRFs), (II) binary-driven hypernovae (BdHNe), and (III) BH-supernovae (BH-SNe). They are framed within the induced gravitational collapse paradigm with a progenitor COcore-NS/BH binary. The SN explosion of the COcore triggers an accretion process onto the NS/BH. If the accretion does not lead the NS to its critical mass, an XRF occurs, while when the BH is present or formed by accretion, a BdHN occurs. When the binaries are not disrupted, XRFs lead to NS-NS and BdHNe lead to NS-BH. The short bursts, originating in NS-NS, are subclassified as (IV) short gamma-ray flashes (S-GRFs) and (V) short GRBs (S-GRBs), the latter when a BH is formed. There are (VI) ultra-short GRBs (U-GRBs) and (VII) gamma-ray flashes (GRFs) formed in NS-BH and NS-WD, respectively. We use the occurrence rate and GW emission of these subclasses to assess their detectability by Advanced LIGO-Virgo, eLISA, and resonant bars. We discuss the consequences of our results in view of the announcement of the LIGO/Virgo Collaboration of the source GW 170817 as being originated by an NS-NS.

5. Becerra, L.; Rueda, J. A.; Lorén-Aguilar, P.; García-Berro, E., *The Spin Evolution of Fast-rotating, Magnetized Super-Chandrasekhar White Dwarfs in the Aftermath of White Dwarf Mergers*, *The Astrophysical Journal* 857, 134, 2018.

The evolution of the remnant of the merger of two white dwarfs is still an open problem. Furthermore, few studies have addressed the case in which the remnant is a magnetic white dwarf with a mass larger than the Chandrasekhar limiting mass. Angular momentum losses might bring the remnant of the merger to the physical conditions suitable for developing a thermonuclear explosion. Alternatively, the remnant may be prone to gravitational or rotational instabilities, depending on the initial conditions reached after the coalescence. Dipole magnetic braking is one of the mechanisms that can drive such losses of angular momentum. However, the timescale on which these losses occur depends on several parameters, like the strength of the magnetic field. In addition, the coalescence leaves a surrounding Keplerian disk that can be accreted by the newly formed white dwarf. Here we compute the post-merger evolution of a super-Chandrasekhar magnetized white dwarf

taking into account all the relevant physical processes. These include magnetic torques acting on the star, accretion from the Keplerian disk, the threading of the magnetic field lines through the disk, and the thermal evolution of the white dwarf core. We find that the central remnant can reach the conditions suitable to develop a thermonuclear explosion before other instabilities (such as the inverse beta-decay instability or the secular axisymmetric instability) are reached, which would instead lead to gravitational collapse of the magnetized remnant.

6. Rodríguez, J. F.; Rueda, J. A.; Ruffini, R., *Comparison and contrast of test-particle and numerical-relativity waveform templates*, Journal of Cosmology and Astroparticle Physics, Issue 02, 030, 2018.

We compare and contrast the emission of gravitational waves and waveforms for the recently established “helical-drifting-sequence” of a test particle around a Kerr black hole with the publicly available waveform templates of numerical-relativity. The merger of two black holes of comparable mass are considered. We outline a final smooth merging of the test particle into the final Kerr black hole. We find a surprising and unexpected agreement between the two treatments if we adopt, for the mass of the particle and the Kerr black hole a Newtonian-center-of-mass description, and for the Kerr black hole spin an effective value whose nature remains to be clarified.

7. Becerra, L.; Guzzo, M. M.; Rossi-Torres, F.; Rueda, J. A.; Ruffini, R.; Uribe, J. D., *Neutrino Oscillations within the Induced Gravitational Collapse Paradigm of Long Gamma-Ray Bursts*, The Astrophysical Journal 852, 120, 2018.

The induced gravitational collapse paradigm of long gamma-ray bursts associated with supernovae (SNe) predicts a copious neutrino-antineutrino ($\nu\bar{\nu}$) emission owing to the hypercritical accretion process of SN ejecta onto a neutron star (NS) binary companion. The neutrino emission can reach luminosities of up to 10^{57} MeV s⁻¹, mean neutrino energies of 20 MeV, and neutrino densities of 10³¹ cm⁻³. Along their path from the vicinity of the NS surface outward, such neutrinos experience flavor transformations dictated by the neutrino-to-electron-density ratio. We determine the neutrino and electron on the accretion zone and use them to compute the neutrino flavor evolution. For normal and inverted neutrino mass hierarchies and within the two-flavor formalism

($\nu_e\nu_x$), we estimate the final electronic and nonelectronic neutrino content after two oscillation processes: (1) neutrino collective effects due to neutrino self-interactions where the neutrino density dominates, and (2) the Mikheyev-Smirnov-Wolfenstein effect, where the electron density dominates. We find that the final neutrino content is composed by 55% (62%) of electronic neutrinos, i.e., $\nu_e + \bar{\nu}_e$, for the normal (inverted) neutrino mass hierarchy. The results of this work are the first step toward the characterization of a novel source of astrophysical MeV neutrinos in addition to core-collapse SNe and, as such, deserve further attention.

3.1.2 Accepted for publication or in press

1. Becerra, L.; Ellinger, C. L.; Fryer, C. L.; Rueda, J. A.; Ruffini, R., *SPH simulations of the induced gravitational collapse scenario of long gamma-ray bursts associated with supernovae*, to appear in *The Astrophysical Journal*.

We present the first three-dimensional (3D) smoothed-particle-hydrodynamics (SPH) simulations of the induced gravitational collapse (IGC) scenario of long-duration gamma-ray bursts (GRBs) associated with supernovae (SNe). We simulate the SN explosion of a carbon-oxygen core (CO_{core}) forming a binary system with a neutron star (NS) companion. We follow the evolution of the SN ejecta, including their morphological structure, subjected to the gravitational field of both the new NS (νNS) formed at the center of the SN, and the one of the NS companion. We compute the accretion rate of the SN ejecta onto the NS companion as well as onto the νNS from SN matter fallback. We determine the fate of the binary system for a wide parameter space including different CO_{core} and NS companion masses, orbital periods and SN explosion geometry and energies. We identify, for selected NS nuclear equations-of-state, the binary parameters leading the NS companion, by hypercritical accretion, either to the mass-shedding limit, or to the secular axisymmetric instability for gravitational collapse to a black hole (BH), or to a more massive, fast rotating, stable NS. We also assess whether the binary remains or not gravitationally bound after the SN explosion, hence exploring the space of binary and SN explosion parameters leading to $\nu\text{NS-NS}$ and $\nu\text{NS-BH}$ binaries. The consequences of our results for the modeling of long GRBs, i.e. X-ray flashes and binary-driven hypernovae, are

discussed.

3.1.3 Submitted for publication

1. Rodríguez, J. F.; Rueda, J. A.; Ruffini, R.; Zuluaga, J. I.; Blanco-Iglesias, J. M.; Lorén-Aguilar, P., *Chirping compact stars and inspiral planets around intermediate-mass black-holes: gravitational radiation and detection degeneracy*, submitted to Physical Review Letters.

Compressible, Riemann-S type ellipsoids can emit gravitational waves (GWs) with a chirp-like structure (*chirping* ellipsoids, CELs). The potential detection of these type of sources with eLISA and other future space-based GW observatories can reveal previously undetected astrophysical processes in system of compact objects (eg. white dwarf binary mergers). In this letter we demonstrate that the GW frequency-amplitude evolution of CELs (mass $\sim 1 M_{\odot}$, radius $\sim 10^3$ km, polytropic equation of state with index $n \approx 3$) is almost indistinguishable from that emitted by extreme mass-ratio inspirals (EMRIs) composed of an intermediate-mass black hole (e.g. $10^3 M_{\odot}$) and a planet-like companion (e.g. $10^{-4} M_{\odot}$). The detection of these EMRIs is relevant for the understanding of planetary formation and dynamics in crowded stellar systems. We estimate that for reasonable astrophysical assumptions, the rate in the local Universe of CEL and EMRIs in the mass range considered here, is very similar. The astrophysical implications of the above CEL-EMRI detection degeneracy, including the consequences on their detectability by space-based GW-detection facilities, are outlined.

2. Becerra, L.; Boshkayev, K.; Rueda, J. A.; Ruffini, R., *Time evolution of isolated massive, fast rotating, highly magnetized white dwarfs losing angular momentum via magnetic dipole braking*, submitted to Monthly Notices of the Royal Astronomical Society.

We investigate the evolution of isolated, zero and finite temperature, massive, uniformly rotating, highly magnetized white dwarfs (WDs) under angular momentum loss driven by magnetic dipole braking. We consider the structure and thermal evolution of the WD isothermal core taking also into account the nuclear burning and neutrino emission processes. We estimate the WD lifetime before it reaches the condition either for a type Ia supernova explosion or for the gravitational collapse

to a neutron star. We analyze the behavior of the WD parameters such as the central density, radius, moment of inertia, angular momentum, angular velocity, central temperature and magnetic field intensity as a function of lifetime. In addition, we compute the characteristic time of nuclear reactions and dynamical time scale. We discuss the astrophysical consequences of our results.

3. Riahi, R.; Kalantari, S. Z., Rueda, J. A., *Universal relations for the Keplerian sequence of rotating neutron stars*, submitted to Physical Review D.

We investigate the Keplerian (mass-shedding) sequence of rotating neutron stars. Twelve different equations of state are used to describe the nuclear structure. We find four fitting relations which connect the rotating frequency, mass and radius of stars in the mass-shedding limit to the mass and radius of stars in the static sequence. We show the breakdown of approximate relation for the Keplerian frequency derived by Lattimer and Prakash [Science, 304, 536, (2004)] and then we present a new, EOS-independent and more accurate relation. This relation fits the Keplerian frequency of rotating neutron stars to about 2% for a large range of the compactness M_S/R_S of the reference non-rotating neutron star, namely the static star with the same central density as the rotating one. The performance of the fitting formula is close to 4% for $M_S/R_S \leq 0.05 M_\odot/\text{km}$ ($f_K \leq 350$ Hz). We present additional EOS-independent relations for the Keplerian sequence including relations for $M_K f_K$ and $R_K f_K$ in terms of $M_S f_S$ and $R_S f_S$, respectively, one of M_K/R_K as a function of f_K/f_S and M_S/R_S , and a relation between the M_K , R_K and f_K . These new fitting relations are approximately EOS-independent with an error in the worst case of 8%. The universality of the Keplerian sequence properties presented here add to the set of other neutron star universal relations in the literature such as the *I-Love-Q* relation, the gravitational binding energy and the energy, angular momentum and radius of the last circular orbit of a test-particle around rotating neutron stars. This set of universal, analytic formulas, facilitate the inclusion of general relativistic effects in the description of relativistic astrophysical systems involving fast rotating neutron stars.

4. Rueda, J. A.; Ruffini, R.; Wang, Y.; Bianco, C. L.; Blanco-Iglesias, J. M.; Karlica, M.; Loren-Aguilar, P.; Moradi, R.; Sahakyan, N., *Electromagnetic emission of white dwarf binary mergers*, submitted to Journal of Cosmology

and Astroparticle Physics.

It has been recently proposed that the ejected matter from white dwarf (WD) binary mergers can produce transient, optical and infrared emission similar to the "kilonovae" of neutron star (NS) binary mergers. To confirm this we calculate the electromagnetic emission from WD-WD mergers and compare with kilonova observations. We simulate WD-WD mergers leading to a massive, fast rotating, highly magnetized WD with an adapted version of the smoothed-particle-hydrodynamics (SPH) code Phantom. We thus obtain initial conditions for the ejecta such as escape velocity, mass and initial position and distribution. The subsequent thermal and dynamical evolution of the ejecta is obtained by integrating the energy-conservation equation accounting for expansion cooling and a heating source given by the fallback accretion onto the newly-formed WD and its magneto-dipole radiation. We apply our model to the most detailed observed kilonova, AT 2017gfo, and its associated gamma-ray burst (GRB) 170817A. We show that magnetospheric processes in the merger can lead to a prompt, short gamma-ray emission of up to $\approx 10^{46}$ erg in a timescale of 0.1-1 s. The bulk of the ejecta initially expands non-relativistically with velocity $0.01c$ and then it accelerates to $0.1c$ due to the injection of fallback accretion energy. The ejecta become transparent at optical wavelengths around ~ 7 days post-merger with a luminosity 10^{41} - 10^{42} erg s^{-1} . The X-ray emission from the fallback accretion becomes visible around ~ 150 -200 day post-merger with a luminosity of 10^{39} erg s^{-1} . Therefore, we show that WD-WD mergers can lead to electromagnetic emission as the one observed in GRB 170817A-AT 2017gfo. We also predict the post-merger time at which the central WD should appear as a pulsar depending on the value of the magnetic field and rotation period.

3.2 Conference Proceedings

1. Rodríguez, J. F.; Rueda, J. A.; Ruffini, R., *Strong-field gravitational-wave emission in Schwarzschild and Kerr geometries: some general considerations*, Joint International Conference of ICGAC-XIII and IK-15 on Gravitation, Astrophysics and Cosmology, Seoul, Korea 2017; EPJ Web of Conferences 168, 02006, 2018.

We have used the perturbations of the exact solutions of the Einstein equations to estimate the relativistic wave emission of a test particle orbiting around a black hole. We show how the hamiltonian equations of motion of a test particle augmented with the radiation-reaction force can establish a priori constraints on the possible phenomena occurring in the merger of compact objects. The dynamical evolution consists of a helicoidal sequence of quasi-circular orbits, induced by the radiation-reaction and the background spacetime. Near the innermost stable circular orbit the evolution is followed by a smooth transition and finally plunges geodesically into the black hole horizon. This analysis gives physical insight of the merger of two equal masses objects.

2. Becerra, Laura M.; Bianco, Carlo; Fryer, Chris; Rueda, Jorge; Ruffini, Remo, *On the Induced Gravitational Collapse*, Joint International Conference of ICGAC-XIII and IK-15 on Gravitation, Astrophysics and Cosmology, Seoul, Korea 2017; EPJ Web of Conferences 168, 02005, 2018.

The induced gravitational collapse (IGC) paradigm has been applied to explain the long gamma ray burst (GRB) associated with type Ic supernova, and recently the Xray flashes (XRFs). The progenitor is a binary systems of a carbon-oxygen core (CO) and a neutron star (NS). The CO core collapses and undergoes a supernova explosion which triggers the hypercritical accretion onto the NS companion (up to $10^{-2} M_{\odot} \text{ s}^{-1}$). For the binary driven hypernova (BdHNe), the binary system is enough bound, the NS reach its critical mass, and collapse to a black hole (BH) with a GRB emission characterized by an isotropic energy $E_{\text{iso}} > 10^{52} \text{ erg}$. Otherwise, for binary systems with larger binary separations, the hypercritical accretion onto the NS is not sufficient to induced its gravitational collapse, a X-ray flash is produced with $E_{\text{iso}} < 10^{52} \text{ erg}$. We are going to focus in identify the binary parameters that limits the BdHNe systems with the XRFs systems.

3. Rueda, J. A.; Ruffini, R.; Rodriguez, J. F.; Muccino, M.; Aimuratov, Y.; Barres de Almeida, U.; Becerra, L.; Bianco, C. L.; Cherubini, C.; Filippi, S.; Kovacevic, M.; Moradi, R.; Pisani, G. B.; Wang, Y., *The binary progenitors of short and long GRBs and their gravitational-wave emission*, Joint International Conference of ICGAC-XIII and IK-15 on Gravitation, Astrophysics and Cosmology, Seoul, Korea 2017; EPJ Web of Conferences 168, 01006, 2018.

We have sub-classified short and long-duration gamma-ray bursts (GRBs) into seven families according to the binary nature of their progenitors. Short GRBs are produced in mergers of neutron-star binaries (NS-NS) or neutron star-black hole binaries (NS-BH). Long GRBs are produced via the induced gravitational collapse (IGC) scenario occurring in a tight binary system composed of a carbon-oxygen core (CO_{core}) and a NS companion. The CO_{core} explodes as type Ic supernova (SN) leading to a hypercritical accretion process onto the NS: if the accretion is sufficiently high the NS reaches the critical mass and collapses forming a BH, otherwise a massive NS is formed. Therefore long GRBs can lead either to NS-BH or to NS-NS binaries depending on the entity of the accretion. We discuss for the above compact-object binaries: 1) the role of the NS structure and the nuclear equation of state; 2) the occurrence rates obtained from X and gamma-rays observations; 3) the predicted annual number of detections by the Advanced LIGO interferometer of their gravitational-wave emission.

SPH SIMULATIONS OF THE INDUCED GRAVITATIONAL COLLAPSE SCENARIO OF LONG GAMMA-RAY BURSTS ASSOCIATED WITH SUPERNOVAE

L. BECERRA^{1,2}, C. L. ELLINGER³, C. L. FRYER³, J. A. RUEDA^{1,2,4}, R. RUFFINI^{1,2,4}

¹Dipartimento di Fisica and ICRA, Sapienza Università di Roma, P.le Aldo Moro 5, I-00185 Rome, Italy

²ICRANet, P.zza della Repubblica 10, I-65122 Pescara, Italy

³CCS-2, Los Alamos National Laboratory, Los Alamos, NM 87545

⁴ICRANet-Rio, Centro Brasileiro de Pesquisas Físicas, Rua Dr. Xavier Sigaud 150, 22290-180 Rio de Janeiro, Brazil

ABSTRACT

We present the first three-dimensional (3D) smoothed-particle-hydrodynamics (SPH) simulations of the induced gravitational collapse (IGC) scenario of long-duration gamma-ray bursts (GRBs) associated with supernovae (SNe). We simulate the SN explosion of a carbon-oxygen core (CO_{core}) forming a binary system with a neutron star (NS) companion. We follow the evolution of the SN ejecta, including their morphological structure, subjected to the gravitational field of both the new NS (ν NS) formed at the center of the SN, and the one of the NS companion. We compute the accretion rate of the SN ejecta onto the NS companion as well as onto the ν NS from SN matter fallback. We determine the fate of the binary system for a wide parameter space including different CO_{core} and NS companion masses, orbital periods and SN explosion geometry and energies. We identify, for selected NS nuclear equations-of-state, the binary parameters leading the NS companion, by hypercritical accretion, either to the mass-shedding limit, or to the secular axisymmetric instability for gravitational collapse to a black hole (BH), or to a more massive, fast rotating, stable NS. We also assess whether the binary remains or not gravitationally bound after the SN explosion, hence exploring the space of binary and SN explosion parameters leading to ν NS-NS and ν NS-BH binaries. The consequences of our results for the modeling of long GRBs, i.e. X-ray flashes (XRFs) and binary-driven hypernovae (BdHNe), are discussed.

1. INTRODUCTION

The induced gravitational collapse (IGC) concept was initially introduced to explain the temporal and spatial coincidence of long gamma-ray bursts (GRBs) with energies $E_{\text{iso}} > 10^{52}$ erg and type Ic supernovae (SNe). In a binary system composed of a carbon-oxygen (CO_{core}) and a neutron star (NS), the explosion of the CO_{core} triggers the hypercritical accretion onto the NS. For the most compact binary systems, the accretion rate onto the NS is such that it can reach the critical mass against gravitational collapse and forming a black hole (BH) with consequence emission of a GRB. These systems have been called binary-driven hypernovae (BdHNe; see Ruffini et al. 2014). Later, the IGC paradigm was extended to X-ray flashes (XRFs) with energies $E_{\text{iso}} < 10^{52}$ erg that occur when the accretion rate onto the NS is lower and so it does not induce its gravitational collapse to a BH but instead leads to a massive, fast rotating, stable NS. For further theoretical and observational details on these two subclasses of long GRBs, we refer the reader to Ruffini et al. (2016), and references therein.

The physical picture of the IGC was first proposed in Ruffini et al. (2001), formally formulated in Rueda & Ruffini (2012), and then applied for the first time for the explanation of GRB 090618 in Izzo et al. (2012). Rueda & Ruffini (2012) presented analytical estimates of the accretion rate and the possible fate of the accreting NS binary companion. This first simple model assumed: 1) a pre-SN uniform density profile following an homologous expansion and 2) approximately constant masses of the NS ($\approx 1.4 M_{\odot}$) and the pre-SN core ($\approx 4-8 M_{\odot}$).

The first 1-dimensional (1D) simulations of the IGC process were presented in Fryer et al. (2014). These simulations included: 1) detailed SN explosions of the CO_{core} obtained from a 1D core-collapse SN code (Fryer et al. 1999a); 2) hydrodynamic details of the hypercritical accretion process; 3) the evolution of the SN ejecta falling into the Bondi-Hoyle accretion region all the way up to its incorporation into the NS surface. Following the Bondi-Hoyle formalism, they estimated accretion rates exceeding $10^{-3} M_{\odot} \text{ s}^{-1}$, making highly possible that the NS reaches the critical mass and the BH formation.

Already from these works, it was clear that the main binary properties that decide the occurrence of the IGC process are: 1) the orbital period, P , 2) the SN ejecta velocity, v_{ej} , and 3) the initial NS companion mass. The shorter the period and the slower the ejecta the higher the Bondi-Hoyle accretion rate and the more massive the NS companion the less mass is needed to induce its gravitational collapse to a BH. Both P and v_{ej} have a direct effect in the Bondi-Hoyle accretion rate via the gravitational capture radius but they have also an indirect role via the density of the accreted matter. Since the ejecta decompress during their expansion until the NS gravitational capture radius position, there is the obvious effect that the shorter the P and the slower the v_{ej} , the higher the density at the accretion site hence the higher the accretion rate. Clearly, the effect of v_{ej} can be seen as the effect of the SN kinetic/explosion energy since the stronger the explosion the higher the kinetic energy and the higher the expansion velocity and viceversa.

There were still additional effects needed to be included in the model to have a more general picture. [Becerra et al. \(2015\)](#) improved the analytical model relaxing assumptions made in [Rueda & Ruffini \(2012\)](#). The ejecta density profile was adopted as a power-law in radius and its evolution with time homologous. The amount of angular momentum transported by the ejecta entering the Bondi-Hoyle region and how much of it can be transferred to the NS was also estimated. It was there shown that the ejecta have enough angular momentum to circularize around the NS forming a disk-like structure and accretes on short timescales. Bearing in mind the above mentioned effect of P on the accretion rate, it was there determined the critical binary period below which, i.e. $P \lesssim P_{\text{max}}$, the NS accretes enough mass and angular momentum such that its gravitational collapse to a BH is induced. Conversely, for $P \gtrsim P_{\text{max}}$, the NS does not gain enough mass and angular momentum to form a BH but just becomes a more massive NS.

Later, we presented in [Becerra et al. \(2016\)](#) a first attempt of a smoothed-particle-hydrodynamics (SPH)-like simulation of the SN ejecta expansion under the gravitational field of the NS companion. Specifically, we described the SN matter formed by point-like particles and modeled the initial power-law density profile of the CO_{core} by populating the inner layer with more particles and defined the initial conditions of the SN ejecta assuming an homologous velocity distribution in free expansion; i.e. $v \propto r$. The particles trajectory were computed by solving the Newtonian equations of motion including the effects of the gravitational field of the NS companion. In these simulations we assumed a circular motion of the NS around the SN center, implemented the changes in the NS gravitational mass owing to the accretion process via the Bondi-Hoyle formalism follow-

ing [Becerra et al. \(2015\)](#) and, accordingly, removed from the system the particles falling within the Bondi-Hoyle surface. The accretion process was shown to proceed hypercritically thanks to the copious neutrino emission near the NS surface, which produces neutrino luminosities of up to $10^{52} \text{ erg s}^{-1}$ and mean neutrino energies of 20 MeV. A detailed analysis of the fundamental neutrino emission properties in XRFs and BdHNe was presented in [Becerra et al. \(2018\)](#).

[Becerra et al. \(2016\)](#) made a first wide exploration of the binary parameters for the occurrence of the IGC process, hence of the systems leading to XRFs ($P \gtrsim P_{\text{max}}$) and BdHNe ($P \lesssim P_{\text{max}}$), as well as of the dependence of P_{max} on the CO_{core} and NS companion mass. In addition, these simulations produced a first visualization of the SN ejecta morphology. Indeed, we showed in [Becerra et al. \(2016\)](#) how the structure of the SN ejecta, becoming asymmetric by the presence of the accreting NS companion, becomes crucial for the inference of observable signatures in the GRB afterglow. The specific example of XRF 060218 was there examined to show the asymmetry effect in the X-ray emission and to show the feedback of the accretion energy injected into the SN ejecta on its optical emission.

It became clear that the SN ejecta morphology and the feedback of a GRB emission onto the SN could be relevant also in BdHNe. In [Ruffini et al. \(2018a\)](#) we showed that the GRB e^+e^- plasma, expanding at relativistic velocities from the newborn BH site, engulfs different amounts of mass along different directions owing to the asymmetries developed in SN density profile, leading to different dynamics and consequently to different signatures for different viewing angles. The agreement of such a scenario with the observed emission from the X-ray flares in the BdHN early afterglow was there shown (see also section 6 below for a discussion on this topic). The SN ejecta geometry affects as well the GeV emission observed in BdHNe ([Ruffini et al. 2018b](#)).

[Ruffini et al. \(2018a\)](#) also showed the relevance of the binary effects and the SN morphology on a most fundamental phenomenon: the GRB exploding within the SN impacts on it affecting its dynamics by transferring energy and momentum and finally transforming the ordinary SN into a hypernova (HN). Therefore, this model predicts that broad-lined SNe or HNe are not born as such but instead they are the outcome of the GRB impact on the SN. We have given evidence of such a SN-HN transition in a BdHN by identifying the moment of its occurrence in the case of GRB 151027A [Ruffini et al. \(2017\)](#).

All these results point to the necessity of a detailed knowledge of the physical properties of the SN ejecta and in general of the binary system, in the 3D space and as a function of time, for the accurate inference of the

consequences on the X, gamma-ray emission in XRFs and BdHNe and also on the GeV emission in BdHNe.

In view of the above we present here the first 3D hydrodynamic simulations of the IGC scenario. We have used the SPH technique as developed in the SNSPH code (Fryer et al. 2006b). The SNSPH is a tree-based, parallel code that has undergone rigorous testing and has been applied to study a wide variety of astrophysical problems (see, e.g., Fryer & Warren 2002; Young et al. 2006; Diehl et al. 2008; Batta et al. 2017). The simulation starts from the moment at which the SN shock front reaches the CO_{core} external radius and, besides to calculate the accretion rate onto the NS companion, we also follow the evolution of the binary parameters (e.g. the binary separation, period, eccentricity) in order to determine if the final configuration becomes disrupted or not. This implies that we have introduced as well the gravitational effects of the remnant neutron star, the νNS formed at the center of the SN explosion, allowing us to calculate also the accretion onto it via matter fallback.

This article is organized as follows. In section 2 we describe the main aspects of the SNSPH code (Fryer et al. 2006b) and the algorithm applied to simulate the accretion process. In section 3 we give the details on the construction of the initial binary configuration. Section 4 shows the results of the simulations. We have covered a wide range of initial conditions for the binary system, i.e. we have varied the CO_{core} progenitors, the binary initial separation, SN total energy and the initial NS mass companion. In Section 5 we analyse if the binary system is disrupted or not by the mass loss due to the SN explosion of the CO_{core} and in Section 6 we compute the evolution of the binary and determine whether the stars' gravitational collapse is possible. In section 7 we discuss the consequences on our results. Specifically, in Section 7.1 we analyze in depth the main parameters of the system that decide the fate of the NS companion, then we discuss, in Section 7.2, how these conditions could be realized in a consistent binary evolutionary path. Section 7.3 contains estimates of the occurrence rate of these systems and Section 7.4 outlines the consequences on the explanation of the GRB prompt and afterglow emission, as well as the prediction of new observables. Finally, in section 8 we present our conclusions and perspectives for future work. In Appendix A we present convergence tests of the numerical simulations.

2. SPH SIMULATION

We use the 3D Lagrangian hydrodynamic code SNSPH (Fryer et al. 2006b) to model the evolution of the binary system after the CO_{core} collapses and the SN explosion occurs. The code follows the prescription of

the SPH formalism in Benz (1990). Basically, the fluid is divided by N particles with determined position, \vec{r}_i , mass, m_i , and smooth length, h_i . Physical quantities for each particle are calculated through an interpolation of the form:

$$A_i(\vec{r}_i) = \sum_j A_j \left(\frac{m_j}{\rho_j} \right) W(|\vec{r}_{ij}|, h_{ij}), \quad (1)$$

where $|\vec{r}_{ij}| = |\vec{r}_i - \vec{r}_j|$, W is the smoothing kernel (that is equal zero if $r > 2h$) and $h_{ij} = (h_i + h_j)/2$ is the symmetric smooth length between particles i and j . The code allows to evolve the smooth length with time as $dh_i/dt = -1/3(h_i/\rho_i)(d\rho_i/dt)$.

Then, the hydrodynamical equations of conservation of linear momentum and energy are written as:

$$\frac{d\vec{v}_i}{dt} = - \sum_{j=1}^N m_j \left(\frac{P_i}{\rho_i^2} + \frac{P_j}{\rho_j^2} + \Pi_{ij} \right) \vec{\nabla}_i W(r, h_{ij}) + \vec{f}_g; \quad (2)$$

$$\frac{du_i}{dt} = \sum_{j=1}^N m_j \left(\frac{P_i}{\rho_i^2} + \frac{1}{2} \Pi_{ij} \right) (\vec{v}_i - \vec{v}_j) \cdot \vec{\nabla}_i W(r, h_{ij}), \quad (3)$$

where \vec{v}_i , P_i , ρ_i and u_i are the particle velocity, pressure, density and internal energy, respectively. In order to handle shocks, an artificial viscosity term is introduced through Π_{ij} as in Monaghan (1992, 2005):

$$\Pi_{ij} = \begin{cases} \frac{-\alpha(c_i+c_j)\mu_{ij}+0.5\beta\mu_{ij}^2}{\rho_i+\rho_j} & \text{if } \vec{v}_{ij} \cdot \vec{r}_{ij} < 0 \\ 0 & \text{otherwise} \end{cases}, \quad (4)$$

where c_i is the sound speed, $\vec{v}_{ij} = \vec{v}_i - \vec{v}_j$ and

$$\mu_{ij} = \frac{h_{ij}\vec{v}_{ij} \cdot \vec{r}_{ij}}{|\vec{r}_{ij}|^2 + \epsilon h_{ij}^2}. \quad (5)$$

The form for the viscosity of Equation (4) can be interpreted as an bulk and von Neuman-Richtmyer viscosity parametrized by α and β viscosity coefficients. In the simulations we adopt, as usual, $\alpha = 1.0$ and $\beta = 2.0$.

The last term of Equation (2) refers to the fluid self-gravity force. The particles are organized in a hashed oct-tree and the gravitational force is evaluated using the multipole acceptability criterion (MAC) described in Warren & Salmon (1993, 1995).

Finally, the equation of state adopted treats the ions as a perfect-gas and takes into account the radiation pressure:

$$P = \frac{1}{3}aT^4 + n_{\text{ion}}\kappa T; \quad (6)$$

$$u = aT^4 + \frac{3}{2}n_{\text{ion}}\kappa T, \quad (7)$$

where n_{ion} is the number density of ions, T , the temperature and a the radiation constant.

2.1. Accretion Algorithm

In the simulation, the remnant of the CO_{core} and the NS companion are model as two point masses that only interact gravitationally with the other particles and between them. Their equation of motion will be:

$$\frac{d\vec{v}_s}{dt} = \sum_{j=1}^N \frac{Gm_j}{|\vec{r}_s - \vec{r}_j|^3} (\vec{r}_j - \vec{r}_s) + \frac{GM_{s'}}{|\vec{r}_s - \vec{r}_{s'}|^3} (\vec{r}_{s'} - \vec{r}_s), \quad (8)$$

where subindex s and s' make reference to the stars. In the same way, each particle of the fluid will feel an additional force from the stars gravitational field:

$$\vec{f}_{s,i} = \frac{GM_s}{|\vec{r}_s - \vec{r}_i|^3} (\vec{r}_s - \vec{r}_i). \quad (9)$$

The stars accrete a particle j from the SN ejecta if the following conditions are fulfilled (Bate et al. 1995):

1. The particle is inside the star accretion radius, i.e.:

$$|\vec{r}_j - \vec{r}_s| < R_{j,\text{acc}}.$$

2. The gravitational potential energy of the particle in the field of the star is larger than its kinetic energy, i.e.:

$$\frac{GM_s m_j}{|\vec{r}_j - \vec{r}_s|} > \frac{1}{2} m_j |\vec{v}_j - \vec{v}_s|^2.$$

3. The angular momentum of the particle relative to the star is less than the one it would have in a Keplerian orbit at $R_{j,\text{acc}}$, i.e.:

$$|(\vec{r}_j - \vec{r}_s) \times (\vec{v}_j - \vec{v}_s)| < \sqrt{GM_s R_{j,\text{acc}}}.$$

The accretion radius for a particle j is defined as:

$$R_{j,\text{acc}} = \min \left(\xi \frac{2GM_s}{v_{js}^2 + c_j^2}, h_j \right), \quad (10)$$

and we adopt in the simulations $\xi = 0.05\text{--}0.1$ (see below for further details on this parameter).

These conditions are evaluated at the beginning of every time step. The particles that fulfill them are removed from the simulation and we update the properties of the star as:

$$M_{s,\text{new}} = M_s + \sum_j m_j; \quad (11)$$

$$\vec{v}_{s,\text{new}} = \frac{M_s \vec{v}_s + \sum_j m_j \vec{v}_j}{M_{s,\text{new}}}; \quad (12)$$

$$L_{s,\text{new}} = M_{s,\text{new}} \frac{L_s \vec{v}_s + \sum_j m_j (\vec{r}_{s,j} \times \vec{v}_{s,j})}{M_s}. \quad (13)$$

The above sum is over the particles accreted during the corresponding time step.

3. INITIAL SETUP

Our calculations include a suite of pre-SN progenitors with zero-age-main-sequence (ZAMS) masses ranging from 15 to 40 M_\odot obtained via the KEPLER code (Heger & Woosley 2010). The SN explosions are simulated with the 1D core-collapse code (Fryer et al. 1999a) and the multi-parameter prescriptions introduced in Fryer et al. (2017) to mimic the supernova engine: the energy deposition rate and duration, the size of the convection cell above the base of the proto-NS and the time after bounce when the convective engine starts. These parameters are designed to include the uncertainties in the convection-enhanced supernova engine (see Herant et al. 1994; Fryer & Young 2007; Murphy et al. 2013, for details).

When the shock front reaches the edge of the CO_{core}, the configuration is mapped into a 3D SPH-configuration of about 1 million particles with variable mass. This is done using the weight Voronoi tessellation (WVT) as described in Diehl et al. (2015).

The SPH configuration of the SN ejecta is constructed in the rotating reference frame of the progenitor star. In order to translate it to the center of mass reference frame of the initial binary system (CO_{core} + NS), the position and velocities of the particles are modified as follow:

$$\vec{r}_{i,\text{new}} = \mathbb{R} \vec{r}_i - \vec{r}_{\text{CO}}; \quad (14)$$

$$\vec{v}_{i,\text{new}} = \mathbb{R} \vec{v}_i - \vec{r}_i \times \vec{\Omega}_{\text{orb}} - \vec{v}_{\text{CO}}, \quad (15)$$

where \mathbb{R} is a rotation matrix, \vec{r}_{CO} and \vec{v}_{CO} are the position and velocity of the CO_{core} before the explosion and Ω_{orb} is the binary orbital angular velocity, that is determined once the orbital separation and star masses are established:

$$\Omega_{\text{orb}} = \sqrt{\frac{G(M_{\text{CO}} + M_{\text{NS}})}{a_{\text{orb}}^3}}, \quad (16)$$

with M_{CO} being the CO_{core} total mass, M_{NS} the NS mass and a_{orb} the binary separation. The equatorial plane of the binary corresponds to the x-y plane, then the initial position of the stars (NS and νNS) are on the x-axis and its initial motion is counter-clockwise.

The minimum binary period that the system can have is given by the condition that the compactness of the CO_{core} is such that there is no Roche lobe overflow before the SN explosion. Then, the minimum binary separation is determined by (Eggleton 1983):

$$\frac{R_{\text{star}}}{a_{\text{orb}}} = \frac{0.49q^{2/3}}{0.6q^{2/3} + \ln(1 + q^{1/3})}, \quad (17)$$

with $q = M_{\text{CO}}/M_{\text{NS}}$.

Since we are interested in identifying the favorable conditions for which the NS companion can accrete enough mass and collapse into a BH, we will explore

Table 1. Properties of the CO_{core} progenitors.

M_{ZAMS} (M_{\odot})	M_{rem} (M_{\odot})	M_{ej} (M_{\odot})	R_{core} (10^8 cm)	R_{star} (10^9 cm)	$v_{\text{star},0}$ (10^8 cm/s)	E_{grav} (10^{51} erg)	m_j ($10^{-6} M_{\odot}$)
15	1.30	1.606	8.648	5.156	9.75	0.2149	0.2 – 4.4
25	1.85	4.995	2.141	5.855	5.43	1.5797	2.2 – 11.4
30 ^a	1.75	7.140	28.33	7.830	8.78	1.7916	1.9 – 58.9
30 ^b	1.75	7.140	13.84	7.751	5.21	1.5131	1.9 – 58.9
40	1.85	11.50	19.47	6.529	6.58	4.4305	2.3 – 72.3

NOTE—Each progenitor was evolved with the KEPLER stellar evolution code (Heger & Woosley 2010) and then was exploded artificially using the 1D core-collapse code presented in Fryer et al. (1999a).

$${}^a E_{\text{sn}} = 1.09 \times 10^{52} \text{ erg}$$

$${}^b E_{\text{sn}} = 2.19 \times 10^{51} \text{ erg}$$

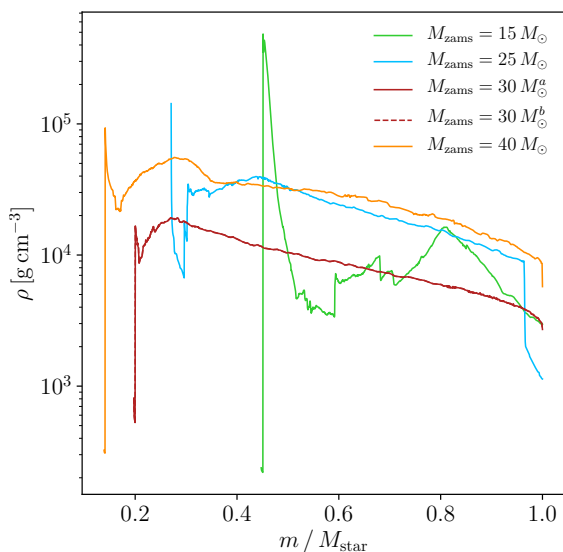


Figure 1. Density profile of the SN ejecta when the shock has reached the carbon-oxygen edge for the $M_{\text{zams}} = 15$, 25, 30 and $40 M_{\odot}$ progenitors (see table 1). The density is given as a function of the variable m/M_{star} , namely the mass coordinate, m , normalized to the total mass of the CO_{core}, M_{star} . At this moment, the 1D simulation is mapped into a 3D SPH-configuration.

different initial conditions for the system. We have worked with four progenitor for the CO_{core} with different ZAMS mass: $M_{\text{zams}} = 15$, 25, 30 and $40 M_{\odot}$. In Table 1 we present the main proprieties of each of these progenitors at the mapping moment: the SN mass ejected, M_{ej} , the the gravitational mass of the remnant star, M_{rem} (i.e. the CO_{core} mass before its collapse is $M_{\text{star}} = M_{\text{ej}} + M_{\text{rem}}$), the SN ejecta innermost radius, R_{core} , the CO_{core} radius when the collapse happens, R_{star} , and the forward shock velocity, $v_{\text{star},0}$. In the last two columns of Table 1 we specify the gravitational energy of the star, E_{grav} , and the maximum and minimum masses of the SPH particles, m_j . Figure 1 shows the density profile of each progenitor at the moment of the

mapping to the 3D SPH configuration (when the shock front of the explosion has reached the star surface). We have two models for the $30 M_{\odot}$ progenitor, each with different SN explosion energy.

It is important to notice that we are working with progenitors that were evolved as isolated stars, i.e. without taking into account that they are part of a binary system. However, as it was indicated in Fryer et al. (2014), there is a 3–4 order of magnitude pressure jump between the CO_{core} and helium layer, this means that the star will not expand significantly when the helium layer is removed: the CO_{core} can be 1.5–2 times larger (Moriya et al. 2010), then the minimum period of the system might increase by a factor of 1.8–2.8.

The final fate of the system also will depend on the characteristics of the SN explosion. We run simulations varying the explosion energy of the SN. Rather than produce a broad range of explosion energies, (as we did with the $30 M_{\odot}$ progenitor), we scaled the kinetic and internal energy of the particles behind the forward shock by a factor η . In this way, the internal structure of the progenitor does not change, just the velocity and the temperature.

In order to study the effect of an asymmetric SN expansion (see, e.g., Janka 2012) we adopt a single-lobe prescription (Hungerford et al. 2005) following Hungerford et al. (2003); Young et al. (2006). Namely, the explosion is modified to a conical geometry parametrized by Θ , the opening angle of the cone, and f , the ratio of the velocities between the particles inside and outside the cone. The velocities of the SPH particles behind the forward shock are then modified as:

$$V_{\text{in-cone}} = f \left[\frac{1-f^2}{2} \cos \Theta + \frac{1+f^2}{2} \right]^{-1/2} V_{\text{symm}}; \quad (18)$$

$$V_{\text{out-cone}} = \left[\frac{1-f^2}{2} \cos \Theta + \frac{1+f^2}{2} \right]^{-1/2} V_{\text{symm}}, \quad (19)$$

where V_{symm} is the radial velocity of the original explosion. This prescription conserves the kinetic energy of the symmetry explosion, and to conserve the total energy of the supernova we scale the particles internal energy in the same way.

In the next section, we present the results of our SPH-simulations.

4. RESULTS

In Table 2 we summarize the properties of the SN and the parameters that characterize the state of the initial binary systems with the different CO_{core} obtained with the progenitors of table 1. The models are labeled as “ $x_1mx_2px_3e$ ”, where x_1 is the M_{zams} of the CO_{core} progenitor star, x_2 is the fraction between the initial orbital period and the minimum orbital period of the system to have no Roche-lobe overflow; and x_3 is the value of the η factor by which the SPH particle velocities and internal energy are scaled. For each model in Table 2 we specify the sum of the ejecta kinetic and internal energy, $E_k + U_i$, the initial orbital period, $P_{\text{orb},i}$ as well as the initial binary separation, $a_{\text{orb},i}$.

For each model, we first run a simulation of the SN expansion assuming that the CO_{core} collapses and explodes as an isolate star, i.e. without the NS companion. In Table 2 we summarize the final mass of the νNS , indicated as $M_{\nu\text{ns,fb}}$, and the magnitude of the νNS kick velocity, V_{kick} . The latter is the νNS velocity due to the linear momentum accreted by the star from the fallback particles.

Then, we run simulations of the SN expansion with the CO_{core} as part of a binary system with a $2 M_{\odot}$ NS as companion. We expect a massive initial NS companion because the binary system evolutionary path leading to these systems have at least one common-envelope episode (see e.g. Fryer et al. 1999b; Becerra et al. 2015, and section 6). However, we have also performed simulations with a NS companion with an initial mass $1.4 M_{\odot}$ and $1.6 M_{\odot}$. In Table 2 we summarize the parameters that characterize the final outcome of these simulations: the νNS final mass, $M_{\nu\text{ns}}$, the NS final mass, M_{NS} , the velocity of the final binary system center-of-mass, V_{CM} , the final orbital period, $P_{\text{orb},f}$, the major semi-axis and eccentricity of the orbit of the final system, $a_{\text{orb},f}$ and e , respectively, and the amount of mass that is still bounded to the binary stars at the moment when the simulation is stopped, m_{bound} . This bound material circularizes around the stars and at some moment might be accreted by any of the them. In the final column of Table 2, we have specified if the system remains bound as a new binary system or if it is disrupted in the explosion.

4.1. Fiducial model: $25 M_{\odot}$ progenitor

We are going to take the $25 M_{\odot}$ progenitor star for the CO_{core} and a $2 M_{\odot}$ NS as our fiducial initial binary system in order to describe in detail the main features of the simulations while the SN expands in presence of the NS companion (model 25m1p1e of table 2). This fiducial binary system has the minimum orbital period allowed for the system to have no Roche-lobe overflow, 4.86 minutes, which corresponds to a binary separation of 1.34×10^{10} cm. Thus, this model presents most favorable conditions for the occurrence of the induced collapse: a short period for the binary system and a massive initial NS companion. Later, we will change one by one the initial conditions and compare the outcomes with the one of this fiducial system.

Figure 2 shows snapshots of the mass density in the x-y plane, the binary equatorial plane (upper panel) and x-z plane (lower panel) at different simulation times. In the plot, the reference system has been rotated and translated in a way that the x-axis is along the line that joins the stars of the binary system and the origin is at the NS companion. In general, when the SN starts to expand, the faster outermost particles of the SN will pass almost without being disturbed by the NS gravitational field. The slower-moving material is gravitationally captured by the NS, initially forming a tail and ultimately forming a thick disk around it. In addition, there are particles from the innermost layers of the SN-ejecta that do not have enough kinetic energy to scape, leading to fallback accretion onto the νNS . Then, at some point, the material that have been capture by the NS companion start to be also attracted by the νNS and being accreted by it.

To confirm the formation of the disk around the NS companion, in Figure 3 has been calculated the angular velocity profile with respect the NS companion position at different times and for two different directions: the line that joins the binary stars with the νNS in the $-x$ direction labeled as $\theta = 0$; and the line perpendicular to it on the orbital binary plane, labeled as $\theta = \pi/2$. The angular velocity of the particles closed to the NS companion ($r/a_0 < 0.25$) superpose the Keplerian angular velocity profile. This confirms the estimates from analytical approximations made in Becerra et al. (2015), where it was shown that the SN ejecta have enough angular momentum to circularize around the NS before being accreted.

Figure 4 shows the mass accretion rate as a function of simulation time onto the binary system stars: the NS companion, the νNS and the sum of both. Either the fallback accretion rate or the NS accretion rate are much greater that the Eddington limit. The NS is allowed to accrete at this high rate by the emission of neutrinos at its surface via e^+e^- pair annihilation that is the most efficient neutrino emission process at these

Table 2. SPH Simulations

Model	$E_k + U_i$ (10^{51} erg)	$P_{\text{orb},i}$ (min)	$a_{\text{orb},i}$ (10^{10} cm)	$M_{\nu\text{ns,fb}}$ (m_{\odot})	V_{kick} (10^4 cm/s)	$M_{\nu\text{ns}}$ (m_{\odot})	M_{ns} (m_{\odot})	V_{CM} (10^7 cm/s)	$P_{\text{orb},f}$ (min)	$a_{\text{orb},f}$ (10^{10} cm)	e	m_{bound} (m_{\odot})	bound
$M_{\text{zams}} = 15 M_{\odot}$ Progenitor													
15m1p07e	1.395	6.58	1.361	1.302	3.99	1.302	2.003	4.05	19.0	2.437	0.443	2.7×10^{-6}	yes
15m1p05e	1.101	6.58	1.361	1.303	4.83	1.303	2.006	4.02	18.6	2.393	0.433	4.8×10^{-5}	yes
15m1p03e	0.607	6.58	1.361	1.304	18.93	1.315	2.023	3.91	15.9	2.182	0.398	6.9×10^{-4}	yes
15m1p01e	0.213	6.58	1.361	2.478	6.62	1.916	2.199	0.39	3.04	0.773	0.233	0.098	yes
15m1p005e	0.135	6.58	1.361	2.731	1.73	2.649	2.034	0.08	5.92	1.257	0.036	0.029	yes
15m2p03e	0.607	11.7	2.000	1.304	18.93	1.304	2.007	0.39	–	–	1.192	5.8×10^{-3}	no
15m2p01e	0.213	11.7	2.000	2.478	6.62	2.238	2.101	0.08	12.9	2.068	0.419	0.0759	yes
15m3p01e	0.213	17.6	2.000	2.478	6.62	2.405	2.057	0.32	14.5	2.249	0.103	0.0313	yes
$M_{\text{zams}} = 25 M_{\odot}$ Progenitor													
25m1p1e	3.14	4.81	1.352	1.924	1.35	1.963	2.085	7.49	116.9	8.747	0.866	0.081	yes
25m1p09e	2.84	4.81	1.352	1.935	2.97	2.013	2.162	7.17	38.29	4.199	0.744	0.043	yes
25m1p08e	2.53	4.81	1.352	1.953	3.57	2.081	2.441	6.09	16.5	2.454	0.600	0.075	yes
25m1p07e	2.22	4.81	1.352	2.172	41.30	2.371	2.621	3.77	4.33	1.043	0.381	0.160	yes
25m2p1e	3.14	8.56	1.988	1.924	1.35	1.929	2.029	6.46	–	–	1.005	0.073	no
25m3p1e	3.14	11.8	2.605	1.924	1.35	1.924	2.024	5.76	–	–	1.086	0.025	no
25m4p1e	3.14	15.9	2.984	1.924	1.35	1.916	2.014	5.34	–	–	1.096	0.013	no
25m2p07e	2.22	8.56	1.988	2.172	41.30	2.352	2.522	3.43	18.3	2.699	0.461	0.185	yes
25m3p07e	2.22	11.8	2.605	2.172	41.30	2.301	2.523	3.25	23.5	3.11	0.477	0.138	yes
25m5p07e	2.22	19.8	3.463	2.172	41.30	2.166	2.401	3.24	27.8	3.49	0.526	0.0051	yes
25m15p07e	2.22	59.4	7.203	2.172	41.30	2.088	2.208	2.72	321.5	17.41	0.639	3.4×10^{-3}	yes
$M_{\text{zams}} = 30 M_{\odot}$ Progenitor - exp 1													
30m1p1ea	8.43	5.82	1.667	1.756	40.80	1.757	2.007	9.67	–	–	1.701	0.0	no
30m1p07ea	5.95	5.82	1.667	1.755	39.36	1.758	2.015	9.58	–	–	1.647	9.6×10^{-4}	no
30m1p05ea	4.26	5.82	1.667	1.758	96.20	1.764	2.031	9.46	–	–	1.501	0.012	no
30m1p03ea	2.59	5.82	1.667	2.178	3.93×10^3	1.869	2.455	7.79	101.5	8.137	0.852	0.168	yes
30m2p03ea	2.59	10.8	2.449	2.178	3.93×10^3	1.837	2.192	7.21	–	–	1.095	0.0854	no
$M_{\text{zams}} = 30 M_{\odot}$ Progenitor - exp 2													
30m1p1eb	3.26	5.82	1.667	4.184	141.30	3.675	2.382	3.59	12.1	2.209	0.569	0.331	yes
30m1p12eb	3.91	5.82	1.667	2.462	147.79	2.515	2.376	5.86	46.1	5.009	0.733	0.133	yes
30m2p12eb	3.91	10.8	2.410	2.462	147.79	2.621	2.228	4.85	157.1	11.302	0.848	0.029	yes
30m1p2eb	6.45	5.82	1.667	1.771	13.89	1.783	2.077	9.50	–	–	1.447	5.7×10^{-3}	no
30m1p31eb	10.02	5.82	1.667	1.766	5.21	1.768	2.017	9.95	–	–	1.712	6.5×10^{-4}	no
$M_{\text{zams}} = 40 M_{\odot}$ Progenitor													
40m1p1e	10.723	3.49	1.295	1.871	176.43	1.874	2.119	13.68	–	–	1.845	0.038	no
40m1p09e	9.670	3.49	1.295	1.872	141.38	1.881	2.274	13.35	–	–	1.538	0.027	no
40m1p08e	8.618	3.49	1.295	1.873	242.93	1.886	2.545	12.52	–	–	1.276	0.016	no
40m1p07e	7.506	3.49	1.295	1.879	464.82	2.095	3.033	10.12	85.9	7.712	0.881	0.051	yes
40m1p06e	6.513	3.49	1.295	6.568	69.73	3.784	3.209	4.57	2.42	0.792	0.612	1.053	yes
40m1p05e	5.145	3.49	–	–	0.91	5.430	3.642	–	0.06	0.339	0.243	1.250	yes
40m2p1e	10.723	6.22	1.904	1.871	176.43	1.873	2.046	10.79	–	–	2.194	6.13×10^{-3}	no
40m2p07e	7.506	6.22	1.904	1.879	464.82	2.064	2.755	8.757	4408	104.26	0.984	0.078	yes
40m4p07e	7.506	12.45	3.022	1.879	464.82	1.959	2.507	7.799	–	–	1.180	0.0744	no
40m2p06e	6.513	6.22	1.904	6.568	69.73	5.581	2.961	2.58	5.79	1.523	0.648	0.509	yes

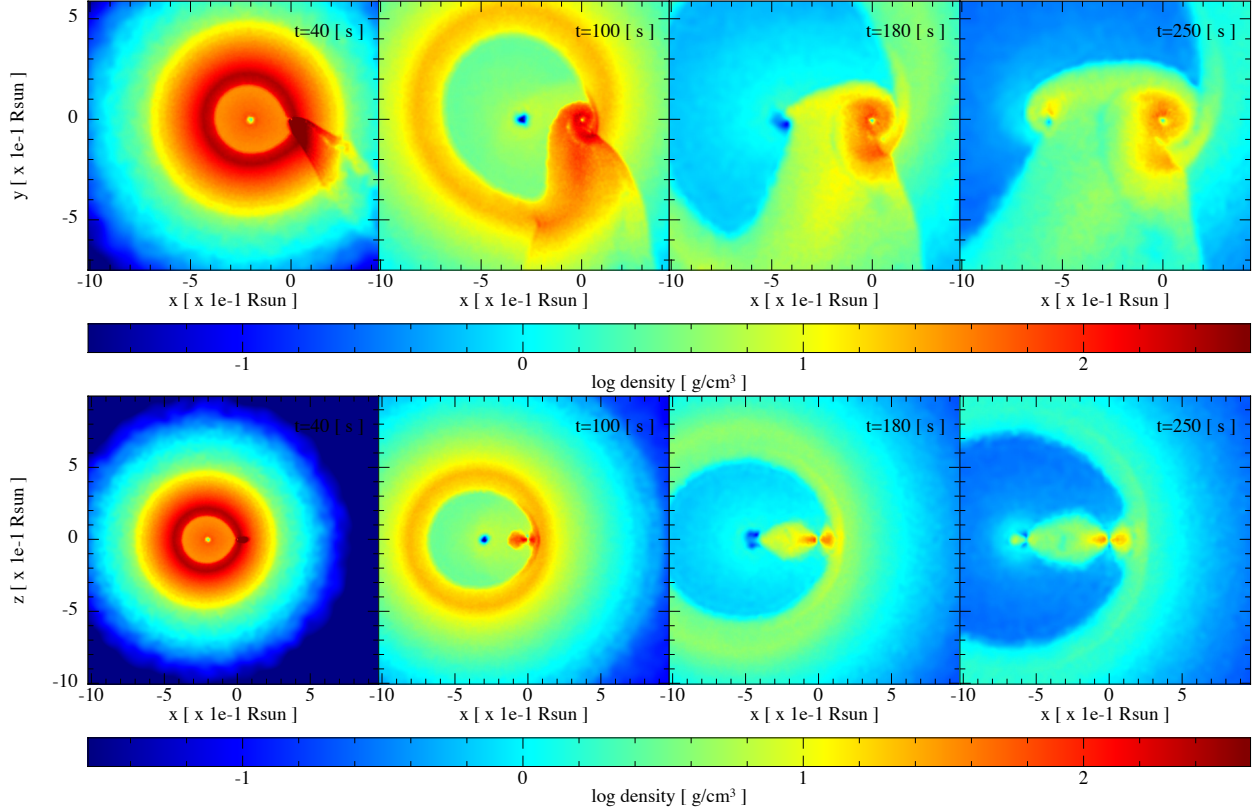


Figure 2. Snapshots of the SPH simulation of the IGC scenario. The initial binary system is formed by a CO_{core} , which progenitor is a $M_{\text{zams}} = 25 M_{\odot}$, and a $2 M_{\odot}$ NS with an initial orbital period of approximately 5 min (Model 25M1ple of table 2). The upper panel shows the mass density on the binary equatorial plane, at different times of the simulation, while the lower panel corresponds to the plane orthogonal to the binary equatorial plane. The reference system was rotated and translated in a way that the x-axis is along the line that joins the binary stars and the origin of the reference system is at the NS position. At $t = 40$ seconds (first frame from left to right), it can be seen that the particles captured by the NS have formed a kind of tail behind it, then this particles start to circularize around the NS and a kind of thick disk is observed at $t = 100$ s (second frame from left to right). The material captured by the gravitational field of the NS companion is also attracted by the νNS and start to be accreted by it as can be seen at $t = 180$ s (third frame). After around one initial orbital period, at $t = 250$ s, around the both stars have been form a kind of disk structure. The νNS is along the x-axis at: -2.02 , -2.92 , -3.73 and -5.64 for $t = 40$, 100, 180 and 250 s, respectively.

NOTE—This figure and all the snapshots figures where done with the SNSPLASH visualization program (Price 2011).

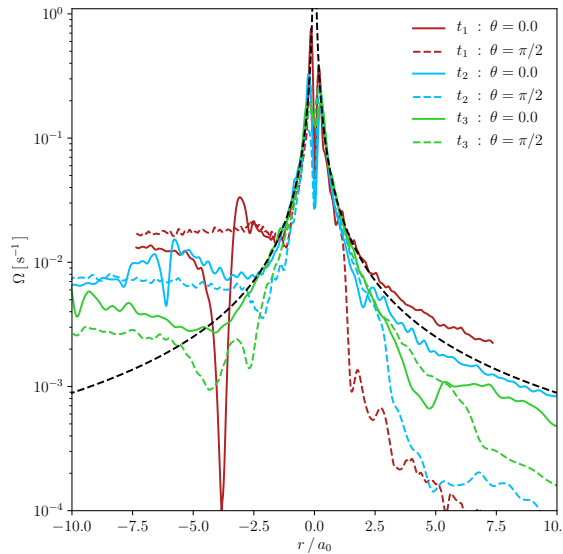


Figure 3. Angular velocity profiles of the SN material closed to the NS companion at three different times: $t_1 = 140.0$ s, $t_2 = 280.0$ s, $t_3 = 599.9$ s. The label $\theta = 0$ corresponds to the line that joins the binary stars and the label $\theta = \pi/2$ is the line perpendicular to the latter and lies on the equatorial binary system. Close to the NS, the angular velocity approaches the Keplerian angular velocity (black line). This suggests that, before being accreted, the particles have enough angular momentum to circularize around the star and form a kind of disk structure. The minimum of the solid line in the $-x$ direction indicates the position of the ν NS: at 3.01, 5.04 and 10.49 for t_1 , t_2 and t_3 respectively.

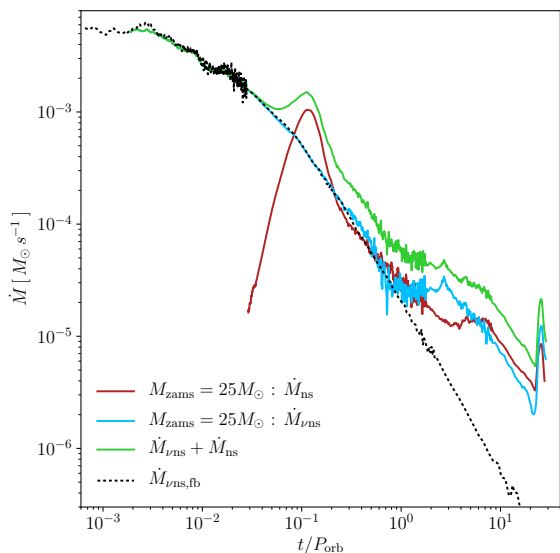


Figure 4. Mass accretion rate onto the NS (red line) and the ν NS (blue line) during the SPH simulation of the expansion of the SN ejecta. The green line shows the sum of both accretion rates. The initial binary system is formed by the CO_{core} of a $M_{\text{zams}} = 25 M_{\odot}$ progenitor and a NS of $2 M_{\odot}$ with an initial binary period of approximately 5 min. The dotted black line corresponds to the fallback mass-accretion onto the ν NS when the CO_{core} collapses in a single-star configuration, i.e., without the presence of the NS companion.

density and temperature conditions (see [Becerra et al. 2016](#), for details). This allows the matter to cool fast enough to be incorporated onto the star and we can add the mass of the particles that fulfill the accretion conditions (see section 2.1 and Equations 13). As we have shown the SN ejecta might transport a high amount of angular momentum and form a thick disk around the NS before the accretion take place. There, the densities and temperatures are not high enough to cool the matter by neutrino emission and outflows might occur ([Blandford & Begelman 1999](#); [Kohri et al. 2005](#); [Dexter & Kasen 2013](#), see, e.g.,). Up to 25% of the infalling matter can be ejected in strong outflows removing much of the system angular momentum ([Fryer et al. 2006a](#); [Fryer 2009](#)). This means that the mass-accretion rate calculated here might overestimate the actual accretion rate onto the star but up to a factor of order unity. It is also important to note that the accretion rate directly depends on the value adopted for the ξ parameter in Equation (10). For this simulation we adopted $\xi = 0.1$. In Section 6.1, we are going to vary this parameter and establish the influence of it on the system final fate.

As we anticipated, we have also run the simulation of the SN ejecta expansion without the NS companion, in order to calculate the fallback accretion rate (black dotted line in Figure 4) and compare it with the accretion rate onto the ν NS in the binary simulation. At the beginning of the simulation, there is no difference between both accretion rates: an almost flatter high accretion phase at early time and then a decline as $t^{-5/3}$ ([Chevalier 1989](#); [Zhang et al. 2008](#); [Fryer 2009](#); [Dexter & Kasen 2013](#); [Wong et al. 2014](#)). However, at around $t/P_{\text{orb}} \lesssim 1.0$, there is a jump in the fallback accretion rate of the binary simulation, that can be associated with the time at which the ν NS starts to accrete the material decelerated by the NS companion. The high early time accretion rate calculated here, is due to the fallback of those particles that did not have enough kinetic energy to escape from the ν NS gravitational field. This can occur, either because after the forward shock is launched the proto-NS cools and contracts sending a rarefaction wave to the ejecta that decelerates it ([Colgate 1971](#)), or because the SN shock is smoothly decelerated when it goes outward pushing the star material out ([Fryer 1999](#); [Woosley & Weaver 1995](#)).

4.2. SN explosion energy

In the following, we start to change systematically the initial parameters that will affect the fate of the final configuration. We will do it one by one, in order to determinate the most favorable conditions that increase the accretion rate onto the NS companion. Figure 5 shows the mass accretion rate onto the NS and onto the ν NS for different energies of the SN explosion, with the

same progenitor star: the $25 M_{\odot}$ of Table 1. As we explained in Section 2, in these simulations we scale the kinetic energy and the internal energy by a factor η (i.e. the velocities of the particles by $\sqrt{\eta}$) once we map the 1D exploded configuration to the 3D one. As expected, the total mass accreted by the NS companion is larger for low energetic SN than for high energetic ones, and then more favorable to the collapse of the NS (see models from 25m1p1e to 25m1p07e in Table 2). On the other hand, the energy of the SN explosion needs to be enough high, otherwise a considerable part of the ejected mass causes fallback and can instead induce the collapse of the ν NS to a BH. This is a novel and alternative possibility not considered in the original version of the IGC scenario (see, e.g., Rueda & Ruffini 2012; Fryer et al. 2014). Additionally, the energy of the SN explosion do not have a big influence on the magnitude of the peak of the mass-accretion rate but do have on its shape. The NS companion accretes more mass in the weakest SN explosion ($\eta = 0.7$) because the accretion rate is maintained almost constant for a longer time than in the strongest explosion ($\eta = 1$) where a clear peak appears. We can see that the late decay of the accretion rate depends on the SN explosion energy.

For these simulations, Figure 6 shows snapshots of the mass density and the specific internal energy on the equatorial plane after about one orbital period of the initial configuration (~ 5 min). Each panel corresponds to a different value of the η parameter: $\eta = 1.0$ and $\eta = 0.9$ for the left and right upper panels, $\eta = 0.8$ and $\eta = 0.7$ for the left and right bottom panels. The asymmetries of the interior ejecta layer are more pronounced for the less energetic explosion. The orbital period of the final configuration shortens with the decreases of the SN energy, i.e. with the accretion of mass by the binaries stars. For example, the accretion onto the ν NS and onto the NS companion is around 20% and 16%, respectively, more efficient for the weakest explosion ($\eta = 0.7$) with respect to the strongest one ($\eta = 1$), and the final orbital period is almost 90% shorter than the one of the final system from the most energetic explosion (see table 2).

As we did before, we calculate the fallback accretion rate for these explosions onto the ν NS for the isolated progenitors and compare and contrast it with its binary system counterpart. The right panel of Figure 5 shows the evolution of the mass accretion rate onto the ν NS. The black lines correspond to the single progenitors simulations. The accretion rate peaks at an early time and then decays as $\dot{M} \propto t^{-5/3}$ (Chevalier 1989). For the binary simulations (colors lines) a late peak on the fallback accretion rate is produced from the accretion of the material captured by the gravitational field of the NS companion. This is higher and even early for low energetic supernova (around one order of magnitude for

the less energetic explosion).

In order to compare the SN evolution in the single and binary simulations, in Figure 7 we show the SN density profile as seen from the ν NS at different times and for two different SN energies (models 25M1p1e and 25M1p07e of table 2). The left-side plots correspond to the explosion of the CO_{core} of the $25 M_{\odot}$ progenitor of table 1, while the right-side plots show its binary counterpart with a $2 M_{\odot}$ NS companion. For the isolated SN explosions, the SN ejecta density profiles evolve approximately following an homologous evolution keeping its spherical symmetry around the explosion center. For the explosions occurring in the close binaries, the NS companion gravitational field induced asymmetries in the SN fronts closer to it, that will be more pronounced for the low energetic explosions (see also Figure 6). We have shown in Becerra et al. (2016) that these asymmetries lead to observational effects both in the supernova optical emission and in the GRB X-ray afterglow.

4.3. Initial binary period

We continue the exploration of the parameter space of the initial binary configuration by running simulations with different values of the initial orbital period. Figure 9 shows the mass-accretion rate onto the NS companion for three different initial orbital periods: 4.8 min, 8.1 min and 11.8 min, and for two different SN energies: the fiducial explosion (with $\eta = 1$) and the $\eta = 0.7$ modified explosion. For the two explosion energies, the accretion rate seems to scale with the initial binary period of the configuration and follow the same power law at the late times of the accretion process. On the other hand, for longer binary periods, as expected, the accretion onto the ν NS tends to equal the fallback accretion when the CO_{core} explodes as an isolated star. This can be seen by comparing the final mass of the ν NS in both scenarios (columns $M_{\nu\text{ns,fb}}$ and $M_{\nu\text{ns}}$ in Table 2).

Figure 8 shows snapshots, at two different times, of the surface density on the orbital plane for the same initial binary periods of Figure 9 and the modified explosion with $\eta = 0.7$. The system appears to evolve self-similarly with the increase of the binary period.

4.4. Initial mass of the NS

Up to now we have considered a massive initial NS companion of $2.0 M_{\odot}$, since we expect the progenitor of the CO_{core} losses its hydrogen and helium layers interacting with its companion (through common envelope and Roche-lobe overflow episodes (Lee & Cho 2014)). Observationally, the measured NS masses in double NS binaries are lighter than $1.5 M_{\odot}$ (Lattimer & Prakash 2007) and massive, $\sim 2 M_{\odot}$ NSs have been measured in binaries with white dwarf companions, i.e. PSR J1614–2230 (Demorest et al. 2010) and PSR J0348+0432 (An-

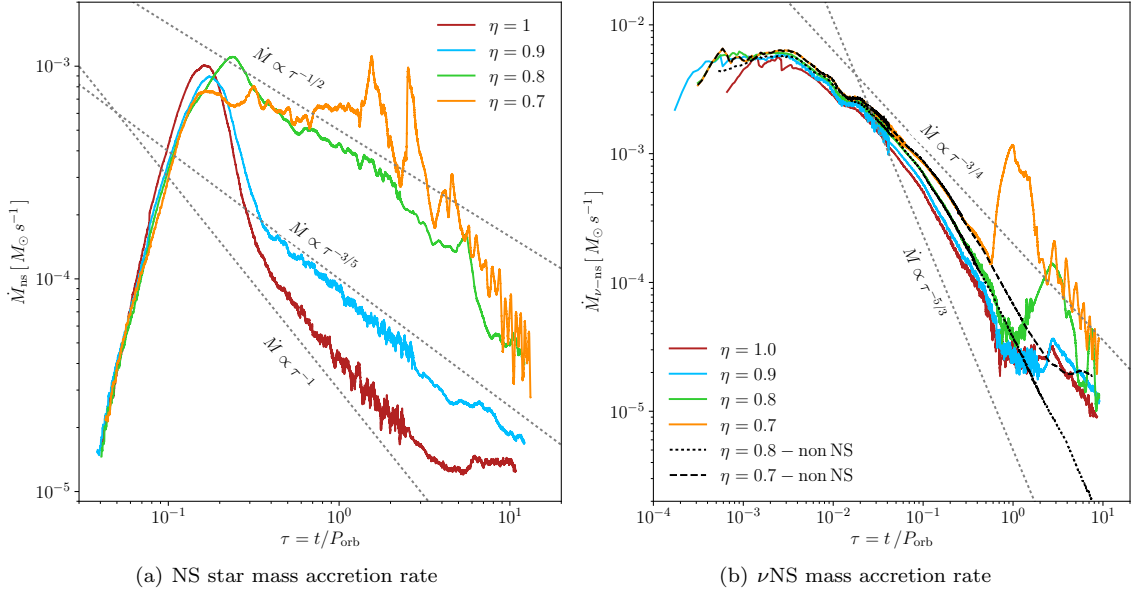


Figure 5. Mass-accretion rate on the NS (left panel) and the ν NS (right panel) in the IGC scenario. The initial binary system is the same as the one of Figure 4 but the SN explosion energy has been varied scaling the kinetic and internal energy of the SPH particles by the factor $\eta < 1$. The accretion rate onto the NS presents a peak for the more energetic SN, while in the weaker ones this peak is flattened, i.e. the accretion happens at a nearly constant rate for a longer time, making the star to increase its mass faster. At early times, the fallback accretion rate onto the ν NS is nearly independent on the SN energy, although the late bump induced by the accretion of the matter gravitational capture by the NS companion is stronger for the weakest explosions.

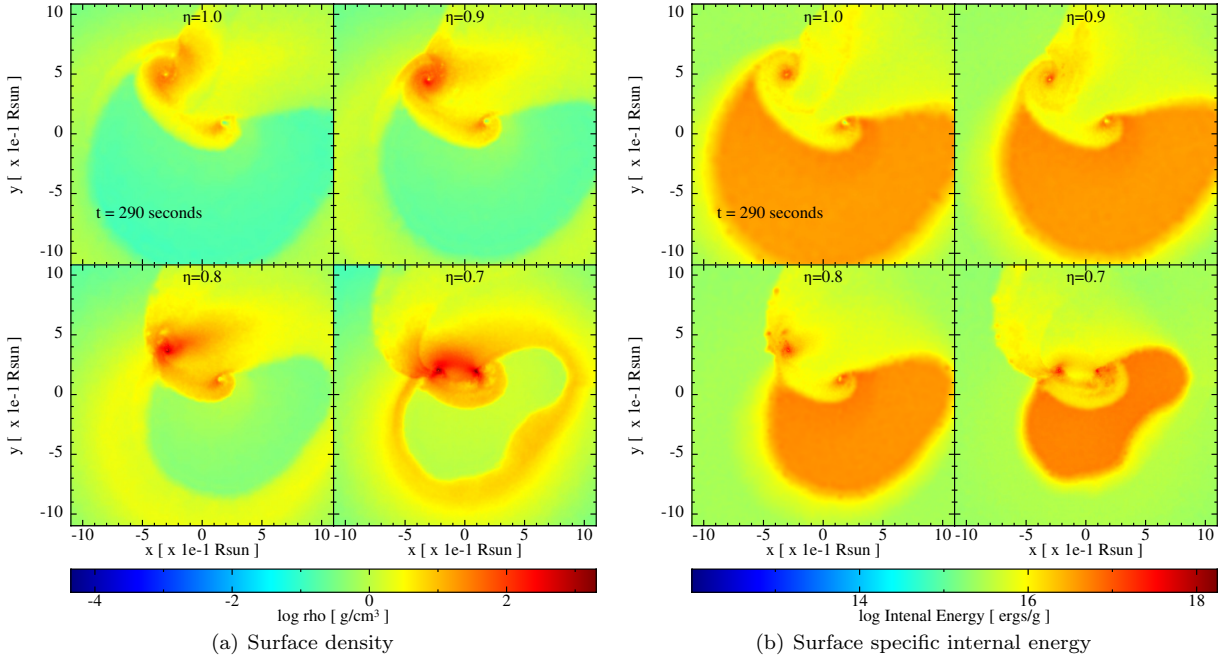


Figure 6. Snapshots of the mass density (left panel) and the specific internal energy (right panel) on the equatorial plane after 290.0 s from the beginning of the SPH simulation (around one orbital period of the initial binary system). The initial binary system parameters are the same as the one represented in Figure 2 but the SN explosion energy has been scaled by a factor η shown at the upper side of each panel (these simulations correspond to models 25M1p1e with $\eta = 1$, 25M1p09e with $\eta = 0.9$, 25M1p08e with $\eta = 0.8$ and 25M1p07e with $\eta = 0.7$ of table 2). The accretion onto the ν NS as the NS companion is higher for the weaker SN explosions, then the star masses increases faster and the final orbital period of the system shortens. In these explosions also the amount of mass accreted by the ν NS is larger.

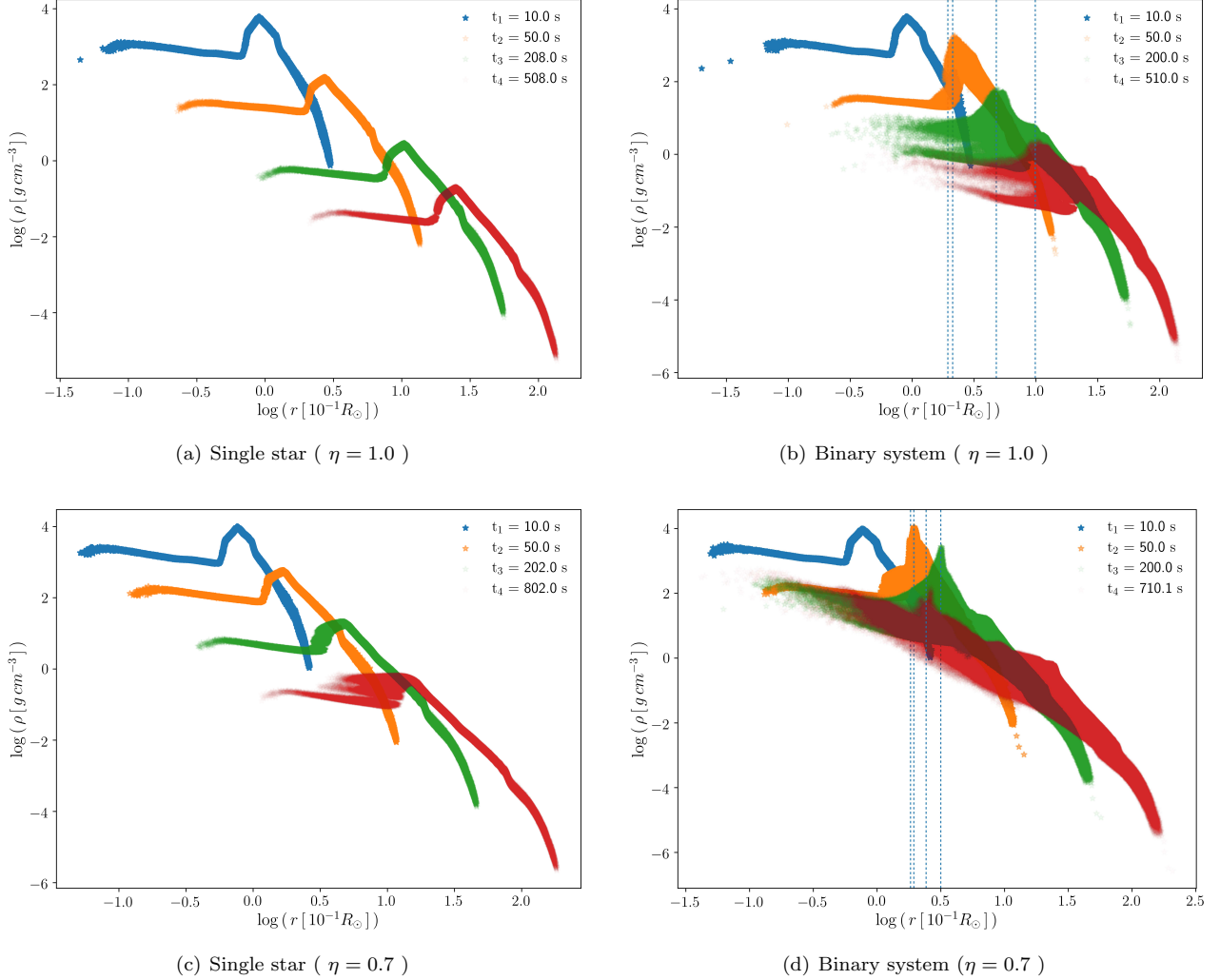


Figure 7. Density profile evolution of the SN ejecta after the core-collapse of the CO_{core} of a $25 M_{\odot}$ progenitor. The r coordinate is measured from the νNS position. The plots at the left panel correspond to the evolution of the SN in a single-star system while, in the ones at the right panel, the CO_{core} belongs to a binary system with a NS companion of $2 M_{\odot}$ and an initial binary separation of 1.36×10^{10} cm. The blue-dotted lines indicate the position of the NS companion. The SN energy of the upper plots is 1.56×10^{51} erg (Model 25M1p1e of table 2) and for the lower plots the SN energy is 6.4×10^{50} erg (Model 25M1p07e of Table 2). For isolated SN explosions (or for very wide binaries), the density of the SN ejecta would approximately follow the homologous evolution as is seen in the left panel plots. For explosions occurring in close binaries with compact companions (as it is the case of the IGC progenitors), the SN ejecta is subjected to a strong gravitational field which produces an accretion process onto the NS companion and a deformation of the SN fronts closer to the accreting NS companion, as seen in the right panel plots.

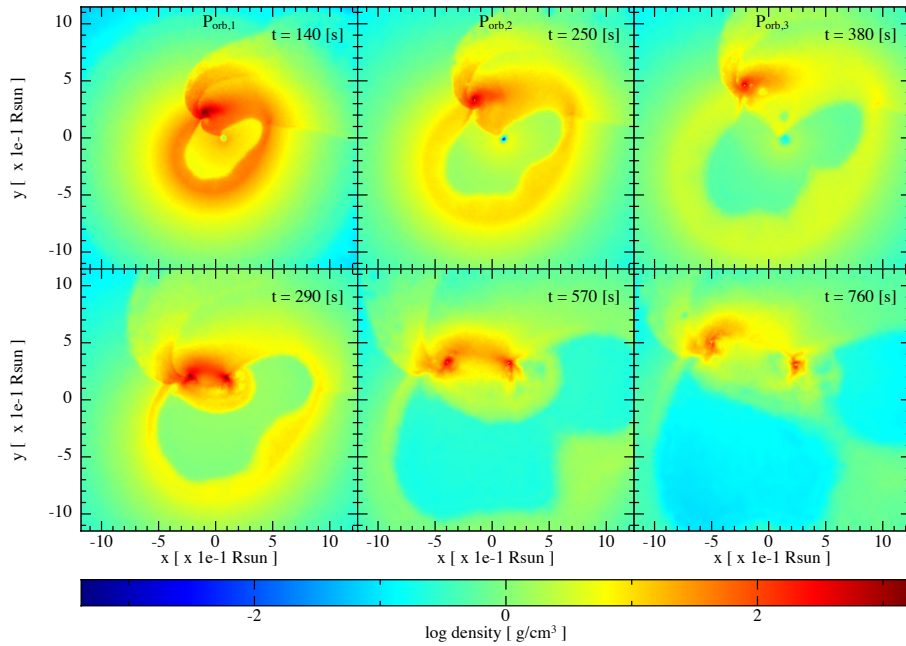


Figure 8. Snapshots of the surface density on the equatorial plane for systems with three different initial binary periods. The initial binary system is formed by the CO_{core} of the $M_{\text{zams}} = 25 M_{\odot}$ progenitor (see table 1) and a $2 M_{\odot}$ NS. The SN energy has been reduced to 6.5×10^{50} erg, scaling the particles velocity and the internal energy by a factor $\eta = 0.7$. The periods of the labels are $P_{\text{orb},1} = 4.8$ min, $P_{\text{orb},1} = 8.1$ min and $P_{\text{orb},1} = 11.8$ min that correspond to Models 25m1p07e, 25m3p07e and 25m2p07e of table 2, respectively.

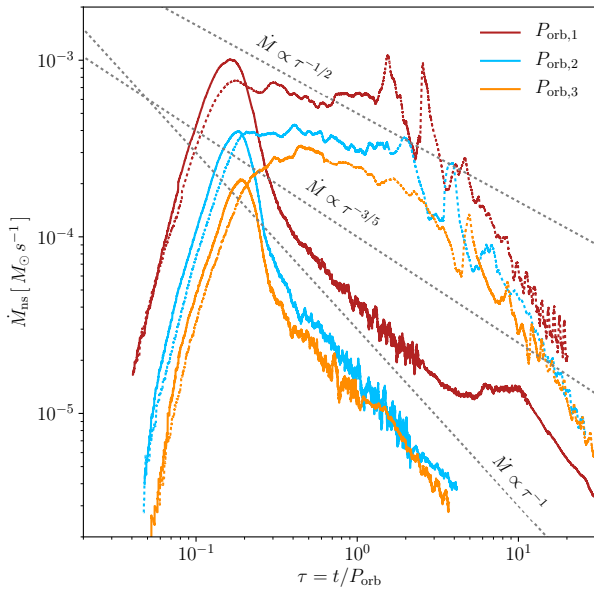


Figure 9. Mass-accretion rate onto the NS companion in the IGC scenario. Different colors correspond to different initial orbital periods: $P_{\text{orb},1} = 4.8$ min (red line), $P_{\text{orb},1} = 8.1$ min (blue line), $P_{\text{orb},1} = 11.8$ min (orange line). The other parameters that characterize the initial binary system are the same as in Figure 4. The solid lines correspond to a SN energy of 1.57×10^{51} erg, while the dotted ones correspond to a lower SN energy of 6.5×10^{50} erg. It can be seen that the mass-accretion rate scales with the binary orbital period.

toniadis et al. 2013).

In order to increase the parameter space, we have also run simulations with different initial masses for the NS companion: $1.4 M_{\odot}$ and $1.6 M_{\odot}$. In Table 3 we summarize the results of these simulations. In these cases, the models are labeled as “ $x_1\text{Mns}x_2\text{p}x_3\text{e}$ ”, where x_1 is the initial mass of the NS companion, x_2 and x_3 have the same meaning as the model labels of Table 2. We report also the same columns as in Table 2. For the progenitor of the CO_{core} we used $M_{\text{zams}} = 25 M_{\odot}$.

Figure 10 shows the evolution of the mass accretion rate onto the NS companion as a function of the time normalized to the initial orbital period. As expected, for an initial binary system with a massive NS companion, the mass accretion rate onto it increases during the SN expansion, i.e. the gravitational force due to a massive NS is stronger. For example, the NS companion gained around 4.2%, 3.9% and 3.1% of its initial mass for the 25Mns1p1e, 16Mns1p1e and 14Mns1p1e models, respectively and 36.3% and 31.1% for the 14Mns1p07e and 25Mns1p07e, respectively. On the other hand, the evolution of the mass accretion rate seems to not be influenced by the NS companion initial mass. For the most energetic explosion ($\eta = 1.0$), there is an early peak, followed by a power-law decay and a late bump. This bump is early and bigger for a more massive NS companion. For the less energetic explosion ($\eta = 0.7$), there is a nearly constant mass accretion phase, followed by some

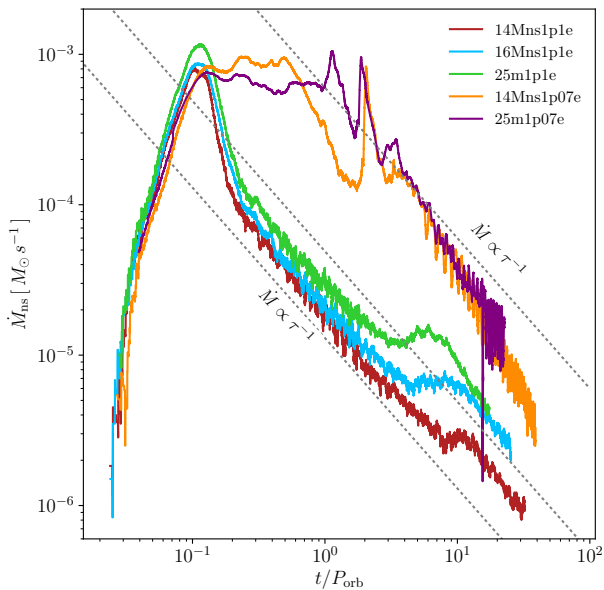


Figure 10. Mass-accretion rate on the NS companion for different initial masses. The initial orbital period is close to the minimum period that the system can have in order that there is no Roche Overflow before the collapse of the CO_{core} .

oscillations and a power-law decay. Finally, the total accreted mass on the νNS from the fallback seems not to be affected by the initial mass of the NS companion. In the case of the most energetic explosion, the νNS final mass, in these simulations, is around $1.9 M_{\odot}$ and for the less energetic one is around $2.4 M_{\odot}$. The differences between the simulations of equal SN energy could be due to numerical errors.

4.5. Asymmetric SN expansion

We now explore how a SN explosion with an asymmetric blastwave affects the evolution of the system. In Table 4 we summarize the results of these simulations. In these cases, the models are labeled as “ $x_1x_2\Theta:x_3$ ”, where x_1 and x_2 are the values of the parameter f and Θ , respectively, of Equations (18) and (19), and x_3 is the direction of the lobe. We started the simulations with the parameters $f = 2.0$ (in-cone to out-cone velocity ratio) and $\Theta = 20.0$ (cone amplitude), with the direction of the lobe in the z -axis (perpendicular to the equatorial binary plane) and in the $+x$ -axis (directed to the NS companion) and $-x$ -axis (opposed to the NS companion). Additionally, we explore the dependence with the opening angle and the velocities ratio, running simulations with $f = 4.0$ and with $\Theta = 40$. Figure 11 shows the accretion rate onto the NS companion for these simulations. We can see that the introduction of asymmetries in the SN expansion velocity increases the accretion rate onto the NS companion as well as the fallback accretion rate onto the νNS . This is expected because, in order to conserved the SN energy explosion, we increased the

velocities of the particles inside the cone while we decreased the velocities of the particles out-side it, then these slower particles are more probably captured by the stars. The direction on the lobe does not introduce great changes in the evolution of the accretion rate or the final star mass of the configurations but it does when the parameters f or Θ are increased.

Figure 12 shows snapshots of the surface density for the simulations of the asymmetric SN expansion. As it was previously done, the reference system was rotated and translated in the way that its center corresponds to the NS companion position and the x -axis joins the binary stars. Contrary to the symmetry cases, the binary orbital plane change after the SN explosion if the lobe of the explosion is outside the equatorial plane of the initial binary. For example, for $f = 2.0$, the final orbital plane makes an angle of 2.55° with respect to the initial orbital plane and for $f = 4.0$, this angle grows up to 11.5° . However, either for the symmetry or the asymmetric explosion, the magnitude of the velocity of the center-of-mass of the final binary system remains around $100\text{--}800 \text{ km s}^{-1}$. The kick velocities given in Table 2 are due to the accretion of linear momentum from the accreted particles and the gravitational attraction that the ejecta material do on the νNS (Janka & Mueller 1994). Another source for the NS kick velocity can be due to the anisotropic emission of the neutrino during the star collapse (Woosley 1987; Bisnovatyi-Kogan 1993; Fryer & Kusenko 2006).

4.6. CO_{core} progenitor mass

Finally, we have varied the progenitor of the CO_{core} . Figure 13 shows the mass-accretion rate onto the NS companion for all the progenitors listed in Table 1. In Table 2 we summarize the results for these simulations, and additionally we have run more simulations with each of these progenitors changing the SN energy and the initial binary separation. We now present the salient properties of these simulations.

The $15 M_{\odot}$ ejects just around $1.6 M_{\odot}$, then the energy of the SN explosion needs to be low (on the order of 10^{50} erg) and the binary system enough compact, in order to have a significant accretion onto the NS companion. However, if the SN energy is considerably reduced, most of the SN material will do fallback onto the νNS . For example, scaling the SN kinetic energy and internal energy by $\eta = 0.05$, almost 80% of the SN ejecta is accreted by the νNS , while scaling the parameter to $\eta = 0.1$, the accreted material via fallback is reduced to the 30%. It is important to point out that, if the initial orbital period is increased by a factor of 1.7, the amount of ejected mass that can not escape the νNS gravitational field grows to the 55%. Namely, the presence of a close NS companion could avoid the collapse

Table 3. SPH Simulations with different mass for the NS companion.

Model	$M_{\nu\text{ns},0}$ (m_{\odot})	$P_{\text{orb},i}$ (min)	$a_{\text{orb},i}$ (10^{10} cm)	$M_{\nu\text{ns}}$ (m_{\odot})	M_{ns} (m_{\odot})	V_{CM} (10^7 cm/s)	$P_{\text{orb},f}$ (min)	$a_{\text{orb},f}$ (10^{10} cm)	e	m_{bound} (M_{\odot})	bound
14Mns1p1e	1.4	4.29	1.216	1.971	1.443	6.47	293	15.28	0.929	4.2×10^{-3}	yes
16Mns1p1e	1.6	4.35	1.244	1.956	1.664	7.19	1872	53.566	0.979	5.1×10^{-2}	yes
14Mns1p07e	1.4	4.29	1.216	2.457	1.909	3.33	4.20	0.977	0.375	9.8×10^{-2}	yes

NOTE—For the progenitor of CO_{core} we used the one with $M_{\text{zams}} = 25 M_{\odot}$.

Table 4. SPH Simulations with an asymmetric blastwave.

Model	$M_{\nu\text{ns},\text{fb}}$ (m_{\odot})	V_{kick} (10^4 cm/s)	$M_{\nu\text{ns}}$ (m_{\odot})	M_{ns} (m_{\odot})	V_{CM} (10^7 cm/s)	$P_{\text{orb},f}$ (s)	$a_{\text{orb},f}$ (10^{10} cm)	e	m_{bound} (M_{\odot})	bound
2f20 Θ : z	1.931	1.18×10^3	2.009	2.161	7.31	2852.15	4.849	0.774	0.065	yes
2f20 Θ : x	1.931	1.18×10^3	1.959	2.142	7.13	8225.79	9.772	0.892	0.056	yes
2f20 Θ : -x	1.931	1.18×10^3	2.002	2.182	7.82	3170.17	5.209	0.801	0.054	yes
4f20 Θ : z	2.826	5.08×10^3	2.382	2.424	5.16	456.51	1.496	0.438	0.189	yes
2f40 Θ : z	2.364	5.38×10^3	2.316	2.395	5.84	529.37	1.643	0.589	0.105	yes

NOTE—The initial binary system is formed by the CO_{core} of the $M_{\text{zams}} = 25 M_{\odot}$ progenitor and a NS of $2 M_{\odot}$. The initial binary parameters are the same of the model 25m1p1e of table 2 but the SN velocity profile was modified with equations (18) and (19).

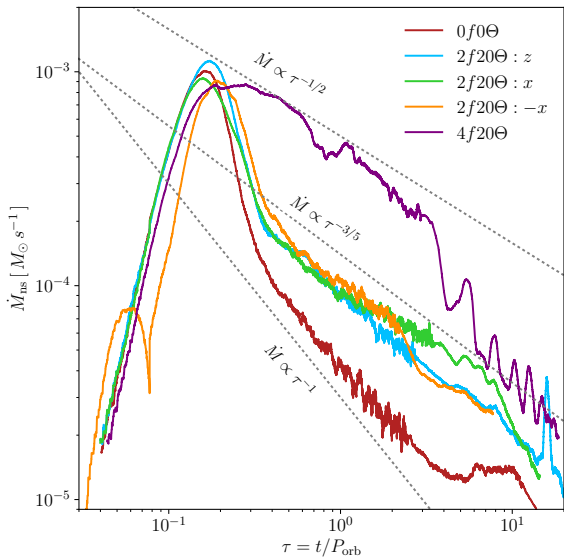


Figure 11. Mass-accretion rate onto the NS companion introducing a conical geometry for the SN velocity profile of the $M_{\text{zams}} = 25 M_{\odot}$ progenitor (see Table 1). The parameter of the initial binary system are the same as the one for Figure 4. The cone was opened along the z -axis (perpendicular to the orbital plane—blue and purple lines) and along the x -axis (on the orbital plane—green and orange lines). Since the SN energy is conserved, the introduction of the asymmetry reduces the particles velocity and increases the accretion rate.

of the νNS in the weak explosion cases.

For the $30 M_{\odot}$ progenitor, we worked with two simulated explosions with different energies, one almost one order of magnitude stronger than the other. For the lowest energetic explosion, $E_{\text{sn},1}$, a significant amount

of mass is making fallback, then the collapse due to the hypercritical accretion onto the νNS is more probable than the one of the NS companion. The mass accretion rate on the NS companion flattens for this SN explosion (see Figure 13). On the other hand, the velocities of the stronger energetic explosion, $E_{\text{sn},2}$, are so high that almost all the SN ejecta surpass the NS companion without being captured by it. For these explosions, the ratio between the total SN energy and the kinetic energy is 0.45 and 0.81, respectively.

We have performed more simulations scaling the energy of these two explosions, and summarize their results in Table 2. In these cases, we can evaluate how accurate is our alternative path of changing the explosion energy by scaling the velocities and the internal energy of the SPH particles, instead of re-run new simulations of the CO_{core} collapse and bounce of the shock. Figure 14 shows the density profile at around the same time for the two explosions of the $30 M_{\odot}$ progenitor and their respective simulations with the scaled SN energy. In general, the internal radius of the low energetic explosion is about two times smaller than the one of the high energetic explosion (see Figure 1). These will increase the material that will make fallback in the single star as well as in the binary system simulations, even when the scaled energy of the explosion becomes comparable.

Finally, we use the $40 M_{\odot}$ progenitor of the CO_{core} . Since for this progenitor the ejected mass in the SN is around $11 M_{\odot}$, the energy of the explosion needs to be low to allow the configuration to remain bound and also for the NS companion to be able to accrete enough mass

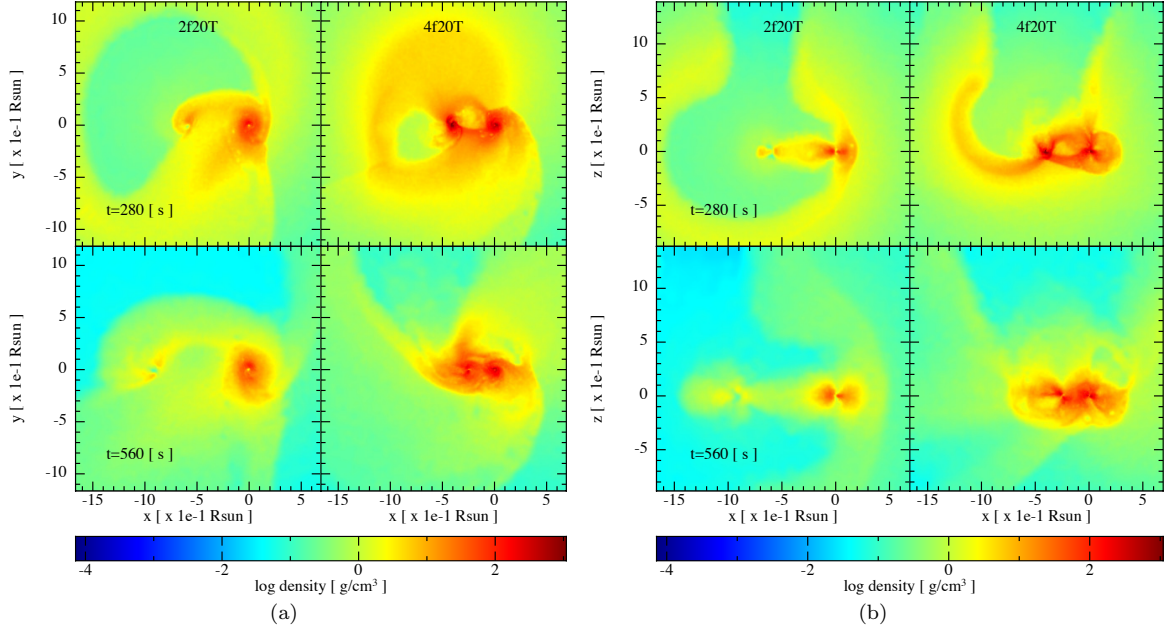


Figure 12. Snapshots of the surface density on the binary equatorial plane (left panel) and the plane orthogonal to it (right panel). The reference system have been rotated and translated in a way that the x -axis becomes directed in the line that joins the binary stars and its origin is at the NS companion companion. The initial binary system is the same as the one represented in Figure 2 but the SN velocity profile has been modified to a conical geometry following Equations (18) and (19). In all the cases, the cone opens along the z -axis. The left frames of each plot have parameters $f = 2.0$ and $\Theta = 20.0$ (Model 25m2f20tz of table 2) while the right ones have $f = 4.0$ and $\Theta = 20.0$ (Model 25m4f20tz of table 2). If the lobe of the explosion is directed outside of the initial orbital plane, as in here, the orbital plane of the final configuration changes. For the case $f = 2.0$, the final orbital plane makes an angle of 2.55° with respect to the initial orbital plane and for $f = 4.0$, this angle grows up to 11.5° .

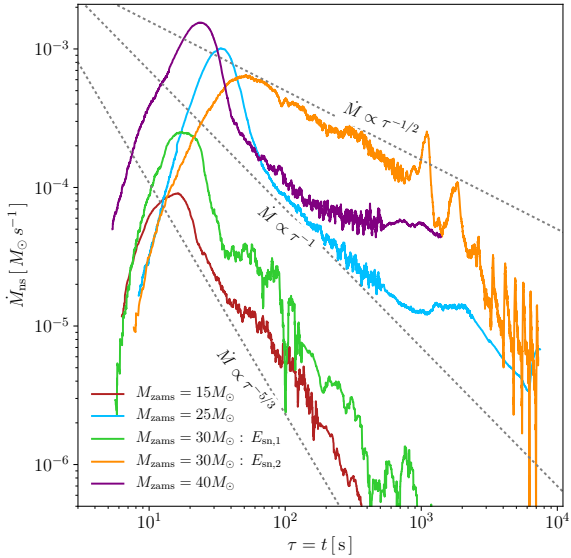


Figure 13. Mass-accretion rate on the NS companion using the explosion of all the CO_{core} progenitors summarized in Table 1. The NS companion has an initial mass of $2 M_\odot$ and the orbital period is close to the minimum period that the system can have in order that there is no Roche-lobe overflow before the collapse of the CO_{core} : 6.5 min, 4.8 min, 6.0 min and 4.4 min for the $M_{\text{zams}} = 15 M_\odot$, $25 M_\odot$, $30 M_\odot$ and $40 M_\odot$ progenitors, respectively.

to collapse. If we use a factor $\eta = 0.7$ to reduce the SPH particles velocity and internal energy, we see that the amount of mass accreted by the νNS is low but the mass accreted by the NS-companion could make it to induced its collapse. Instead, for $\eta = 0.5$, most of the ejecta make fallback accretion onto the νNS . In table 5, we estimate the initial and final mean bulk SN velocity in the simulations, $\langle v \rangle_{\text{initial}}$ and $\langle v \rangle_{\text{final}}$, computed as:

$$\langle v \rangle = \sqrt{\frac{2E_k}{M_{\text{ej}}}}, \quad (20)$$

where E_k is the total kinetic energy of the SPH-particles and M_{ej} is the total mass of the expanding material particles. We compute this for all the CO_{core} progenitors and for different values of the η parameter. We do not account here for the acceleration of the SN ejecta arising from the energy injection in the accretion process and in the GRB emission via the impact onto the SN by the e^+e^- plasma. As it has been shown in Ruffini et al. (2018a), the high velocities that characterize the HNe associated with GRBs are explained by this mechanism.

Fryer et al. (2014) performed a 1D numerical simulations of the CO_{core} collapse, bounce and explosion and it was estimated the accretion rate onto the NS companion using the Bondy-Hoyle formalism (Hoyle & Lytleton 1939; Bondi & Hoyle 1944; Bondi 1952). In these

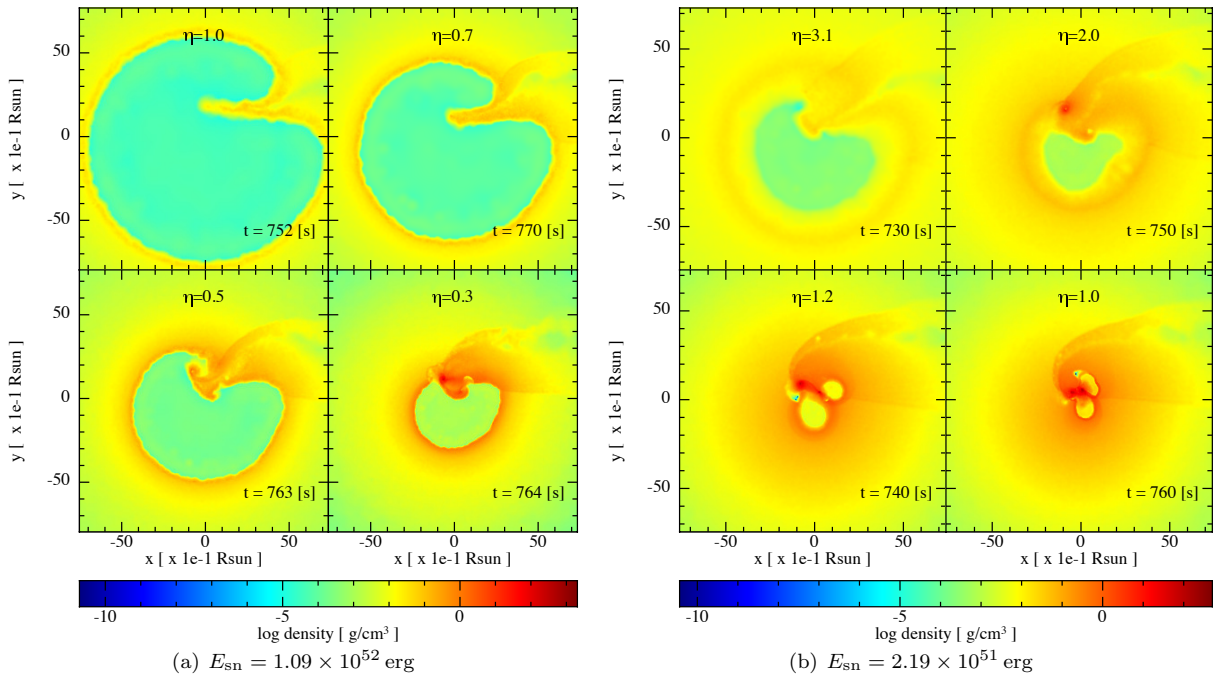


Figure 14. Snapshots of the surface density on the binary equatorial plane. The initial binary system is formed by the CO_{core} of the $M_{\text{zams}} = 30 M_{\odot}$ progenitor and a $2 M_{\odot}$ NS with an orbital period of around 6 min. We have simulated the collapse and bounce of the $30 M_{\odot}$ progenitor with two different SN energies as is specified in the left and right panel labels. We show the simulations scaling the SN energy of these two explosions by a factor η (specified in the upper part of each frame). In general, the internal radius of the low energetic explosion is about two times smaller than the one of the high energetic explosion. This increases the fallback accretion onto the νNS and the region near to the binary system becomes denser.

Table 5. Supernova initial and final mean bulk velocity

Progenitor	η	$\langle v \rangle_{\text{initial}}$	$\langle v \rangle_{\text{final}}$	Progenitor	η	$\langle v \rangle_{\text{initial}}$	$\langle v \rangle_{\text{final}}$
M_{zams}		10^8 cm s^{-1}	10^8 cm s^{-1}	M_{zams}		10^8 cm s^{-1}	10^8 cm s^{-1}
$15 M_{\odot}$	0.7	7.316	8.763	$30 M_{\odot}^a$	0.7	7.931	7.931
	0.5	6.183	7.103		0.7	4.912	6.227
	0.3	4.789	5.066	$30 M_{\odot}^b$	1.0	3.097	4.845
			1.2		3.393	5.538	
$25 M_{\odot}$	1.0	4.186	5.805		1.0	4.949	7.232
	0.9	3.889	5.079	$40 M_{\odot}$	0.9	4.667	6.624
	0.8	3.560	4.341		0.8	4.405	5.976
	0.7	3.217	3.945		0.7	4.114	5.288

simulations, at the beginning of the accretion process, there is a burst in the accretion rate, growing up to the $10^{-1} M_{\odot} \text{ s}^{-1}$, that is two order of magnitude greater than the accretion rate that we are obtaining with the SPH simulation. However, the total time of the accretion process is much shorter in those simulations than the one presented here, making the amount of mass accreted by the NS companion comparable between the simulations. This discrepancy is a direct consequence of the increase of dimension of the simulation. While the 1D simulation is stopped when the SN innermost layer reaches the NS, the 3D simulation can continue because

there are particles that remain bound to the NS companion in a kind of disk structure, and the star continues the accretion process.

5. BOUND AND UNBOUND SYSTEMS

We have also studied the evolution of the binary parameters during the SN expansion.

If we were to assume that the ejected mass in the SN explosion leaves the system instantaneously, the semi-major axis of the post-explosion system, a , is given by $a/a_0 = (M_0 - \Delta M)/(M_0 - 2a_0 \Delta M/r)$, where M_0 and a_0 is the total mass and the semi-major axis of the initial

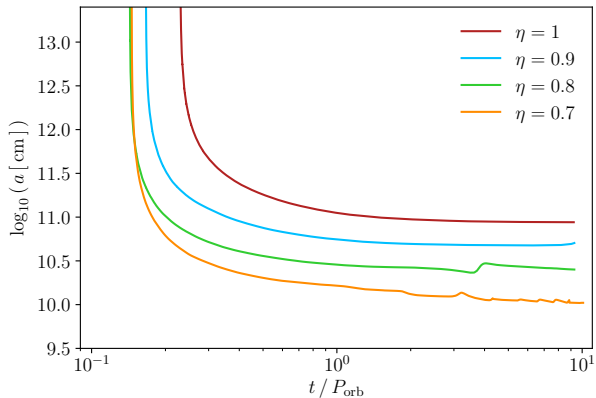


Figure 15. Evolution of the semi-major axis of the ν NS-NS binary system. The initial configuration is a binary system formed by the CO_{core} of a $M_{\text{zams}} = 25 M_{\odot}$ progenitor and a NS of $2 M_{\odot}$ with an initial binary period of approximately 5 min. The CO_{core} collapses and undergoes a SN explosion ejecting around $5 M_{\odot}$ and leaving a proto-NS of $1.85 M_{\odot}$. Not all the material ejected in the SN leaves the binary system. Some part of this material fallback and is accreted by the remnant star from the collapse of the CO_{core} while, some other part, is accreted by the NS companion. The final binary configuration can remain bound even when the system lost most of the half of its initial total mass.

binary system, ΔM is the mass ejected in the SN and r is the star separation at the moment of the explosion (Hills 1983). Then, binaries with circular initial orbits become unbound after a SN event if more than half of its total initial mass is lost. However, as it was shown in Fryer et al. (2015), in the IGC scenario the mass loss can not be considered instantaneous because the binary initial periods are of the same order than the time it takes for the slowest SN layer to reach the NS companion. For example, the innermost layers of the $25 M_{\odot}$ progenitor have a velocity of the order of 10^8 cm s^{-1} so they reach the NS initial position in a time $\sim 100 \text{ s}$, nearly $2/5$ of the initial binary period. Moreover, it has to be considered that either the ν NS or the NS companion will accrete mass and momentum from the SN ejecta, and this will reduce the system mass loss.

Figure 15 shows the evolution of the binary semi-major axis with time for the same cases of Figure 5. In these simulations, that correspond to the minimum orbital period of the initial binary system ($\sim 5 \text{ min}$), independently on the SN energy, the post-explosion system remains bound. This occurs even if the system loses more than the half of its total initial mass. For example, for the $\eta = 1$ case, the mass loss in the system is around $4.82 M_{\odot}$, namely about 54.7% of its total initial mass.

For the fiducial SN model, an increase by a factor 1.7 of the orbital period changes the fate of the post-explosion binary system, leading to an unbound final configuration. While, for the less energetic explosion, the system remains bounded in all scenarios in which we have increased the initial binary period (up to \approx

60 min, i.e. ≈ 12 times the minimum orbital period). The determination of the maximum orbital period that the system can have in order to remain bound after the SN explosion is left for a future work.

6. MASS-ACCRETION RATE, NS CRITICAL MASS AND GRAVITATIONAL COLLAPSE

We turn now to evaluating whether the NS companion collapses or not to a BH due to the accretion of part of the SN ejecta. For this, we need both to study how the NS gravitational mass and angular momentum evolve with time, and to set a value to the NS critical mass. As a first approximation, we assume that the NS evolves from an equilibrium configuration to the next, using the uniformly rotating NS equilibrium configurations in Cipolletta et al. (2015); Cipolletta et al. (2017). These configurations were constructed using the public code RNS (Stergioulas & Friedman 1995) to solve the axisymmetric Einstein equations for three selected relativistic mean-field nuclear matter equations of state (EOS) models: NL3, GM1 and TM1. The mass-radius relations obtained for these EOS satisfy current observational constraints (see figure 5 in Cipolletta et al. 2015). The most stringent constraint is that the critical mass for gravitational collapse of a non-rotating NS must be larger than the mass of the most massive NS observed: the pulsar PSR J0348+0432 with $2.01 \pm 0.04 M_{\odot}$ (Antoniadis et al. 2013)¹. Recently, it was claimed the measurement of a more massive NS, PSR J2215+5135 with $2.27^{+0.17}_{-0.15} M_{\odot}$ (Linares et al. 2018) and $f \approx 383 \text{ Hz}$ (Breton et al. 2013). This measurement is still under debate and, for this paper, we use constraint imposed by the mass of PSR J0348+0432. The current measurements of NS radii e.g. from X-ray observations, unfortunately, poorly constrain the mass-radius relation and so the nuclear EOS (see e.g. Cipolletta et al. 2015, for details).

In general, for uniformly rotating NS configurations, when the star accretes an amount of baryonic mass, M_b , and angular momentum, J_{ns} , its gravitational mass, M_{ns} , evolves as:

$$\dot{M}_{\text{ns}} = \left(\frac{\partial M_{\text{ns}}}{\partial M_b} \right)_{J_{\text{ns}}} \dot{M}_b + \left(\frac{\partial M_{\text{ns}}}{\partial J_{\text{ns}}} \right)_{M_b} \dot{J}_{\text{ns}}. \quad (21)$$

From Cipolletta et al. (2015), we know the relation $M_{\text{ns}}(M_b, J_{\text{ns}})$:

$$\frac{M_b}{M_{\odot}} = \frac{M_{\text{ns}}}{M_{\odot}} + \frac{13}{200} \left(\frac{M_{\text{ns}}}{M_{\odot}} \right)^2 \left(1 - \frac{1}{130} j_{\text{ns}}^{1.7} \right), \quad (22)$$

¹ We recall that this pulsar constrains the non-rotating NS mass-radius relation because the structure of a NS rotating at the measured rate of PSR J0348+0432, $f \approx 26 \text{ Hz}$ (Antoniadis et al. 2013), in practice “overlaps” with the one of a non-rotating NS (see e.g. Cipolletta et al. 2015).

Table 6. Properties of the NS critical mass for NL3, TM1 and GM1 EOS.

EOS	$M_{\max}^{J_{\text{ns}}=0}$ (M_{\odot})	$M_{\max}^{J_{\text{ns}}\neq 0}$ (M_{\odot})	f_{\max} (kHz)
NL3	2.81	3.38	1.40
GM1	2.39	2.84	1.49
TM1	2.20	2.62	1.34

NOTE— $M_{\max}^{J_{\text{ns}}=0}$: critical mass for non-rotating case. $M_{\max}^{J_{\text{ns}}\neq 0}$: maximum critical mass value, i.e. the mass of the configuration along the secular instability line and rotating at the Keplerian value. f_{\max} : rotation frequency of the NS with $M_{\max}^{J_{\text{ns}}\neq 0}$. Table taken from [Cipolletta et al. \(2015\)](#).

where $j_{\text{ns}} \equiv cJ_{\text{ns}}/(GM_{\text{ns}}^2)$. This relation is common to all the NS matter EOS studied in [Cipolletta et al. \(2015\)](#) within an error of 2%. The mass and angular momentum of the accreted particle add to the baryonic mass and the angular momentum of NS, thus we can integrate Equation (21) and follow the evolution of the gravitational mass of both the ν NS and the NS companion. The NS accretes mass until it reaches an instability point: the mass shedding limit or the secular axisymmetric instability. The first limit is met if the star angular velocity has growth enough that the gravitational force at the stellar equator equals the centrifugal force, then a faster rotation will induce the ejection of matter. Although the dimensionless angular momentum parameter has a nearly EOS-independent value along the mass-shedding sequence, $cJ_{\text{ns}}/(GM_{\text{ns}}^2) \approx 0.7$ ([Cipolletta et al. 2015](#)), the numerical value of J_{ns} at the shedding point depends on the specific EOS since M_{ns} is different. On the other hand, the secular axisymmetric instability which defines the critical mass for gravitational collapse arises because the star became unstable to axisymmetric perturbations. From [Cipolletta et al. \(2015\)](#), we have that, within at maximum error of 0.45%, the critical mass is given by:

$$M_{\max}^{J_{\text{ns}}\neq 0} = M_{\max}^{J_{\text{ns}}=0} (1 + k j_{\text{ns}}^l), \quad (23)$$

where $M_{\max}^{J_{\text{ns}}=0} = [2.81, 2.39, 2.20]$, $l = [1.68, 1.69, 1.61]$ and $k = [0.006, 0.011, 0.017]$ for the NL3, GM1 and TM1 EOS.

Table 6 lists some properties of the NS critical mass configurations for the NL3, GM1 and TM1 EOS. In particular, we show the minimum and maximum values of the critical mass, $M_{\max}^{J_{\text{ns}}=0}$ and $M_{\max}^{J_{\text{ns}}\neq 0}$, respectively: $M_{\max}^{J_{\text{ns}}=0}$ corresponds to the configuration along the secular axisymmetric instability line which is the non-rotating and $M_{\max}^{J_{\text{ns}}\neq 0}$ to the maximally rotating one which is the configuration that intersects the Keplerian, mass-shedding sequence. We also list the rotation frequency of the maximally rotating critical configuration, f_{\max} .

In the upper panel of Figure 16 we show the track followed by the NS companion (solid line) and the ν NS (dashed line) in the $M_{\text{star}} - j_{\text{star}}$ plane for the $25 M_{\odot}$ progenitor of the CO_{core}, for two different SN explosion energies (models 25M1p1e and 25M1p07e of table 2). For the system with the stronger SN explosion, the ν NS and the NS companion reach the mass-shedding limit at $t = 21.66$ min with $1.93 M_{\odot}$ and $t = 20.01$ min with $2.055 M_{\odot}$, respectively. For the less energetic SN explosion this occurs early, at $t = 5.51$ min with $2.04 M_{\odot}$ for the ν NS, and at $t = 2.91$ min with $2.09 M_{\odot}$ for the NS companion. The dotted line shows the continuation of the integration of Equation (22) for all the simulation time. For the NS companion, there is a decreasing of angular momentum. This occurs because there is a change in the direction of rotation of the accreted particles with respect to the one of the accreting NS.

Since we are assuming that the angular momentum of the accreted particles is totally transferred to the NS, even the accretion of a little amount of mass might bring it soon to the mass-shedding limit (see Figure 16). However, we see in the simulations that a kind of disk is formed around the NS, then before they being actually accreted, circularize and loose angular momentum owing to the friction force developed in the disk. In this picture, we need to integrate Equation (21) assuming that the star angular momentum evolution is given by the disk accretion torque, i.e.:

$$\dot{J}_{\text{ns}} = l(R_d) \dot{M}_b, \quad (24)$$

where $l(R_d)$ is the specific angular momentum of the particles at the disk interior radius, R_d . We adopt now that the disk interior radius is given by the radius of the last circular orbit (LCO) of a test particle around the NS. From [Cipolletta et al. \(2017\)](#), we have that the specific angular momentum of the LCO, independently on the studied EOS, is given by:

$$l(R_d) = l_{\text{LCO}} = \frac{GM_{\text{ns}}}{c} \left[2\sqrt{3} \mp 0.37 \left(\frac{j_{\text{ns}}}{M_{\text{ns}}/M_{\odot}} \right)^{0.85} \right], \quad (25)$$

where the upper sign corresponds to the corotating particles and the lower sign to the counter-rotating particles. This fitting formula is accurate with a maximum error of 0.3%.

In the bottom panel of Figure 16 we show the evolution of the ν NS and the NS companion in the $M_{\text{star}} - j_{\text{star}}$ plane, for the same models of the upper panel. In this case, we have integrated Equations (21) and (25) assuming, again, that the particles mass sums to the star baryonic mass and the disk viscous timescale is smaller than the accretion timescale, i.e. we used the mass-accretion rate obtained from the SPH simulations. In this case only the NS companion for the less energetic SN simu-

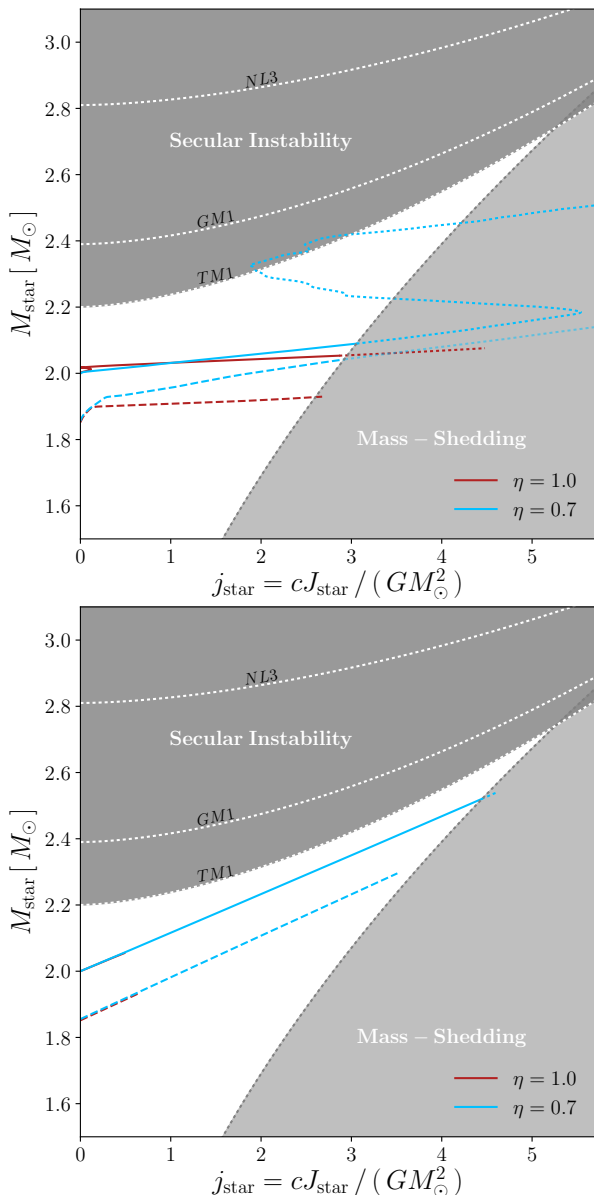


Figure 16. Evolution of the ν NS (dashed line) and the NS companion (solid line) in the mass-dimensionless angular momentum ($M_{\text{star}}-j_{\text{star}}$) plane. The mass of the particles accreted contributes to the NS baryonic mass. In the upper plot we adopt that the star accretes all the particles angular momentum. In the lower plot we adopt that the star accretes from a disk-like structure, namely that the angular momentum evolution is dictated by the disk-accretion torque (see text for details). In this example the initial binary system is formed by the CO_{core} of the $M_{\text{zams}} = 25 M_{\odot}$ progenitor and a $2 M_{\odot}$ NS with an orbital period of about 5 min. The red lines correspond to a SN explosion of $\times 10^{51}$ erg, while for the blue line the explosion energy has been scaled by a factor $\eta = 0.7$, leading to $\times 10^{51}$ erg.

lation reaches the mass-shedding limit.

The evolution equations (21) and (24) are general while the binding energy and LCO angular momentum equations are, in general, EOS-dependent relations. For-

tunately, it has been shown in Cipolletta et al. (2017) that equations (22) and (25) remain valid for the set of EOS used in this work (and for a wider variety of EOS) with high accuracy, namely they are nearly EOS-independent. This implies that the evolution track followed by the NS, given the initial mass, is the same for all these EOS. However, This does not imply that the fate of the NS is the same since the instability boundaries depend on the EOS, namely the numerical values of the mass and angular momentum of the NS at the mass-shedding and at the secular instability depend on the EOS, as it can be seen from figures 16 and 17.

We have assumed until now a totally efficient angular momentum transfer of the particles from the inner disk to the NS surface. However, additional angular momentum losses should be taken into account. We model these losses introducing a parameter for the efficiency of the angular momentum transfer, $\chi \leq 1$ (see e.g. Becerra et al. 2016), defined as:

$$\dot{J}_{\text{ns}} = \chi l(R_d) \dot{M}_b. \quad (26)$$

Therefore, $\chi = 1.0$ implies that the particles lose angular momentum only in their downward motion within the disk, while $\chi < 1$ introduces the possible losses in their final infall to the NS, e.g. from accretion outflows and/or from the deceleration of the matter from the inner disk radius to its final incorporation to the NS surface (see e.g. Shakura & Sunyaev 1988; Inogamov & Sunyaev 1999; Babkovskaia et al. 2008; Inogamov & Sunyaev 2010; Philippov et al. 2016, and references therein). In Figure 17 we compare the evolutionary path on the mass-dimensionless angular momentum plane for two values of the efficiency parameter, $\chi = 0.5$ and $\chi = 1.0$. It can be seen that angular momentum losses make the star to reach the secular instability limit of the TM1 and the GM1 EOS, namely the critical mass to collapse to a BH, instead of the mass-shedding limit. This result is in agreement with previous results presented in Becerra et al. (2015, 2016).

Table 7 lists the total angular momentum of the particles accreted by the stars when it crosses an instability limit (if it does) or when the simulation was stopped. In these cases we worked with the TM1 EOS. We show the results for two selected values of the angular momentum transfer efficiency parameter, $\chi = 1.0$ and 0.5 . For low energetic SN explosions, it is more probable that the ν NS arrives to the mass-shedding limit when $\chi = 1.0$ or the secular instability limit when $\chi = 0.5$. This is the case for the less energetic explosion of the $15 M_{\odot}$ progenitor, the $30 M_{\odot}$ and the $40 M_{\odot}$ ones. On the other hand, there are few cases in which the NS companion arrive first to the mass-shedding limit. The case for the $25 M_{\odot}$ progenitor with SN energy scaled by $\eta = 0.7$ and the minimum orbital period, and for the $40 M_{\odot}$ progenitor

Table 7. Final state of the ν NS and the NS companion

		ν NS							NS						
		$\chi = 0.5$			$\chi = 1.0$				$\chi = 0.5$			$\chi = 1.0$			
CO _{core}	Model	L_{tot}	$M_{\nu\text{ns}}$	$j_{\nu\text{ns}}$	Fate	$M_{\nu\text{ns}}$	$j_{\nu\text{ns}}$	Fate	L_{tot}	M_{ns}	j_{ns}	Fate	M_{ns}	j_{ns}	Fate
M_{zams}		$c/(GM_{\odot}^2)$	M_{\odot}	$c/(GM_{\odot}^2)$		M_{\odot}	$c/(GM_{\odot}^2)$		$c/(GM_{\odot}^2)$	M_{\odot}	$c/(GM_{\odot}^2)$		M_{\odot}	$c/(GM_{\odot}^2)$	
15 M_{\odot}	15m1p07e	0.027	1.302	0.007	Stb	1.302	0.008	Stb	0.085	2.004	0.009	Stb	2.002	0.018	Stb
	15m1p05e	0.069	1.303	0.009	Stb	1.303	0.016	Stb	0.323	2.004	0.019	Stb	2.004	0.037	Stb
	15m1p03e	0.019	1.315	0.041	Stb	1.315	0.077	Stb	0.362	2.023	0.101	Stb	2.023	0.204	Stb
	15m2p03e	0.091	1.303	0.08	Stb	1.303	0.017	Stb	0.579	2.006	0.026	Stb	2.006	0.056	Stb
	15m1p01e	13.63	1.815	1.571	Stb	1.636	1.874	M-sh	19.373	2.157	0.701	Stb	2.159	1.377	Stb
	15m2p01e	38.38	2.077	2.534	Stb	1.639	1.892	M-sh	12.533	2.080	0.35	Stb	2.080	0.693	Stb
	15m3p01e	30.95	1.759	1.377	Stb	1.862	3.253	M-sh	2.004	2.045	1.197	Stb	2.045	0.388	Stb
25 M_{\odot}	25m1p1e	3.469	1.931	0.321	Stb	1.933	0.627	Stb	4.746	2.055	0.2467	Stb	2.056	0.497	Stb
	25m2p1e	1.779	1.912	0.242	Stb	1.914	0.472	Stb	1.927	2.022	0.099	Stb	2.022	0.198	Stb
	25m3p1e	1.085	1.912	0.229	Stb	1.912	0.399	Stb	1.944	2.018	0.0813	Stb	2.019	0.1639	Stb
	25m1p09e	6.243	1.982	0.513	Stb	1.983	1.010	Stb	6.538	2.127	0.584	Stb	2.129	1.187	Stb
	25m1p08e	7.331	2.038	1.449	Stb	2.031	1.365	Stb	9.870	2.258	1.242	Sc-in	2.348	3.576	Stb
	25m1p07e	18.146	2.284	1.826	Stb	2.289	3.434	Stb	8.491	2.246	1.105	Sc-in	2.528	4.506	M-sh
	25m2p07e	19.51	2.250	1.663	Stb	2.265	3.215	Stb	9.908	2.252	1.135	Sc-in	2.426	3.648	Stb
	25m3p07e	21.34	2.214	1.476	Stb	2.226	2.812	Stb	17.292	2.004	2.246	Sc-in	2.425	3.638	Stb
14 M_{\odot}	14M1p1e	6.61	1.945	0.399	Stb	1.951	0.791	Stb	3.933	1.438	0.110	Stb	1.437	0.221	Stb
	16M1p1e	5.172	1.935	0.672	Stb	1.935	0.672	Stb	5.742	1.652	0.357	Stb	1.652	0.178	Stb
	14M1p07e	22.87	2.312	1.972	Sc-in	2.327	3.788	M-sh	3.079	1.837	1.509	Stb	1.711	2.05	M-sh
30 M_{\odot} ^a	30m1p1ea	0.077	1.756	0.021	Stb	1.756	0.044	Stb	0.059	2.006	0.026	Stb	2.006	0.052	Stb
	30m1p07ea	0.954	1.758	0.032	Stb	1.758	0.062	Stb	0.366	2.012	0.053	Stb	2.012	0.106	Stb
	30m1p05ea	1.828	1.764	0.053	Stb	1.764	0.107	Stb	4.073	2.028	0.125	Stb	2.028	0.251	Stb
	30m1p03ea	3.560	1.842	0.3494	Stb	1.843	0.692	Stb	33.083	2.246	2.358	Sc-in	2.356	3.532	Stb
	30m2p03ea	4.266	1.821	0.267	Stb	1.821	0.522	Stb	36.161	2.151	0.7006	Stb	2.154	1.426	Stb
30 M_{\odot} ^b	30m1p1eb	64.935	2.379	2.614	Sc-in	2.215	3.507	M-sh	19.995	2.244	1.099	Sc-in	2.307	2.634	Stb
	30m1p12eb	28.432	2.362	2.541	Stb	2.200	3.392	M-sh	33.681	2.244	1.100	Sc-in	2.304	2.606	Stb
	30m2p12eb	26.508	2.397	2.807	Sc-in	2.162	3.297	M-sh	23.922	2.1801	0.802	Stb	2.1827	1.572	Stb
	30m1p2eb	2.819	1.777	0.106	Stb	1.777	0.196	Stb	7.846	2.061	0.271	Stb	2.061	0.546	Stb
	30m1p31eb	0.721	1.766	0.0611	Stb	1.766	0.105	Stb	1.6715	2.014	0.062	Stb	2.014	0.122	Stb
40 M_{\odot}	40m1p1e	1.125	1.874	0.081	Stb	1.873	0.132	Stb	11.504	2.056	0.2453	Stb	2.056	0.4918	Stb
	40m1p09e	2.189	1.875	0.087	Stb	1.875	0.164	Stb	25.669	2.236	1.097	Stb	2.236	2.247	Stb
	40m1p08e	3.468	1.879	0.105	Stb	1.879	0.199	Stb	30.146	2.254	1.22	Sc-in	2.405	4.060	M-sh
	40m1p07e	9.963	2.042	0.7631	Stb	2.042	1.486	Stb	34.074	2.243	1.09	Sc-in	2.526	4.491	M-sh
	40m2p07e	9.6264	2.023	0.689	Stb	2.024	1.343	Stb	42.97	2.245	1.100	Sc-in	2.522	4.458	M-sh
	40m4p07e	10.333	1.942	0.342	Stb	1.942	0.652	Stb	27.474	2.246	1.129	Sc-in	2.4135	3.6104	Stb
	40m1p06e	171.063	2.310	1.948	Sc-in	2.338	3.857	M-sh	63.31	2.244	1.098	Sc-in	2.529	4.518	M-sh
	40m2p06e	121.594	2.318	1.987	Sc-in	2.331	3.793	M-sh	45.944	2.244	1.096	Sc-in	2.527	4.506	M-sh
40m1p05e	11.593	2.316	1.197	Sc-in	2.338	3.861	M-sh	5.434	2.133	0.588	Stb	2.134	1.158	Stb	

NOTE—Stb: stable configuration; M-sh: mass-shedding limit; Sc-in: secular axisymmetric instability. In this table, we report the results for the TM1 EOS and the gravitational mass value takes into account the angular momentum transfer by accretion. These values could differ from those reported in table 2 where the angular momentum transfer is not considered.

$${}^a E_{\text{sn}} = 1.09 \times 10^{52} \text{ erg}$$

$${}^b E_{\text{sn}} = 2.19 \times 10^{51} \text{ erg}$$

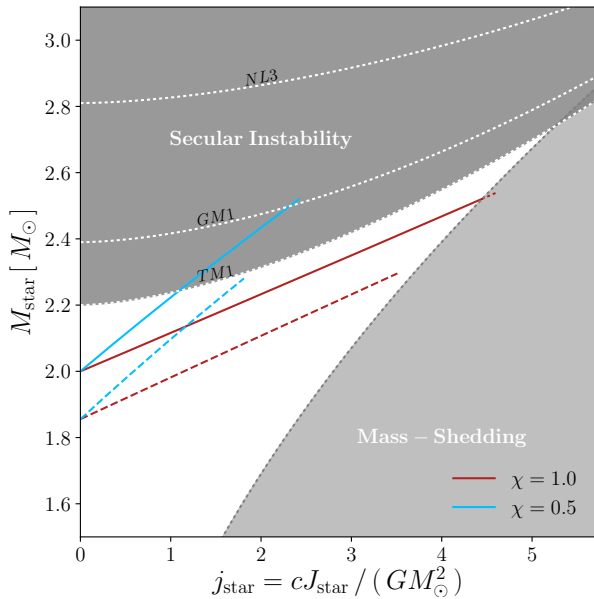


Figure 17. Evolution of the ν NS (dashed line) and the NS companion (solid line) in the mass-dimensionless angular momentum ($M_{\text{star}}-j_{\text{star}}$) plane. The angular momentum evolution is dictated by the disk-accretion torque given by Equation (26), where we have introduced the efficiency parameter, $\chi \leq 1$, that accounts for angular momentum losses between the disk and the stellar surface. The initial binary system is formed by the CO_{core} of the $M_{\text{zams}} = 25 M_{\odot}$ progenitor and a $2 M_{\odot}$ NS with an orbital period of about 5 min. The SN explosion energy has been scaled by $\eta = 0.7$ (Model 25M1p07e of Table 2).

with SN energy scaled by $\eta = 0.8$, $\eta = 0.7$ and $\eta = 0.6$. Notice that in the case with $\eta = 0.8$ and $\chi = 1.0$ the NS companion arrives to the mass-shedding limit, but the final system is unbound after the SN ejecta leave the system.

6.1. Accuracy of the mass accretion rate

We turn now to analyze the relevance of the ξ -parameter of Equation (10) on the mass-accretion rate onto the star. Until now, we have assumed a value $\xi = 0.1$ for this parameter. A larger value of ξ results in higher accretion rates: it allows a bigger gravitational capture radius and then more particles can be accreted by the star. In this way, a $\xi = 1.0$, the maximum value that ξ can have, will establish an upper limit for the mass accretion rate onto the star. We can also establish a lower limit for the accretion rate, if we allow the star to just accrete the particle which angular momentum is equals or smaller that the angular momentum that a particle orbiting the star would have at the LCO. An equivalent condition is to adopt a varying ξ parameter that equals the capture radius to the radius of the last circular orbit, r_{LCO} . But, since the r_{LCO} for the NS is of the order of the NS radius, i.e. ~ 10 km, we will need to increase considerably the number of particles to be

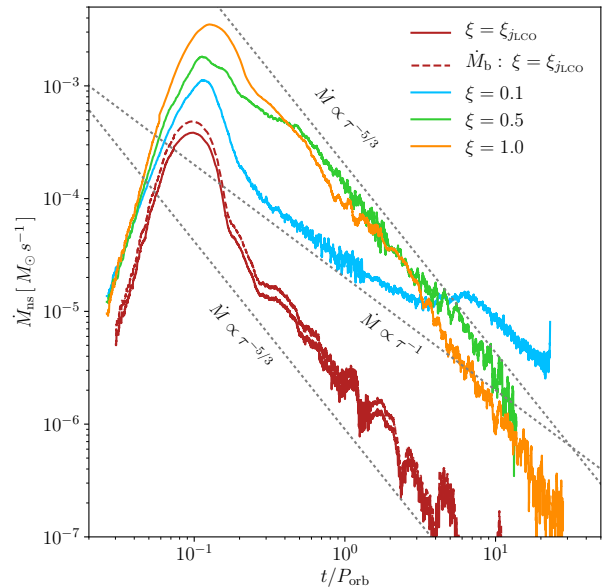


Figure 18. Mass-accretion rate onto the NS companion adopting different values for the ξ parameter in Equation (10). This parameter controls the size of the NS capture radius. A value $\xi = 1.0$ establishes an upper limit on the mass-accretion rate. We also defined a lower limit on the accretion (red line), allowing to the star just accreted those particles that have an angular momentum smaller than the one of the LCO around the NS. The initial binary configuration is the one of Figure 4.

able to resolve the NS surface.

We have re-run the SPH simulations adopting different values of ξ , for the binary system formed by the CO_{core} of the $25 M_{\odot}$ progenitor and a $2 M_{\odot}$ NS companion, and orbital period of about 5 min. In Figure 18 we show the accretion rate onto the NS companion for $\xi = 1.0$, 0.5 and 0.1 . The label $\xi = \xi_{j_{\text{LCO}}}$ corresponds to the case in which the star just accretes the particles with angular momentum lower than the one of the LCO. The late mass-accretion rate of the simulations with $\xi = \xi_{j_{\text{LCO}}}$ and $\xi = 0.5$ and 1.0 fall almost with the same power-law, $\dot{M} \propto t^{-5/3}$. Also, for the same simulation, Figure 19 shows snapshots of the density surface at the binary equatorial plane at two different times. The simulation with $\xi = 1.0$ and $\xi = 0.5$ gives greater peaks for the mass-accretion rate. This is expected since in these cases the NS capture radius is larger, the star cleans up its surrounding and produces, at later times, a quickly dropping accretion rate. Comparing this simulation with the one with $\xi = 0.1$, we can deduce that there is a delay time between the particles that are gravitationally captured by the star and the time it is actually accreted by it. We expect that the simulation with $\xi_{j_{\text{LCO}}}$ gives a better resolution of the disk around the NS companion. However, the artificial viscosity used in the code was introduced in order to resolve shocks and does not model the disk viscosity. Then, we are seeing

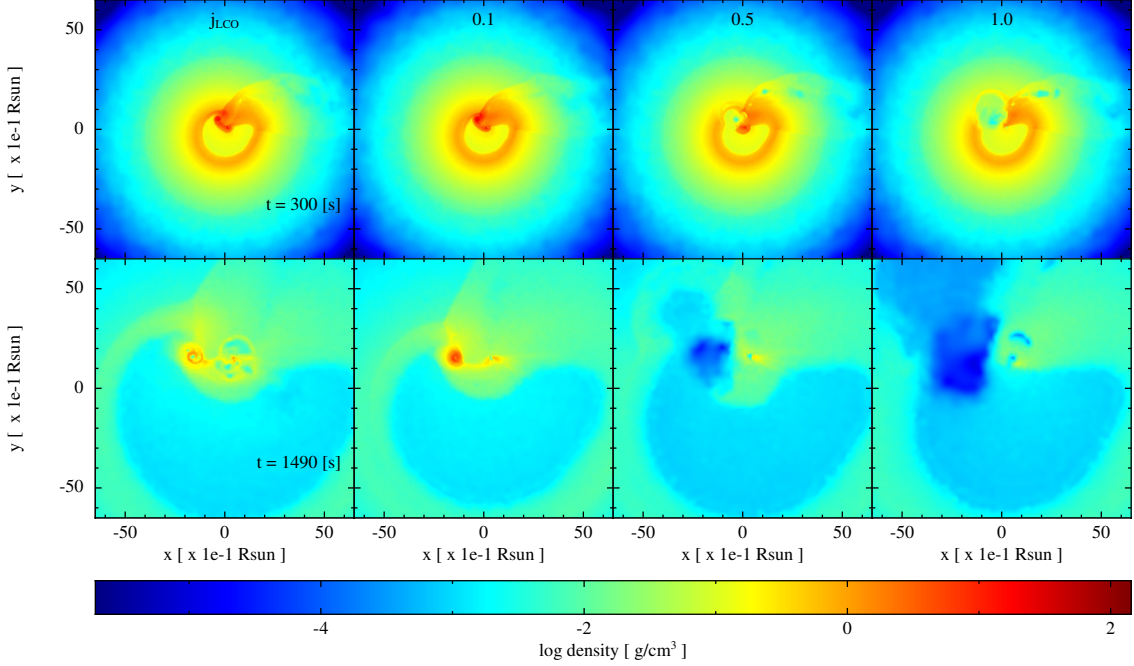


Figure 19. Snapshots of the surface mass density. The initial binary system is formed by the CO_{core} of a $25M_{\odot}$ progenitor and a $2M_{\odot}$ NS with an initial orbital period of around 5 min. For the plots in the upper panel the system has evolved a time close to one initial orbital period, 300 s, and for the plots of the bottom panel, the time corresponds to about 24 min from the beginning of the simulation. The vertical panels correspond to different values for the ξ parameter in Equation (10), from the second to the fourth it is: 0.1, 0.5 and 1.0. In the simulation label j_{LCO} the star accretes just the particles with angular momentum lower than the one of the NS LCO.

Table 8. NS companion final state

Progenitor M_{zams}	η	ξ	ΔM_{acc} M_{\odot}	ΔI_{acc} $c/(GM_{\odot}^2)$	m_{bound} M_{\odot}	$a_{orb,f}$ 10^{10} cm
$25M_{\odot}$	1.0	j_{LCO}	0.011	0.0097	0.00238	14.96
		0.1	0.078	4.7460	0.08100	8.110
		0.5	0.171	31.921	0.00497	9.780
		1.0	0.211	42.148	0.00131	48.87
	0.7	j_{LCO}	0.049	0.0870	0.07700	1.724
		0.1	0.659	7.7650	0.16030	1.021
		1.0	0.633	225.64	0.00453	1.575
$30M_{\odot}$	2.0	0.1	0.077	7.8460	0.00560	—
	2.0	1.0	0.172	22.166	0.00053	—
$40M_{\odot}$	0.8	0.1	0.457	30.147	0.01650	—
	0.8	1.0	0.545	56.835	0.00703	—

that the particles that circularize around the star, at some point scape from the NS gravitational field, making the mass-accretion rate to drop (see Figure 19). In Table 8 we summarize the parameters that characterize the final state of the NS companion as well as the final binary system. We have re-run simulation with the $25M_{\odot}$, $30M_{\odot}$ and $40M_{\odot}$ progenitors of the CO_{core} . For each model, we summarized the total mass and angular momentum on the accreted particles, ΔM_{acc} and ΔI_{acc} , the mass bound to the system when the simulation is

stopped, m_{bound} , and the final orbital separation, $a_{orb,f}$. In general, the larger the ξ parameter the larger the ΔI_{acc} and ΔM_{acc} depends both on ξ and on the SN explosion energy. The accreted mass increases with ξ but the increment decreases with a decrease of the SN energy, e.g.: for $M_{zams} = 25M_{\odot}$ and $\eta = 1.0$, the accreted mass increases by $\approx 170\%$ when going from $\xi = 0.1$ to $\xi = 1.0$ while, for $\eta = 0.7$, the accreted mass is almost the same for both values of ξ .

7. CONSEQUENCES OF THE SIMULATIONS ON THE XRF/BDHN MODEL

7.1. Parameters leading to a successful IGC

The accretion rate increases for higher densities and lower velocities, so we expect it increases with time as the inner ejecta layers, which are denser and slower, pass by the NS. Using an homologously expanding SN ejecta density profile, [Becerra et al. \(2016\)](#) derived approximate, analytic formulas for the peak accretion rate, \dot{M}_{peak} , and the corresponding peak time, t_{peak} (see Equations (33)–(34) there). From this estimate they show that, at the lowest order in M_{ns}/M , the system satisfies:

$$t_{\text{peak}} \propto \frac{M^{1/3} P_{\text{orb},i}^{2/3}}{v_{\text{star},0}}, \quad \dot{M}_{\text{peak}} \propto \left(\frac{M_{\text{ns}}}{M} \right)^{5/2} \frac{1}{P_{\text{orb},i}} \quad (27)$$

where M_{ns} is the initial mass of the NS companion, $M = M_{\text{ns}} + M_{\text{CO}}$ is the initial total binary mass, $M_{\text{CO}} = M_{\nu\text{ns}} + M_{\text{ej}}$ is the mass of the CO_{core}, $P_{\text{orb},i}$ is the initial orbital period and $v_{\text{star},0}$ is the velocity of the outermost layer of the SN ejecta. The above dependence confirms that the shorter/smaller the orbital period/separation, the higher the peak accretion rate, \dot{M}_{peak} and the shorter the peak time, t_{peak} . It is also confirmed that the highest velocity layer have a negligible contribution to the accretion rate but it is important in the determination of the time at which accretion starts and, consequently, of the peak time. These formulas are relevant to have an insight on the properties of the system and are valid to obtain typical and/or order-of-magnitude estimates of the accretion rate. An analysis of the performance of the analytic formulas with respect to the values obtained from a full numerical integration can be found in the appendix A of [Becerra et al. \(2016\)](#).

Using the above and approximating the accreted mass as $\Delta M_{\text{acc,an}} \approx \dot{M}_{\text{peak}} t_{\text{peak}}$, it can be checked that it satisfies:

$$\Delta M_{\text{acc,an}} \propto \frac{M_{\text{ns}}^2}{P_{\text{orb},i}^{1/3} v_{\text{star},0}}, \quad (28)$$

for a fixed CO_{core} mass. For some of the models of table 2, we summarize in table 9 their corresponding order-of-magnitude values of t_{peak} , \dot{M}_{peak} and ΔM_{acc} from equations (27) and (28). In order to evaluate the accuracy of these analytic estimates, we have calculated the ratio

$$\eta^* \equiv \frac{\Delta M_{\text{acc,sim}}}{\Delta M_{\text{acc,an}}}, \quad (29)$$

between the mass accreted by the NS companion obtained numerically in the simulation and the one predicted by equation (28). We confirm the behavior found in [Becerra et al. \(2016\)](#) that the accuracy of the analytic estimate increases (η^* parameter approaches unity) for

longer orbital periods (less compact binaries) and we found here that also for more energetic SNe. We also confirm that the analytic formula underestimates (η^* much larger than unity) the accretion rate for the short orbital period binaries. Indeed, we found that when η^* is in excess of unity the gravitational collapse of the NS is more probable. It is important to recall that the equations (27) were derived assuming that the binary period is constant while the SN ejecta expand and neglecting the contribution of the ν NS in the evolution of the system. In order to have an idea of the goodness of those assumptions, we also show in table 9 the ratio between the final and initial binary separation, and the final and initial mass of the ν NS.

From equation (28), we see that not only the larger the M_{ns} the less the mass it needs to accrete to reach the critical mass for gravitational collapse and BH formation,

$$\Delta M_{\text{crit}} \equiv M_{\text{crit}} - M_{\text{ns}}, \quad (30)$$

where $M_{\text{crit}} = M_{\text{max}}^{J_{\text{ns}} \neq 0}$ (see Equation 23), but also the larger the M_{ns} the higher the accretion rate and the larger the mass it accretes in a time t_{peak} . The above analysis places as main parameters of the system for the occurrence of an XRF or a BdHN are the initial mass of the NS companion, the orbital period and the SN velocity, or equivalently, the SN explosion/kinetic energy.

We defined in [Becerra et al. \(2016\)](#) the orbital period P_{max} separating the XRFs and BdHNe subclasses, namely the maximum orbital period up to which the collapse of the NS companion to a BH, induced by accretion, occurs. Thus, P_{max} is set by the orbital period for which $\Delta M_{\text{acc}} = \Delta M_{\text{crit}}$, which leads to

$$P_{\text{max}} \propto \frac{M_{\text{ns}}^6}{v_{\text{star},0}^3 (M_{\text{crit}} - M_{\text{ns}})^3}, \quad (31)$$

which is a monotonically increasing function of M_{ns} , as obtained in [Becerra et al. \(2016\)](#) (see Figure 5 there) from the full numerical integration of the NS evolution equations.

7.2. Binary evolutionary path

As we have discussed, in our binary scenario the presence of the CO_{core} provides a natural explanation for the association of long GRBs with type Ic SNe/HNe. The requirement of the CO_{core}, at the same time, leads to the formation of compact orbits (few minutes orbital period) needed for the occurrence of high accretion rates onto the NS companion. The HNe, i.e. the high-velocity SNe associated with GRBs, are explained by the feedback of the energy injected into the SN by the hypercritical accretion ([Becerra et al. 2016](#)) and by the GRB e^+e^- plasma ([Ruffini et al. 2018a](#)). This implies that the initial SN explosion/kinetic energy is initially ordinary.

Table 9. Comparison between the analytic estimate of the accretion process and the full numerical results. In the first two columns is presented the label of the model and the SN velocity of the last layer at the beginning of the simulation. The next three columns correspond to the estimations of t_{peak} , \dot{M}_{peak} and M_{acc} , calculated from equations (27) and (28). The η^* parameter from sixth columns corresponds to the ratio between the mass accreted obtained from the simulations and the one calculated with equation (28). The last two columns are the ratio between the initial and final orbital separation and the initial and final mass of the ν NS, respectively. We reported these two last quantities since in the analytical approximation they were assumed as constant.

Model	$v_{\text{star},0}$ 10 ⁸ cm/s	t_{peak} s	\dot{M}_{peak} 10 ⁻⁴ M_{\odot} /s	$\Delta M_{\text{acc,an}}$ M_{\odot}	η^*	$\frac{a_{\text{orb,f}}}{a_{\text{orb,i}}}$	$\frac{M_{\nu\text{ns}}}{M_{\nu\text{ns},0}}$	Model	$v_{\text{star},0}$ 10 ⁸ cm/s	t_{peak} s	\dot{M}_{peak} 10 ⁻⁴ M_{\odot} /s	$\Delta M_{\text{acc,an}}$ M_{\odot}	η^*	$\frac{a_{\text{orb,f}}}{a_{\text{orb,i}}}$	$\frac{M_{\nu\text{ns}}}{M_{\nu\text{ns},0}}$
$M_{\text{ZAMS}} = 25 M_{\odot}$ Progenitor ($\rho_{\text{core}} R_{\text{star}}^3 = 3.237 M_{\odot}$)								$M_{\text{ZAMS}} = 30 M_{\odot}$ Progenitor - exp2 ($\rho_{\text{core}} R_{\text{star}}^3 = 5.280 M_{\odot}$)							
25m1p1e	9.5	48.14	5.87	0.028	3.01	6.47	1.06	30m1p1e	5.21	340.06	0.984	0.033	11.428	1.32	2.10
25m2p1e	9.5	70.69	3.30	0.023	1.24	–	1.04	30m2p1e	5.21	513.53	0.767	0.039	5.784	–	1.02
25m3p1e	9.5	87.56	2.39	0.021	1.14	–	1.04	30m1p12e	5.71	310.43	0.984	0.031	11.428	3.01	1.44
25m4p1e	9.5	106.8	1.77	0.019	0.74	–	1.04	30m1p2e	5.21	239.91	0.984	0.023	0.719	–	1.02
25m1p09e	9.1	50.74	5.87	0.029	5.43	3.10	1.09	30m1p31e	9.18	193.15	0.984	0.019	0.895	–	1.01
25m1p08e	8.5	53.82	5.87	0.032	13.95	1.82	1.12	$M_{\text{ZAMS}} = 40 M_{\odot}$ Progenitor ($\rho_{\text{core}} R_{\text{star}}^3 = 7.47 M_{\odot}$)							
25m1p07e	7.9	57.54	5.87	0.034	18.37	0.77	1.28	40m1p1e	6.58	33.74	9.39	0.032	3.74	–	1.01
25m2p07e	7.9	84.49	3.30	0.028	18.71	1.99	1.27	40m2p1e	6.58	49.67	5.58	0.028	1.65	–	1.01
25m3p07e	7.9	104.65	2.39	0.025	20.87	2.30	1.24	40m1p09e	6.24	35.62	9.39	0.033	8.14	–	1.012
25m5p07e	7.9	147.78	1.43	0.021	19.02	2.58	1.17	40m1p08e	5.88	37.78	9.39	0.035	15.06	–	1.02
14Mns1p1e	9.5	43.58	3.71	0.016	2.65	12.6	1.07	40m1p07e	5.51	40.39	9.39	0.038	27.21	8.08	1.13
14Mns1p07e	7.9	52.08	3.71	0.019	21.16	0.80	1.33	40m2p07e	5.51	59.38	5.59	0.033	22.76	54.8	1.12
$M_{\text{ZAMS}} = 30 M_{\odot}$ Progenitor -exp 1 ($\rho_{\text{core}} R_{\text{star}}^3 = 5.280 M_{\odot}$)								40m4p07e	5.51	94.29	2.99	0.028	17.97	–	1.06
30m1p1e	8.78	96.22	0.91	0.009	0.798	–	1.004								
30m1p07e	7.35	115.01	0.91	0.018	1.431	–	1.004								
30m1p05e	6.213	136.07	0.91	0.022	2.498	–	1.008								
30m1p03e	4.81	175.67	0.91	0.016	28.41	4.88	1.068								
30m2p03e	4.81	265.28	0.52	0.013	13.84	–	1.05								

Once we have established the main binary parameters needed for the explanation of the XRFs and BdHNs following the IGC scenario, it is natural to discuss whether these conditions, namely CO_{core}-NS binaries with these features, occur in a given evolutionary path. It is known that massive binaries can evolve into compact-object binaries such as NS-NS and NS-BH. Typical formation scenarios argue that, after the first SN explosion, the compact remnant enters a common-envelope phase with the companion. Such a phase leads to a compaction of the binary orbit. Finally, after the collapse of the companion star, a NS-BH or NS-NS binary is formed if the system remains bound (Fryer et al. 1999b; Dominik et al. 2012; Postnov & Yungelson 2014). More recently, a different evolutionary scenario has been proposed in which, after the collapse of the primary star to a NS, namely after the first SN, the binary undergoes a series of mass transfer phases leading to the ejection of both the hydrogen and helium shells of the secondary. This process naturally leads to a binary composed of a CO_{core} and a NS. When the CO_{core} collapses, namely after the second SN in the binary evolutionary path, a compact binary system is formed. The X-ray binary/SN community refer to these systems as “ultra-stripped” binaries. Such systems have been also called into cause to explain the population of NS-NS and low-luminosity SNe (see

e.g. Tauris et al. 2013, 2015). The rate of these ultra-stripped binaries are expected to be 0.1–1% of the total SN rate (Tauris et al. 2013). Most of the theoretically derived population of these binaries show tight orbital periods in the range 50–5000 h. Ultra-stripped systems have been proposed in these works to dominate the formation channel of NS-NS. In addition, the formation of NS-BH systems was not there considered since 1) they did not find systems where the CO_{core} collapses directly to a BH and 2) they did not consider the possibility of an IGC process in which the BH is formed by the NS companion and not by the collapse of the CO_{core}.

Binary evolutionary paths similar to the above one of ultra-stripped binaries and leading to the tight CO_{core}-NS binaries studied here were proposed in Rueda & Ruffini (2012); Becerra et al. (2015); Fryer et al. (2015). However, population synthesis analyses scrutinizing the possibility of even tighter binaries than the ones previously considered as well as the physics of the hypercritical accretion process onto the NS companion in the second SN explosion, leading to XRFs and/or BdHNe, have not been yet considered in the literature and deserve a dedicated analysis.

7.3. Occurrence rate density

The existence of ultra-stripped binaries supports our

scenario from the stellar evolution side. Clearly, XRF and BdHN progenitors should be only a small subset that result from the binaries with initial orbital separation and component masses leading to CO_{core} -NS binaries with short orbital periods, e.g. 100–1000 s for the occurrence of BdHNe. This requires fine-tuning both of the CO_{core} mass and the binary orbit. From an astrophysical point of view the IGC scenario is characterized by the BH formation induced by the hypercritical accretion onto the NS companion and the associated GRB emission. Indeed, GRBs are a rare phenomenon and the number of systems approaching the conditions for their occurrence must be low. If we assume that XRFs and BdHNe can be final stages of ultra-stripped binaries, then the percentage of the ultra-stripped population leading to these long GRBs must be very small. The observed occurrence rate of XRFs and BdHNe has been estimated to be $\sim 100 \text{ Gpc}^{-3} \text{ y}^{-1}$ and $\sim 1 \text{ Gpc}^{-3} \text{ y}^{-1}$, respectively (Ruffini et al. 2016), namely the 0.5% and 0.05% of the Ibc SNe rate, $2 \times 10^4 \text{ Gpc}^{-3} \text{ y}^{-1}$ (see e.g. Guetta & Della Valle 2007). Since it has been estimated that (0.1–1%) of the SN Ibc could originate from ultra-stripped binaries (Tauris et al. 2013), then only (0.005–0.05%) of the ultra-stripped population would be needed to explain the occurrence of XRFs and only even 100 times smaller to explain the BdHNe. It is interesting that these numbers are consistent with traditional estimates that only ~ 0.001 –1% of massive binaries lead to double compact-object binaries (see e.g. Fryer et al. 1999b; Dominik et al. 2012; Postnov & Yungelson 2014).

7.4. Consequences on GRB observations and analysis

We have recently addressed in Ruffini et al. (2018a) the essential role of X-ray flares in differentiating and act as separatrix between the BdHN model and the “collapsar-fireball” model of GRBs (Woosley 1993). The gamma-ray spikes in the GRB prompt emission occur at 10^{15} – 10^{17} cm from the source and have Lorentz factor $\Gamma \sim 10^2$ – 10^3 . Instead, the analysis of the thermal emission in the X-ray flares in the early (source rest-frame time $t \sim 10^2$ s) afterglow of BdHNe, showed that X-ray flares occur at radii $\sim 10^{12}$ cm and expand mildly-relativistically, e.g. $\Gamma \lesssim 4$ (Ruffini et al. 2018a). These model independent observations are in contrast with an ultra-relativistic expansion all the way from the GRB prompt emission to the afterglow, as traditionally adopted in the majority of the GRB literature in the context of the collapsar-fireball scenario.

In Ruffini et al. (2018a) we tested whether the BdHN scenario could explain both the ultra-relativistic gamma-ray prompt emission as well as the mildly-relativistic X-ray flare data. Our numerical simulations in Becerra et al. (2016) have shown that, at the moment

of BH formation and GRB emission, the SN ejecta become highly asymmetric around the collapsing NS. In the direction pointing from the CO_{core} to the accreting NS outwards and lying on the orbital plane, the NS caves a region of low baryonic contamination in which the GRB e^+e^- plasma, created once the NS collapses and forms the BH, can expand with high $\Gamma \sim 10^2$ – 10^3 explaining the GRB prompt emission. In the other directions, the GRB e^+e^- plasma impacts the SN ejecta at approximately 10^{10} cm, evolves carrying a large amount of baryons reaching transparency at radii 10^{12} cm with a mildly $\Gamma \lesssim 4$. This result is in clear agreement with the X-ray flares data (see Ruffini et al. 2018a; Melon Fuksman et al. 2018, for details). A most important prediction of this scenario is that the injection of energy and momentum from the GRB plasma into the ejecta transforms the SN into a HN (see Ruffini et al. 2017, for a detailed analysis of GRB 151027A).

The strong dependence of P_{max} on the initial mass of the NS companion opens the interesting possibility of producing XRFs and BdHNe from binaries with similar short (e.g. $P \sim$ few minutes) orbital periods and CO_{core} properties: while a system with a massive (e.g. $\gtrsim 2 M_{\odot}$) NS companion would lead to a BdHN, a system with a lighter (e.g. $\lesssim 1.4 M_{\odot}$) NS companion would lead to an XRF. This predicts systems with a similar initial SN, leading to a similar νNS , but with different GRB prompt and afterglow emission. Clearly being the GRB energetics different, the final SN kinetic energy should be also different being it larger for the BdHNe.

Besides confirming that XRFs and BdHNe can be produced by these binaries, the present new 3D SPH simulations have also shown new, possibly observable features in GRB light-curves and spectra, e.g.:

- 1) the hypercritical accretion occurs both on the NS companion and on the νNS with a comparable accretion rate, hence roughly doubling the accretion power of the system.

- 2) The above leads to the clear possibility that, under specific conditions, a BH-BH binary can be produced; see e.g. the simulation ‘30m1p1eb’ in Table 7. Since the system remains bound (see Table 2), the two stellar-mass BHs will merge in due time owing to the emission of gravitational waves. However, no electromagnetic emission is expected from such a merger and, in view of the typically large cosmological distances of GRBs, their detection by gravitational-wave detectors such as the ground-based interferometers of the LIGO-Virgo network appears to be difficult.

- 3) The SNe with lower explosion energy create a long-live hypercritical accretion process and produce an enhancement at late times of the accretion rate onto the νNS . Such a revival of the accretion rate does not exist in the case of single SN namely in absence of the

NS companion (see Figure 5). In these cases there is a higher probability for the detection of the early phase of an XRF/BdHN by X-ray detectors.

4) The asymmetric SN explosions lead to a quasi-periodic behavior of the accretion rate which could be detectable by the X-rays instruments (see e.g. Figure 11). A possible detection of this feature would be a further test of the binary nature and would pinpoint the orbital period of the binary progenitor.

On the other hand, we have evaluated in our simulations whether the binary remains gravitationally bound or it becomes unbound by the SN explosion. Therefore, we are determining the space of initial binary and SN explosion parameters leading to the formation of ν NS-NS or ν NS-BH binaries. This shows the interesting feature that long GRBs (XRFs and BdHNe) lead to the binary progenitors of short GRBs, hence this topic is relevant for the understanding of their relative density rate and will be further analyzed in forthcoming works.

8. CONCLUSIONS

We have performed the first full numerical 3D SPH simulations of the IGC scenario: in a CO_{core} -NS binary system, the CO_{core} collapses and explodes in a SN triggering a hypercritical accretion process onto the NS companion. The initial conditions for the simulations were constructed as follows. The CO_{core} stars are evolved using the KEPLER evolution code (Heger & Woosley 2010) until the conditions for the collapse are met. Then, the stars are exploded with the 1D core-collapse code (Fryer et al. 1999a). When the forward SN shock reaches the stellar radius, we map the explosion to a 3D-SPH configuration and continue the evolution of the SN expansion with a NS binary companion using the SNSPH code (Fryer et al. 2006b).

We followed the evolution of the SN ejecta, including their morphological structure, under the action of the gravitational field of both the ν NS and the NS companion. We estimated the accretion rate onto both stars with the aid of Equation (22). The baryonic mass-accretion rates are calculated from the mass of the SPH particles accreted. We have shown that matter circularizes in a disk-like structure around the NS companion (see, e.g., Figure 2). Therefore, for the angular momentum transfer to the NS, we have adopted that the particles are accreted from the LCO.

We determined the fate of the binary system for a wide parameter space including different CO_{core} masses (see Table 1), orbital periods, SN explosion geometry and energies, as well as different masses of the NS companion. We evaluated, for selected NS nuclear EOS, if the accretion process leads the NS either to the mass-shedding limit, or to the secular axisymmetric instability for gravitational collapse to a BH, or to a more massive, fast

rotating, but stable NS. We have also analyzed the case of asymmetric SN explosions. We assessed if the binary remains gravitationally bound or it becomes unbound by the explosion. With this information we determined the space of initial binary and SN explosion parameters leading to the formation of ν NS-NS or ν NS-BH binaries.

It is worth mentioning some issues not included in the numerical calculations presented here and which deserve to be further studied and/or improved:

1) We need to improve the resolution of the code to handle the spatial region in the vicinity of the NS companion at scales 10^6 – 10^7 cm. This will allow to resolve better the structure of the circularized matter (accretion disk) near the NS and evaluate more accurately the angular momentum transfer to the NS (e.g. the value of the angular momentum efficiency parameter, χ). These distances are of the order of the NS Schwarzschild radius, therefore a general relativistic code is needed for this task.

2) The above will also allow to study the possible outflows from the hypercritical accretion process previously found in the case of fallback accretion (Fryer 2009) and in which heavy nuclei via r-process nucleosynthesis can be produced (Fryer et al. 2006a).

3) The transformation of the SN into a HN by the impact of the GRB into the ejecta. We are currently performing the hydrodynamical simulations of the interaction of the GRB e^+e^- plasma using a one-dimensional relativistic hydrodynamical module included in the freely available PLUTO (see Ruffini et al. 2018a, for further details). We have used in these calculations the SN ejecta profiles at the moment of the NS collapse obtained by Becerra et al. (2016), and evolved them from that instant on under the assumption of homologous expansion.

4) In view of the above, the present simulations remain accurate/valid up to the instant where the NS reaches the critical mass, hence forming a BH. After that instant the GRB-SN interaction becomes relevant. In the systems when the NS companion does not reach the critical mass, our simulations remain accurate/valid all the way up to the instant where the entire SN ejecta blows past the NS position.

We discussed in section 6 some of the consequences of our simulations in the analysis of GRBs within the context of the IGC scenario. The simulations have confirmed, extended and improved important previous results. In particular:

1) We showed that long GRBs (XRFs and BdHNe) can be produced by these binaries depending on the binary parameters. We have shown that the main parameters defining the fate of the system are: the initial mass of the NS companion, the orbital period and the SN velocity (or kinetic/explosion energy).

2) The accreting NS companion induces high asymmetries in the SN ejecta which are relevant in the GRB analysis. Recent results on the thermal emission of the X-ray flares in the early (source rest-frame times $t \sim 10^2$ s) afterglow of long GRBs show that they occur at radii $\sim 10^{12}$ cm and expand mildly-relativistically with $\Gamma \lesssim 4$. This was shown to be in agreement with the BdHNe of the IGC scenario (see Ruffini et al. 2018a, and section 6 above for details): the e^+e^- plasma of the GRB, relativistically expanding from the newborn BH, collides with the SN ejecta at distances of the order of 10^{10} cm, to then reach transparency at 10^{12} cm with $\Gamma \lesssim 4$. The 3D simulations presented in this work will be essential to explore the dynamics of the e^+e^- plasma along all spatial directions and to estimate, as a function of the viewing angle, the light-curve and spectral properties of BdHNe (see e.g. Ruffini et al. 2018a,b, 2017).

3) One of the most interesting issues is that we have confirmed that some of the systems remain bound after the explosion, implying that XRFs form ν NS-NS binaries and BdHNe form ν NS-BH systems. Therefore, long GRBs (XRFs and BdHNe) produce the binary progenitors of short GRBs, after the shrinking of their orbit until the coalescence by the emission of gravitational waves. The analysis of the number of systems leading to ν NS-NS and ν NS-BH binaries becomes very important for the explanation of the relative occurrence rate of long and short GRBs.

4) We have also outlined consequences on the accretion process and its observational features in the case

of relatively weak SN explosion energies as well as for intrinsically asymmetric ones. We have addressed possible new observable features in GRB light-curves and spectra, e.g. systems experiencing longer, stronger and quasi-periodic accretion episodes to be possibly observed by X-ray instruments. The observation of this kind of phenomena in the early phases of a GRB would benefit from a new mission operating in soft X-rays like, e.g., THESEUS (Amati et al. 2018).

5) We have also shown that there is also the possibility that some CO_{core}-NS binaries could produce BdHNe leading to BH-BH binaries due to the collapse to a BH not only of the NS companion but also of the ν NS due to a massive fallback accretion. The final merger of the two stellar-mass BHs has no electromagnetic counterpart to be detected and its gravitational-wave emission, in view of the large distances of these sources, appears to be extremely weak to be detected by current interferometers such as LIGO-Virgo.

Acknowledgements: We thank the Referee for the comments and suggestions to improve the presentation of our results. The work of L.B., C.E., and C.F. was partially funded under the auspices of the U.S. Dept. of Energy, and supported by its contract W-7405-ENG-36 to Los Alamos National Laboratory. Simulations at LANL were performed on HPC resources provided under the Institutional Computing program.

REFERENCES

- Amati, L., O’Brien, P., Götz, D., et al. 2018, *Advances in Space Research*, 62, 191
- Antoniadis, J., Freire, P. C. C., Wex, N., et al. 2013, *Science*, 340, 448
- Babkovskaia, N., Brandenburg, A., & Poutanen, J. 2008, *MNRAS*, 386, 1038
- Bate, M. R., Bonnell, I. A., & Price, N. M. 1995, *MNRAS*, 277, 362
- Batta, A., Ramirez-Ruiz, E., & Fryer, C. 2017, *ApJL*, 846, L15
- Becerra, L., Bianco, C. L., Fryer, C. L., Rueda, J. A., & Ruffini, R. 2016, *ApJ*, 833, 107
- Becerra, L., Cipolletta, F., Fryer, C. L., Rueda, J. A., & Ruffini, R. 2015, *ApJ*, 812, 100
- Becerra, L., Guzzo, M. M., Rossi-Torres, F., et al. 2018, *ApJ*, 852, 120
- Benz, W. 1990, in *Numerical Modelling of Nonlinear Stellar Pulsations Problems and Prospects*, ed. J. R. Buchler, 269
- Bisnovatyi-Kogan, G. S. 1993, *Astronomical and Astrophysical Transactions*, 3, 287
- Blandford, R. D., & Begelman, M. C. 1999, *MNRAS*, 303, L1
- Bondi, H. 1952, *MNRAS*, 112, 195
- Bondi, H., & Hoyle, F. 1944, *MNRAS*, 104, 273
- Breton, R. P., van Kerkwijk, M. H., Roberts, M. S. E., et al. 2013, *ApJ*, 769, 108
- Chevalier, R. A. 1989, *ApJ*, 346, 847
- Cipolletta, F., Cherubini, C., Filippi, S., Rueda, J. A., & Ruffini, R. 2015, *PhRvD*, 92, 023007
- Cipolletta, F., Cherubini, C., Filippi, S., Rueda, J. A., & Ruffini, R. 2017, *Phys. Rev. D*, 96, 024046
- Colgate, S. A. 1971, *ApJ*, 163, 221
- Demorest, P. B., Pennucci, T., Ransom, S. M., Roberts, M. S. E., & Hessels, J. W. T. 2010, *Nature*, 467, 1081
- Dexter, J., & Kasen, D. 2013, *ApJ*, 772, 30
- Diehl, S., Fryer, C., & Herwig, F. 2008, in *Astronomical Society of the Pacific Conference Series*, Vol. 391, *Hydrogen-Deficient Stars*, ed. A. Werner & T. Rauch, 221
- Diehl, S., Rockefeller, G., Fryer, C. L., Riethmiller, D., & Statler, T. S. 2015, *PASA*, 32, e048
- Dominik, M., Belczynski, K., Fryer, C., et al. 2012, *ApJ*, 759, 52
- Eggleton, P. P. 1983, *ApJ*, 268, 368
- Fryer, C., Benz, W., Herant, M., & Colgate, S. A. 1999a, *ApJ*, 516, 892
- Fryer, C. L. 1999, *ApJ*, 522, 413
- . 2009, *ApJ*, 699, 409
- Fryer, C. L., Andrews, S., Even, W., Heger, A., & Safi-Harb, S. 2017, *ArXiv e-prints*, arXiv:1712.03415
- Fryer, C. L., Herwig, F., Hungerford, A., & Timmes, F. X. 2006a, *ApJL*, 646, L131
- Fryer, C. L., & Kusenko, A. 2006, *ApJS*, 163, 335
- Fryer, C. L., Oliveira, F. G., Rueda, J. A., & Ruffini, R. 2015, *Physical Review Letters*, 115, 231102

- Fryer, C. L., Rockefeller, G., & Warren, M. S. 2006b, *ApJ*, 643, 292
- Fryer, C. L., Rueda, J. A., & Ruffini, R. 2014, *ApJL*, 793, L36
- Fryer, C. L., & Warren, M. S. 2002, *ApJL*, 574, L65
- Fryer, C. L., Woosley, S. E., & Hartmann, D. H. 1999b, *ApJ*, 526, 152
- Fryer, C. L., & Young, P. A. 2007, *ApJ*, 659, 1438
- Guetta, D., & Della Valle, M. 2007, *ApJL*, 657, L73
- Heger, A., & Woosley, S. E. 2010, *ApJ*, 724, 341
- Herant, M., Benz, W., Hix, W. R., Fryer, C. L., & Colgate, S. A. 1994, *ApJ*, 435, 339
- Hills, J. G. 1983, *ApJ*, 267, 322
- Hoyle, F., & Lyttleton, R. A. 1939, *Proceedings of the Cambridge Philosophical Society*, 35, 405
- Hungerford, A. L., Fryer, C. L., & Rockefeller, G. 2005, *ApJ*, 635, 487
- Hungerford, A. L., Fryer, C. L., & Warren, M. S. 2003, *ApJ*, 594, 390
- Inogamov, N. A., & Sunyaev, R. A. 1999, *Astronomy Letters*, 25, 269
- . 2010, *Astronomy Letters*, 36, 848
- Izzo, L., Rueda, J. A., & Ruffini, R. 2012, *A&A*, 548, L5
- Janka, H.-T. 2012, *Annual Review of Nuclear and Particle Science*, 62, 407
- Janka, H.-T., & Mueller, E. 1994, *A&A*, 290, 496
- Kohri, K., Narayan, R., & Piran, T. 2005, *ApJ*, 629, 341
- Lattimer, J. M., & Prakash, M. 2007, *PhR*, 442, 109
- Lee, C.-H., & Cho, H.-S. 2014, *Nuclear Physics A*, 928, 296
- Linares, M., Shahbaz, T., & Casares, J. 2018, *ApJ*, 859, 54
- Melon Fuksman, J. D., Becerra, L., Bianco, C. L., et al. 2018, in *European Physical Journal Web of Conferences*, Vol. 168, *European Physical Journal Web of Conferences*, 04009
- Monaghan, J. J. 1992, *ARA&A*, 30, 543
- . 2005, *Reports on Progress in Physics*, 68, 1703
- Moriya, T., Tominaga, N., Tanaka, M., et al. 2010, *ApJ*, 719, 1445
- Murphy, J. W., Dolence, J. C., & Burrows, A. 2013, *ApJ*, 771, 52
- Philippov, A. A., Rafikov, R. R., & Stone, J. M. 2016, *ApJ*, 817, 62
- Postnov, K. A., & Yungelson, L. R. 2014, *Living Reviews in Relativity*, 17, 3
- Price, D. J. 2011, *SPLASH: An Interactive Visualization Tool for Smoothed Particle Hydrodynamics Simulations*, *Astrophysics Source Code Library*, , ascl:1103.004
- Rueda, J. A., & Ruffini, R. 2012, *ApJL*, 758, L7
- Ruffini, R., Bianco, C. L., Fraschetti, F., Xue, S.-S., & Chardonnet, P. 2001, *ApJL*, 555, L117
- Ruffini, R., Muccino, M., Bianco, C. L., et al. 2014, *A&A*, 565, L10
- Ruffini, R., Rueda, J. A., Muccino, M., et al. 2016, *ApJ*, 832, 136
- Ruffini, R., Becerra, L., Bianco, C. L., et al. 2017, *ArXiv e-prints*, arXiv:1712.05001
- Ruffini, R., Wang, Y., Aimuratov, Y., et al. 2018a, *ApJ*, 852, 53
- Ruffini, R., Moradi, R., Wang, Y., et al. 2018b, *ArXiv e-prints*, arXiv:1803.05476
- Shakura, N. I., & Sunyaev, R. A. 1988, *Advances in Space Research*, 8, 135
- Stergioulas, N., & Friedman, J. L. 1995, *ApJ*, 444, 306
- Tauris, T. M., Langer, N., Moriya, T. J., et al. 2013, *ApJL*, 778, L23
- Tauris, T. M., Langer, N., & Podsiadlowski, P. 2015, *MNRAS*, 451, 2123
- Warren, M. S., & Salmon, J. K. 1993, in *Proceedings of the 1993 ACM/IEEE Conference on Supercomputing (New York: ACM)*, 12–21
- Warren, M. S., & Salmon, J. K. 1995, *Computer Physics Communications*, 87, 266
- Wong, T.-W., Fryer, C. L., Ellinger, C. I., Rockefeller, G., & Kalogera, V. 2014, *ArXiv e-prints*, arXiv:1401.3032
- Woosley, S. E. 1987, in *IAU Symposium*, Vol. 125, *The Origin and Evolution of Neutron Stars*, ed. D. J. Helfand & J.-H. Huang, 255–270
- Woosley, S. E. 1993, *ApJ*, 405, 273
- Woosley, S. E., & Weaver, T. A. 1995, *ApJS*, 101, 181
- Young, P. A., Fryer, C. L., Hungerford, A., et al. 2006, *ApJ*, 640, 891
- Zhang, W., Woosley, S. E., & Heger, A. 2008, *ApJ*, 679, 639

APPENDIX

A. NUMERICAL CONVERGENCE

In order to evaluate the convergence of our SPH simulation, we have done some numerical experiments varying the number of the particles with which we model the SN ejecta for the different pre-SN progenitors.

We performed simulations with 1, 1.5, 2 and 3 million particles with different progenitors and with different values of the ξ parameter in Equation (10). We summarize the results of these simulations in Table A1. We compare and contrast the final accreted mass and angular momentum of the ν NS and the NS companion, the final orbital period and eccentricity of the orbit. We also report the relative error of these quantities taking as the reference values the ones of the simulation of about 1 million of particles.

We show in Figure A1 profiles of the density on the binary orbital plane and along different directions, taking the NS companion as the center of the reference frame. Figure A2 shows the mass-accretion rate on the ν NS and the NS companion. Finally, we plot in Figure A3, the flux of mass and angular momentum onto the NS companion at two different distances from it: $r = 0.02 R_{\odot}$ and at $r = R_{\text{cap}}$, defined as the maximum capture radius of the NS in each iteration. All these figures corresponds to the simulation of an initial binary system formed by the CO_{core} of the $25 M_{\odot}$ progenitor (see Table 1) and a $2 M_{\odot}$ NS with an initial orbital period of ≈ 2 min.

Table A1. Convergence study of the SPH simulation of the IGC scenario.

Progenitor	N	η	ξ	$m_{\nu ns}$	$\text{Er}(m_{\nu ns})$	$L_{\nu - ns}$	$\text{Er}(L_{\nu ns})$	m_{ns}	$\text{Er}(m_{ns})$	L_{ns}	$\text{Er}(L_{ns})$	$p_{orb,f}$	$\text{Er}(p_{orb})$	e	$\text{Er}(e)$	
M_{zams}	million			(M_{\odot})		($10^{51} \text{ g cm}^2 / \text{s}$)		(M_{\odot})		($10^{51} \text{ g cm}^2 / \text{s}$)		(s)				
$25M_{\odot}$	1.0			1.964		3.478		2.078		3.288		6298.29		0.860		
	1.5	1.0	0.1	1.951	0.0066	3.522	0.0127	2.064	0.0067	3.323	0.0106	8274.54	0.3137	0.883	0.0267	
	2.0			1.943	0.0106	3.455	0.0066	2.065	0.0063	3.250	0.0115	7868.58	0.2493	0.880	0.0232	
	3.0			1.935	0.0147	3.482	0.0012	2.051	0.0129	3.292	0.0012	10744.9	0.706	0.897	0.0430	
	1.0			1.915		3.627		2.126		3.255		9843.52		0.892		
	1.5	1.0	0.5	1.906	0.0046	3.434	0.053	2.099	0.0126	3.118	0.0428	14031.1	0.4254	0.923	0.0348	
	2.0			1.900	0.0078	3.499	0.035	2.102	0.0112	3.155	0.0307	12871.2	0.3075	0.913	0.0235	
	1.0			1.937		3.669		2.209		3.217		91557.2		0.979		
	1.5	1.0	1.0	1.926	0.0056	3.119	0.1499	2.189	0.0091	2.745	0.1467	25489.6	0.7215	0.962	0.0174	
	2.0			1.919	0.0092	3.461	0.0566	2.179	0.0135	3.047	0.0528	145340.6	0.5874	0.985	0.0061	
	$30M_{\odot}^a$	1.0	2.0	0.1	1.783		4.499		2.077		3.861		—		1.44	
		2.0			1.772	0.0061	4.451	0.0106	2.043	0.0164	3.859	0.00051	—		1.50	0.0416
1.0		2.0	1.0	1.781		4.087		2.172		3.351		—		1.38		
2.0				1.769	0.0067	4.614	0.1289	2.115	0.0262	3.859	0.1550	—		1.55	0.1096	
$40M_{\odot}$	1.0	1.0	0.1	1.875		4.419		2.124		3.902		—		1.84		
	2.0			1.869	0.0032	4.276	0.0323	2.069	0.0259	3.862	0.0102	—		2.00	0.0869	

NOTE—For each simulation, the four first columns show the progenitor of the CO_{core} , the number of particles used in the simulation, the η factor that scales the kinetic and internal energy of the SPH particles to mimic a weaker or stronger SN explosions and the ξ parameter that determines the size of the capture radius. In the following columns we show the final mass and angular momentum of the νNS and the NS companion as well as the orbital period and eccentricity of the final binary system. For each of these values we give the relative errors with respect to the 1 million particles simulation.

$$^a E_{\text{sn}} = 2.19 \times 10^{51} \text{ erg}$$

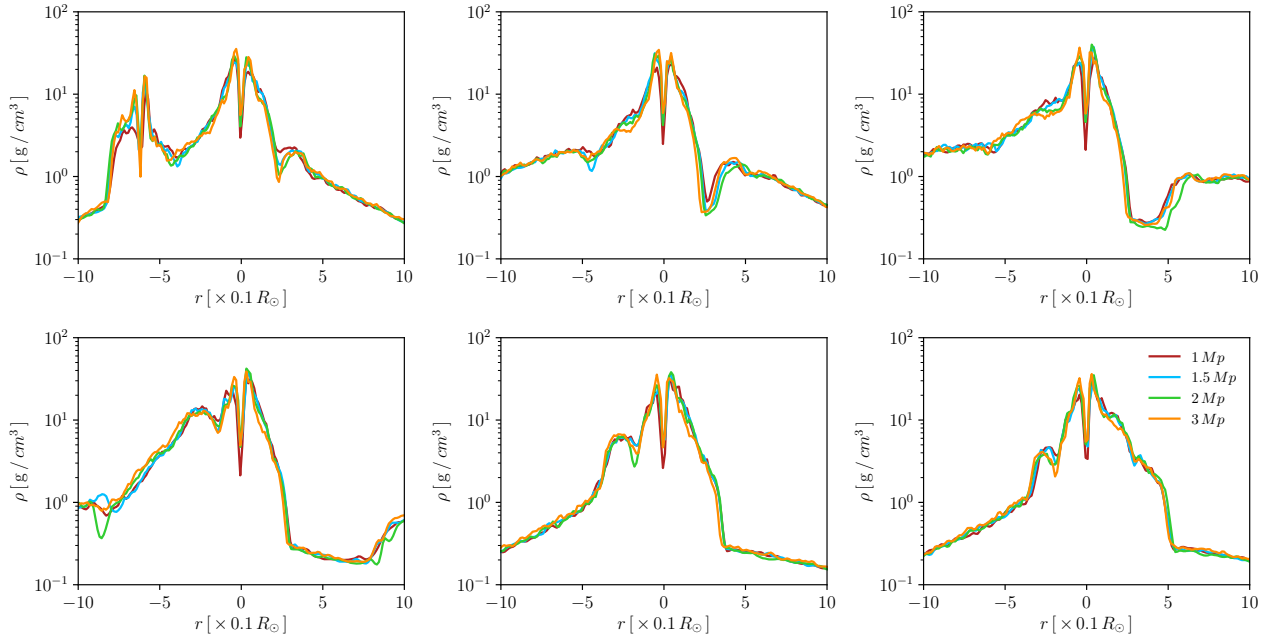


Figure A1. Density along different directions θ on the orbital binary system plane (νNS -NS). From left to right of upper panel: $\theta = 0.0, \pi/6$ and $\pi/3$ and in the bottom panel $\theta = \pi/2, 2\pi/3$ and $5\pi/6$. The center of the reference system is on the NS position and the νNS is on the $-x$ axis. The initial binary system is formed by the CO_{core} of the $M_{zams} = 25 M_{\odot}$ progenitor and a $2 M_{\odot}$ NS in an orbital period of about 5 min. Different colors correspond to different number of particles: 1 million (red line), 1.5 million (blue line), 2 million (green line) and 3 million (orange line).

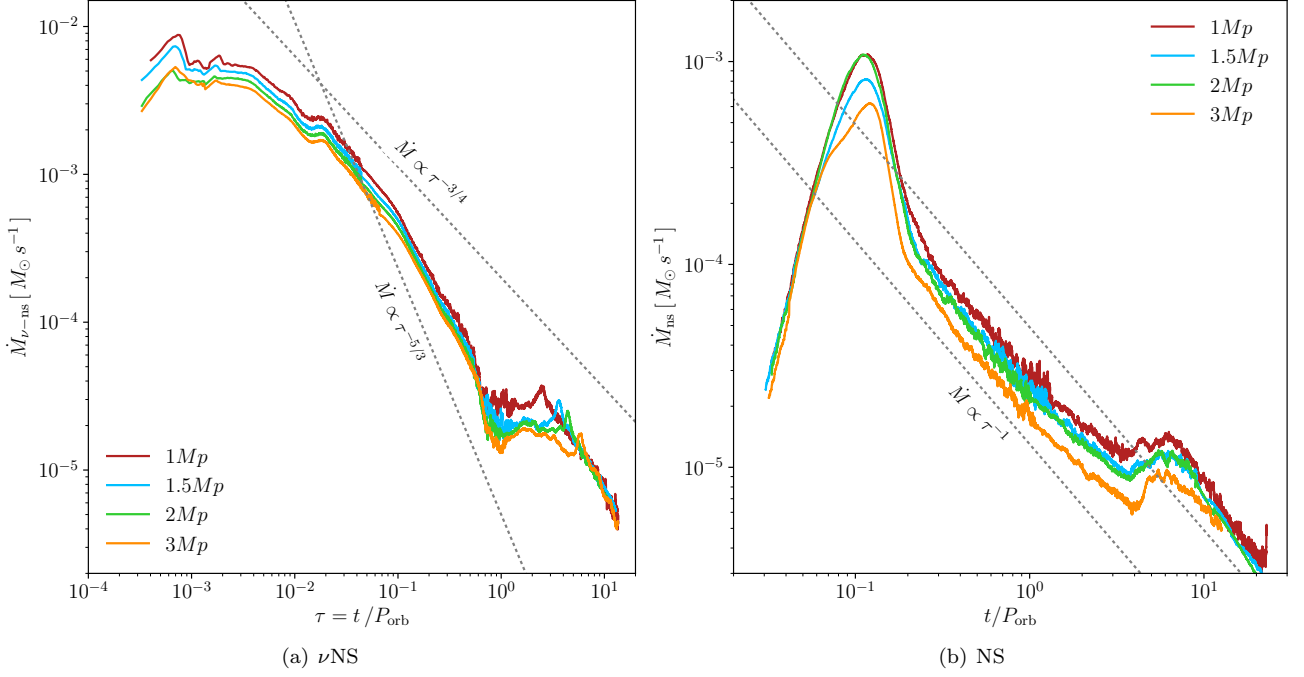


Figure A2. Mass-accretion rate on the ν NS (left panel) and the NS companion (right panel) for different number of particles modeling the SN expansion in the simulation. The initial binary period is the same as in Figure A1.

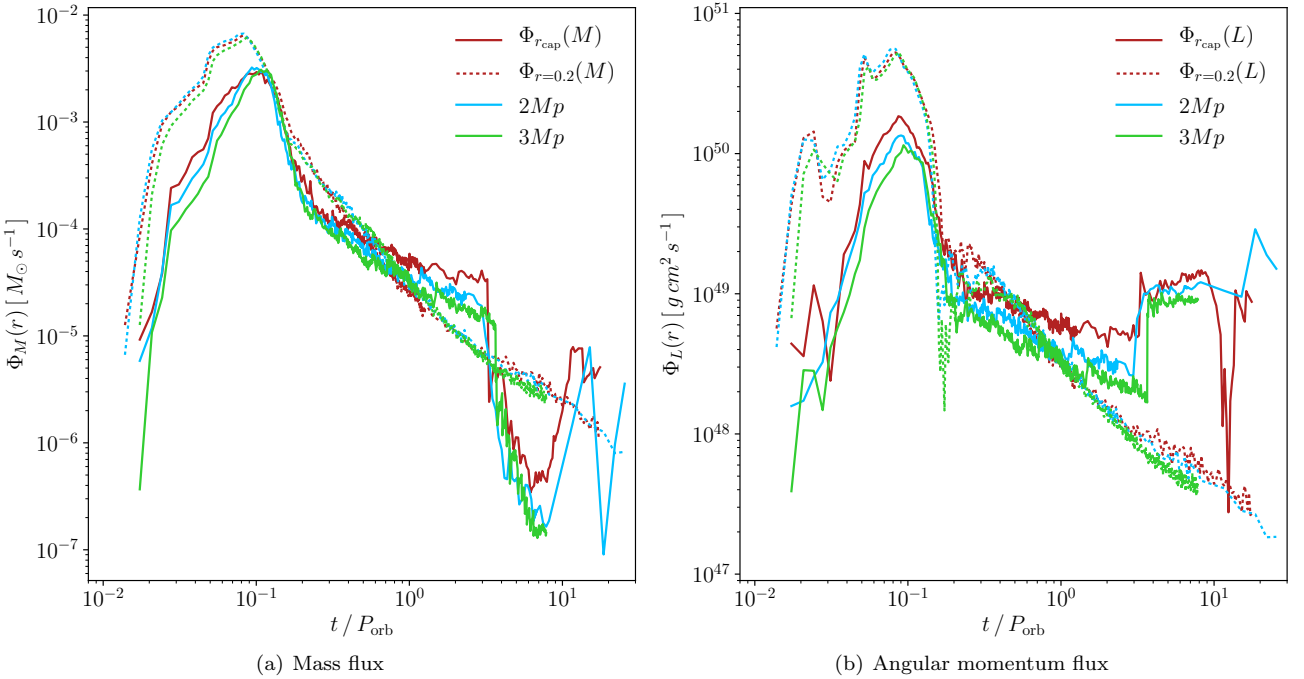


Figure A3. Mass (left panel) and angular momentum flux (right panel) through spheres of radius $r = 0.2 R_\odot$ and $r = R_{\text{cap}}$ with the NS in the center. R_{cap} surface is defined as the maximum capture radius between the particles accreted by the NS in each iteration. The initial binary period is the same as in Figure A1.

On the Final Gravitational Wave Burst from Binary Black Holes Mergers*[‡]

J. F. Rodriguez¹, J. A. Rueda^{1**}, and R. Ruffini¹

¹ICRANet, Pescara, Italy

Received August 1, 2018; in final form, August 25, 2018

Abstract—We use perturbation theory in the strong-field regime to study the inspiral-to-plunge transition of a test particle into a Kerr black hole. We found a smooth transition, without burst, and with lower energy and angular momentum radiated in gravitational waves with respect to previous treatments in the literature. Besides their theoretical interest, our results are relevant for the waveform templates of binary black hole mergers used for gravitational waves detection which are constructed on the basis of a inspiral-to-plunge transition with a high energetic burst.

DOI: 10.1134/S1063772918120338

1. INTRODUCTION

Relativistic astrophysics has flourished taking advantage on the developments in the physics of neutron stars and black holes, thanks to the discovery of quasars [1], of pulsars [2], of binary X-ray sources [3–5], of gravitational waves from binary neutron stars [6, 7], and of gamma-ray bursts [8]. From the above experience one can recognize two aspects of an experimental discovery: 1) the reproducibility of the experimental data and 2) the consistency of the data with the physical laws and the theoretical treatment. In view of the recent interest on gravitational waves due to claimed “observation of gravitational waves from a binary black hole merger” by the LIGO-Virgo Collaboration [9–11], we focus here on the second aspect and consider some theoretical issues concerning the gravitational-wave emission of a merging black hole binary.

We limit ourselves to the case of perturbations in the strong-field limit and we do not consider the post-Newtonian approaches to this problem (see Section 4 for a brief discussion on this issue). Two main idealized processes have been introduced in the strong-field regime to describe the motion of a test particle plunging into an already formed black hole. The first one of a particle initially at rest or with a finite kinetic

energy *plunging in a geodesic* from infinity. Both the Schwarzschild and the Kerr metric have been considered. Broadly speaking, all particles starting from infinite distance give rise to “*a precursor, a main burst and a ringing tail*” of gravitational-wave emission, with energy $\Delta E = \eta\mu(\mu/M)$, where μ and M are the particle and black-hole mass. The parameter η is a function of the nature of the black hole and of the initial energy and the angular momentum of the particle. It ranges from 0.01 to ≈ 1 in the fully general relativistic treatment. The second case is the particle initially in a (stable) circular orbit and finally plunging into the black hole. This case turns out to be of extreme interest in the analysis of binary black holes mergers. The emission of gravitational waves induces an energy and angular momentum loss, which in turn makes the particle to in-spiral in a sequence of quasi-circular orbits. However, as it will be shown, the final plunge is nearly geodesic. It has been relevant the introduction of the “effective potential technique” to understand the general properties of these phenomena. The evolution of the circular orbits all the way down to the last circular orbit (LCO), and also the final plunge to the horizon, can be understood with the effective potential. It is worthy to emphasize that unstable orbits are not physically relevant, i.e., they are not realizable in nature. Therefore, we consider as circular orbits only the stable ones. The LCO follows then follows the traditional definition [12], quoted in [13], as the effective potential inflection point (see Section 3) and it is the circular orbit closest to the black-hole horizon.

For a Kerr black hole, we shall show that the gravitational-wave emission leads to a “helical drifting sequence” (HDS) giving rise to a smooth

*The article is published in the original.

**E-mail: jorge.rueda@ICRA.it

[‡]Paper presented at the Third Zeldovich meeting, an international conference in honor of Ya.B. Zeldovich held in Minsk, Belarus on April 23–27, 2018. Published by the recommendation of the special editors: S.Ya. Kilin, R. Ruffini, and G.V. Vereshchagin.

transition to the plunge phase without a final burst. We have recently used this treatment to compare the numerical relativity binary black hole merger waveforms of the SXS catalog [14] with HDS ones up to the LCO (plunge)[15]. We have found an unexpected and yet theoretically unexplained agreement between both waveforms in the comparable-mass regime, for different values of the spin and mass-ratio.

Concerning the transition and the final plunge, we show here that our results differ with the ones presented in the literature (e.g. [16]). More exactly, we have found a larger amount of energy and angular momentum radiated in their treatment. A comparable energetic plunge leading to a burst also appears in the numerical-relativity waveforms (see e.g., the SXS catalog [14]). Such a feature is also found in the binary coalescence process modeled via the effective one-body (EOB) formalism [17] (see [18] for details). In view of the large use of these waveforms by the LIGO-Virgo Collaboration for the estimation of binary parameters, see e.g. the case of the GW150914 event [9], these results are far from being just an academic exercise.

The paper is organized as follows. We recall in the Section 2 the main results on the gravitational-wave emission of particles falling into a black hole from infinite distance. In the Section 3 we recall the results on the case of circular orbits without taking into account radiation-reaction and show the gravitational-wave energy and angular momentum flux at infinity, following the Sasaki–Nakamura method. Section 4 is devoted to the formulation of the equations of motion of the HDS, taking into account the radiation reaction. In Section 5 we discuss the numerical results of the evolution up to the passage of the LCO. In Section 6 we discuss the plunging of the particle into the black hole. We explicitly show the difference with the results in the literature (see e.g. [16]). Finally, we present our conclusions in Section 7.

2. TEST-PARTICLE INFALL FROM INFINITY

The gravitational radiation emitted by a test particle radially falling into a Schwarzschild black hole, was shown in a simple computation by assuming that the particle follows a geodesic, and that the radiation is described by linearized perturbation theory in flat spacetime [19] (see also [20]). Both the energy emitted, $\Delta E = 0.0025\mu(\mu/M)$, and the gravitational-wave spectrum were estimated there. In [21, 22] a mathematically more advanced treatment was introduced using the decomposition of the perturbation into tensorial spherical harmonics arriving to the Zerilli equation [23]. Its numerical integration by means of the Green’s function technique in [24] led to an improvement by a factor of

6 the previous estimate in [19], and by a factor of 4 the one in [21, 22]. It allowed the determination of the multipole components of the spectrum, and lead to the conclusion that the associated gravitational wave is composed of “*a precursor, a main burst and a ringing tail*” (see Fig. 1 in [25]). In [26], still using the Regge–Wheeler–Zerilli approach, it was studied the gravitational-wave emission of a particle projected from infinity with finite kinetic energy, into a Schwarzschild black hole. It was found a difference in the spectrum in the low-frequency region and a larger amount of radiation emitted by increasing the Lorentz gamma-factor of the injected particle.

To these works a vast activity followed, on one side the extension of the Ruffini–Wheeler formulation of a particle thrust into a Schwarzschild black hole [27], showing the corresponding increase of the burst structure. On the other side, the study of curvature perturbations using the Newman–Penrose formalism [28], was started with the pioneer work of [29] and [30] for the Schwarzschild and Kerr case, respectively. One of the first applications of the aforementioned method, was in the analysis of an in-falling particle with finite angular momentum in the field of a Schwarzschild black hole [31]. It was shown that the energy emitted may be enhanced by a factor of 50 with respect to the radial in-fall. They confirmed that the gravitational-wave burst was still composed of the above three components. The further development needed the fundamental progress introduced in [32, 33] by means of a change of variable. Teukolsky’s original radial equation has a long-range potential, making its numerical solution difficult. This change of variable introduced a short-range potential allowing to obtain an entire family of new results (see the Section 3 for further details). Among these, the gravitational emission of a test particle in-falling along the rotational axis of a Kerr black hole with spin parameter $a/M = 0.99$ ($0 \leq a \equiv J_{\text{BH}}/M \leq 1$, where J_{BH} and M are the black-hole spin and mass, respectively), showed a new multipole distribution of the radiation following the above three components. It was also shown that the total energy radiated is $0.0170\mu(\mu/M)$, i.e., a factor 1.65 larger than the energy radiated found in [24]. A second important step was made in [34] by the study of the gravitational radiation of a particle with non-zero orbital angular momentum plunging on the equatorial plane of a Kerr black hole. This proved that the energy radiated, for a Kerr black hole of $a/M \sim 1$, could reach the limiting case $\Delta E \sim \mu(\mu/M)$. We shall come back to this point in Section 6 where the transition of a particle from the inspiral (quasi-circular phase) to the final plunge into the black hole, is analyzed. We shall estimate the amount of energy radiated to infinity in such a transition and compare with some existent

treatment in the literature, e.g. the one in [16]. In conclusion, all particles plunging or thrusting from infinite distance into both a Schwarzschild and a Kerr black hole, present a characteristic burst composed of “a precursor, a main burst and a ringing tail.”

3. CIRCULAR ORBITS AROUND THE BLACK HOLE

The first relativistic treatment of the radiation of a test particle in a circular orbit around a Schwarzschild black hole was motivated by the declaration in [35] of the discovery of gravitational waves and, by the contention of their explanation in terms of synchrotron gravitational radiation [36] (see also [37]). For this reason, the multipole modes of gravitational radiation by a particle moving in a circular orbit were studied in [38]. It was found that the enhancement of high-multipoles indicated in [36], does not exist and consequently no synchrotron gravitational radiation can occur. This treatment of circular orbits in the Schwarzschild metric was reproduced in [39], and also in [40] where it was used as the “exact result” over which construct their model connecting the post-Newtonian treatment to the strong-field regime. The extension of this treatment to eccentric orbits can be found in [41]. The problem of circular orbits in the field of a Kerr black hole was formulated in [42]. The fundamental works [43, 44] treat the same physical problem but within the Sasaki–Nakamura treatment. More recently, this problem has been extended to the case of both non-equatorial and eccentric orbits [45, 46].

We proceed to compare and contrast the results in the Schwarzschild [38] with the ones developed in the Kerr metric. It is appropriate to clarify that the considerations in this section do address the gravitational energy emitted by a circular orbit, initially neglecting all effects of radiation reaction. Therefore, we consider idealized circular orbits on the equatorial plane, at constant radii, including the LCO. The effective potential is given by [12] (reproduced in [20])

$$V_{\text{eff}} = 1 - \frac{2M}{r} + \frac{l^2 - a^2(\epsilon^2 - 1)}{r^2} - \frac{2M(l - a\epsilon)^2}{r^3}, \quad (1)$$

which leads to a radial equation of motion

$$\epsilon^2 = \left(\frac{dr}{d\tau}\right)^2 + V_{\text{eff}}, \quad (2)$$

where $\epsilon \equiv E/\mu$ and $l \equiv L/\mu$ are the particle’s energy and angular momentum per unit mass, and τ is the proper time. We are interested in corotating circular orbits (obtained from the conditions $dr/d\tau = 0$ and

$\partial V_{\text{eff}}/\partial r = 0$), which have energy and orbital angular momentum given by [12, 20]

$$\epsilon = \frac{E}{\mu} = \frac{r^2 - 2Mr + aM^{1/2}r^{1/2}}{r(r^2 - 3Mr + 2aM^{1/2}r^{1/2})^{1/2}}, \quad (3)$$

$$\frac{l}{M} = \frac{L}{\mu M} = \frac{r^2 - 2aM^{1/2}r^{1/2} + a^2}{r^{3/4}(r^{3/2} - 3Mr^{1/2} + 2aM^{1/2})^{1/2}}. \quad (4)$$

The LCO is given by the inflection point of the effective potential, i.e., the radius for which $\partial^2 V_{\text{eff}}/\partial r^2 = 0$. In the case of $a/M = 0$ (Schwarzschild metric), it is located at $r_{\text{LCO}} = 6M$, $E_{\text{LCO}}/\mu = 2\sqrt{2}/3$, and $L_{\text{LCO}}/(\mu M) = 2\sqrt{3}$. In the case of an extreme Kerr black hole, $a/M = 1$, the LCO is located very close (but not coincident) to the black-hole horizon, i.e. $r_{\text{LCO}} \rightarrow r_+$ where $r_+ = M$, and $E_{\text{LCO}}/\mu = \sqrt{3}/3$, $L_{\text{LCO}}/(\mu M) = 2\sqrt{3}/3$. Namely, for an extreme black hole there exist circular orbits very close to the black-hole horizon (see e.g. [47] for additional details).

Now we turn to the calculation of the energy and momentum fluxes. It can be done by using standard metric perturbation theory, e.g., the pioneering work of Regge–Wheeler. However, this method is not appropriate for the Kerr spacetime. As already mentioned, there is an alternative approach developed by Teukolsky, involving curvature perturbations. Within this approach the scalar, vector and tensor perturbations are governed by a single equation. The master equation can be separated and the solution is an expansion in Fourier and spheroidal harmonic modes [30, 48, 49]. Unfortunately, Teukolsky’s radial equation has a long-range potential and its numerical integration with boundary conditions is difficult. In [32, 33] it was found a change of variables that transforms the Teukolsky’s radial equation into the Sasaki–Nakamura equation whose potential is short-ranged. In the case of circular orbits, the gravitational radiation of energy and angular momentum to infinity are given by

$$\frac{dE}{dt} = \sum_{l \geq 2} \sum_{m=-l}^l \frac{|Z_{lm\omega}^H|^2}{4\pi\omega_m^2},$$

$$\frac{dJ}{dt} = \sum_{l \geq 2} \sum_{m=-l}^l \frac{m|Z_{lm\omega}^H|^2}{4\pi\omega_m^3}, \quad (5)$$

where $\omega_m = m\Omega$, and $Z_{lm\omega}^H$ is a complex number which depends on the orbital frequency Ω and it is obtained from the solution of the Sasaki–Nakamura equation (see [50] for the explicit expression).

Without introducing further technical details which can be found in the aforementioned references,

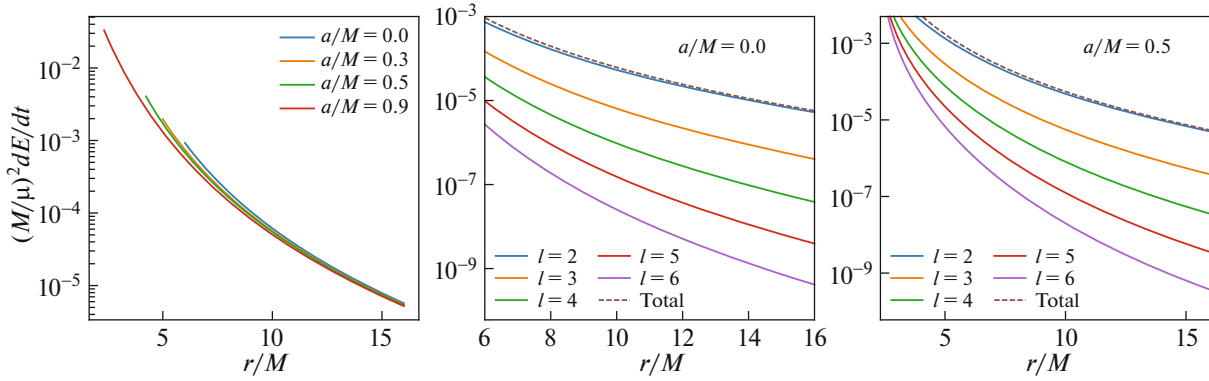


Fig. 1. Left: comparison of the total gravitational-wave energy flux at infinity, $\dot{E} \equiv dE/dt$, emitted by the test particle in circular orbits around the black hole for selected values of the black-hole dimensionless spin, as a function of the dimensionless radial position, r/M . Center and right: contribution of the gravitational-wave modes $l \geq 2$ ($m = -l$) to the total gravitational-wave energy flux at infinity in the case of a test particle in circular orbits of radius r around a Schwarzschild (center panel) and around a Kerr black hole with $a/M = 0.5$ (right panel). It can be seen that the $(2, 2)$ highly dominates the gravitational-wave emission at any radius down to the marginally unstable orbit.

we present the numerical results. Figure 1 shows the total energy flux dE/dt for selected values of the black-hole dimensionless spin. We also show in Fig. 1 the contribution of the gravitational-wave modes $l \geq 2$ to the total gravitational-wave energy flux to infinity. We explicitly show that the enhancement of higher multipoles does not occur either in the case of the Kerr metric, where also the quadrupole contribution is largely predominant. No synchrotron gravitational radiation can occur either in the Schwarzschild or the Kerr case. The contribution of higher multipoles becomes relevant only for near-horizon orbits around nearly extremal black holes [51].

4. HELICOIDAL DRIFTING SEQUENCE

In order to analyze the dynamics of a test particle we use the Hamiltonian formalism. The Hamiltonian of a test particle of mass μ in the field of a Kerr black hole of mass M is given by (see e.g. [52] and references therein)

$$H = -p_t = -N^i p_i + N \sqrt{\mu^2 + \gamma^{ij} p_i p_j}, \quad (6)$$

where $N = 1/\sqrt{-g^{00}}$, $N^i = -g^{ti}/g^{tt}$, and $\gamma^{ij} = g^{ij} + N^i N^j / N^2 = g^{ij} - g^{ti} g^{tj} / g^{tt}$, and $g^{\mu\nu}$ are the standard contravariant components of the Kerr spacetime metric in the Boyer–Lindquist coordinates. We recall that the latin indexes stands for the spatial Boyer–Lindquist coordinates (r, θ, ϕ) . The momenta p_r and p_ϕ are the radial and the angular momentum of the particle, respectively. The Hamilton’s canonical equations for a test particle on the

equatorial plane $\theta = \pi/2$ under the action of radial and azimuthal dissipative effects are

$$\begin{aligned} \frac{dr}{dt} &= \frac{\partial H}{\partial p_r}, & \frac{d\phi}{dt} &\equiv \Omega = \frac{\partial H}{\partial p_\phi}, \\ \frac{dp_r}{dt} &= -\frac{\partial H}{\partial r} + \mathcal{F}_r^{\text{nc}}, & \frac{dp_\phi}{dt} &= \mathcal{F}_\phi^{\text{nc}}. \end{aligned} \quad (7)$$

We consider only the *gravitational-radiation-reaction* part of the non-conservative force (see e.g., [53] for a review on the subject), so we adopt for the radial and azimuthal the following non-conservative forces, $\mathcal{F}_r^{\text{nc}} = 0$, $\mathcal{F}_\phi^{\text{nc}} = -dJ/dt$, where J is the angular momentum carried out to infinity by the gravitational waves given by Eq. (5). This assumption is supported from previous results that show that the linear momentum carried out by the waves to infinity satisfies $dp_r^{\text{GW}}/dt \ll |\partial H/\partial r|$ [54]. We recall that for purely quadrupole waves in strict circular orbits the following equality is satisfied:

$$\frac{dJ}{dt} = \frac{1}{\Omega} \frac{dE}{dt}. \quad (8)$$

However, since there is the radial drift and a small contribution of higher order multipoles, the above equality must not be strictly satisfied (see Eq. (5)). We have checked from our numerical computations that $|1 - \Omega(dJ/dt)/(dE/dt)| \sim 10^{-6}$ during the evolution. The smallness of this value imply that the motion is indeed quasi-circular, but it is sufficiently large (with respect to the numerical precision of our calculations) to conclude that the equality (8) is not verified in the HDS evolution, as expected.

It has been traditional to treat the evolution using the so-called adiabatic approximation that assumes a particle moving from a circular orbit to the next

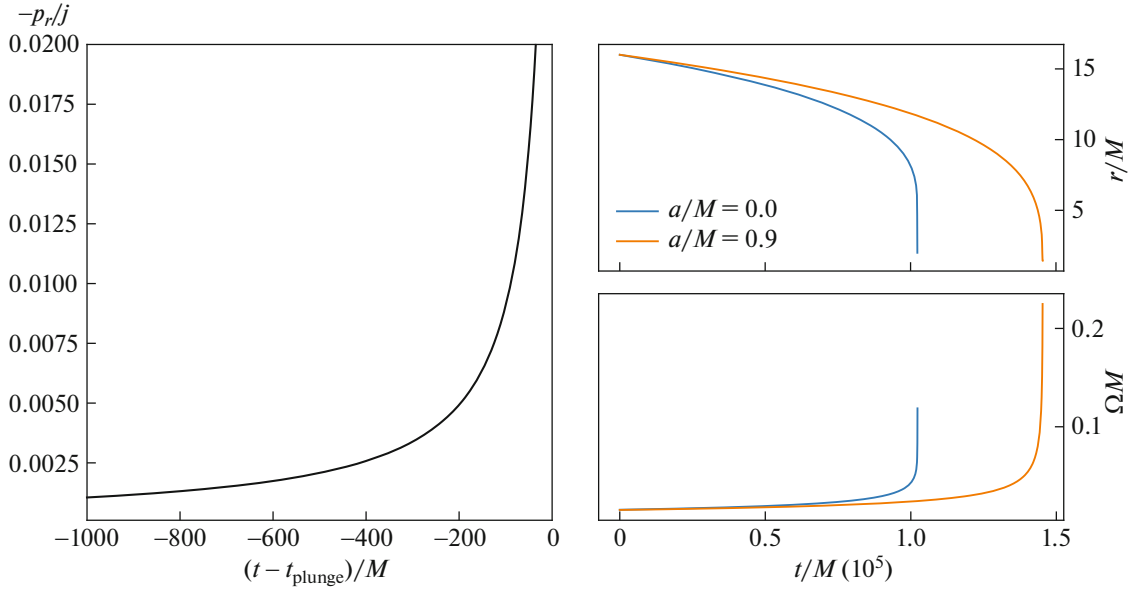


Fig. 2. On the left, the ratio p_r/j of the radial momentum to the angular momentum per unit mass, of a test particle around a Kerr black hole with $a/M = 0.9$, and mass-ratio $\mu/M = 1/100$. The plot shows the ratio from $r \approx 4.53M$ up to the location of the LCO at $r \approx 2.32M$. The upper and lower panels on the right show the dimensionless radial position, r/M , and dimensionless orbital angular velocity, ΩM , respectively. The initial position at time $t/M = 0$ is $r/M = 15.9$. The case of a Schwarzschild black hole is shown in blue while the case of a Kerr black hole with $a/M = 0.9$ is shown in orange.

(see, e.g., [45, 55]), due to the energy and angular momentum radiation. For example, since the energy can be expressed in terms of r , a change in the energy induces a change in r . Thus, it can be found a dynamical equation for r by differentiating (3) and equating it to the gravitational energy flux. The evolution is found by integrating this equation instead of solving the equations of motion (7). This approximation, although sufficient to estimate some general properties of the evolution, lacks of the appropriate inclusion of the non-zero radial motion of the particle in the equations of motion. As we shall show below, this radial drift becomes essential to trigger the final plunge to the black hole. When the radial momentum is properly included, the LCO location does not represent any longer a point where the equations of motion break down. Indeed, the conditions of “adiabaticity” are kept up to such distances (see Fig. 3 and related discussion in Sec. 5). In contrast, within the adiabatic approach it is needed the introduction of a separate treatment of the transition to the plunge phase (see [45, 55] and Sec. 5 for details).

It is appropriate to mention other treatments in the literature on the problem of a binary system under the action gravitational radiation. In [17] it was proposed the EOB approximation to overcome the known problem of the non-convergence of the higher-order post-Newtonian successive approximations. The EOB treatment “maps” the post-Newtonian binary into a “Schwarzschild deformed

metric” which depends on the mass-ratio. In the extreme mass-ratio limit $\mu/M \rightarrow 0$, the metric becomes the Schwarzschild one. However, the treatment of the waveform and/or the gravitational-wave fluxes stands on a post-Newtonian basis. The Kerr metric, within EOB, has been used to treat spinning merging components [56]. However, also that EOB treatment is based on a post-Newtonian treatment for the waveforms and/or fluxes. Thus although “calibrated” to fit strong-field results, the EOB approach remains conditioned by the non-convergence of the post-Newtonian formalism.

The set of equations of motion (7) was first used in [57], also using the radiation-reaction term obtained from the numerical solution of the Teukolsky. However, they analyze the case of intermediate mass-ratios with the conservative dynamics given by the aforementioned EOB treatment. A different method was also introduced to compute the evolution of the circular orbits that is based on linking one to the next by describing changes in the “constants” of motion [58], and finding the envelope. Such reference circular orbits, called “osculating orbits,” with a planar force have been applied to the inspiral of a particle in the Schwarzschild [58] and in the Kerr spacetime [59]. Since we do not include the radial velocity in the calculation of the gravitational-wave, namely we use exact circular orbits, our scheme and the osculating orbits become equivalent under these assumptions. However, we use the fully relativistic

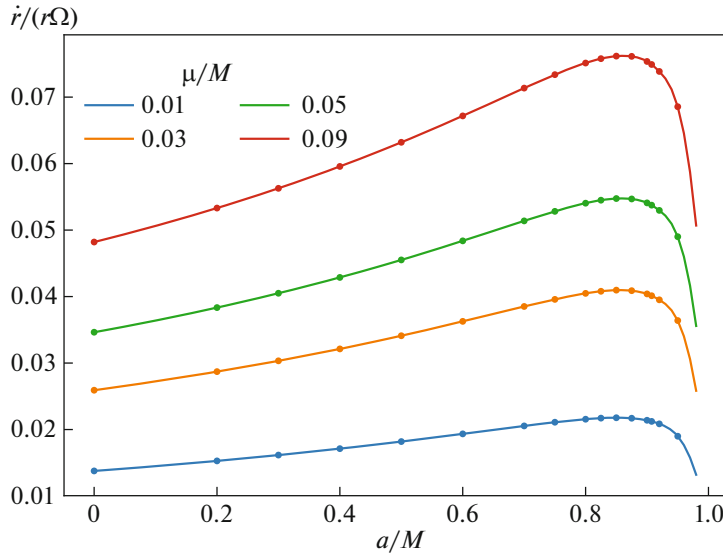


Fig. 3. Ratio of the orbital to radiation-reaction timescale $T_{\text{orb}}/T_{\text{rad}} = |\dot{r}|/(r\Omega)$ evaluated at the location of the LCO, for selected mass-ratios and selected values of the black-hole spin parameter.

gravitational-wave flux instead of a post-Newtonian as in [58]. More recently, a test particle inspiraling into a Kerr black hole was treated in [60], similarly as we do here, but with the drawback of incorporating the gravitational-wave flux after the LCO up to the light ring (unstable circular orbits), even though it is given by the Teukolsky equation.

On the other hand, full numerical-relativity simulations are available only for relatively large mass-ratios $\gtrsim 1/10$ as it can be seen from the SXS catalog of binary black-hole mergers [14] performed with the Spectral Einstein Code (SpEC). Therefore, it is not currently possible to perform a one-to-one comparison between numerical-relativity simulations and the test-particle treatment. However, we have recently performed a comparison of the SXS waveforms with the ones obtained in the present study, in the comparable-mass regime [15]. Unexpectedly, we have found a great agreement of both waveforms for spinless, as well as for aligned and anti-aligned binaries, with equal or unequal values of mass-ratio.

5. NUMERICAL RESULTS

We integrate Eqs. (7) numerically with initial conditions appropriate for quasi-circular orbits on the equatorial plane. At the initial time $t_0 = 0$ we set the initial distance r_0 , and the initial phase is $\phi(t_0, r_0) = 0$. The angular momentum is $p_\phi(t_0, r_0) = L_0$, where $L_0 \equiv L(r_0)$ is given by Eq. (4). The initial condition for the radial momentum can be obtained from the

equations of motion as follows. The radiative force induces a radial velocity

$$\left(\frac{dp_\phi}{dt}\right)\Big|_{t_0, r_0} = \left(\frac{dp_\phi}{dr}\right)\left(\frac{dr}{dt}\right)\Big|_{t_0, r_0} = \mathcal{F}_\phi^{\text{nc}}\Big|_{r_0}. \quad (9)$$

The non-zero radial velocity is related to p_r via Eqs. (7), and by introducing into the above expression a non-linear algebraic equation for $p_r|_{r_0}$ is obtained. Such equation can be solved numerically given the above conditions and, at leading order, it can be solved analytically:

$$p_r|_{r_0} = \sqrt{\left(\mu^2 + \frac{r_0^2 L_0^2}{\Lambda_0}\right) \frac{r_0^2 \Delta_0}{\Lambda_0}} \times \frac{\Lambda_0 \mathcal{F}_\phi^{\text{nc}}\Big|_{r_0}}{dL/dr_0(r_0^2 + a^2)^2}, \quad (10)$$

where $\Delta_0 = r_0^2 - 2Mr_0 + a^2$ and $\Lambda_0 = (r_0^2 + a^2)^2 - a^2 \Delta_0$. This equation gives the initial condition for p_r with very high accuracy and can be safely used provided that the initial radius is sufficiently far from the radius of the LCO. For instance, the initial position $r_0 = 15.9M$, with Kerr black hole spin parameter $a/M = 0.9$ and a mass-ratio $\mu/M = 1/100$, gives the initial p_r accurate within nine digits. This initial radial velocity condition, if given at a large enough radius r_0 , reduces to the ‘‘adiabatic’’ approximation. This can be seen from Eqs. (9) and (5), which imply $dr/dt = -(dJ/dt)/(dp_\phi/dr)$. As we have mentioned, the property of a strict circular orbit, namely Eq. (8), is satisfied in our sys-

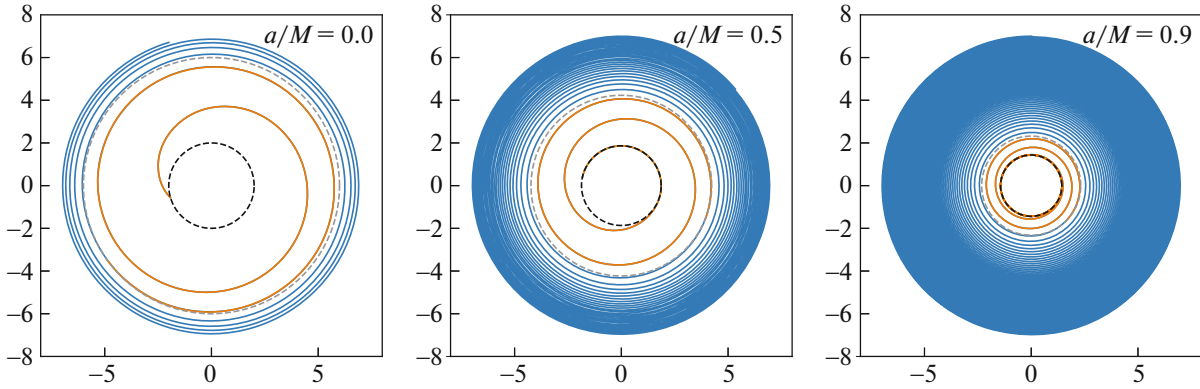


Fig. 4. Trajectory of a test particle in the HDS around a Schwarzschild black hole, $a/M = 0$ (left panel) and around a Kerr black hole with $a/M = 0.5$ (center panel) and with $a/M = 0.9$ (right panel). The blue part of the trajectory goes from $r = 7M$ up to the location of the corresponding LCO (marked with a gray-dashed circle), while the orange color indicates the plunge regime. The black-hole horizon is indicated with a black-dashed circle. The mass-ratio is $\mu/M = 1/100$.

tem by one part in a million, therefore the condition $dr/dt = -(1/\Omega)(dE/dt)/(dp_\phi/dr)$ is approximately satisfied with the same accuracy. Now, by replacing Ω via Eqs. (7), we finally obtain $dr/dt = (dE/dt)/(dE/dr)$, which is the flux-balance condition of the adiabatic approximation, adopted e.g. in [16].

Figure 2 shows the ratio of the radial momentum, p_r , to the angular momentum per unit mass, $j \equiv p_\phi/\mu$, during the HDS obtained for the aforementioned initial conditions. It can be seen how the contribution of the radial momentum increases as the particle approaches the location of the LCO. In this example, p_r becomes $\sim 4\%$ of the angular momentum per unit mass. It is also shown the sharp decrease (increase) of r (Ω) near the location of the LCO, which suggests that the ‘‘adiabaticity’’ of the system may be loose at such distance. The system can be considered to evolve adiabatically if the ratio of orbital to radiation-reaction timescale is much smaller than unity. Following [61], we can define $T_{\text{orb}}/T_{\text{rad}}$ in terms of the tangential and radial velocity, namely $T_{\text{orb}}/T_{\text{rad}} = |\dot{r}|/(r\Omega)$. Since this ratio increases for decreasing values of r , it reaches its largest value during the HDS at the location of the LCO. We show in Fig. 3 the above ratio evaluated at the location of the LCO, for selected values of μ/M and black-hole spin parameters. It can be seen that for the current example with $a/M = 0.9$, we have $T_{\text{orb}}/T_{\text{rad}} \sim 0.02$ at $r_{\text{LCO}}/M = 2.32$. And finally, Fig. 4 shows the trajectory of the test particle in the HDS around a Schwarzschild black hole, $a/M = 0$ (left panel) and around a Kerr black hole with $a/M = 0.5$ (center panel) and with $a/M = 0.9$ (right panel). It can be seen the effect of the black-hole spin in the particles’

trajectory. The bigger a/M the more the particle rotates before reaching the LCO.

6. PLUNGE INTO THE BLACK HOLE

We consider now the evolution of the particle after reaching the LCO, namely the plunge into the black hole. A physical insight of this process can be obtained from the radial effective potential (1). Figure 5 compares V_{eff} with $a/M = 0$ (Schwarzschild) and with $a/M = 0.9$, for three selected values of the orbital angular momentum of the particle, L : one larger, one equal, and one smaller than the value at the LCO, L_{LCO} . For $L > L_{\text{LCO}}$, a small decrease in L due to the gravitational radiation makes the particle to change from one minimum to the next, namely it goes from one circular orbit to another with smaller radius. At $L = L_{\text{LCO}}$ the particle reaches the LCO and, for $L < L_{\text{LCO}}$, the effective potential has no minima, i.e., no circular orbits exist and the particle fall into the black hole.

In the realistic situation, the full numerical integration of the equations of motion shows that, indeed, when the particle passes the location of the LCO, it possesses a large radial momentum (see Fig. 2) and angular momentum $L < L_{\text{LCO}}$, so it continues its infall towards the black hole, smoothly, without any further radiation loss. Figure 5 shows that the plunge to the black hole is markedly different in the Schwarzschild and Kerr cases. While the effective potential for $L = L_{\text{LCO}}$ is zero at the horizon in the Schwarzschild, it reaches a finite non-zero value for the Kerr case. The flatness of the effective potential from the LCO to the horizon, in the Kerr case, implies a very little amount of energy and angular momentum radiated out to infinity during the final plunge. This

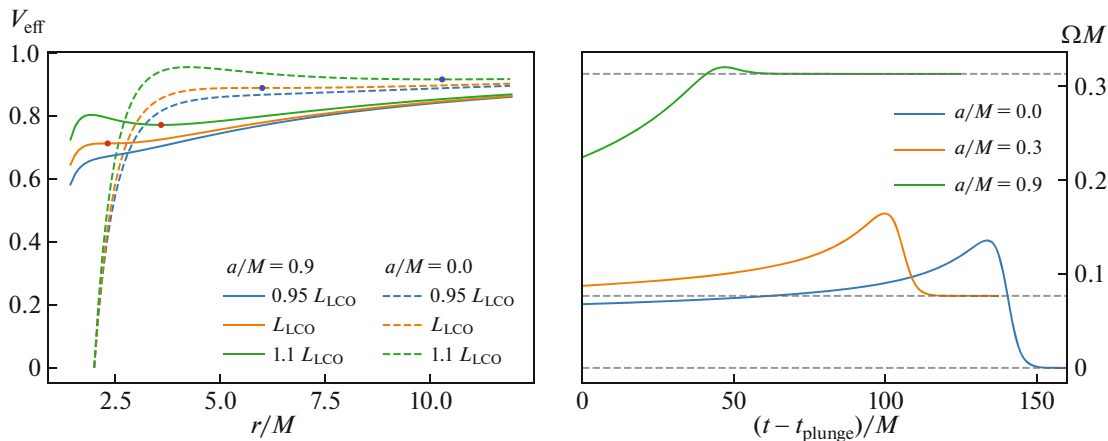


Fig. 5. Left: V_{eff} for different values of the particle angular momentum in the case of a Schwarzschild (dashed curves) and of a Kerr black hole with $a/M = 0.9$ (solid curves). The blue and red dots indicate the minimum of the potential in the Schwarzschild and Kerr cases, respectively. Right: angular velocity of the particle, $\Omega = d\phi/dt$ after the crossing of the LCO, in the case of Kerr with $a/M = 0.9$ (green), $a/M = 0.3$ (orange), and in the case of Schwarzschild (blue). The mass-ratio is $\mu/M = 1/100$. The gray-dashed horizontal lines show the corresponding values of the angular velocity of the black-hole horizon.

can be also understood from the fact that, due to the frame-dragging effect, the particle is forced to approach the Kerr black-hole horizon tidally locked, hence it approaches the black hole with non-zero angular momentum. These features are confirmed by our numerical integration (see Fig. 5).

Since the plunge is (nearly) geodesic we integrate the equations of motion during this part of the evolution without energy and momentum losses. It is worth to emphasize that there is an uncertainty in the definition of the end of the inspiral phase. We have defined it as the time when the particle, following the HDS, reaches the LCO, but one could have used instead, for instance, the time when the particle's angular velocity reaches the corresponding value of the LCO (see e.g. [18]). Despite of the fact that these two times do not generally coincide, in both cases a region around the adiabatic time of the LCO is created (see Fig. 7). Within this region, extending out and in the LCO adiabatic time, the particle radiates following the radiation law of circular orbits (5). This region connects the inspiral (quasi-circular orbits) regime to the plunge (geodesic) regime where the gravitational radiation is negligible. It is also important to mention that in order to approach the horizon we have used the momentum p_{r^*} , conjugate to the tortoise radial coordinate r^* defined by $dr^*/dr = (r^2 + a^2)/(r^2 - 2Mr + a^2)$. We have shown in Fig. 5 the full evolution of the test particle until it reaches the black-hole horizon, for three selected cases: $a/M = 0, 0.5, 0.9$. The fact that the particle corotates and approaches tidally locked to the black hole is shown in Fig. 5.

We recall that the angular velocity of the black-hole horizon is given by $\Omega_+ = a/(r_+^2 + a^2)$ [62], where $r_+ = M + \sqrt{M^2 - a^2}$ is the black hole outer horizon radius. The evolution of the energy, the radial and angular momentum of the particle during this phase is shown in Fig. 6. It can be seen that both the energy and the angular momentum are conserved, and that the difference in the effective potential between the LCO and outer the horizon (see Fig. 5) is fully converted into the particle's in-falling kinetic energy. We can see that for non-zero black hole rotation, in agreement with the effective potential shown in Fig. 5, the difference is smaller. Consequently, the particle approaches the horizon with lower radial velocity than in the Schwarzschild case where it tends to the speed of light. We have also included the radial position in order to show the particle's approach to the horizon.

We can now contrast our results with the different treatments in the literature, in particular with the approach found in [16]. They derived approximated equations of motion and their corresponding semi-analytic solutions for “the transition to plunge” regime. Their approximation basically consist in a Taylor expansion of the energy and the angular momentum around the LCO values, which is equivalent to the use of an approximate effective potential. Both the angular velocity and the energy radiated in gravitational waves, are assumed to be equal to their values around the LCO. The boundary conditions are set by imposing that the solution matches before the LCO the adiabatic motion, and after the LCO

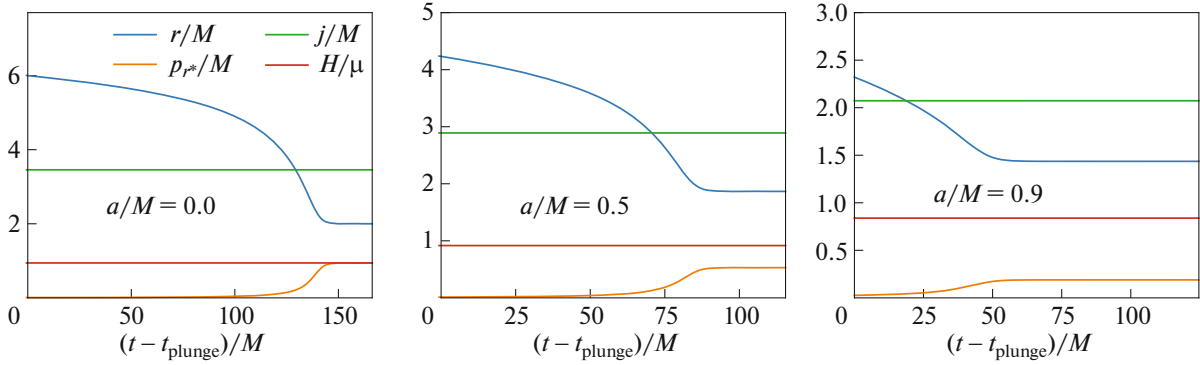


Fig. 6. Physical properties of a test particle in the final plunging into a Schwarzschild black hole, $a/M = 0$ (left panel), into a Kerr black hole with $a/M = 0.5$ (center panel) and with $a/M = 0.9$ (right panel). The mass-ratio is $\mu/M = 1/100$. We show the particle radial position, r/M (blue), dimensionless angular momentum, j/M (green), dimensionless radial momentum, p_{r^*} (orange), and the dimensionless energy, H/μ (red).

a fully geodesic (i.e. non-radiative) plunge. From these results, they obtained semi-analytic formulas for the particle’s energy and angular-momentum in the “transition” regime, E_f and L_f , which are expressed as “deficits” with respect to the LCO values, i.e. their Eq. (3.26),

$$\Delta E \equiv E_f - E_{\text{LCO}}, \quad \Delta L \equiv L_f - L_{\text{LCO}}, \quad (11)$$

which are both negative. In other words, they evaluate through the above differences the deviation of the particle’s motion from the strict circular adiabatic one. Although we agree with their general qualitative picture, it can be checked from their Eq. (3.26) and Table 1, that the “deficits” are much larger than the ones obtained by the full numerical integration of the HDS equations of motion.

A first contrast of the two approaches, for the case of a black hole with spin parameter $a/M = 0.9$, is shown in Fig. 7, where it is compared the particle’s radial trajectory near the location of the LCO. It can be seen that the two solutions converge at a large distance from the black hole. This indicates, as we have explained in Section 5, that these two solutions satisfy the same initial condition set by the adiabatic approximation. We also show in Fig. 8 the comparison, for the same case, of the energy and the angular momentum “deficits,” ΔE and ΔL , obtained from our approach, i.e., by adopting $E_f \equiv H(t_{\text{plunge}})$ and $L_f = p_\phi(t_{\text{plunge}})$, with the ones obtained by them.

The above result implies a larger amount of gravitational radiation in the treatment of [16]. The main reason for this additional gravitational-wave emission is their assumption of keeping the particle radiating at the rate of the LCO (which is the highest one of all circular orbits; see Fig. 1), before and long after crossing it ($T > 1$ in Fig. 7). We found that the extrapolation of such an approximation much beyond the LCO is

the cause of the larger discrepancy with our results. It is clear that this extra radiation is needed under the assumption of strict circular orbits. This is due to the fact that in the absence of such a radiation, there is no reason for the particle to plunge into the black hole given that the LCO is stable. When the radial drift is considered, as in the HDS, there is an increasing contribution of the radial momentum (see Figs. 2 and 6) that modifies the effective potential. In this context the LCO does not play any special role and only assists the passing of the particle in virtue of the previously acquired radial momentum. As a consequence, we expect that in the HDS the test particle smoothly falls into the Kerr black hole with a negligible gravitational-wave emission. The radiation comes only from the non-circular plunge trajectory followed by the particle (e.g., the orange-color trajectories in Fig. 4) which must be much smaller than the gravitational radiation per orbit at the LCO. This explains the additional gravitational-wave radiation obtained in [16] with respect to our results.

We proceed to evaluate the consequences of these differences in the estimation of the mass of the final black hole. The latter can be expressed as $M_f = M + \Delta E_{\text{rad}}$, where $\Delta E_{\text{rad}} \equiv E_f - \mu < 0$, M is the total mass of the black-hole binary, and E_f is the final energy of the test particle. Thus, we can write the energy radiated as,

$$\Delta E_{\text{rad}} = \Delta E_{\text{ad}} + \Delta E, \quad (12)$$

where $\Delta E_{\text{ad}} \equiv E_{\text{LCO}} - \mu$ is the energy radiated up to the location of the LCO within the adiabatic strict circular motion approximation, and ΔE is the energy “deficit” with respect to the approximation defined in Eq. (11). It can be checked that, for the case of an equal-mass binary, the contribution of ΔE to M_f (in the $a/M = 0.9$ case) is about 10%, while in our

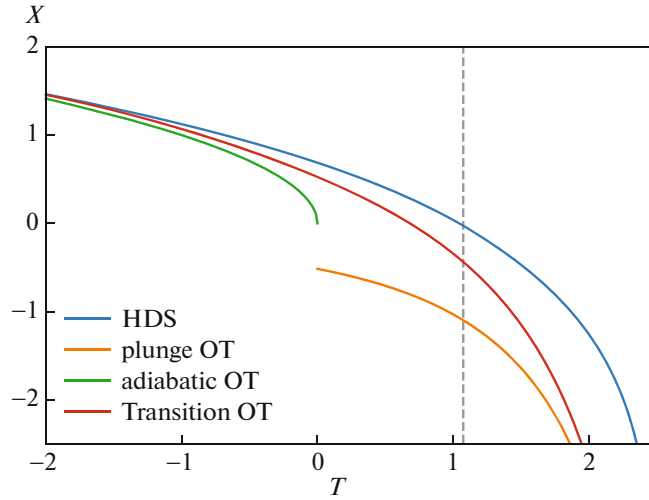


Fig. 7. Comparison for the case $a/M = 0.9$, during the transition regime of our treatment and the one of [16]. The variable X is the normalized difference between the particle’s radial position and the LCO. The variable T is the normalized proper time with $T = 0$ at $r = r_{\text{LCO}}$ in the strict adiabatic sequence. The details on the normalization can be found in [16]. It can be seen that near the LCO, i.e., around $X = 0$ and for $T < 0$, the two trajectories are similar, but for $T > 0$ they become separated. This is consistent with the expansion of the effective potential around the LCO which is expected to be valid only near $X = T = 0$. The vertical dashed line corresponds to t_{plunge} in our present HDS approach, $T \approx 1$.

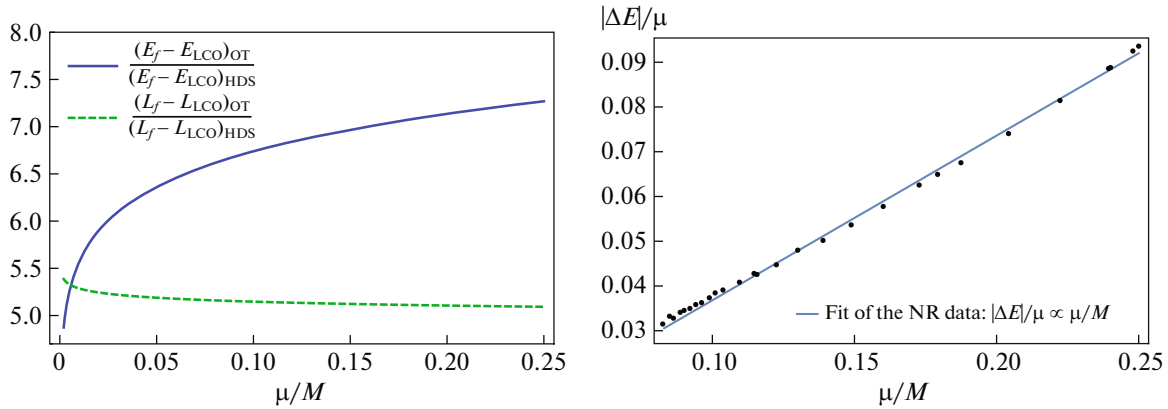


Fig. 8. Left: comparison for the case $a/M = 0.9$, of the quantities $E_f - E_{\text{LCO}}$ and $L_f - L_{\text{LCO}}$ obtained from our HDS, and the semi-analytic formulas of [16]. Right: energy “deficit” $\Delta E/\mu$ estimated from the numerical-relativity simulations of the SXS catalog [14]. It is surprising that it scales in the same way as the energy radiated in a purely radial plunge into a Schwarzschild black hole [24] (see also Section 2).

HDS case it is only about 1% (see Fig. 8). This additional amount of gravitational radiation in [16] will lead to a more energetic gravitational waveform in the final merging phase. It is interesting that a similarly energetic plunge leading to a burst of radiation, is present in the numerical-relativity waveforms of the SXS catalog [14]. Such a feature is also found in the binary mergers modeled via the EOB formalism [17] which adopts a treatment similar to the one in [16] (see [18] for details). Therefore, the above discrepancy acquires relevance in view of the large use, by the

LIGO-Virgo Collaboration, of the above waveforms with such a burst (see e.g. [9] for the case of the event GW150914). In this line, we recall the recent result of an independent analysis of the GW150914 event, that shows an issue with this final burst which is clearly in contrast with the current templates (see Figs. 5 and 10 in [63] and also [64–66], for further details).

Now, we assess the dependence of the radiated energy and angular momentum on the mass-ratio, μ/M . For a given a black-hole spin, the semi-analytic treatment of [16] predicts that the above-

defined energy and angular momentum “deficits” scale with the mass-ratio as $|\Delta E|_{\text{OT}}/\mu \propto (\mu/M)^{4/5}$ and $|\Delta L|_{\text{OT}}/(\mu M) \propto (\mu/M)^{4/5}$. We find from our numerical computations that, approximately, $\Delta E_{\text{HDS}}/\mu \propto (\mu/M)^{0.72}$ and $\Delta L_{\text{HDS}}/(\mu M) \propto (\mu/M)^{0.81}$. The different scaling with the mass-ratio of the radiated energy and angular momentum, within our treatment, implies that the ratio $\Delta E/\Delta L$ depends on the mass-ratio. This is consistent with the fact that the particle in the HDS case does not follow strict circular orbits, as in the case of [16]. For strict circular orbits, the energy to angular momentum ratio gives, at any radius, the value of the particle’s angular velocity which depends only on the black-hole spin. Figure 8 shows these differences explicitly.

It is also interesting to compare the energy radiated predicted by the above models with the one declared in numerical-relativity simulations. We recall that a qualitative and quantitative comparison in the comparable mass regime of the HDS and the numerical-relativity waveforms has been recently performed in [15] finding a great agreement. We thus proceed further here adopting the working hypothesis that the test particle treatment might be a good approximation of the real two-body system of comparable masses. First, we compute from the data available in the SXS catalog [14], the corresponding energy “deficit” $\Delta E/\mu$, for different mass-ratios μ/M . We do this following Eq. (12), namely, we subtract the value of ΔE_{ad} , which depends only on the black hole spin, to the mass of the final Kerr black hole obtained in the simulation. Figure 8 shows the results for $\mu/M = 0.08\text{--}0.25$. It can be seen that the value of $\Delta E/\mu$ obtained from the numerical-relativity data scales linearly with μ/M . It is quite surprising that these simulations follow exactly the same scaling of the energy radiated in the case of a purely radial plunge of a test particle into a Schwarzschild black hole, i.e., $\Delta E/\mu \propto \mu/M$ [24] (see also Section 2), and not the one expected from the particle plunge derived either in [16] or in the present work.

7. CONCLUSIONS

Two different cases of gravitational radiation, in the strong-field limit, from test particles falling into an already formed black hole have been considered. The first is a test particle plunging from infinity either initially at rest or with finite kinetic energy. It leads to a gravitational waves emission composed of three different parts: “*a precursor, a main burst, and a ringing tail.*” The amplitude of the burst depends on the angular momentum of the particle and of the black hole. The comparison between a Schwarzschild and a Kerr black hole shows quantitative but not qualitative

differences. The structure of the multipoles can be in used principle to determine the angular momentum of both the particle and the black hole. The second case, a particle starting from a finite radius in a circular orbit, leads to a novel HDS, smoothly merging into the black hole. The difference between the Schwarzschild and the Kerr metric is specially manifest at and after the LCO. When radiation reaction is taken into account (see Fig. 4) there is an increasing contribution of the radial momentum in the HDS as the particle approaches the horizon (see Figs. 2 and 6). This phenomenon is further enhanced by the different effective potential of the Schwarzschild and Kerr cases. The final phase is the one of a test particle smoothly merging in the Kerr black hole without any burst. We have compared and contrasted our treatment with the result of [16] and found that in the latter a larger amount of gravitational radiation is emitted in the transition to the plunge. We have shown the consequences of such a difference in the estimation of the mass of the final black hole formed in the merger of a binary black hole.

We have shown within the HDS treatment how the energy and the angular momentum radiated scale with the mass-ratio, μ/M , and show the difference of the scaling with the results of [16]. Stimulated by the unexpected agreement of the HDS and numerical-relativity waveforms in the comparable mass regime recently found in [15], we have made here a comparison of the energy radiated and its scaling with the mass-ratio. Surprisingly, we found that $\Delta E/\mu$ in the numerical-relativity simulations scales linearly with μ/M , following exactly the scaling of a purely radial plunge of a test particle into a Schwarzschild black hole [24], but not the scaling predicted in [16] nor the one of the HDS treatment presented here for a particle inspiraling and plunging into a Kerr black hole.

Besides the theoretical interest, the above results are relevant in view of the large use by the LIGO-Virgo Collaboration (see e.g. the case of GW150914 in [9]) of waveforms adopting a plunge phase following the treatment of [18]; see e.g. [17]. Thus, it appears that such a gravitational-wave detection analysis uses a “centaur” (the half-man, half-horse of the Greek mythology) approach, namely hand-matched inspiral-burst waveform templates (see [15], and references therein) to the plunge analysis (see Section 6 and [24, 25]), at this point unjustified. Along these lines, it is also important to mention the recent result of an independent analysis of GW150914 which shows the incompatibility (in the final burst) of the LIGO-Virgo waveform templates with their results (see Figs. 5 and 10 in [63] and also [64–66]).

REFERENCES

1. M. Schmidt, *Nature* (London, U.K.) **197**, 1040 (1963).
2. A. Hewish, S. J. Bell, J. D. H. Pilkington, P. F. Scott, and R. A. Collins, *Nature* (London, U.K.) **217**, 709 (1968).
3. R. Giacconi, S. Murray, H. Gursky, E. Kellogg, E. Schreier, and H. Tananbaum, *Astrophys. J.* **178**, 281 (1972).
4. R. W. Leach and R. Ruffini, *Astrophys. J.* **180**, L15 (1973).
5. *Physics and Astrophysics of Neutron Stars and Black Holes, Proceedings of the International School of Physics Enrico Fermi, Varenna, Italy*, Ed. by R. Giacconi and R. Ruffini (North-Holland, Amsterdam, New York, 1978).
6. R. A. Hulse and J. H. Taylor, *Astrophys. J.* **195**, L51 (1975).
7. J. M. Weisberg and J. H. Taylor, in *Binary Radio Pulsars*, Ed. by F. A. Rasio and I. H. Stairs, ASP Conf. Ser. **328**, 25 (2005); astro-ph/0407149.
8. *Neutron Stars, Black Holes and Binary X-Ray Sources, Proceedings of the Annual Meeting, San Francisco, CA, Feb. 28, 1974*, Ed. by H. Gursky and R. Ruffini, *Astrophys. Space Sci. Lib.* **48** (1975).
9. B. P. Abbott, R. Abbott, T. D. Abbott, M. R. Abernathy, F. Acernese, K. Ackley, C. Adams, T. Adams, P. Addesso, R. X. Adhikari, et al., *Phys. Rev. Lett.* **116**, 061102 (2016); arXiv: 1602.03837.
10. B. P. Abbott, R. Abbott, T. D. Abbott, M. R. Abernathy, F. Acernese, K. Ackley, C. Adams, T. Adams, P. Addesso, R. X. Adhikari, et al., *Phys. Rev. Lett.* **116**, 241103 (2016); arXiv: 1606.04855.
11. B. P. Abbott, R. Abbott, T. D. Abbott, F. Acernese, K. Ackley, C. Adams, T. Adams, P. Addesso, R. X. Adhikari, V. B. Adya, et al., *Phys. Rev. Lett.* **118**, 221101 (2017); arXiv: 1706.01812.
12. R. Ruffini and J. A. Wheeler, *ESRO, SP* **52**, 45 (1969).
13. L. D. Landau and E. M. Lifshitz, *Course of Theoretical Physics, Vol. 2: The Classical Theory of Fields* (Nauka, Moscow, 1988; Pergamon, Oxford, 1975).
14. <http://www.black-holes.org/waveforms>.
15. J. F. Rodríguez, J. A. Rueda, and R. Ruffini, *J. Cosmol. Astropart. Phys.* **2**, 030 (2018); arXiv: 1706.07704.
16. A. Ori and K. S. Thorne, *Phys. Rev. D* **62**, 124022 (2000); gr-qc/0003032.
17. A. Buonanno and T. Damour, *Phys. Rev. D* **59**, 084006 (1999); gr-qc/9811091.
18. A. Buonanno and T. Damour, *Phys. Rev. D* **62**, 064015 (2000); gr-qc/0001013.
19. R. Ruffini and J. A. Wheeler, in *Proceedings of the Cortona Symposium on Weak Interactions*, Ed. by L. Radicati (Accad. Nazionale dei Lincei, Rome, 1971).
20. M. Rees, R. Ruffini, and J. A. Wheeler, *Black Holes, Gravitational Waves and Cosmology* (Gordon and Breach Science, New York, 1974).
21. F. J. Zerilli, *Phys. Rev. Lett.* **24**, 737 (1970).
22. F. J. Zerilli, *Phys. Rev. D* **2**, 2141 (1970).
23. T. Regge and J. A. Wheeler, *Phys. Rev.* **108**, 1063 (1957).
24. M. Davis, R. Ruffini, W. H. Press, and R. H. Price, *Phys. Rev. Lett.* **27**, 1466 (1971).
25. M. Davis, R. Ruffini, and J. Tiomno, *Phys. Rev. D* **5**, 2932 (1972).
26. R. Ruffini, *Phys. Rev. D* **7**, 972 (1973).
27. R. Ruffini and M. Sasaki, *Prog. Theor. Phys.* **66**, 1627 (1981).
28. E. Newman and R. Penrose, *J. Math. Phys.* **3**, 566 (1962).
29. R. H. Price, *Phys. Rev. D* **5**, 2419 (1972).
30. S. A. Teukolsky, *Astrophys. J.* **185**, 635 (1973).
31. S. L. Detweiler and E. Szedenits, Jr., *Astrophys. J.* **231**, 211 (1979).
32. M. Sasaki and T. Nakamura, *Phys. Lett. A* **89**, 68 (1982).
33. M. Sasaki and T. Nakamura, *Prog. Theor. Phys.* **67**, 1788 (1982).
34. Y. Kojima and T. Nakamura, *Prog. Theor. Phys.* **71**, 79 (1984).
35. J. Weber, *Phys. Rev. Lett.* **22**, 1320 (1969).
36. C. W. Misner, *Phys. Rev. Lett.* **28**, 994 (1972).
37. C. W. Misner, R. A. Breuer, D. R. Brill, P. L. Chrzanowski, H. G. Hughes, and C. M. Pereira, *Phys. Rev. Lett.* **28**, 998 (1972).
38. M. Davis, R. Ruffini, J. Tiomno, and F. Zerilli, *Phys. Rev. Lett.* **28**, 1352 (1972).
39. C. Cutler, L. S. Finn, E. Poisson, and G. J. Sussman, *Phys. Rev. D* **47**, 1511 (1993).
40. T. Damour, B. R. Iyer, and A. Nagar, *Phys. Rev. D* **79**, 064004 (2009), 0811.2069.
41. T. Tanaka, M. Shibata, M. Sasaki, H. Tagoshi, and T. Nakamura, *Prog. Theor. Phys.* **90**, 65 (1993).
42. S. L. Detweiler, *Astrophys. J.* **225**, 687 (1978).
43. M. Shibata, *Phys. Rev. D* **48**, 663 (1993).
44. M. Shibata, *Prog. Theor. Phys.* **90**, 595 (1993).
45. S. A. Hughes, *Phys. Rev. D* **64**, 064004 (2001); gr-qc/0104041.
46. S. Drasco and S. A. Hughes, *Phys. Rev. D* **73**, 024027 (2006); gr-qc/0509101.
47. J. M. Bardeen, W. H. Press, and S. A. Teukolsky, *Astrophys. J.* **178**, 347 (1972).
48. S. A. Teukolsky, *Phys. Rev. Lett.* **29**, 1114 (1972).
49. S. A. Teukolsky and W. H. Press, *Astrophys. J.* **193**, 443 (1974).
50. S. A. Hughes, *Phys. Rev. D* **61**, 084004 (2000); gr-qc/9910091.
51. S. E. Gralla, S. A. Hughes, and N. Warburton, *Class. Quantum Grav.* **33**, 155002 (2016); arXiv: 1603.01221.
52. R. T. Jantzen, P. Carini, and D. Bini, *Ann. Phys.* **215**, 1 (1992), gr-qc/0106043.
53. E. Poisson, A. Pound, and I. Vega, *Living Rev. Relativ.* **14**, 7 (2011); arXiv: 1102.0529.
54. M. J. Fitchett and S. Detweiler, *Mon. Not. R. Astron. Soc.* **211**, 933 (1984).
55. L. S. Finn and K. S. Thorne, *Phys. Rev. D* **62**, 124021 (2000); gr-qc/0007074.

56. T. Damour, Phys. Rev. D **64**, 124013 (2001); gr-qc/0103018.
57. W.-B. Han and Z. Cao, Phys. Rev. D **84**, 044014 (2011); arXiv: 1108.0995.
58. A. Pound and E. Poisson, Phys. Rev. D **77**, 044013 (2008); arXiv: 0708.3033.
59. J. R. Gair, É. É. Flanagan, S. Drasco, T. Hinderer, and S. Babak, Phys. Rev. D **83**, 044037 (2011); arXiv: 1012.5111.
60. A. Taracchini, A. Buonanno, G. Khanna, and S. A. Hughes, Phys. Rev. D **90**, 084025 (2014); arXiv: 1404.1819.
61. C. Cutler, D. Kennefick, and E. Poisson, Phys. Rev. D **50**, 3816 (1994).
62. R. Ruffini, in *Black Holes (Les Astres Occlus)*, Ed. by C. Dewitt and B. S. Dewitt (Gordon and Breach, New York, 1973), p. 451.
63. H. Liu, J. Creswell, S. von Hausegger, A. D. Jackson, and P. Naselsky, J. Cosmol. Astropart. Phys. **2**, 013 (2018); arXiv: 1802.00340.
64. P. Naselsky, A. D. Jackson, and H. Liu, J. Cosmol. Astropart. Phys. **8**, 029 (2016); arXiv: 1604.06211.
65. H. Liu and A. D. Jackson, J. Cosmol. Astropart. Phys. **10**, 014 (2016); arXiv: 1609.08346.
66. J. Creswell, S. von Hausegger, A. D. Jackson, H. Liu, and P. Naselsky, J. Cosmol. Astropart. Phys. **8**, 013 (2017); arXiv: 1706.04191.

Simulating the induced gravitational collapse scenario of long gamma-ray bursts

J. A. Rueda* and R. Ruffini†

ICRANet, Piazza della Repubblica 10, Pescara, 65122, Italy

**jorge.rueda@icra.it*

†*ruffini@icra.it*

L. M. Becerra

*Escuela de Física, Universidad Industrial de Santander,
A.A. 678, Bucaramanga 680002, Colombia*

C. L. Fryer

CCS-2, Los Alamos National Laboratory, Los Alamos, NM 87545, USA

Published 19 November 2018

We present the state-of-the-art of the numerical simulations of the supernova (SN) explosion of a carbon-oxygen core (CO_{core}) that forms a compact binary with a neutron star (NS) companion, following the *induced gravitational collapse* (IGC) scenario of long gamma-ray bursts (GRBs) associated with type Ic supernovae (SNe). We focus on the consequences of the hypercritical accretion of the SN ejecta onto the NS companion which either becomes a more massive NS or gravitationally collapses forming a black hole (BH). We summarize the series of results on this topic starting from the first analytic estimates in 2012 all the way up to the most recent three-dimensional (3D) smoothed-particle-hydrodynamics (SPH) numerical simulations in 2018. We present a new SN ejecta morphology, highly asymmetric, acquired by binary interaction and leading to well-defined, observable signatures in the gamma- and X-rays emission of long GRBs.

Keywords: Gamma-ray bursts; neutron stars; binaries; accretion.

1. Introduction

The analysis of the multiwavelength data of GRBs, namely the gamma-rays in the prompt, the X-rays in the early and late afterglow, as well as the presence or absence of GeV emission, points to an increasing observational evidence of their separation in eight (8) different subclasses, each one with specific energy release, spectra, duration, etc. and all of them originating in well-defined binary progenitors.^{1–6}

*Corresponding author.

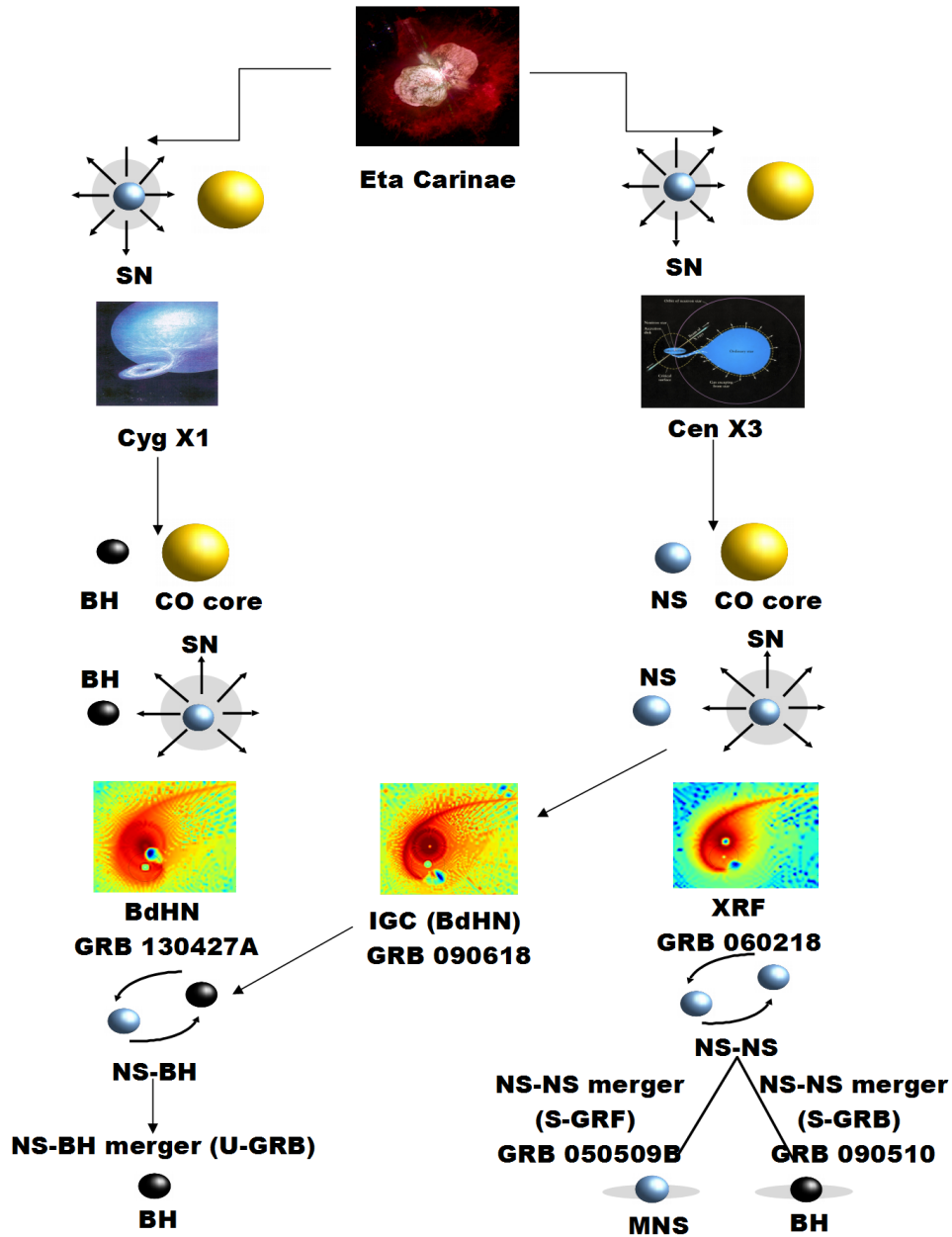


Fig. 1. Binary evolutionary path leading to $\text{CO}_{\text{core}}\text{-NS}$ and $\text{CO}_{\text{core}}\text{-BH}$ binaries, leading to XRFs and BdHNe (I and II). It can be also seen how the outcome systems of these long GRBs become the progenitors of short GRBs. We recall to the reader that S-GRBs and S-GRFs stand for, respectively, authentic short GRBs and short gamma-ray flashes, the two subclasses of short bursts from NS–NS mergers, the former produced when the merger leads to a more massive NS and the latter when a BH is formed.¹

We treat in this paper the case of long GRBs within the IGC paradigm: a CO_{core} exploding as a type Ic SN in presence of a NS or BH companion.^{1,6} The $\text{CO}_{\text{core}}\text{-NS}$ binaries lead to (1) X-ray flashes (XRFs) when the NS does not collapse forming a more massive NS and (2) binary-driven hypernovae I (BdHNe I) when the NS forms a BH, while (3) the $\text{CO}_{\text{core}}\text{-BH}$ binaries lead to what have been recently called BdHNe II.⁶ Figure 1 shows a comprehensive summary of the binary path leading

to this variety of compact binaries that are progenitors of the above subclasses of long GRBs and that at the same time, have an intimate connection with the short GRBs. This latter point will be touched upon later on in this paper.

We emphasize on the $\text{CO}_{\text{core}}\text{-NS}$ binaries which have been extensively studied by our group in a series of publications.^{7–12} The CO_{core} explodes as SN produces an accretion process onto the NS. For sufficiently compact binaries, e.g. orbital periods of the order of few minutes, the accretion is highly super-Eddington (hypercritical) leading to the possibility of the IGC of the NS once it reaches the critical mass, and forms a BH. If the binary is not disrupted by the explosion, XRFs and BdHNe produce new binaries composed of a new NS (νNS) formed at the center of the SN, and a more massive NS or a BH companion (see Fig. 1).

The BH formation leads to the GRB prompt gamma-ray emission. The interaction/feedback of the GRB into the SN makes it become the hypernova (HN)¹³ that is observed in the optical (due to the nickel decay) few days after the GRB trigger. The hypercritical accretion can be observed as an X-ray precursor.¹² The GRB feedback onto the SN ejecta produces also gamma- and X-ray flares observed in the early afterglow.¹⁴ The synchrotron emission by relativistic electrons from the νNS in the expanding magnetized HN ejecta and the νNS pulsar emission explain the early and late X-ray afterglow.¹⁵

In this contribution, we summarize recent efforts and new details of the theoretical simulations that support all the above rich long GRB phenomenology. In Sec. 2, we present a chronological summary of the simulations of the IGC process up to 2016. The most recent detailed 3D SPH simulations of the process will be presented in Sec. 3. Finally, we devote Sec. 4 to discuss the implications of the theoretical results on the analysis and interpretation of the GRB data.

2. Previous IGC Simulations: 2012–2016

2.1. *First analytic estimates*

The IGC scenario was formulated in 2012 in Ref. 7 presenting a comprehensive astrophysical scenario supporting this idea as well as a possible evolutionary scenario leading to the progenitor $\text{CO}_{\text{core}}\text{-NS}$ binaries. It was also there presented an analytic formula for the accretion rate onto the NS companion on the basis of the following simplified assumptions: (1) a uniform density profile of the pre-SN CO_{core} ; (2) the ejecta was evolved following a homologous expansion; (3) the mass of the NS (assumed to be initially $1.4 M_{\odot}$) and the CO_{core} (in the range $4\text{--}8 M_{\odot}$) were assumed nearly constant. It was so shown that the accretion rate onto the NS is highly super-Eddington, namely it is hypercritical, reaching values of up to $0.1 M_{\odot} \text{ s}^{-1}$ for compact binaries with orbital periods of the order of few minutes. This estimate implied that the hypercritical accretion could induce the gravitational collapse of the NS which, in few seconds, would reach the critical mass with consequence formation of a BH. A first test of this IGC first model in real data was soon presented in the case of GRB 090618.⁸

2.2. First numerical simulations: 1D approximation

The first numerical simulations were implemented in 2014 via a 1D code including:⁹

- (1) the modeling of the SN via the 1D core-collapse SN code of Los Alamos;¹⁶
- (2) the microphysics experienced by the inflow within the accretion region including the neutrino (ν) emission and hydrodynamics processes such as shock formation;
- (3) with the above it followed the evolution of the material reaching the Bondi–Hoyle capture region and the subsequent in-fall up to the NS surface. Hypercritical accretion rates in the range 10^{-3} – $10^{-1} M_{\odot} \text{ s}^{-1}$ were inferred, confirming the first analytic estimates and the IGC of the NS companion for binary component masses similar to the previous ones and for orbital periods of the order of 5 min.

The above simulations were relevant in determining that the fate of the system is mainly determined by the binary period (P); the SN ejecta velocity (v_{ej}) and the NS initial mass. P and v_{ej} enter explicitly in the Bondi–Hoyle accretion rate formula through the capture radius expression, and implicitly via the ejecta density since they influence the decompression state of the SN material at the NS position.

2.3. 2D simulations including angular momentum transfer

Soon after, in 2015, we implemented in Ref. 11 a series of improvements to the above calculations by relaxing some of the aforementioned assumptions. We adopted for the ejecta a density profile following a power-law with the radial distance and evolved it with a homologous expansion. The angular momentum transport, not included in the previous estimates, was included. With this addition, it was possible to estimate the spin-up of the NS companion by the transfer of angular momentum from the in-falling matter which was shown to circularize around the NS before being accreted. General relativistic effects were also introduced, when calculating the evolution of the structure parameters (mass, radius, spin, etc.) of the accreting NS, in the NS gravitational binding energy, and in the angular momentum transfer by the circularized particles being accreted from the innermost circular orbit.

One of the most important results of Ref. 11 was that taking into account that the longer the orbital P , the lower the accretion rate, it was there computed the maximum orbital period (P_{max}) for which the NS reaches the critical mass for gravitational collapse for BH formation. The dependence of P_{max} on the initial mass of the NS was also there explored. The orbital period P_{max} was then presented as the separatrix of two families of long GRBs associated with these binaries: at the time we called them *Family-1*, the systems in which the NS does not reach the critical mass, and *Family-2* the ones in which it reaches the critical mass and forms a BH. It can be seen that the Family-1 and Family-2 long GRBs evolve subsequently into the concepts of XRFs and BdHNe, respectively.

2.4. First 3D simulations

A great step toward the most recent simulations was achieved in 2016 in Ref. 12 where a SPH-like simulation was implemented in which the SN ejecta was emulated by “point-like” particles. The mass and number of the particles populating each layer were assigned, for self-consistency, according to the power-law density profile. The initial velocity of the particles of each layer was set, in agreement with the chosen power-law density profile, following a radial velocity distribution; i.e. $v \propto r$.

The evolution of the SN particles was followed by Newtonian equations of motion in the gravitational field of the NS companion, also taking into account the orbital motion which was included under the assumption that the NS performs a circular orbit around the CO_{core} center that acts as the common center-of-mass, namely assuming that the mass of the pre-SN core is much larger than the NS mass.

The accretion rate onto the NS was computed, as in Ref. 11, using the Bondi–Hoyle accretion formula and, every particle reaching the Bondi–Hoyle surface, was removed from the system. The maximum orbital period P_{max} in which the NS collapses by accretion could be further explored including the dependence on the mass of the pre-SN CO_{core} , in addition to the dependence on the NS mass.

A detailed study of the hydrodynamics and the neutrino emission in the accretion region on top of the NS surface was performed. Concerning the neutrino emission, several ν and antineutrino ($\bar{\nu}$) production processes were considered and showed that electron–positron annihilation ($e^+e^- \rightarrow \nu\bar{\nu}$) overcomes by orders of magnitude for any other mechanism of neutrino emission in the range of accretion rates 10^{-8} – $10^{-2} M_{\odot} \text{ s}^{-1}$, relevant for XRFs and BdHNe. The neutrino luminosity can reach values of up to $10^{52} \text{ erg s}^{-1}$ and the neutrino mean energy of 20 MeV for the above upper value of the accretion rate. For the reader interested in the neutrino emission, we refer to Ref. 17 for a detailed analysis of the neutrino production in XRFs and BdHNe including flavor oscillations experienced by the neutrinos before abandoning the system.

Concerning the hydrodynamics, the evolution of the temperature and density of outflows occurring during the accretion process owing to convective instabilities was estimated. It showed the interesting result that the temperature of this outflow and its evolution can explain the early (i.e. precursors) X-ray emission that have been observed in some BdHNe and in XRFs, exemplified there analyzing the early X-ray emission observed in GRB 090618 (a BdHN) and in GRB 060218 (an XRF).

A most important result of these simulations was the possibility of having a first glance of the morphology acquired by the SN ejecta: the matter density, initially spherically symmetric, becomes highly asymmetric due to the accretion process and the action of the gravitational field of the NS companion (see Fig. 2). Such pronounced asymmetries in the SN ejecta become a key ingredient in the analysis and interpretation of the GRB data. Indeed, in Ref. 14 the implications of the expansion of the GRB e^+e^- plasma through the resulting distorted ejecta density distribution obtained from the 3D numerical simulations were evaluated. It was also shown

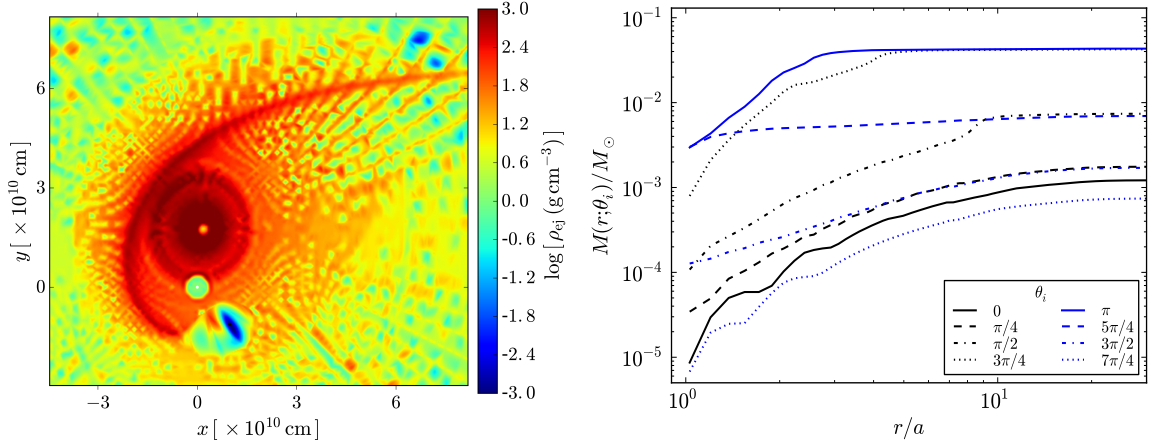


Fig. 2. Left panel (from Ref. 12): snapshot of the SN ejecta density in the orbital plane of the CO_{core}-NS binary. The plot corresponds to the instant when the NS (black dot) reaches the critical mass and forms the BH, approximately 250 s from the SN explosion. The ν NS is represented by the white dot. Right panel (from Ref. 14): cumulative radial mass profiles of the SN ejecta shown in the left panel, enclosed within a cone of 5° of semi-aperture angle, whose vertex is at the position of the BH at the moment of its formation. The binary parameters are: the initial mass of the NS companion is $2.0 M_\odot$; the CO_{core} leading to an ejecta mass of $7.94 M_\odot$, and the orbital period is $P \approx 5$ min, namely a binary separation $a \approx 1.5 \times 10^{10}$ cm.

that as a consequence of the new morphology, the e^+e^- plasma, expanding from the newborn BH site in all directions with equal initial conditions, by engulfing different amounts of mass along different directions (see Fig. 2), consequently experiences different dynamics and a variety of signatures as a function of the viewing angle. This explains the prompt gamma-ray emission as well as the gamma- and X-ray flares observed in the early afterglow.¹⁴ The SN ejecta morphology also explains the presence or absence of GeV emission in BdHNe (see Ref. 6 for details).

The above results showed the relevance of the role of the 3D SN ejecta morphology in the analysis of the X- and gamma-ray data observed in XRFs and BdHNe and also on the GeV emission of BdHNe.

3. New 3D SPH Simulations

In view of this, we presented in Ref. 18 3D hydrodynamic simulations of the IGC scenario by adapting the SPH code developed at Los Alamos, SNSPH,¹⁹ which has been tested and applied in a variety of astrophysical situations.^{20–23}

The time $t = 0$ of the simulation is set as the time at which the SN shock breaks out the CO_{core} external radius. We calculate the accretion rate both onto the NS companion and onto the ν NS (via fallback), and calculate the evolution of other binary parameters such as the orbital separation, eccentricity, etc. Figure 3 shows an example of simulation for a binary system composed of a CO_{core} of mass $\approx 6.85 M_\odot$, the end stage of a zero-age main-sequence (ZAMS) progenitor star of $M_{\text{zams}} = 25 M_\odot$, and a $2 M_\odot$ NS companion. The initial orbital period is ≈ 5 min.

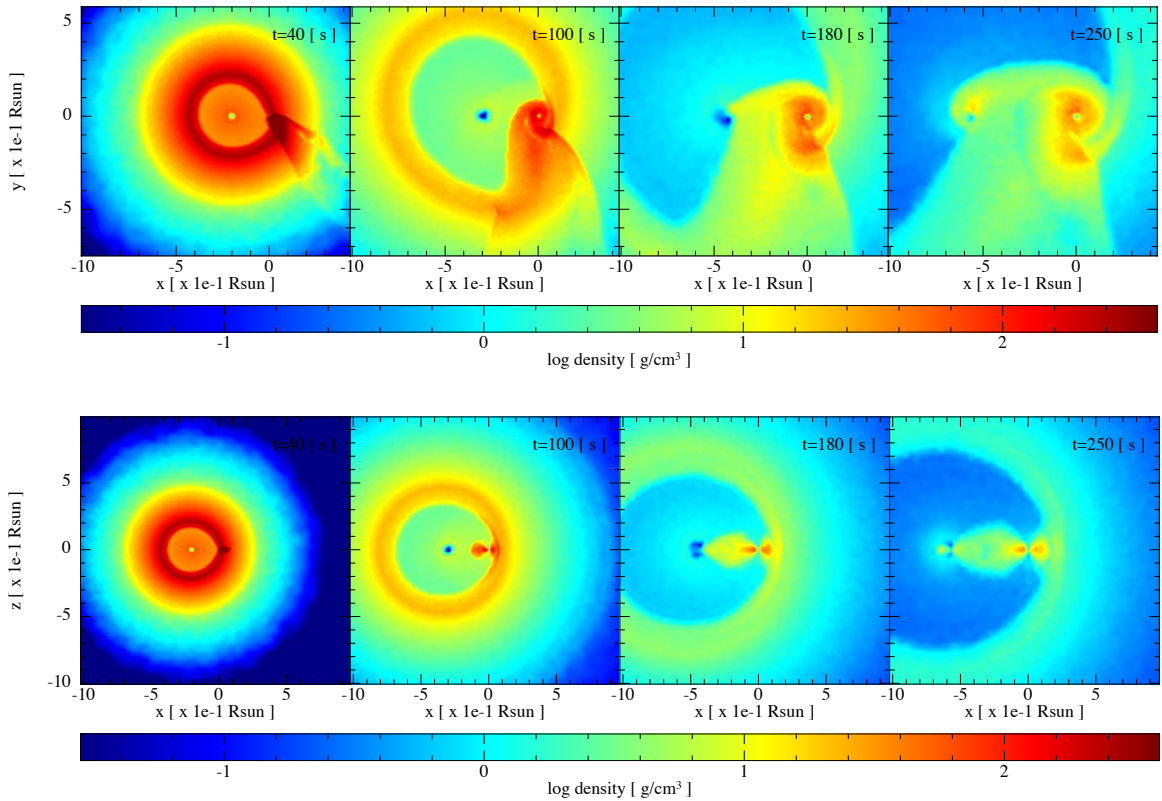


Fig. 3. Snapshots of the 3D SPH simulation of the IGC scenario taken from Ref. 18. The initial binary system is formed by a CO_{core} of mass $\approx 6.85 M_{\odot}$, from a ZAMS progenitor star of $M_{\text{zams}} = 25 M_{\odot}$, and a $2 M_{\odot}$ NS with an initial orbital period of approximately 5 min. The upper panel shows the mass density on the equatorial (orbital) plane, at different times of the simulation. The time $t = 0$ is set in our simulations at the moment of the SN shock breakout. The lower panel shows the plane orthogonal to the orbital one. The reference system has been rotated and translated for the x -axis to be along the line joining the νNS and the NS centers, and its origin is at the NS position.

The accretion rate onto both stars was estimated from the flux of SPH particles falling, per unit time, into the Bondi–Hoyle accretion region of the NS. It is confirmed that the accretion onto the NS companion occurs from a disk-like structure formed by the particles that circularize before being accreted; see vortexes in the upper panel of Fig. 3 and the disk structure is clearly seen in the lower panel.

Several binary parameters were explored thanks to the new code. We performed simulations changing the CO_{core} mass, the NS companion mass, the orbital period, the SN explosion energy (so the SN kinetic energy or velocity). We also explored intrinsically asymmetric SN explosion. We checked if the νNS and/or the NS companion reach the mass-shedding (Keplerian) limit or the secular axisymmetric instability, i.e. the critical mass. The NS can also become just a more massive, fast rotating, stable NS when the accretion is moderate. All this was done for various NS nuclear equations of state (NL3, TM1 and GM1).

We followed the orbital evolution up to the instant when most of the ejecta has abandoned the system to determine if the system remains bound or becomes

unbound by the explosion. We thus assessed the $\text{CO}_{\text{core}}\text{-NS}$ parameters leading to the formation of $\nu\text{NS}\text{-NS}$ (from XRFs) or $\nu\text{NS}\text{-BH}$ (from BdHNe) binaries. The first proof that BdHNe remain bound leading to $\nu\text{NS}\text{-BH}$ binaries was presented in Ref. 10.

4. Discussion and Conclusions: Implications on GRB Phenomenology

We have made a chronological summary of the simulations of the IGC scenario, starting from the first analytic estimates of the process in 2012 all the way to sophisticated 3D SPH simulations in 2018. We have discussed the consequences of the simulations in the analysis and interpretation of GRBs within the IGC paradigm.

Most interesting results worth to be underlined are:

- (1) In general, the main parameters for the fate of the $\text{CO}_{\text{core}}\text{-NS}$ binary are: the initial mass of the NS companion, the orbital period and the SN (initial) velocity. Long GRBs, namely XRFs and BdHNe, are produced by these binaries and the occurrence of either one or the other depends only on the orbital period once the component masses have been fixed.
- (2) The strong gravitational field of the NS companion and the accretion process in action onto it, influence the morphology of the SN ejecta, inducing asymmetries, needed to be accounted for in the GRB data analysis and interpretation.
- (3) The GRB e^+e^- plasma, expanding at relativistic velocities from the newborn BH, collides with the SN ejecta at a distance of the order of the radius of the “cavity” formed around the accreting NS (see Figs. 2 and 3). The cavity radius is $\approx 10^{10}$ cm. The plasma carry on baryons from the ejecta and finally reaches transparency (breaks out) after traveling inside the remnant up to a distance of 10^{12} cm, in practice the remnant border, and having a Lorentz factor $\Gamma = 2\text{--}5$.¹⁴ This dynamics occurs qualitatively in a similar way along all directions but with the crucial difference that the amount of engulfed baryons depends on the direction of propagation (see right panel of Fig. 2). This implies that there is an angular dependence of the transparency/breakout properties (e.g. Lorentz factor and energy emission).
- (4) Indeed, it was shown that the thermal emission observed in the X-ray flares of the early (source rest-frame times $t \sim 10^2$ s) afterglow of long GRBs is associated with an emission radius of $\approx 10^{12}$ cm. In addition, by measuring the evolution of such a thermal emission, it was derived that its motion is mildly-relativistic with Lorentz factor $\Gamma \lesssim 4$. It is clear the consistency of these observations agrees with the 3D morphology of BdHNe and the above-described dynamics of the GRB e^+e^- plasma. Therefore, the high quality of the new 3D SPH simulations presented in Ref. 18 (see e.g. Fig. 3) allows to explore with great detail the above dynamics in each spatial direction and obtain, as a function of the viewing angle, light-curves and spectra of XRFs and BdHNe to be compared and contrasted with the observations.

- (5) A relevant and most interesting aspect of the IGC paradigm is the interconnection between long and short GRBs. Namely, the fact that the outcome systems of long GRBs become the progenitors of short GRBs. If the binary is not disrupted in the SN explosion, an XRF leads to a ν NS–NS binary, while a BdHN leads to a ν NS–BH binary. These systems, in turn, driven by gravitational wave emission merge in due time to produce short GRBs. It is then clear that the relative observed occurrence rates of XRFs, BdHN and short bursts encode crucial information on the originally CO_{core}–NS binary progenitor parameters, on the value of the NS critical mass and so on the NS equation of state.

In order to complete the picture of the short GRBs, we recall that Ref. 1 divided them in subclasses including, besides the NS–NS (S-GRFs and S-GRBs) and NS–BH mergers already mentioned in this work (see e.g. Fig. 1), also NS–WD mergers (GRFs), and their gravitational wave emission has been also studied.³ The claimed detection of the gravitational wave — electromagnetic emissions from a NS–NS merger, the GW170817-GRB 170817A-AT 2017gfo association,^{24–26} was recently analyzed in Ref. 4. It is there shown that this “triptych” association is not yet sufficiently established, which brought them to introduce WD–WD mergers as a new, compact-object merger GRB subclass that explains systems like GRB 170817A-AT 2017gfo.

Acknowledgments

The work of L. M. Becerra and C. L. Fryer was partially funded under the auspices of the U.S. Department of Energy, and supported by its contract W-7405-ENG-36 to LANL. Simulations at LANL were performed on HPC resources provided under the Institutional Computing program.

References

1. R. Ruffini *et al.*, *Astrophys. J.* **832**, 136 (2016).
2. J. A. Rueda *et al.*, *Int. J. Mod. Phys. D* **26**, 1730016 (2017).
3. R. Ruffini *et al.*, *Astrophys. J.* **859**, 30 (2018).
4. J. A. Rueda *et al.*, *J. Cosmol. Astropart. Phys.* **10**, 006 (2018).
5. J. A. Rueda *et al.*, Electromagnetic emission of white dwarf binary mergers, arXiv:1807.07905.
6. R. Ruffini *et al.*, On the universal GeV emission in binary-driven hypernovae and their inferred morphological structure, arXiv:1803.05476.
7. J. A. Rueda and R. Ruffini, *Astrophys. J. Lett.* **758**, L7 (2012).
8. L. Izzo, J. A. Rueda and R. Ruffini, *Astron. Astrophys.* **548**, L5 (2012).
9. C. L. Fryer, J. A. Rueda and R. Ruffini, *Astrophys. J. Lett.* **793**, L36 (2014).
10. C. L. Fryer, F. G. Oliveira, J. A. Rueda and R. Ruffini, *Phys. Rev. Lett.* **115**, 231102 (2015).
11. L. Becerra, F. Cipolletta, C. L. Fryer, J. A. Rueda and R. Ruffini, *Astrophys. J.* **812**, 100 (2015).
12. L. Becerra, C. L. Bianco, C. L. Fryer, J. A. Rueda and R. Ruffini, *Astrophys. J.* **833**, 107 (2016).

13. R. Ruffini *et al.*, On the ultra-relativistic prompt emission (UPE), the hard and soft X-ray flares, and the extended thermal emission (ETE) in GRB 151027A, arXiv:1712.05001.
14. R. Ruffini *et al.*, *Astrophys. J.* **852**, 53 (2018).
15. R. Ruffini, M. Karlica, N. Sahakyan, J. A. Rueda, Y. Wang, G. J. Mathews, C. L. Bianco and M. Muccino, On a GRB afterglow model consistent with hypernovae observations, *Astrophys. J.*, in press, arXiv:1712.05000.
16. C. Fryer, W. Benz, M. Herant and S. A. Colgate, *Astrophys. J.* **516**, 892 (1999).
17. L. Becerra, M. M. Guzzo, F. Rossi-Torres, J. A. Rueda, R. Ruffini and J. D. Uribe, *Astrophys. J.* **852**, 120 (2018).
18. L. Becerra, C. L. Ellinger, C. L. Fryer, J. A. Rueda and R. Ruffini, SPH simulations of the induced gravitational collapse scenario of long gamma-ray bursts associated with supernovae, arXiv:1803.04356.
19. C. L. Fryer, G. Rockefeller and M. S. Warren, *Astrophys. J.* **643**, 292 (2006).
20. C. L. Fryer and M. S. Warren, *Astrophys. J. Lett.* **574**, L65 (2002).
21. P. A. Young, C. L. Fryer, A. Hungerford, D. Arnett, G. Rockefeller, F. X. Timmes, B. Voit, C. Meakin and K. A. Eriksen, *Astrophys. J.* **640**, 891 (2006).
22. S. Diehl, C. Fryer and F. Herwig, The formation of hydrogen deficient stars through common envelope evolution, in *Hydrogen-Deficient Stars*, eds. A. Werner and T. Rauch, Astronomical Society of the Pacific Conference Series, Vol. 391 (ASP, 2008).
23. A. Batta, E. Ramirez-Ruiz and C. Fryer, *Astrophys. J. Lett.* **846**, L15 (2017).
24. B. P. Abbott *et al.*, *Phys. Rev. Lett.* **119**, 161101 (2017).
25. A. Goldstein *et al.*, *Astrophys. J. Lett.* **848**, L14 (2017).
26. D. A. Coulter *et al.*, *Science* **358**, 1556 (2017).

GRB 170817A-GW170817-AT 2017gfo and the observations of NS-NS, NS-WD and WD-WD mergers

To cite this article: J.A. Rueda *et al*/JCAP10(2018)006

View the [article online](#) for updates and enhancements.



AAS | **IOP Astronomy** ebooks

Part of your publishing universe and your first choice for
astronomy, astrophysics, solar physics and planetary
science ebooks.

iopscience.org/books/aas

GRB 170817A-GW170817-AT 2017gfo and the observations of NS-NS, NS-WD and WD-WD mergers

J.A. Rueda,^{a,b,c} R. Ruffini,^{a,b,c,d} Y. Wang,^{a,b} Y. Aimuratov,^{a,b}
U. Barres de Almeida,^{c,e} C.L. Bianco,^{a,b} Y.C. Chen,^{a,b}
R.V. Lobato,^{a,b,f} C. Maia,^g D. Primorac,^{a,b} R. Moradi^{a,b} and
J.F. Rodriguez^{a,b}

^aDipartimento di Fisica and ICRA, Sapienza Università di Roma,
P.le Aldo Moro 5, I-00185 Rome, Italy

^bICRANet, P.zza della Repubblica 10, I-65122 Pescara, Italy

^cICRANet-Rio, Centro Brasileiro de Pesquisas Físicas,
Rua Dr. Xavier Sigaud 150, 22290-180 Rio de Janeiro, Brazil

^dUniversité de Nice Sophia Antipolis,
CEDEX 2, Grand Château Parc Valrose, Nice, France

^eCentro Brasileiro de Pesquisas Físicas,
Rua Dr. Xavier Sigaud 150, 22290-180 Rio de Janeiro, Brazil

^fDepartamento de Física, Instituto Tecnológico de Aeronáutica, ITA,
São José dos Campos, 12228-900 SP, Brazil

^gInstituto de Física, Universidade de Brasília, 70910-900 Brasília, DF, Brazil

E-mail: jorge.rueda@icra.it, ruffini@icra.it

Received February 28, 2018

Revised September 25, 2018

Accepted September 27, 2018

Published October 3, 2018

Abstract. The LIGO-Virgo Collaboration has announced the detection of GW170817 and has associated it with GRB 170817A. These signals have been followed after 11 hours by the optical and infrared emission of AT 2017gfo. The origin of this complex phenomenon has been attributed to a neutron star-neutron star (NS-NS) merger. In order to probe this association we confront our current understanding of the gravitational waves and associated electromagnetic radiation with four observed GRBs originating in binaries composed of different combinations NSs and white dwarfs (WDs). We consider 1) GRB 090510 the prototype of NS-NS merger leading to a black hole (BH); 2) GRB 130603B the prototype of a NS-NS merger leading to massive NS (MNS) with an associated kilonova; 3) GRB 060614 the prototype of a NS-WD merger leading to a MNS with an associated kilonova candidate; 4) GRB

170817A the prototype of a WD-WD merger leading to massive WD with an associated AT 2017gfo-like emission. None of these systems support the above mentioned association. The clear association between GRB 170817A and AT 2017gfo has led to introduce a new model based on a new subfamily of GRBs originating from WD-WD mergers. We show how this novel model is in agreement with the exceptional observations in the optical, infrared, X- and gamma-rays of GRB 170817A-AT 2017gfo.

Keywords: gamma ray burst experiments, gravitational waves / experiments, gravitational waves / sources, X-rays

ArXiv ePrint: [1802.10027](https://arxiv.org/abs/1802.10027)

Contents

1	Introduction	1
2	GRB subclasses and observational properties of NS-NS and NS-WD mergers	2
3	Gravitational-wave emission of NS-NS, NS-WD and WD-WD mergers	3
4	Comparison of the prompt, X-rays and optical light-curves of NS-NS and NS-WD mergers	4
5	WD-WD mergers as an alternative mildly relativistic uncollimated emission for GRB 170817A-AT 2017gfo	8
6	Discussion and conclusions	9

1 Introduction

The LIGO-Virgo Collaboration announced the detection of the gravitational-wave signal GW170817, at a luminosity distance of 40_{-14}^{+8} Mpc, as consistent with the merging of a neutron star-neutron star (NS-NS) binary [1]. The best-constrained parameter from the GW170817 data is the binary chirp mass, $\mathcal{M} \equiv (m_1 m_2)^{3/5} / M^{1/5} = 1.188_{-0.002}^{+0.004} M_\odot$, where m_1 and m_2 are the binary merging components and $M = m_1 + m_2$ is the binary total mass. The 90% confidence level of the total binary mass leads to the range $M = (2.73\text{--}3.29) M_\odot$. The lowest value, i.e. $M = 2.73 M_\odot$, corresponds to the case of equal-mass components, $m_1 = m_2 \equiv m = M/2 = 1.365 M_\odot$.

GW170817 has been associated with a short-duration gamma-ray burst (GRB) observed by the Gamma-ray Burst Monitor (GBM) on board the Fermi-satellite, GRB 170817A [2, 3], as well as with the optical-infrared-ultraviolet “kilonova” emission, AT 2017gfo [4]; see also [5–7].

If the above associations were correct, then they would support the hypothesis that GW170817-GRB 1709817A-AT 2017gfo was produced by a NS-NS merger. The aim of this article is to gain additional insight into the nature of the electromagnetic signal of GRB 170817A by comparing and contrasting it with GRBs associated with four relevant systems: NS-NS mergers leading to a black hole (BH), NS-NS mergers leading to a more massive NS (MNS), NS-WD mergers leading to a MNS and WD-WD leading to a massive WD.

The article is organized as follows. In section 2 we recall the GRB subclasses associated with NS-NS and NS-WD mergers and we have introduced as a new subclass of GRBs originating from WD-WD mergers leading to a massive WD and their observational properties. In section 3 we analyze the gravitational-wave emission of NS-NS, NS-WD and WD-WD mergers. In section 4 we compare and contrast the X-ray and optical isotropic light-curves of GRB 090510A, GRB 130603B, GRB 060614 and GRB 170817A including as well the infrared light-curve. In section 5 we describe a new subclass of GRB originating from WD-WD merger. This model is an alternative mildly-relativistic uncollimated emission as oppose to the NS-NS ultra-relativistic merger. In figure 5 we model the data of AT 2017gfo in the r, V, Ks and i bands following the WD-WD merger model. In section 6 we present the conclusions.

2 GRB subclasses and observational properties of NS-NS and NS-WD mergers

Short-duration GRBs are expected to be produced in the mergers of NS-NS and NS-BH binaries (see, e.g., refs. [8–12]). Two different subclasses of short bursts from NS-NS mergers, depending on whether they lead to a MNS or to a BH, have been identified [13–15]:

- *Authentic short GRBs (S-GRBs)*: they occur when the NS-NS merger leads to a BH [14, 16, 17]. These bursts have $E_{\text{iso}} \gtrsim 10^{52}$ erg and $E_{p,i} \gtrsim 2$ MeV, and their electromagnetically inferred isotropic occurrence rate is $\rho_{\text{S-GRB}} \approx (1.9_{-1.1}^{+1.8}) \times 10^{-3} \text{ Gpc}^{-3} \text{ yr}^{-1}$ [15, 18]. The distinct signature of the formation of a BH in a NS-NS merger in S-GRBs follows from the observations of the 0.1–100 GeV emission by the *Fermi*-LAT [19], as observed in the best prototype case of GRB 090510. This is supported by the additional information of the following sources: GRB 090227B [17], GRB 140619B [14], GRB 090510 [16] and more recently in GRB 081024B and GRB 140402A [20]. The luminosity of the GeV emission follows a decreasing power-law with index $\gamma = -1.29 \pm 0.06$, when measured in the rest frame of the source [19].
- *Short gamma-ray flashes (S-GRFs)*: they occur when the NS-NS merger leads to a MNS; i.e. there is no BH formation [15, 18]. These bursts have isotropic energy $E_{\text{iso}} \lesssim 10^{52}$ erg, peak energy $E_{p,i} \lesssim 2$ MeV, and their electromagnetically inferred isotropic occurrence rate is $\rho_{\text{S-GRF}} \approx 3.6_{-1.0}^{+1.4} \text{ Gpc}^{-3} \text{ yr}^{-1}$ [15, 18].

Besides the gamma-ray and X-ray emission, NS-NS mergers are expected to emit a kilonova in the infrared, optical and ultraviolet wavelengths, observable days after the merger [21–24]. This signal comes from the radioactive decay of $\sim 0.01 M_{\odot}$ r-process heavy material synthesized in the merger and it is expected to be nearly isotropic (see, e.g., refs. [21, 22]). The first kilonova associated with a short burst was established for GRB 130603B [23, 24]. With $E_{\text{iso}} \approx 2 \times 10^{51}$ erg [25], GRB 130603B belongs to the S-GRF subclass. The second association has been claimed for GRB 050709 [26] which, with an $E_{\text{iso}} \approx 8 \times 10^{49}$ erg, is also a S-GRF.

In addition to the above short bursts there is a subclass which show hybrid gamma-ray properties between long and short bursts. These gamma-ray flashes (GRFs) occur in a low-density circumburst medium (CBM), e.g. $n_{\text{CBM}} \sim 10^{-3} \text{ cm}^{-3}$, and are not associated with supernovae (SNe) [15, 27, 28].

- *Gamma-ray flashes (GRFs)*: they are thought to originate in NS-WD mergers, see, e.g., [15, 18]. NS-WD binaries are notoriously common astrophysical systems [29] and possible evolutionary scenarios leading to these mergers have been envisaged (see, e.g., refs. [30–32]). These bursts, which show an extended and softer emission, have $10^{51} \lesssim E_{\text{iso}} \lesssim 10^{52}$ erg, peak energy $0.2 \lesssim E_{p,i} \lesssim 2$ MeV, and their electromagnetically inferred isotropic occurrence rate is $\rho_{\text{GRF}} = 1.02_{-0.46}^{+0.71} \text{ Gpc}^{-3} \text{ yr}^{-1}$ [15, 18]. This density rate appears to be low with respect to the number of estimated NS-WD binaries [29] which can be of $(0.5-1) \times 10^4 \text{ Gpc}^{-3} \text{ yr}^{-1}$ [33]. From the GRB side, we note that indeed only one NS-WD merger has been identified (see analysis of GRB 060614, in ref. [28]). This implies that the majority of the expected mergers are under the threshold of the existing X- and gamma-ray detectors. A kilonova has been associated with GRB 060614 [34]. Detail spectral and luminosity analysis has been presented in [33]. GRFs form a more massive NS and not a BH (see [15] and references therein).

Finally, the case of GRB 170817A opens a new problematic: both its very low energetic $E_{\text{iso}} \approx 5 \times 10^{46}$ erg [1, 3, 35] and the unprecedented details of the optical, infrared, radio and X-ray information of AT 2017gfo (see, e.g., refs. [5–7]) which promise to give most precise information on the Lorentz factor of the different episodes underline the nature of this source. The observational features of GRB 170817A and AT 2017gfo lead us to consider here the possibility of an additional subclass of GRBs produced in WD-WD mergers leading to the formation of a massive WD.

- *WD-WD mergers*: the WD-WD merger rate has been recently estimated to be $(1-80) \times 10^{-13} \text{ yr}^{-1} M_{\odot}^{-1}$ (at 2σ) and $(5-9) \times 10^{-13} \text{ yr}^{-1} M_{\odot}^{-1}$ (at 1σ) [36, 37]. For a Milky Way-like stellar mass $6.4 \times 10^{10} M_{\odot}$ and using an extrapolating factor of Milky Way equivalent galaxies, 0.016 Mpc^{-3} [38], it leads to a local cosmic rate $(0.74-5.94) \times 10^6 \text{ Gpc}^{-3} \text{ yr}^{-1}$ (2σ) and $(3.7-6.7) \times 10^5 \text{ Gpc}^{-3} \text{ yr}^{-1}$ (1σ).

We are interested in WD-WD mergers forming as central remnant a massive ($\sim 1.2-1.5 M_{\odot}$), highly magnetized (10^9-10^{10} G), fast rotating ($P = 1-10$ s) WD (see [39] and references therein). Since there is no SN associated with GRB 170817A the merger should not lead to a SN explosion (see e.g. [40] and references therein). This is therefore different, for instance, to the WD-WD mergers considered in [41] where the existence of a SN was explicitly envisaged. The above occurrence rate implies that (12–22)% of WD-WD mergers may explain the entire population of SN Ia. This is consistent with previous estimated rates of WD-WD mergers leading to SNe Ia (see e.g. [42]). The rest of the population is indeed sufficient to explain the population of GRB 170817A-like sources (see section 5).

We show below in section 5 that the expected observables of these WD-WD mergers in the X- and gamma-rays, and in the optical and in the infrared wavelengths are suitable for the explanation of the GRB 170817A-AT 2017gfo association.

We recall that the name kilonova was coined in [22] to the optical transient produced in NS-NS mergers in view of their optical luminosity, $\sim 10^{41} \text{ erg s}^{-1}$, which is approximately 1000 times the one of novae, $\sim 10^{38} \text{ erg s}^{-1}$. The results of this work show that indeed this designation can be extended to the optical transient produced in WD-WD mergers. In this case the kilonova is not powered by the decay of r-process material but by the energy released by accretion onto the new WD formed in the merger (see section 5).

In addition, it is interesting that the above mentioned physical properties (e.g. mass, rotation period and magnetic field) of the WD formed in the merger process correspond to the ones described by the WD model of soft gamma-repeaters (SGRs) and anomalous X-ray pulsars (AXPs) [39, 43]. Indeed, the WD-WD merger rate is high enough to explain the Galactic population of SGRs/AXPs. Therefore the possible evolution of GRB 170817A-AT 2017gfo into this kind of sources has to be attentively scrutinized in the forthcoming months (see section 5).

3 Gravitational-wave emission of NS-NS, NS-WD and WD-WD mergers

We first compare and contrast the gravitational-wave emission expected from the above GRBs originating from mergers and their observed electromagnetic emissions with the ones associated with GW170817, namely GRB 170817A and AT 2017gfo [1].

We here consider our canonical model of GRBs assuming uncollimated emission, in absence of observational evidence of an achromatic jet break (see [18, 44] and references therein). We understand that a vast literature exists on alternative models based on a large variety of structured beamed emission which we do not consider here in view of the above considerations. A different approach leading to an agreement with the observational data is here proposed.

In figure 1 we show the gravitational-wave source amplitude spectral density (ASD), $h_c(f)/\sqrt{f}$, together with the one-sided ASD of the Advanced LIGO detector's noise, $\sqrt{S_n}$ [45]. The gravitational-wave characteristic strain is $h_c = (1+z)\sqrt{(1/10)(G/c^3)dE/df_s/d_L(z)}$, where $d_L(z)$ is the luminosity distance to the source, $f = f_s/(1+z)$ and f_s are the gravitational-wave frequency in the detector's and in the source's frame and dE/df_s is the gravitational-wave spectrum, respectively. For the luminosity distance we adopt a Λ CDM cosmology with $H_0 = 71 \text{ km s}^{-1}$, $\Omega_M = 0.73$ and $\Omega_\Lambda = 0.23$ [46]. The spectrum of the binary inspiral can be adopted from the traditional quadrupole formula, $dE/df_s = (2^{1/3}/3)(\pi G)^{2/3}\mathcal{M}^{5/3}f_s^{-1/3}$, where we recall $\mathcal{M} \equiv (m_1 m_2)^{3/5}/M^{1/5}$ and $M = m_1 + m_2$ are, respectively, the chirp mass and total mass of the binary. We cut the gravitational-wave emission of the inspiral at the point where the two stars enter into contact, namely at a distance $r = R_1 + R_2$, where R_1 and R_2 are the stellar radii. For the NS radii we use the mass-radius relation shown in [47] obtained with the GM1 equation of state while, for the WDs, we use the mass-radius relation in [48] obtained with the relativistic Feynman-Metropolis-Teller equation of state.

To represent the emission of a S-GRB we adopt the parameters of GRB 090510A, the first identified NS-NS merger leading to a BH [16]. We thus use $m_1 = m_2 = 1.36 M_\odot$, consistent with the condition that the merging mass exceeds the NS critical mass in the case of the GM1 nuclear equation of state which, for a non-rotating NS, is $M_{\text{crit}} \approx 2.4 M_\odot$ [47]. We are here neglecting, for simplicity, the angular momentum distribution of the post-merger configuration which would lead to a more complex analysis of the initial merging masses leading to BH formation (Rodríguez, et al., in preparation).

For a S-GRF, we assume a GRB 130603B-like source with $m_1 = m_2 = 1.1 M_\odot$, consistent with the condition that the merged object is a massive but stable NS, consistent with the adopted NS critical mass value.

For a GRF, we adopt a GRB 060614-like source, namely a NS-WD binary with $m_1 = 1.2 M_\odot$ and $m_2 = 0.5 M_\odot$ [28].

To compare and contrast the gravitational-wave emission, we have located all the sources at a distance of $d = 40 \text{ Mpc}$, as the one of GW170817 [1]. The gravitational-wave emission associated with the inspiral phase of the NS-NS mergers (GRB 090510A-like and GRB 130603B-like) would be consistent, both in the characteristic strain and the spanned frequency range, with the ones of GW170817 (see ref. [1], for details on this source). Instead, the emission of NS-WD and WD-WD mergers is outside the Advanced LIGO frequency band. For details of the gravitational-wave emission from these binaries see [18].

4 Comparison of the prompt, X-rays and optical light-curves of NS-NS and NS-WD mergers

We turn now to the comparison of the electromagnetic emission of all these binaries, namely of S-GRBs, S-GRFs and GRFs, with the ones of GRB 170817A - AT 2017gfo.

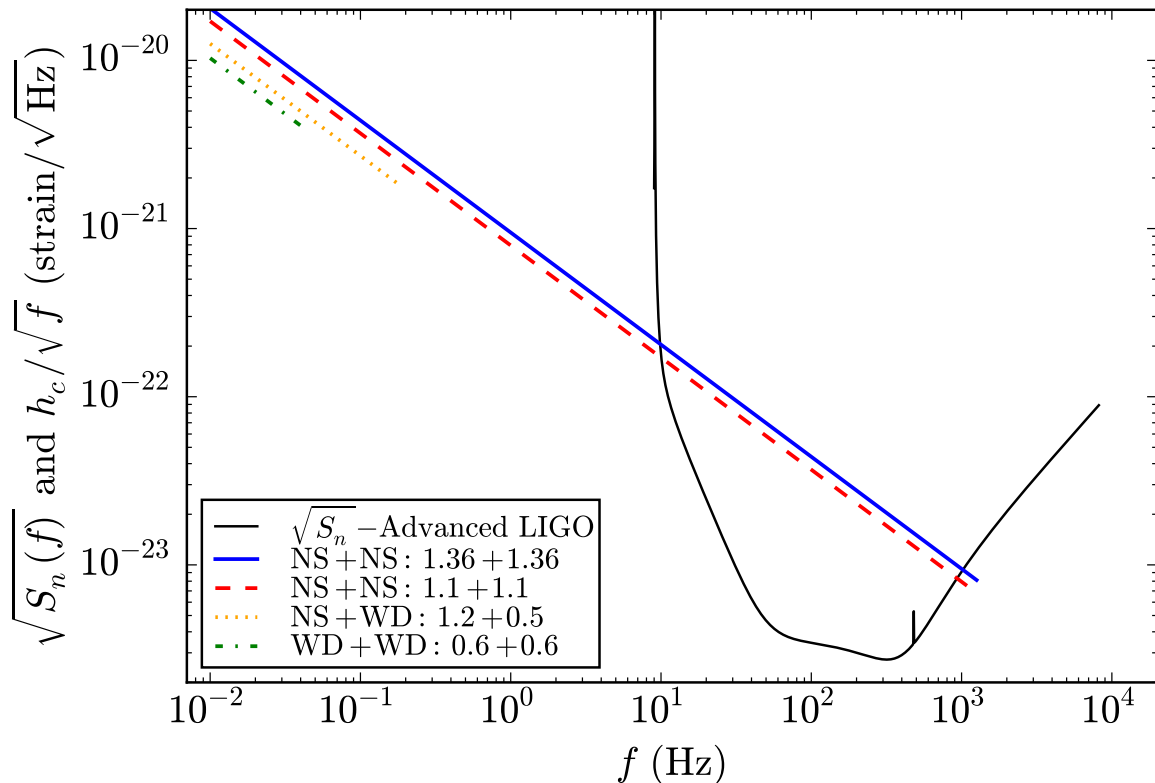


Figure 1. Source ASD, $h_c(f)/\sqrt{f}$, together with the one-sided ASD of the Advanced LIGO detector’s noise, $\sqrt{S_n}$, for representative examples of S-GRBs (GRB 090510A-like), S-GRFs (GRB 130603B-like) and GRFs (GRB 060614-like). We have also included the expected ASD for a representative WD-WD binary. For the sake of the comparison all sources have been artificially assumed to be at a luminosity distance of 40 Mpc (cosmological redshift $z \approx 0.009$). For details of the gravitational-wave emission of these binaries see [18].

GeV emission. A first general conclusion can be directly inferred for the absence in GRB 170817A of the GeV emission (see e.g. [49, 50]): we can at once conclude that GRB 170817A is not consistent with a S-GRB, a NS-NS merger leading to a BH formation (see figure 2 and [19]). This conclusion is in agreement with the one obtained from the analysis of the gamma-ray prompt emission and the X-ray emission; see below and figures 3–4 and tables 1–2.

Gamma-ray prompt emission. Figure 3 shows the gamma-ray (10–1000 keV) prompt emission isotropic rest-frame light-curves of GRBs 090510, 130603B, 060614 and 170817A. In table 1 we compare and contrast the isotropic energy, peak luminosity and peak energy of the prompt emission for the same GRBs.

We can conclude that the gamma-ray prompt emission from GRB 170817A is not consistent with the one observed in GRBs 090510A, 130603B and 060614.

X-rays. In addition, we also show in figure 3 the corresponding X-ray isotropic light-curves, in the rest-frame 0.3–10 keV energy band. It can be seen the overlapping of the light-curves at times $t \gtrsim 5000$ s from the BAT trigger [54]. We recall that we had presented a first comparison of the X-ray light-curves of GRBs 090510A and 130603B in [55]. The match of the X-ray light-curves occurs irrespectively of their isotropic energies which differ up to a

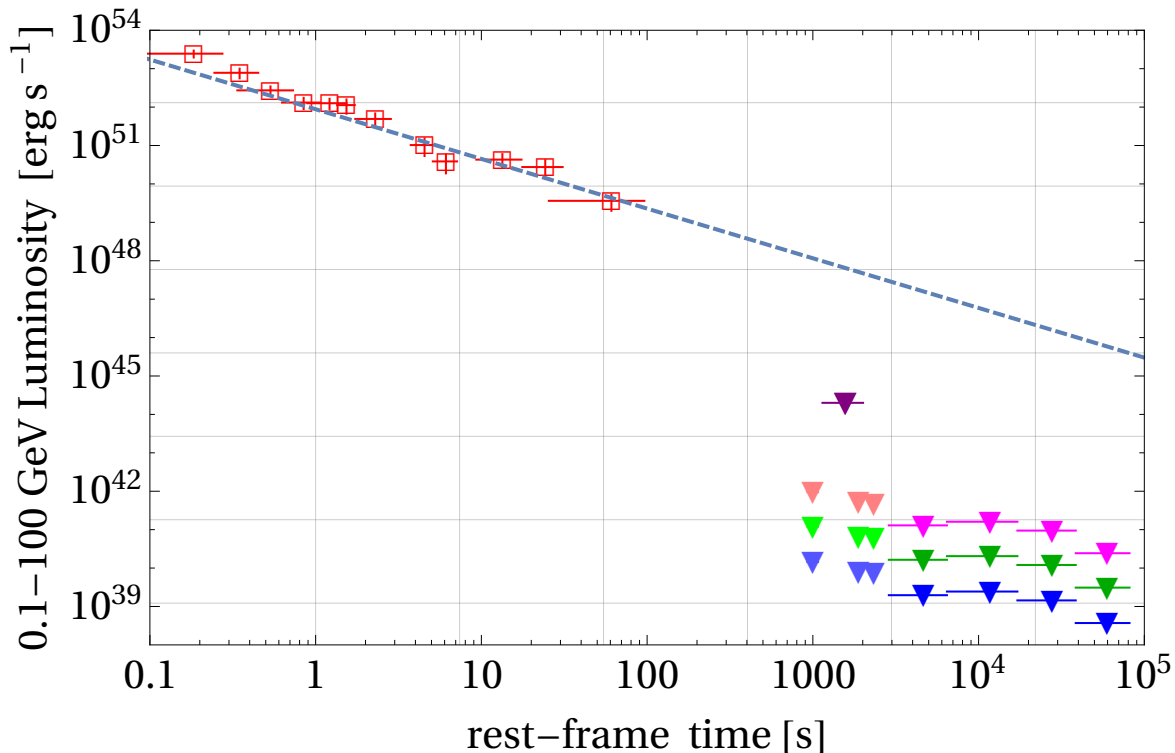


Figure 2. Comparison of the rest-frame, 0.1–100 GeV band light-curve of GRB 090510A (red empty squares) with the corresponding observational upper limits of GRB 170817A (filled triangles). The dashed line indicates the power-law decay with slope index -1.29 ± 0.06 , observed in S-GRBs (see [19] for details, and references therein). The purple triangle indicates the upper limit by Fermi-LAT of $9.7 \times 10^{43} \text{ erg s}^{-1}$ from 1151 to 2025 s from the Fermi trigger time. AGILE upper limits (pink, green and blue triangles) were calculated through extrapolation to the Fermi-LAT working energy band (0.1–100 GeV). We assume the spectral indices -2.0 (blue triangles), -1.0 (green triangles), -0.1 (pink triangles). The data of GRB 170817A were retrieved from [49, 50].

GRB	E_{iso} (erg)	L_{peak} (erg s^{-1})	E_{peak} (MeV)	Reference
060614	2.17×10^{51}	3×10^{49}	$0.34^{+0.24}_{-0.1}$	GCN Circular 5264 [51]
090510	3.95×10^{52}	9.1×10^{52}	7.89 ± 0.76	[15]
130603B	2.1×10^{51}	4.1×10^{51}	0.90 ± 0.14	GCN Circular 14771 [52]
170817A	3.1×10^{46}	1.2×10^{47}	0.082 ± 0.021	GCN Circular 21520 [53]

Table 1. The isotropic energy, luminosity of the peak and peak energy of GRBs 060614, 090510, 130603B and 170817A in the prompt gamma-ray emission phase.

factor of ≈ 20 for instance in the case of GRB 130603B, $E_{\text{iso}} = 2.1 \times 10^{51} \text{ erg}$ [56] and GRB 090510A, $E_{\text{iso}} = 3.95 \times 10^{52} \text{ erg}$ [16]).

We can see that the X-ray emission from GRB 170817A is not consistent with the one observed in GRBs 090510A, 130603B and 060614.

Optical and infrared. We show in figure 4 the optical (r band) and infrared (H and Ks bands) light-curve of GRB 090510A [57, 58], GRB 130603B [23, 24], GRB 060614 [28, 34], and GRB 170817A (i.e. AT 2017gfo [4–7]).

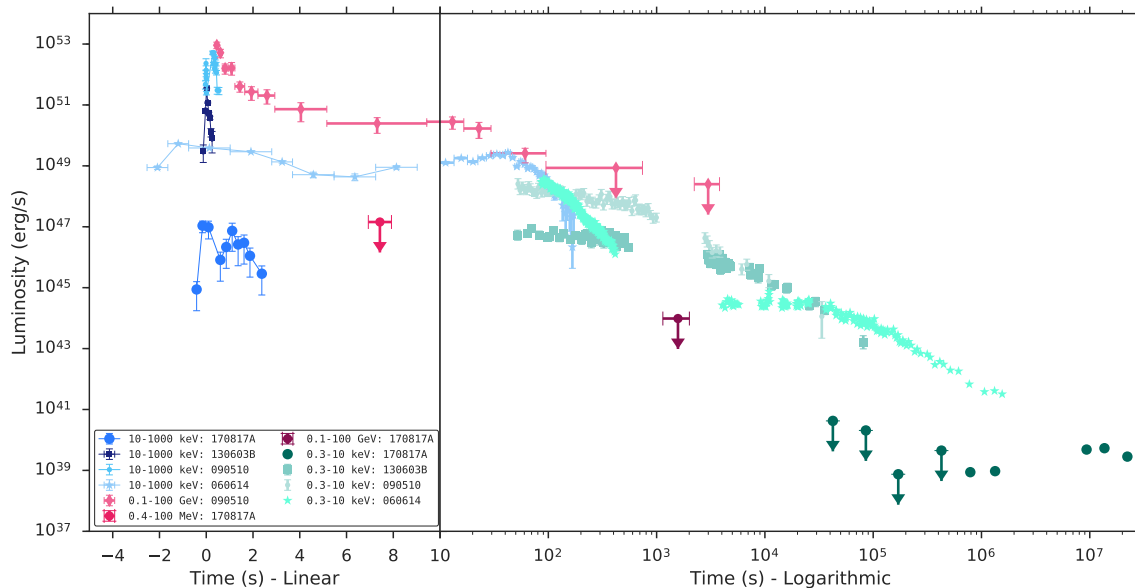


Figure 3. Light-curves of GRBs 060614, 090510A, 130603 and 170817A in the cosmological rest-frame. We show the gamma-ray (10–1000 keV) prompt and the X-ray (0.3–10 keV) emissions. The first 10 seconds are plotted in a linear scale and longer times in the logarithmic scale.

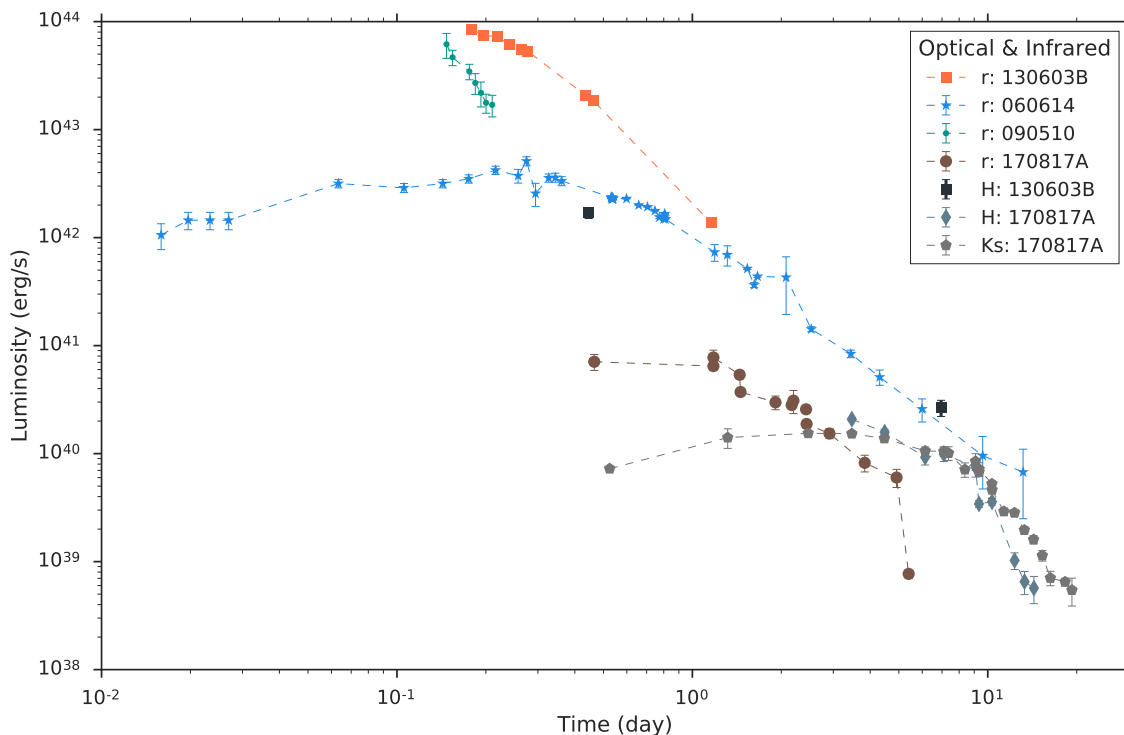


Figure 4. Optical (r band) and infrared (H and Ks bands) light-curves of GRBs 060614, 090510A, 130603 and 170817A in the cosmological rest-frame.

Since a kilonova emission had been associated with GRB 130603B [23], the similarity of this GRB in the X-rays with GRB 090510A boosted us to seek for a kilonova signature in the case GRB 090510A. This appears to be confirmed by figure 4. We can conclude that all of these sources, S-GRFs, S-GRBs and GRFs, can produce a kilonova emission in line with the source AT 2017gfo, the kilonova associated with GRB 170817A.

Some of the above correlations of the electromagnetic emissions clearly originate from the traditional kilonova models based on ultra-relativistic regimes in NS-NS and NS-WD mergers pioneered in [10, 21, 59], following the classical work of [60, 61].

The common asymptotic behavior at late times of the X-ray and optical emission of GRB 090510A [55] and GRB 130603B [23] are a manifestation of a common synchrotron emission as recently outlined in [62]. This approach is also supported by the parallel behavior of the optical and X-ray emission of GRB 060614 (see figures 3 and 4). Similar behavior was already indicated in the case of long GRBs (BdHNe) [63, 64]. In fact, it is interesting to use this similarity to set a lower limit to the mass of the expanding matter by equating the energy emitted in the X-rays, $E_{\text{iso,X}}$ (see table 2), to the kinetic energy, $E_{\text{kin}} = (\Gamma - 1)Mc^2$, where Γ is the Lorentz factor. By using for instance $\Gamma \sim 1.2$ ($v/c \sim 0.5$), a typical value obtained for the expanding blackbody component in the X-ray afterglow of BdHNe [44], we obtain $9.2 \times 10^{-4} M_{\odot}$, $9.4 \times 10^{-5} M_{\odot}$ and $2.4 \times 10^{-4} M_{\odot}$ for GRBs 090510A, 130603B and 060614. These lower limits are indeed in line with the ejecta mass obtained from an independent analysis of the optical emission (see e.g. [22–24, 26]). The same analysis of the X-ray emission applied to GRB 170817A would lead to a nearly ten orders of magnitude less massive ejecta, giving further support to a possible different nature of this source.

The above contrast of the gamma- and X-rays observational properties of GRB 170817A with respect to GRBs produced by NS-NS and NS-WD mergers has led us to consider the possibility of an additional subclass of GRBs produced by the merger of a still different compact-star binary, a WD-WD merger, leading to a massive WD. We proceed now to discuss the framework of such a model to explain the electromagnetic properties of the association GRB 170817A - AT 2017gfo.

5 WD-WD mergers as an alternative mildly relativistic uncollimated emission for GRB 170817A-AT 2017gfo

The estimated WD-WD merger rate (see section 2) implies that 0.1% of WD-WD mergers can explain the GRB 170817A-like population for which a lower limit of $(30\text{--}630) \text{ Gpc}^{-3} \text{ yr}^{-1}$ has been recently obtained (see [65] for details).

The energy observed in gamma-rays in GRB 170817A, $E_{\text{iso}} \approx 3 \times 10^{46} \text{ erg}$, can originate from flares owing to the twist and stress of the magnetic field lines during the merger process: a magnetic energy of $2 \times 10^{46} \text{ erg}$ is stored in a region of radius 10^9 cm and magnetic field of 10^{10} G [43].

The emission at optical and infrared wavelengths (see figure 5), can be explained from the adiabatic cooling of $10^{-3} M_{\odot}$ ejecta from the merger [66, 67] heated by fallback accretion onto the newly-formed WD [66]. The ejecta becomes transparent at times $t \sim 1 \text{ day}$ with a peak bolometric luminosity of $L_{\text{bol}} \sim 10^{42} \text{ erg s}^{-1}$. The fallback accretion injects to the ejecta $10^{47}\text{--}10^{49} \text{ erg s}^{-1}$ at early times and fall-off following a power-law behavior (see [66] for details). The kilonovae from WD-WD mergers are therefore powered by a different mechanism with respect to the kilonovae from NS-NS mergers which are powered by the radioactive decay of r-process heavy material.

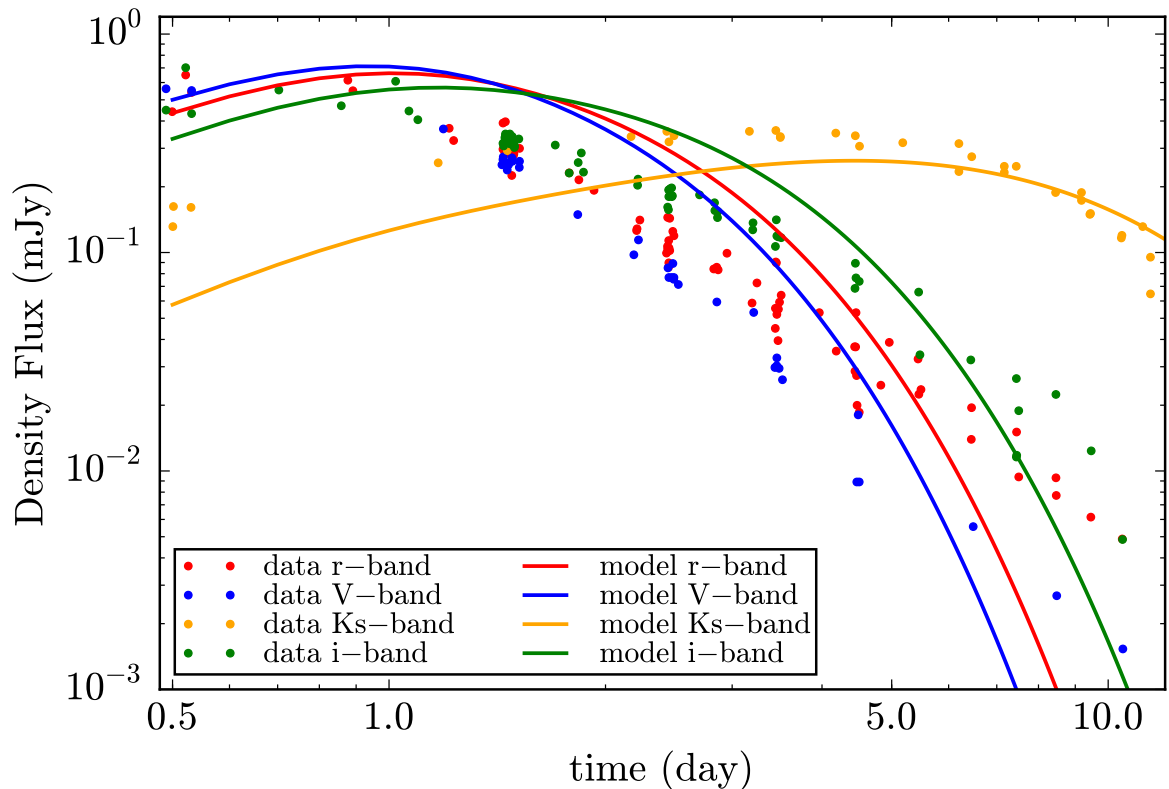


Figure 5. Points: observed optical and infrared density flux of AT 2017gfo [6, 7]. Solid curves: corresponding theoretical expectation from the cooling of $10^{-3} M_{\odot}$ of WD-WD merger ejecta heated by fallback accretion onto the newly-formed central WD.

At times $t \sim 100$ – 200 day, the ejecta are expected to become transparent to the X-rays leading to a luminosity of $\approx 10^{39}$ erg s^{-1} as the one recently observed in GRB 170817A (see figure 3). At earlier times, the X-rays from fallback accretion are instead absorbed by the ejecta and are mainly transformed into kinetic energy then increasing the expansion velocity of the ejecta, from an initial non-relativistic value $0.01 c$ typical of the escape velocity from the WD, to a mildly relativistic velocity $0.1 c$. This mildly relativistic velocity is also consistent with the value derived from the evolution of blackbody spectra observed from ~ 0.5 day to ~ 7 day. We present the detailed analysis of all the above properties of WD-WD mergers in [68].

As we have mentioned in section 2, the WD formed in the merger can become an SGR/AXP [39, 43]. Thus, there is the possibility that, if a WD-WD merger produced GRB 170817A-AT 2017gfo, an SGR/AXP (a WD-pulsar) will show in this sky position in the near future.

The observational features of these WD-WD mergers in the X- and the gamma-rays as well as in the optical and infrared wavelengths are an important topic by their own. We are going to present elsewhere additional details on the multiwavelength observables of the merger, of the post-merger and of the ejected matter.

6 Discussion and conclusions

In this work we have compared and contrasted the gravitational-wave and the electromagnetic emission of canonical GRBs associated with NS-NS (both S-GRBs and S-GRFs), NS-

Subclass	<i>In-state</i> → <i>Out-state</i>	T_{90} (s)	$E_{p,i}$ (MeV)	E_{iso} (erg)	$E_{\text{iso,GeV}}$ (erg)	$E_{\text{iso,X}}$ (erg)	Kilonova	$L_{p,\text{KN}}$ (erg s ⁻¹)	Hz-kHz GW
S-GRFs	NS-NS → MNS	$\lesssim 2$	$\lesssim 2$	$10^{49}\text{--}10^{52}$	—	$10^{49}\text{--}10^{51}$	RPKN	10^{41}	Yes
S-GRBs	NS-NS → BH	$\lesssim 2$	$\gtrsim 2$	$10^{52}\text{--}10^{53}$	$10^{52}\text{--}10^{53}$	$\lesssim 10^{51}$	RPKN	10^{41}	Yes
GRFs	NS-WD → MNS	2–100	0.2–2	$10^{51}\text{--}10^{52}$	—	$10^{49}\text{--}10^{50}$	TBD	10^{41}	No
GR-K	WD-WD → MWD	$\lesssim 1$	$\lesssim 0.1$	$\lesssim 10^{47}$	—	$10^{38}\text{--}10^{39}$	FBKN	10^{41}	No

Table 2. Summary of the GRB subclasses discussed in this article: short gamma-ray flashes (S-GRFs), authentic short GRBs (S-GRBs) and gamma-ray flash kilonovae (GR-K) introduced in this work. See further details in [15, 18, 68] and references therein. The columns indicate the GRB subclass, *in-states* (progenitor) and *out-states* (final outcome), the T_{90} in the rest-frame, the rest-frame spectral peak energy $E_{p,i}$ and E_{iso} (rest-frame 1– 10^4 keV), the isotropic energy of the GeV emission $E_{\text{iso,GeV}}$ (rest-frame 0.1–100 GeV), the isotropic energy of the X-ray data $E_{\text{iso,X}}$ (rest-frame 0.3–10 keV), the presence or not of kilonova and its nature (radioactive-powered kilonova, RPKN; fallback-powered kilonova, FBKN), the typical associated kilonova peak luminosity, and finally the presence or not of Hz-kHz gravitational-wave emission, e.g. as the one detectable by LIGO-Virgo. As for the kilonova from NS-WD mergers we have specified “to be defined (TBD)” since this possibility has not been yet explored in the literature.

WD (GRFs) and WD-WD mergers with the one of the associated sources GRB 170817A-GW170817-AT 2017gfo. We present in table 2 a summary. As a canonical S-GRB we use GRB 090510A, for S-GRF we use GRB 130603B and for GRF we use GRB 060614 and for GRB 170817 a twin WD with component masses $M = 0.6M_{\odot}$, see figure 1.

We can conclude:

1. The comparison of the properties of NS-NS (S-GRFs and S-GRBs) and NS-WD (S-GRFs) with GRB 170817A-GW170817-AT 2017gfo shows that all of them may include a kilonova (AT 2017gfo-like). Only in NS-NS there could be the Hz-kHz gravitational-wave emission needed to explain the energetics of GW170817 (see figure 1). However, this solution necessarily implies an X and gamma-ray emission in the prompt phase that is missing in the case of GRB 170817A (see data up to 10 s in figure 3). Indeed, the observational features in gamma- and X-rays of GRB 170817A contrasts with any other GRB associated with the above binary progenitors (see figures 3–4 and tables 1–2). In conclusion, the NS-NS scenario cannot explain the association GRB170817A-GW170817.
2. Indeed, the X-ray and gamma-ray observations of GRB 170817A clearly show that we are in presence of a phenomenon much less energetic than the one observed in any S-GRB, S-GRF, GRF, or BdHN, and perhaps with a substantially larger occurrence rate (see e.g. [65]). These observations have led us to consider a new subclass of GRBs, also with binary progenitors, originating from WD-WD mergers leading to a massive WD. The occurrence rate of these mergers can explain the rate of GRB 170817A-like sources, they produce a gamma- and X-ray emission consistent with the ones observed in GRB 170817A and cannot be associated with GW170817.
3. The optical and infrared emission AT 2017gfo can be powered by a different physical mechanism with respect to the radioactive decay of r-process heavy material synthesized in the much more energetic NS-NS mergers: it can be alternatively explained by the cooling of the ejecta expelled in a WD-WD merger and heated up by fallback accretion onto the newly-formed massive WD, see figure 5. In view of the above difference

we propose to call radioactive-powered kilonovae (RPKNe) the optical transient produced by NS-NS mergers and fallback-powered kilonovae (FBKNe) the one by WD-WD mergers. See table 2.

4. The ejecta from a WD-WD merger are different from the ejecta from a NS-NS merger in that they have a lighter nuclear composition with respect to the one of the ejecta of NS-NS mergers which is made of r-processed heavy nuclei. The spectroscopic identification of atomic species can therefore discriminate between the two scenarios. However, such an identification has not been possible in any of the observed kilonovae since it needs accurate models of atomic spectra, nuclear reaction network, density profile, as well as radiative transport (opacity) that are not yet available.
5. These WD-WD mergers opens the possibility to a new subclass of GRBs with a much less energetic and softer prompt emission whose observation would benefit from a new mission operating in soft X-rays like, e.g., THESEUS [69]. In addition, as we have shown, the outcome of such a GRB, namely a massive, highly magnetized, fast rotating WD, may become in due time observable as SGRs/AXP.
6. Since the early submission of our paper additional observations in the optical and in the X-rays have appeared (see e.g. [70, 71]) which have allowed to strength our conclusions (see e.g. figure 5 and [68]). What we can do at this stage from a theoretical point of view is to formulate what conventional physics can tell us about these events and this has been done in this article.
7. It is clear that the only possibility of a null chance coincidence of GRB 170817A and GW170817 is to assume that one of the events does not exist in reality. If the two events exist then there is non-null chance coincidence by definition and its evaluation has been estimated (see e.g. [2]). The association of these events, from an observational point of view is, in our opinion, not yet sufficiently established to formulate a well-motivated answer. It is auspicious, as soon as the LIGO collaboration releases the templates of the gravitational-wave source GW170817 in the interferometers, to reconstruct the precise chronology of the space-time sequence of events in the LIGO detectors and in the Fermi and Integral satellites, necessary to validate the association between GW170817 and GRB 170817A.

Acknowledgments

We thank P. Lorén-Aguilar for discussions on WD-WD mergers. We thank both the Referee and Scientific Editor for valuable help in optimizing the presentation of our paper as well as for the detailed and constructive discussions.

References

- [1] VIRGO and LIGO SCIENTIFIC collaborations, B. Abbott et al., *GW170817: Observation of Gravitational Waves from a Binary Neutron Star Inspiral*, *Phys. Rev. Lett.* **119** (2017) 161101 [[arXiv:1710.05832](#)] [[INSPIRE](#)].
- [2] VIRGO, FERMI-GBM, INTEGRAL and LIGO SCIENTIFIC collaborations, B.P. Abbott et al., *Gravitational Waves and Gamma-rays from a Binary Neutron Star Merger: GW170817 and GRB 170817A*, *Astrophys. J.* **848** (2017) L13 [[arXiv:1710.05834](#)] [[INSPIRE](#)].

- [3] A. Goldstein et al., *An Ordinary Short Gamma-Ray Burst with Extraordinary Implications: Fermi-GBM Detection of GRB 170817A*, *Astrophys. J.* **848** (2017) L14 [[arXiv:1710.05446](#)] [[INSPIRE](#)].
- [4] D.A. Coulter et al., *Swope Supernova Survey 2017a (SSS17a), the Optical Counterpart to a Gravitational Wave Source*, *Science* (2017) [[arXiv:1710.05452](#)] [[INSPIRE](#)].
- [5] I. Arcavi et al., *Optical emission from a kilonova following a gravitational-wave-detected neutron-star merger*, *Nature* **551** (2017) 64 [[arXiv:1710.05843](#)] [[INSPIRE](#)].
- [6] P.S. Cowperthwaite et al., *The Electromagnetic Counterpart of the Binary Neutron Star Merger LIGO/Virgo GW170817. II. UV, Optical and Near-infrared Light Curves and Comparison to Kilonova Models*, *Astrophys. J.* **848** (2017) L17 [[arXiv:1710.05840](#)] [[INSPIRE](#)].
- [7] M. Nicholl et al., *The Electromagnetic Counterpart of the Binary Neutron Star Merger LIGO/VIRGO GW170817. III. Optical and UV Spectra of a Blue Kilonova From Fast Polar Ejecta*, *Astrophys. J.* **848** (2017) L18 [[arXiv:1710.05456](#)] [[INSPIRE](#)].
- [8] J. Goodman, *Are gamma-ray bursts optically thick?*, *Astrophys. J.* **308** (1986) L47 [[INSPIRE](#)].
- [9] B. Paczynski, *Gamma-ray bursters at cosmological distances*, *Astrophys. J.* **308** (1986) L43 [[INSPIRE](#)].
- [10] D. Eichler, M. Livio, T. Piran and D.N. Schramm, *Nucleosynthesis, Neutrino Bursts and Gamma-Rays from Coalescing Neutron Stars*, *Nature* **340** (1989) 126 [[INSPIRE](#)].
- [11] R. Narayan, T. Piran and A. Shemi, *Neutron star and black hole binaries in the galaxy*, *Astrophys. J.* **379** (1991) L17 [[INSPIRE](#)].
- [12] R. Narayan, B. Paczynski and T. Piran, *Gamma-ray bursts as the death throes of massive binary stars*, *Astrophys. J.* **395** (1992) L83 [[astro-ph/9204001](#)] [[INSPIRE](#)].
- [13] C.L. Fryer, F.G. Oliveira, J.A. Rueda and R. Ruffini, *On the Neutron Star-Black Hole Binaries Produced by Binary-driven-Hypernovae*, *Phys. Rev. Lett.* **115** (2015) 231102 [[arXiv:1505.02809](#)] [[INSPIRE](#)].
- [14] R. Ruffini et al., *GRB 140619B: a short GRB from a binary neutron star merger leading to black hole formation*, *Astrophys. J.* **808** (2015) 190 [[arXiv:1412.1018](#)] [[INSPIRE](#)].
- [15] R. Ruffini et al., *On the classification of GRBs and their occurrence rates*, *Astrophys. J.* **832** (2016) 136 [[arXiv:1602.02732](#)] [[INSPIRE](#)].
- [16] R. Ruffini et al., *GRB 090510: a genuine short-GRB from a binary neutron star coalescing into a Kerr-Newman black hole*, *Astrophys. J.* **831** (2016) 178 [[arXiv:1607.02400](#)] [[INSPIRE](#)].
- [17] M. Muccino, R. Ruffini, C.L. Bianco, L. Izzo and A.V. Penacchioni, *GRB 090227B: the missing link between the genuine short and disguised short GRBs*, *Astrophys. J.* **763** (2013) 125 [[arXiv:1205.6600](#)] [[INSPIRE](#)].
- [18] R. Ruffini et al., *On the rate and on the gravitational wave emission of short and long GRBs*, *Astrophys. J.* **859** (2018) 30 [[arXiv:1602.03545](#)] [[INSPIRE](#)].
- [19] R. Ruffini et al., *On the Short GRB GeV emission from a Kerr Black hole*, [arXiv:1802.07552](#) [[INSPIRE](#)].
- [20] Y. Aimuratov et al., *GRB 081024B and GRB 140402A: two additional short GRBs from binary neutron star mergers*, *Astrophys. J.* **844** (2017) 83 [[arXiv:1704.08179](#)] [[INSPIRE](#)].
- [21] L.-X. Li and B. Paczynski, *Transient events from neutron star mergers*, *Astrophys. J.* **507** (1998) L59 [[astro-ph/9807272](#)] [[INSPIRE](#)].
- [22] B.D. Metzger et al., *Electromagnetic Counterparts of Compact Object Mergers Powered by the Radioactive Decay of R-process Nuclei*, *Mon. Not. Roy. Astron. Soc.* **406** (2010) 2650 [[arXiv:1001.5029](#)] [[INSPIRE](#)].

- [23] N.R. Tanvir et al., A “kilonova” associated with short-duration gamma-ray burst 130603B, *Nature* **500** (2013) 547 [[arXiv:1306.4971](#)] [[INSPIRE](#)].
- [24] E. Berger, W. Fong and R. Chornock, An *r*-process Kilonova Associated with the Short-hard GRB 130603B, *Astrophys. J.* **774** (2013) L23 [[arXiv:1306.3960](#)] [[INSPIRE](#)].
- [25] W. Fong et al., Short GRB 130603B: Discovery of a Jet Break in the Optical and Radio Afterglows and a Mysterious Late-time X-Ray Excess, *Astrophys. J.* **780** (2014) 118 [[arXiv:1309.7479](#)] [[INSPIRE](#)].
- [26] Z.-P. Jin et al., The Macronova in GRB 050709 and the GRB/macronova connection, *Nature Commun.* **7** (2016) 12898 [[arXiv:1603.07869](#)] [[INSPIRE](#)].
- [27] M. Della Valle et al., GRB 060614: An enigmatic long-duration gamma-ray burst not due to a hypernova, *Nature* **444** (2006) 1050 [[astro-ph/0608322](#)] [[INSPIRE](#)].
- [28] L. Caito, M.G. Bernardini, C.L. Bianco, M.G. Dainotti, R. Guida and R. Ruffini, GRB060614: a ‘fake’ short GRB from a merging binary system, *Astron. Astrophys.* **498** (2009) 501 [[arXiv:0810.4855](#)] [[INSPIRE](#)].
- [29] M. Cadelano et al., Optical Identification of He White Dwarfs Orbiting Four Millisecond Pulsars in the Globular Cluster 47 Tucanae, *Astrophys. J.* **812** (2015) 63 [[arXiv:1509.01397](#)] [[INSPIRE](#)].
- [30] C.L. Fryer, S.E. Woosley, M. Herant and M.B. Davies, Merging white dwarf/black hole binaries and gamma-ray bursts, *Astrophys. J.* **520** (1999) 650 [[astro-ph/9808094](#)] [[INSPIRE](#)].
- [31] P. Lazarus et al., Timing of a Young Mildly Recycled Pulsar with a Massive White Dwarf Companion, *Mon. Not. Roy. Astron. Soc.* **437** (2014) 1485 [[arXiv:1310.5857](#)] [[INSPIRE](#)].
- [32] T.M. Tauris, E.P. J. v.d. Heuvel and G.J. Savonije, Formation of millisecond pulsars with heavy white dwarf companions - extreme mass transfer on sub-thermal timescales, *Astrophys. J.* **530** (2000) L93 [[astro-ph/0001013](#)] [[INSPIRE](#)].
- [33] T.A. Thompson, M.D. Kistler and K.Z. Stanek, A High Rate of White Dwarf-Neutron Star Mergers & Their Transients, [arXiv:0912.0009](#) [[INSPIRE](#)].
- [34] B. Yang et al., A possible Macronova in the late afterglow of the ‘long-short’ burst GRB 060614, *Nature Commun.* **6** (2015) 7323 [[arXiv:1503.07761](#)] [[INSPIRE](#)].
- [35] B.P. Abbott et al., Multi-messenger Observations of a Binary Neutron Star Merger, *Astrophys. J.* **848** (2017) L12 [[arXiv:1710.05833](#)] [[INSPIRE](#)].
- [36] D. Maoz and N. Hallakoun, The binary fraction, separation distribution and merger rate of white dwarfs from SPY, *Mon. Not. Roy. Astron. Soc.* **467** (2017) 1414 [[arXiv:1609.02156](#)] [[INSPIRE](#)].
- [37] D. Maoz, N. Hallakoun and C. Badenes, The separation distribution and merger rate of double white dwarfs: improved constraints, *Mon. Not. Roy. Astron. Soc.* **476** (2018) 2584 [[arXiv:1801.04275](#)] [[INSPIRE](#)].
- [38] V. Kalogera, R. Narayan, D.N. Spergel and J.H. Taylor, The coalescence rate of double neutron star systems, *Astrophys. J.* **556** (2001) 340 [[astro-ph/0012038](#)] [[INSPIRE](#)].
- [39] J.A. Rueda et al., A white dwarf merger as progenitor of the anomalous X-ray pulsar 4U 0142+61?, [arXiv:1306.5936](#) [[INSPIRE](#)].
- [40] L. Becerra, J.A. Rueda, P. Loren-Aguilar and E. Garcia-Berro, The Spin Evolution of Fast-Rotating, Magnetized Super-Chandrasekhar White Dwarfs in the Aftermath of White Dwarf Mergers, *Astrophys. J.* **857** (2018) 134 [[arXiv:1804.01275](#)] [[INSPIRE](#)].
- [41] V.M. Lipunov, Double O-Ne-Mg white dwarfs merging as the source of the Powerful Gravitational Waves for LIGO/VIRGO type interferometers, *New Astron.* **56** (2017) 84 [[arXiv:1703.04000](#)] [[INSPIRE](#)].

- [42] A.J. Ruiter, K. Belczynski and C.L. Fryer, *Rates and Delay Times of Type Ia Supernovae*, *Astrophys. J.* **699** (2009) 2026 [[arXiv:0904.3108](#)] [[INSPIRE](#)].
- [43] M. Malheiro, J.A. Rueda and R. Ruffini, *SGRs and AXPs as rotation powered massive white dwarfs*, *Publ. Astron. Soc. Jap.* **64** (2012) 56 [[arXiv:1102.0653](#)] [[INSPIRE](#)].
- [44] R. Ruffini et al., *Early X-ray Flares in GRBs*, *Astrophys. J.* **852** (2018) 53 [[arXiv:1704.03821](#)] [[INSPIRE](#)].
- [45] VIRGO, KAGRA and LIGO SCIENTIFIC collaborations, B.P. Abbott et al., *Prospects for Observing and Localizing Gravitational-Wave Transients with Advanced LIGO, Advanced Virgo and KAGRA*, *Living Rev. Rel.* **21** (2018) 3 [[arXiv:1304.0670](#)] [[INSPIRE](#)].
- [46] M. Rigault et al., *Confirmation of a Star Formation Bias in Type Ia Supernova Distances and its Effect on Measurement of the Hubble Constant*, *Astrophys. J.* **802** (2015) 20 [[arXiv:1412.6501](#)] [[INSPIRE](#)].
- [47] F. Cipolletta, C. Cherubini, S. Filippi, J.A. Rueda and R. Ruffini, *Fast Rotating Neutron Stars with Realistic Nuclear Matter Equation of State*, *Phys. Rev. D* **92** (2015) 023007 [[arXiv:1506.05926](#)] [[INSPIRE](#)].
- [48] M. Rotondo, J.A. Rueda, R. Ruffini and S.-S. Xue, *The relativistic Feynman-Metropolis-Teller theory for white dwarfs in general relativity*, *Phys. Rev. D* **84** (2011) 084007 [[arXiv:1012.0154](#)] [[INSPIRE](#)].
- [49] FERMI-LAT collaboration, D. Kocevski, N. Omodei and G. Vianello, *Fermi-LAT observations of the LIGO/Virgo event GW170817*, [arXiv:1710.05450](#) [[INSPIRE](#)].
- [50] F. Verrecchia et al., *AGILE Observations of the Gravitational-wave Source GW170817: Constraining Gamma-Ray Emission from a NS-NS Coalescence*, *Astrophys. J.* **850** (2017) L27 [[arXiv:1710.05460](#)] [[INSPIRE](#)].
- [51] S. Golenetskii, R. Aptekar, E. Mazets, V. Pal'Shin, D. Frederiks and T. Cline, *Konus-wind observation of GRB 060614*, GRB Coordinates Network 5264 (2006).
- [52] S. Golenetskii et al., *Konus-wind observation of GRB 130603B*, GRB Coordinates Network, Circular Service, No. 14771, #1 (2013).
- [53] A. von Kienlin, C. Meegan and A. Goldstein, *GRB 170817A: Fermi GBM detection*, GRB Coordinates Network, Circular Service, No. 21520, #1 (2017).
- [54] A. Melandri et al., *GRB 130603B: Swift detection of a bright short burst*, GRB Coordinates Network, Circular Service, No. 14735, #1 (2013).
- [55] R. Ruffini et al., *GRB 130603B: analogy with GRB 090510A and possible connection with a supernova*, GRB Coordinates Network, Circular Service, No. 14913, #1 (2013).
- [56] D. Frederiks, *GRB 130603B: rest-frame energetics in gamma-rays*, GRB Coordinates Network, Circular Service, No. 14772, #1 (2013).
- [57] GBM and FERMI-LAT collaborations, M. De Pasquale et al., *Swift and Fermi observations of the early afterglow of the short Gamma-Ray Burst 090510*, *Astrophys. J.* **709** (2010) L146 [[arXiv:0910.1629](#)] [[INSPIRE](#)].
- [58] A.N. Guelbenzu et al., *The late-time afterglow of the extremely energetic short burst GRB 090510 revisited*, *Astron. Astrophys.* **538** (2012) L7 [[arXiv:1201.3885](#)] [[INSPIRE](#)].
- [59] J.M. Lattimer, F. Mackie, D.G. Ravenhall and D.N. Schramm, *The decompression of cold neutron star matter*, *Astrophys. J.* **213** (1977) 225 [[INSPIRE](#)].
- [60] W.D. Arnett, *Analytic solutions for light curves of supernovae of Type II*, *Astrophys. J.* **237** (1980) 541.
- [61] W.D. Arnett, *Type I supernovae. I - Analytic solutions for the early part of the light curve*, *Astrophys. J.* **253** (1982) 785.

- [62] R. Ruffini et al., *On a GRB afterglow model consistent with hypernovae observations*, [arXiv:1712.05000](#) [INSPIRE].
- [63] R. Ruffini et al., *On Binary Driven Hypernovae and their nested late X-ray emission*, *Astron. Astrophys.* **565** (2014) L10 [[arXiv:1404.3946](#)] [INSPIRE].
- [64] R. Ruffini et al., *GRB 130427A and SN 2013cq: A multi-wavelength Analysis of An Induced Gravitational Collapse Event*, *Astrophys. J.* **798** (2015) 10 [[arXiv:1405.5723](#)] [INSPIRE].
- [65] B.B. Zhang et al., *A peculiar low-luminosity short gamma-ray burst from a double neutron star merger progenitor*, *Nature Commun.* **9** (2018) 447 [[arXiv:1710.05851](#)] [INSPIRE].
- [66] P. Lorén-Aguilar, J. Isern and E. García-Berro, *High-resolution smoothed particle hydrodynamics simulations of the merger of binary white dwarfs*, *Astron. Astrophys.* **500** (2009) 1193.
- [67] M. Dan, S. Rosswog, J. Guillochon and E. Ramirez-Ruiz, *Prelude to a double degenerate merger: the onset of mass transfer and its impact on gravitational waves and surface detonations*, *Astrophys. J.* **737** (2011) 89 [[arXiv:1101.5132](#)] [INSPIRE].
- [68] J.A. Rueda et al., *Electromagnetic emission of white dwarf binary mergers*, [arXiv:1807.07905](#) [INSPIRE].
- [69] THESEUS collaboration, L. Amati et al., *The THESEUS space mission concept: science case, design and expected performances*, *Adv. Space Res.* **62** (2018) 191 [[arXiv:1710.04638](#)] [INSPIRE].
- [70] P. D’Avanzo et al., *The evolution of the X-ray afterglow emission of GW 170817/ GRB 170817A in XMM-Newton observations*, *Astron. Astrophys.* **613** (2018) L1 [[arXiv:1801.06164](#)] [INSPIRE].
- [71] J.D. Lyman et al., *The optical afterglow of the short gamma-ray burst associated with GW170817*, *Nat. Astron.* **2** (2018) 751 [[arXiv:1801.02669](#)] [INSPIRE].



On the Rate and on the Gravitational Wave Emission of Short and Long GRBs

R. Ruffini^{1,2,3,4}, J. Rodriguez^{1,2}, M. Muccino^{1,2} , J. A. Rueda^{1,2,4} , Y. Aimuratov^{1,2}, U. Barres de Almeida^{4,5}, L. Becerra^{1,2},
C. L. Bianco^{1,2} , C. Cherubini^{6,7}, S. Filippi^{6,7}, D. Gizzi¹, M. Kovacevic^{1,2,3} , R. Moradi^{1,2}, F. G. Oliveira^{1,2,3},
G. B. Pisani^{1,2} , and Y. Wang^{1,2}

¹ Dipartimento di Fisica and ICRA, Sapienza Università di Roma, P.le Aldo Moro 5, I-00185 Rome, Italy

² ICRANet, P.zza della Repubblica 10, I-65122 Pescara, Italy

³ Université de Nice Sophia Antipolis, CEDEX 2, Grand Château Parc Valrose, Nice, France

⁴ ICRANet-Rio, Centro Brasileiro de Pesquisas Físicas, Rua Dr. Xavier Sigaud 150, 22290-180 Rio de Janeiro, Brazil

⁵ Centro Brasileiro de Pesquisas Físicas, Rua Dr. Xavier Sigaud 150, 22290-180 Rio de Janeiro, Brazil

⁶ Unit of Nonlinear Physics and Mathematical Modeling, Università Campus Bio-Medico di Roma, Via A. del Portillo 21, I-00128 Rome, Italy

⁷ ICRA, Università Campus Bio-Medico di Roma, Via A. del Portillo 21, I-00128 Rome, Italy

Received 2016 October 25; revised 2018 April 6; accepted 2018 April 15; published 2018 May 18

Abstract

On the ground of the large number of gamma-ray bursts (GRBs) detected with cosmological redshift, we classified GRBs in seven subclasses, all with binary progenitors which emit gravitational waves (GWs). Each binary is composed of combinations of carbon–oxygen cores (CO_{core}), neutron stars (NSs), black holes (BHs), and white dwarfs (WDs). The long bursts, traditionally assumed to originate from a BH with an ultrarelativistic jetted emission, not emitting GWs, have been subclassified as (I) X-ray flashes (XRFs), (II) binary-driven hypernovae (BdHNe), and (III) BH–supernovae (BH–SNe). They are framed within the induced gravitational collapse paradigm with a progenitor CO_{core}–NS/BH binary. The SN explosion of the CO_{core} triggers an accretion process onto the NS/BH. If the accretion does not lead the NS to its critical mass, an XRF occurs, while when the BH is present or formed by accretion, a BdHN occurs. When the binaries are not disrupted, XRFs lead to NS–NS and BdHNe lead to NS–BH. The short bursts, originating in NS–NS, are subclassified as (IV) short gamma-ray flashes (S-GRFs) and (V) short GRBs (S-GRBs), the latter when a BH is formed. There are (VI) ultrashort GRBs (U-GRBs) and (VII) gamma-ray flashes (GRFs) formed in NS–BH and NS–WD, respectively. We use the occurrence rate and GW emission of these subclasses to assess their detectability by Advanced LIGO–Virgo, eLISA, and resonant bars. We discuss the consequences of our results in view of the announcement of the LIGO/Virgo Collaboration of the source GW 170817 as being originated by an NS–NS.

Key words: binaries: general – black hole physics – gamma-ray burst: general – gravitational waves – stars: neutron – white dwarfs

1. Introduction

Thanks to the extensive observations carried out by γ -ray telescopes, such as AGILE, BATSE, *BeppoSAX*, *Fermi*, *HETE-II*, *INTEGRAL*, *Konus/WIND*, and *Swift*, our understanding of “long” and “short” gamma-ray burst (GRB) progenitor systems has greatly improved. This has led also to a vast literature devoted to the estimate of their relative occurrence rates, all in general agreement. For long bursts see, e.g., Soderberg et al. (2006b), Guetta & Della Valle (2007), Liang et al. (2007), Virgili et al. (2009), Rangel Lemos et al. (2010), Wanderman & Piran (2010), Guetta et al. (2011), and Kovacevic et al. (2014); for short bursts see, e.g., Virgili et al. (2011) and Wanderman & Piran (2015); and for both long and short bursts see, e.g., Sun et al. (2015) and Ruffini et al. (2016b). The rates of gravitational wave (GW) emission from GRBs have been calculated in the literature at a time in which short GRBs were considered to originate in neutron star–neutron star (NS–NS) binaries, while long GRBs were considered to originate in single events,⁸ e.g., *collapsars* (Woosley 1993; MacFadyen & Woosley 1999; MacFadyen et al. 2001; Woosley & Bloom 2006; see, however, Ruffini et al. 2018b) and *magnetars* (Usov 1992; Dai & Lu 1998a, 1998b; Kluźniak & Ruderman 1998; Zhang & Mészáros 2001; see, however, Ruffini et al.

2016b). Thus, only short GRBs have been up to now considered to estimate the simultaneous detection rate of GWs and GRBs. For instance, Wanderman & Piran (2015) used the luminosity function of short GRBs observed by *Swift*; Yonetoku et al. (2014), by BATSE; Patricelli et al. (2016), by *Fermi*; and Ghirlanda et al. (2016), by *Swift* and *Fermi*.

In our recent works (see Ruffini et al. 2016b, and references therein) we have introduced a new classification in which all GRBs, namely, both long and short, originate from merging and/or accreting binary systems, each composed of a different combination of carbon–oxygen cores (CO_{core}), NSs, black holes (BHs), and white dwarfs (WDs). For each system the initial state and the final state are here referred to as “in-state” and “out-state,” respectively. This opens an ample new scenario for the role of GWs both as detectable sources and as a determining factor in the coalescence process of the GRB progenitors.

We interpret the traditional long GRBs within the induced gravitational collapse (IGC) paradigm (Ruffini et al. 2006, 2007, 2008, 2015b; Izzo et al. 2012a; Rueda & Ruffini 2012; Fryer et al. 2014) that proposes as in-state a tight binary system composed of a CO_{core} undergoing a supernova (SN) explosion and a companion compact object, e.g., an NS (or a BH). The SN explosion triggers a hypercritical accretion onto the NS companion, whose details have been studied, simulated, and presented in several publications (see, e.g., Fryer et al. 2014, 2015b; Becerra et al. 2015, 2016, and references therein;

⁸ With the exception of the binary progenitors proposed in Fryer & Woosley (1998), Fryer et al. (1999a, 1999b), and Belczynski et al. (2002).

Appendix A). Depending on the binary parameters, the hypercritical accretion can lead to three very different outcomes:

- I. X-ray flashes (XRFs) with isotropic energy $E_{\text{iso}} \lesssim 10^{52}$ erg and rest-frame spectral peak energy $E_{p,i} \lesssim 200$ keV. This class occurs in CO_{core}-NS binaries when the hypercritical accretion onto the NS companion is not enough to induce gravitational collapse into a BH (Becerra et al. 2015, 2016). Following this definition, Ruffini et al. (2016b) estimated for the XRF a local observed rate of $\rho_{\text{XRF}} = 100^{+45}_{-34} \text{ Gpc}^{-3} \text{ yr}^{-1}$ (Ruffini et al. 2016b). This rate is in agreement with that of low-luminosity long GRBs, e.g., $325^{+352}_{-177} \text{ Gpc}^{-3} \text{ yr}^{-1}$ (Liang et al. 2007), $\sim 200 \text{ Gpc}^{-3} \text{ yr}^{-1}$ (Virgili et al. 2009), and $164^{+98}_{-65} \text{ Gpc}^{-3} \text{ yr}^{-1}$ (Sun et al. 2015). After the SN explosion, the binary can either get disrupted or remain bound depending on the mass loss and/or natal kick imparted to the system (see Postnov & Yungelson 2014, references therein; Appendix A.5). In the former case the XRF leads to two runaway NSs, while in the latter one the out-states of XRFs are binaries composed of a newly formed $\sim 1.4\text{--}1.5 M_{\odot}$ NS (hereafter ν NS) born in the SN explosion and a massive NS (MNS) that accreted matter from the SN ejecta. Typical periods of these binaries are $P_{\text{orb}} \gtrsim 30$ minutes (Becerra et al. 2016).
- II. Binary-driven hypernovae (BdHNe) with $E_{\text{iso}} \gtrsim 10^{52}$ erg and $E_{p,i} \gtrsim 200$ keV. BdHNe occur in more compact CO_{core}-NS binaries, which leads to a more massive hypercritical accretion onto the NS, hence leading to BH formation. Following this definition, Ruffini et al. (2016b) estimated for the BdHNe a local observed rate $\rho_{\text{BdHN}} = 0.77^{+0.09}_{-0.08} \text{ Gpc}^{-3} \text{ yr}^{-1}$ (Ruffini et al. 2016b). This rate is in agreement with that for high-luminosity long GRBs, e.g., $1.3^{+0.6}_{-0.7} \text{ Gpc}^{-3} \text{ yr}^{-1}$ (Wanderman & Piran 2010) and $0.8^{+0.1}_{-0.1} \text{ Gpc}^{-3} \text{ yr}^{-1}$ (Sun et al. 2015). As in the case of XRFs, the SN explosion can disrupt the binary depending on the mass loss and/or natal kick. In the case when the system remains bound, the out-states of BdHNe are ν NS-BH binaries (see Fryer et al. 2015b; Appendix A.5). Typical periods of these binaries are 5 minutes $\lesssim P_{\text{orb}} \lesssim 30$ minutes (Becerra et al. 2016).
- III. BH-SNe with $E_{\text{iso}} \gtrsim 10^{54}$ erg and $E_{p,i} \gtrsim 2$ MeV. BH-SNe occur in close CO_{core} (or helium or Wolf-Rayet star)-BH binaries (Ruffini et al. 2001) in which the hypercritical accretion occurs onto a previously formed BH. Such BH-SN systems correspond to the late evolutionary stages of X-ray binaries such as Cyg X-1 (Giacconi & Ruffini 1978; Belczynski et al. 2011) or microquasars (Mirabel & Rodríguez 1998). These systems might be also formed following the binary evolutionary patch leading to scenario XI in Fryer et al. (1999a). Since the estimated rate of BdHNe covers systems with the above E_{iso} and $E_{p,i}$ range, we can adopt the rate of BdHNe as an upper limit to the rate of BH-SNe, i.e., $\rho_{\text{BH-SN}} \lesssim \rho_{\text{BdHN}} = 0.77^{+0.09}_{-0.08} \text{ Gpc}^{-3} \text{ yr}^{-1}$ (Ruffini et al. 2016b). As in the above cases of XRFs and BdHNe, the SN explosion may disrupt the binary. If the binary survives, then the out-states of BH-SNe can be a ν NS-BH or a BH-BH if the SN central remnant directly collapses to a BH. However, the latter scenario is currently ruled out by the observations of pre-SN cores

that appear to have masses $\lesssim 18 M_{\odot}$, very low to lead to direct BH formation (see, e.g., Smartt 2009, 2015, for details).

In the current literature such a difference between an XRF, a BdHN, and a BH-SN in the evaluation of GWs, here implemented, is still missing.

We turn now to the short bursts. Although their progenitors are still under debate, there is an ample consensus in the scientific community that they originate from NS-NS and/or NS-BH merging binaries (see, e.g., Goodman 1986; Paczynski 1986; Eichler et al. 1989; Narayan et al. 1991; Meszaros & Rees 1997; Rosswog et al. 2003; Lee et al. 2004; Berger 2014). By adopting the same in-states as in the above traditional models, namely, NS-NS and/or NS-BH mergers, they can be divided into three subclasses (Fryer et al. 2015b; Ruffini et al. 2015a, 2016b):

Short gamma-ray flashes (S-GRFs), with $E_{\text{iso}} \lesssim 10^{52}$ erg and $E_{p,i} \lesssim 2$ MeV, occur when no BH is formed in the NS-NS merger, i.e., they lead to an MNS. Following this definition, Ruffini et al. (2016b) estimated for the S-GRFs a local observed rate $\rho_{\text{S-GRF}} = 3.6^{+1.4}_{-1.0} \text{ Gpc}^{-3} \text{ yr}^{-1}$.

Authentic short GRBs (S-GRBs), with $E_{\text{iso}} \gtrsim 10^{52}$ erg and $E_{p,i} \gtrsim 2$ MeV, occur when a BH is formed in the NS-NS merger (Muccino et al. 2013; Ruffini et al. 2015a, 2016a). Following this definition, Ruffini et al. (2016b) estimated for the S-GRBs a local observed rate $\rho_{\text{S-GRB}} = (1.9^{+1.8}_{-1.1}) \times 10^{-3} \text{ Gpc}^{-3} \text{ yr}^{-1}$ (Ruffini et al. 2016b).

Ultrashort GRBs (U-GRBs), a new subclass of short bursts originating from ν NS-BH merging binaries. They can originate from BdHNe (see subclass II above) or from BH-SN events (see subclass III above). Since in Fryer et al. (2015b) it was shown that the majority of BdHN out-states remain bound, we can assume as an upper limit of their local density rate $\rho_{\text{U-GRB}} \approx \rho_{\text{BdHN}} = 0.77^{+0.09}_{-0.08} \text{ Gpc}^{-3} \text{ yr}^{-1}$ (Ruffini et al. 2016b). U-GRBs are yet unobserved/unidentified and present a great challenge not only in the case of high energy but also possibly in the radio band, where they could manifest themselves, prior to the merger phase, as pulsar-BH binaries (see, e.g., Tauris et al. 2015a, and references therein).

It is important to mention that the sum of the occurrence rates of the above short burst subclasses IV-VI is in agreement with the estimates obtained from the whole short burst population reported in the literature (see, e.g., Sun et al. 2015; Wanderman & Piran 2015). It is then clear that what in the current literature are indicated as short GRBs are actually just S-GRFs.

In addition to the above three subclasses of long bursts and three subclasses of short bursts, we recall the existence of a class of bursts occurring in a low-density circumburst medium (CBM), e.g., $n_{\text{CBM}} \sim 10^{-3} \text{ cm}^{-3}$, which show hybrid properties between short and long bursts in γ -rays. These bursts are not associated with SNe, even at low redshift, where the SN detection would not be precluded (Della Valle et al. 2006). We have called such bursts gamma-ray flashes (GRFs; Ruffini et al. 2016b).

GRFs have $10^{51} \text{ erg} \lesssim E_{\text{iso}} \lesssim 10^{52} \text{ erg}$ and $0.2 \text{ MeV} \lesssim E_{p,i} \lesssim 2 \text{ MeV}$. These bursts, which show an extended and softer emission, are thought to originate in NS-WD mergers (Ruffini et al. 2016b). NS-WD binaries are notoriously

common astrophysical systems (Cadelano et al. 2015), and possible evolutionary scenarios leading to such mergers have been envisaged (see, e.g., Fryer et al. 1999b; Tauris et al. 2000; Lazarus et al. 2014).⁹ GRFs form an MNS and not a BH (see Ruffini et al. 2016b, for details). Following this definition, Ruffini et al. (2016b) estimated for the GRFs a local observed rate $\rho_{\text{GRF}} = 1.02_{-0.46}^{+0.71} \text{ Gpc}^{-3} \text{ yr}^{-1}$ (Ruffini et al. 2016b). This density rate appears to be low with respect to the current number of known NS–WD binaries in the Galaxy (see, e.g., Cadelano et al. 2015). From the GRB side, we note that indeed only one NS–WD merger has been identified (see analysis of GRB 060614 in Caito et al. 2009). The above implies that, very likely, the majority of the expected mergers are under the threshold of the existing X-ray and gamma-ray detectors.

The aforementioned density rates for all GRB subclasses have been estimated in Ruffini et al. (2016b) assuming no beaming. The presence of beaming would require the observation of achromatic jet breaks in the afterglow light curve. In the present case of short bursts such clear achromatic jet breaks have never been observed. Fong et al. (2015) reported four measured jet breaks in a sample of 11 short bursts: GRB 051221A, GRB 090426A, GRB 111020A, and GRB 130603B (see Table 5 there). However:

(1) GRB 051221A: The break is inferred only from the X-ray light curve, while the contemporary optical and radio data do not support such an interpretation (see Soderberg et al. 2006a).

(2) GRB 090426A: The break is inferred from the optical band only, and there are no contemporary observations in other bands (see Nicuesa Guelbenzu et al. 2011).

(3) GRB 111020A: The break is inferred only from the X-ray light curve, but this interpretation is based on a single upper limit by *Chandra* and no data points (see Fong et al. 2012).

(4) GRB 130603B: The break is inferred from the optical band and is compatible with the radio data. However, contemporary X-ray observations are clearly contradicting this interpretation and present no break at all. In fact, the authors invoke the presence of an extra source to justify what they call “late time X-ray excess” (see Fong et al. 2014).

In addition, Aimuratov et al. (2017a) and Ruffini et al. (2018a) have shown that, in all the identified S-GRBs, the GeV emission has been always observed when the source was within the *Fermi*-LAT field of view. This result points as well to no significant presence of beaming in the GeV emission of S-GRBs.

Therefore, all the above points imply that there is still no evidence for the need to assume beaming.

We show in Table 1 a summary of the astrophysical aspects related to the GRB subclasses and their observational properties.

The aim of this article is to use the rate of occurrence of the above GRB subclasses to assess the detectability of their associated GW emission by the ground-based interferometers

⁹ An additional (but less likely) scenario leading to merging NS–WD systems might occur in an NS–NS approaching the merger phase (Ruffini et al. 2016b). According to Bildsten & Cutler (1992) and Clark & Eardley (1977) (see also references therein), in a very close, NS–NS binary with unequal-mass components, stable mass transfer from the less massive to the more massive NS might occur for appropriate mass ratios in such a way that the donor NS moves outward in the mass-loss process until it reaches the beta-decay instability becoming a low-mass WD.

Advanced LIGO and Advanced Virgo, by the space-based interferometer eLISA, and by the resonant bars, for completeness.

We show in Table 2 a summary of acronyms used in this work.

2. Relevance of the NS Structure and Critical Mass

Having introduced the above seven subclasses of GRBs, the relevance of the NS physics becomes clear, in particular the NS critical mass value, in the definition of subclasses I–II and IV–V.

First, we recall that in our previous works we have adopted an NS critical mass within the range $2.2\text{--}3.4 M_{\odot}$, depending on the equation of state (EOS) and on the NS angular momentum (Belvedere et al. 2014; Becerra et al. 2015; Cipolletta et al. 2015). These quoted values are for EOSs based on relativistic nuclear mean-field models (in this case the NL3, TM1, and GM1 models) and for an NS angular momentum from $J=0$ up to $J_{\text{max}} \approx 0.7GM^2/c$ (Cipolletta et al. 2015). Hereafter, we adopt the stiffest model, namely, the NL3 EOS, which leads to the largest NS critical mass: from $M_{\text{crit}} \approx 2.7 M_{\odot}$ at $J=0$, which, as expected, is lower than the nonrotating critical mass upper limit of $3.2 M_{\odot}$ established by Rhoades & Ruffini (1974), to $M_{\text{crit}} \approx 3.4 M_{\odot}$ at J_{max} (Cipolletta et al. 2015). Our choice of relativistic mean-field theory models is based on the fact that they satisfy important properties such as Lorentz covariance, relativistic self-consistency (hence they do not violate causality), intrinsic inclusion of spin, and a simple mechanism of nuclear matter saturation (see, e.g., Dutra et al. 2014, 2016, for further details on these kinds of models). The above three representative EOSs that we have explored satisfy in addition the astrophysical constraint of leading to an NS critical mass larger than the heaviest massive NS observed, PSR J0348+0432, with $M = 2.01 \pm 0.04 M_{\odot}$ (Antoniadis et al. 2013).

As discussed in Ruffini et al. (2016b), the separatrix energy value of $\approx 10^{52}$ erg between subclasses I and II appears as a theoretical estimate of the upper limit to the energy emitted in the hypercritical accretion process onto a $\sim 1.4 M_{\odot}$ NS (see, e.g., Becerra et al. 2016) and the aforementioned adopted critical mass. This has been shown to be in agreement with the observations of 20 XRFs and 233 BdHNe (up to the end of 2014). In fact, observationally, the current upper limit for XRFs is $(7.3 \pm 0.7) \times 10^{51}$ erg, and the lower limit for BdHNe is $(9.2 \pm 1.3) \times 10^{51}$ erg (see Ruffini et al. 2016b, for further details). It is clear that the separatrix energy should have some dependence on the initial NS mass undergoing accretion and on the precise value of the nonrotating critical mass. Although the precise value of the latter is yet unknown, it is constrained within the range $2.0\text{--}3.2 M_{\odot}$, where the lower value is the mass of PSR J0348+0432 and the upper value is the well-established absolute maximum NS mass of Rhoades & Ruffini (1974).

It is clear that similar arguments apply also to the case of subclasses IV and V (Ruffini et al. 2015a), namely, the amount of energy emitted during the NS–NS merger leading to a BH should be $\gtrsim 10^{52}$ erg. Observationally, the current upper limit for S-GRFs is $(7.8 \pm 1.0) \times 10^{51}$ erg, and the lower limit for BdHNe is $(2.44 \pm 0.22) \times 10^{52}$ erg (see Ruffini et al. 2016b, for further details).

The above subclassification is further supported by the fact that GeV emission, expected in the presence of a rotating BH, is indeed observed only in BdHNe (e.g., Ruffini et al. 2015b) and in S-GRBs (e.g., Muccino et al. 2013; Ruffini et al. 2015a,

Table 1
Summary of the Astrophysical Aspects of the Different GRB Subclasses and of Their Observational Properties

Subclass	In-state	Out-state	$E_{\text{P},i}$ (MeV)	E_{iso} (erg)	$E_{\text{iso},X}$ (erg)	$E_{\text{iso,GeV}}$ (erg)	z_{max}	ρ_{GRB} (Gpc ⁻³ yr ⁻¹)	
I	XRFs	CO _{core} -NS	ν NS-NS	$\lesssim 0.2$	$\sim 10^{48}-10^{52}$	$\sim 10^{48}-10^{51}$...	1.096	100^{+45}_{-34}
II	BdHNe	CO _{core} -NS	ν NS-BH	$\sim 0.2-2$	$\sim 10^{52}-10^{54}$	$\sim 10^{51}-10^{52}$	$\lesssim 10^{53}$	9.3	$0.77^{+0.09}_{-0.08}$
III	BH-SN	CO _{core} -BH	ν NS-BH	$\gtrsim 2$	$> 10^{54}$	$\sim 10^{51}-10^{52}$	$\gtrsim 10^{53}$	9.3	$\lesssim 0.77^{+0.09}_{-0.08}$
IV	S-GRFs	NS-NS	MNS	$\lesssim 2$	$\sim 10^{49}-10^{52}$	$\sim 10^{49}-10^{51}$...	2.609	$3.6^{+1.4}_{-1.0}$
V	S-GRBs	NS-NS	BH	$\gtrsim 2$	$\sim 10^{52}-10^{53}$	$\lesssim 10^{51}$	$\sim 10^{52}-10^{53}$	5.52	$(1.9^{+1.8}_{-1.1}) \times 10^{-3}$
VI	U-GRBs	ν NS-BH	BH	$\gtrsim 2$	$> 10^{52}$	$\gtrsim 0.77^{+0.09}_{-0.08}$
VII	GRFs	NS-WD	MNS	$\sim 0.2-2$	$\sim 10^{51}-10^{52}$	$\sim 10^{49}-10^{50}$...	2.31	$1.02^{+0.71}_{-0.46}$

Note. In the first four columns we indicate the GRB subclasses and their corresponding in-states and out-states. In the fifth through eighth columns we list the ranges of $E_{\text{P},i}$ and E_{iso} (rest-frame $1-10^4$ keV), $E_{\text{iso},X}$ (rest-frame 0.3–10 keV), and $E_{\text{iso,GeV}}$ (rest-frame 0.1–100 GeV). The ninth and tenth columns list, for each GRB subclass, the maximum observed redshift and the local observed rate ρ_{GRB} obtained in Ruffini et al. (2016b). We refer the reader to Appendix B for details on the method used to calculate ρ_{GRB} .

Table 2
Acronyms Used in This Work in Alphabetic Order

Extended Wording	Acronym
Binary-driven hypernova	BdHN
Black hole	BH
Carbon-oxygen core	CO _{core}
Gamma-ray burst	GRB
Gamma-ray flash	GRF
Induced gravitational collapse	IGC
Massive neutron star	MNS
Neutron star	NS
New neutron star created in the SN explosion	ν NS
Short gamma-ray burst	S-GRB
Short gamma-ray flash	S-GRF
Supernova	SN
Ultrashort gamma-ray burst	U-GRB
White dwarf	WD
X-ray flash	XRF

2016a; Aimuratov et al. 2017b) and absent in XRFs and S-GRFs where no BH is formed (see Figure 10 and the Appendix in Ruffini et al. 2016b, for more details).

Therefore, the direct observation of the separatrix energy between XRFs and BdHNe, as well as between S-GRFs and S-GRBs, and their precise occurrence rate ratio give crucial information on the actual NS critical mass value.

3. Ingredient Setup for the Computation of the GW Emission and Its Detectability

We have recalled in Section 1 that the evolution of the binary progenitors of both short and long GRBs leads to compact binaries that will eventually merge in a characteristic timescale and emit GWs. We turn in the following sections to assessing the detectability of the GW emission by these merging binaries by Advanced LIGO.

In order to do this, we make the following drastic simplified assumptions:

1. Although it is manifest that the release of gravitational energy of the system in the merger phase is dominated by the X-ray, gamma-ray, and GeV emission (see Table 1), we assume that the binary dynamics is only driven by the GW emission.

2. Consistent with the above GW emission dominance assumption, we further assume that the GW waveform is known and thus one can use the matched filtering technique to estimate the signal-to-noise ratio. The actual GW waveform under the realistic conditions of electromagnetic emission dominance is still unknown.
3. To estimate the maximum distance of GW detectability, we adopt optimally oriented sources with respect to the detector.

The above assumptions are made with the only aim of establishing an absolute upper limit to the GW emission and its putative detectability under the most optimistic conditions. Similarly, we assume that the binarity of the system does not compromise the interior structure of the NS (see Section 2).

The minimum GW frequency detectable by the broadband Advanced LIGO interferometer is $f_{\text{min}}^{\text{aLIGO}} \approx 10$ Hz (LIGO Scientific Collaboration et al. 2015). Since during the binary inspiral the GW frequency is twice the orbital one, the above implies that a binary is inside the Advanced LIGO band for orbital periods $P_{\text{orb}} \lesssim 0.2$ s.

3.1. Systems to Be Analyzed

The CO_{core}-NS binaries, in-states of XRFs and BdHNe, and CO_{core}-BH binaries, in-states of BH-SNe, are not detectable by Advanced LIGO since they have orbital periods $P_{\text{orb}} \gtrsim 5$ minutes $\gg 0.2$ s (Becerra et al. 2016). After their corresponding hypercritical accretion processes, it is clear that the out-states of both XRFs and BdHNe can become the in-states of short GRBs, as follows (Becerra et al. 2015; Fryer et al. 2015b; Ruffini et al. 2016b).

First, let us discuss the out-states of XRFs. We have mentioned that XRFs can either get disrupted by the SNe and lead to runaway NSs or, in the case in which the binary remains bound, lead to a ν NS-NS system. Since $\rho_{\text{XRF}} > \rho_{\text{S-GRF}} + \rho_{\text{S-GRB}}$, such ν NS-NS binaries, out-states of XRFs, could be the in-states of S-GRFs (NS-NS mergers leading to an MNS) and/or S-GRBs (NS-NS mergers leading to a BH). By denoting the total rate of short bursts as $\rho_{\text{short}} \equiv \rho_{\text{S-GRF}} + \rho_{\text{S-GRB}}$, our estimated rates would imply that the fraction of systems that appear to remain bound as ν NS-NS is $(\rho_{\text{short}}/\rho_{\text{XRF}}) \approx 2\%-8\%$, while 92%–98% of XRFs are disrupted by the SN explosion. Interestingly, this is consistent with the fraction of bound NS-NS obtained in population synthesis analyses (see, e.g., Dominik et al. 2012, 2015; Postnov & Yungelson 2014; Fryer et al. 2015a; Belczynski

et al. 2016, and references therein; Appendix A.4 and A.5). Therefore, these merging ν NS–NS binaries are clearly included in the S-GRF and S-GRB population. Such binaries are at birth undetectable by Advanced LIGO since they have initially $P_{\text{orb}} \gtrsim 5$ minutes $\gg 0.2$ s, but their merging can become detectable.

We have already recalled in the Introduction that in Fryer et al. (2015b) it was shown that, contrary to the case of XRFs, most BdHNe are expected to remain bound after the SN explosion in view of their short orbital periods and more massive accretion process. We have argued that those mergers would lead to the new class of short bursts, the U-GRBs (Fryer et al. 2015b), which, however, have still to be electromagnetically identified. The same applies to the ν NS–BH systems produced by BH–SN systems, with the only difference being the mass of the BH, which, by definition of this subclass, can be larger than the NS critical mass since this BH is formed from direct collapse of a massive star. All the above merging ν NS–BH binaries are, by definition, the U-GRB population. Such binaries are at birth undetectable by Advanced LIGO because their initial orbital periods $P_{\text{orb}} \gtrsim 5$ minutes $\gg 0.2$ s, but their merger can become detectable.

In the case of NS–WD binaries, the WD large radius and its very likely tidal disruption by the NS make their GW emission hard to detect (see, e.g., Paschalidis et al. 2009). Thus, we do not consider NS–WD binaries in the following GW discussion.

To summarize, we are going to analyze below the GW emission and detectability of S-GRF and S-GRB, the mergers of ν NS–NS produced by XRFs, as well as of U-GRBs, which are the mergers of the ν NS–BH produced by BdHNe and BH–SNe.

3.2. Binary Component Masses

For S-GRFs, we consider the simple case of nonspinning, equal-mass NS–NS merging binaries, i.e., $m_1 = m_2 = m$. The precise value of the merging NS masses leading to a BH is still poorly known; thus, we have chosen as an upper limit roughly half the maximum NS critical mass (see Section 2). Thus, we shall explore mass values $m \approx 1\text{--}1.7 M_{\odot}$.

For S-GRBs, we also consider nonspinning, equal-mass NS–NS merging binaries. For self-consistency, we choose a range of component masses starting from the upper edge of the S-GRF one, i.e., $m \approx 1.7 M_{\odot}$, up to the maximum nonrotating stable mass, i.e., $m \approx 2.8 M_{\odot}$.

For U-GRBs, we adopt in the case of out-states of BdHNe $m_1 = 1.5 M_{\odot}$ for the ν NS and $m_{\text{BH}} = 2.7\text{--}3.4 M_{\odot}$ for the BH (see Section 2). In the case of out-states of BH–SNe, we adopt $m_1 = 1.5 M_{\odot}$ for the ν NS and $m_{\text{BH}} = 3.4\text{--}10 M_{\odot}$ for the BH, consistent with the assumption that the BH in this subclass has been previously formed in the binary evolution and therefore it can have a mass larger than the NS critical mass.

3.3. Signal-to-noise Ratio

We first recall the main ingredients needed to estimate the detectability of the aforementioned merging binaries associated with the different GRB classes. The signal $h(t)$ induced in the detector is

$$h(t) = F_+(\theta, \phi, \psi)h_+(t, \iota, \beta) + F_{\times}(\theta, \phi, \psi)h_{\times}(t, \iota, \beta), \quad (1)$$

where h_+ and h_{\times} are the two polarizations of the GW; ι and β are the polar and azimuthal angles of the unit vector from the

source to the detector, relative to a coordinate system centered in the source. The detector pattern functions F_+ and F_{\times} depend on the localization of the source with respect to the detector, i.e., they depend on the spherical polar angles θ and ϕ of the source relative to a coordinate system centered in the detector. The pattern functions also depend on the polarization angle ψ .

Since the GW signal might be deep inside the noise, the signal-to-noise ratio, denoted hereafter by ρ , is usually computed using the matched filter technique, i.e. (Flanagan & Hughes 1998),

$$\rho^2 = 4 \int_0^{\infty} \frac{|\tilde{h}(f)|^2}{S_n(f)} df, \quad (2)$$

where f is the GW frequency in the detector's frame, $\tilde{h}(f)$ is the Fourier transform of $h(t)$, and $\sqrt{S_n(f)}$ is the one-sided amplitude spectral density (ASD) of the Advanced LIGO noise. We recall that in the detector's frame the GW frequency is redshifted by a factor of $1+z$ with respect to the one in the source's frame, f_s , i.e., $f = f_s/(1+z)$.

The exact position of the binary relative to the detector and the orientation of the binary rotation plane are usually unknown; thus, it is a common practice to estimate the signal-to-noise ratio averaging over all the possible locations and orientations, i.e.,

$$\langle \rho^2 \rangle = 4 \int_0^{\infty} \frac{\langle |\tilde{h}(f)|^2 \rangle}{S_n(f)} df = 4 \int_0^{\infty} \frac{h_c^2(f)}{f^2 S_n(f)} df, \quad (3)$$

with $h_c(f)$ the characteristic strain (Flanagan & Hughes 1998)

$$h_c = \frac{(1+z)}{\pi d_l} \sqrt{\frac{\langle F_+^2 \rangle}{2} \frac{G}{c^3} \frac{dE}{df_s} [(1+z)f]}, \quad (4)$$

where

$$d_l = \frac{(1+z)c}{H_0} \int_0^z [\Omega_M(1+x)^3 + \Omega_{\Lambda}]^{-1/2} dx \quad (5)$$

is the source luminosity distance and we have used the fact that $\langle F_+^2 \rangle = \langle F_{\times}^2 \rangle$ and $\langle F_+ F_{\times} \rangle = 0$. We recall that $\langle F_+^2 \rangle = 1/5$ for an interferometer and $\langle F_+^2 \rangle = 4/15$ for a resonant bar (see, e.g., Maggiore 2007). We adopt a Λ CDM cosmology with $H_0 = 71 \text{ km s}^{-1} \text{ Mpc}^{-1}$, $\Omega_M = 0.27$, and $\Omega_{\Lambda} = 0.73$ (Rigault et al. 2015). It is important to recall that, as we have mentioned, we are interested in estimating the GW detectability under the most optimistic conditions. Thus, to estimate the maximum distance of GW detectability, we adopt in Section 3 the ansatz of optimally oriented sources with respect to the detector. The above averaging procedure is here used with the only aim of giving an estimate of the GW strain amplitude, h_c , compared and contrasted below in Section 5 with the detector's strain noise.

4. GW Energy Spectrum

In general, a GW-driven binary system evolves in time through two regimes: the first is the *inspiral regime*, and the second, which we refer hereafter to as the *merger regime*, is composed in the most general case of the final plunge, the merger, and the ringdown (oscillations) of the newly formed object.

4.1. Inspiral Regime

During the inspiral regime, the system evolves describing quasi-circular orbits, and it is well described by the traditional point-like quadrupole approximation (Peters & Mathews 1963; Peters 1964; Rees et al. 1974; Landau & Lifshitz 1975). The GW frequency is twice the orbital frequency ($f_s = 2f_{\text{orb}}$) and grows monotonically. The energy spectrum during the inspiral regime is

$$\frac{dE}{df_s} = \frac{1}{3}(\pi G)^{2/3} M_c^{5/3} f_s^{-1/3}, \quad (6)$$

where $M_c = \mu^{3/5} M^{2/5} = \nu^{3/5} M$ is the called *chirp mass*, $M = m_1 + m_2$ is the total binary mass, $\mu = m_1 m_2 / M$ is the reduced mass, and $\nu \equiv \mu / M$ is the symmetric mass-ratio parameter. A symmetric binary ($m_1 = m_2$) corresponds to $\nu = 1/4$, and the test-particle limit is $\nu \rightarrow 0$. The total energy emitted during this regime can be estimated as the difference of the energy of the binary between infinity and the one at the last circular orbit (LCO). For a test particle in the Schwarzschild background the LCO is located at $r_{\text{LCO}} = 6GM/c^2$, its energy is $\sqrt{8/9} \mu c^2$, and then

$$\Delta E_{\text{insp}} = (1 - \sqrt{8/9}) \mu c^2. \quad (7)$$

4.2. Merger Regime

The GW spectrum of the merger regime is characterized by a GW burst (see, e.g., Davis et al. 1971; Shibata & Taniguchi 2011; Bernuzzi et al. 2015). Thus, to estimate whether this part of the signal contributes to the signal-to-noise ratio, it is sufficient to estimate the location of the GW burst in the frequency domain and its energy content. We recall that, in general, the merger regime is composed of plunge+merger+ringdown. The frequency range spanned by the GW burst is $\Delta f = f_{\text{qnm}} - f_{\text{merger}}$, where f_{merger} is the frequency at which the merger starts and f_{qnm} is the frequency of the ringing modes of the newly formed object after the merger, and the energy emitted is ΔE_{merger} . With these quantities defined, we can estimate the typical value of the merger regime spectrum as

$$\left(\frac{dE}{df_s} \right)_{\text{merger}} \sim \frac{\Delta E_{\text{merger}}}{\Delta f}. \quad (8)$$

Numerical relativity simulations (e.g., Shibata & Taniguchi 2011; Bernuzzi et al. 2015) show that finite size effects might end the inspiral regime before the LCO. After this point, the GW spectrum damps exponentially. For the case of NS–NS the merger starts in an orbit larger than the LCO, and for the case of an NS–BH, as we will see below, the merger can occur below the LCO, making the spectrum similar to a BH–BH merger. When the merger occurs well before the LCO, there is no plunge. Therefore, the emitted energy will be less than the case when the plunge is present. We can therefore obtain an upper limit to ΔE_{merger} by adopting the energy emitted during the plunge-merger-ringdown of a BH–BH merger (Detweiler & Szedenis 1979)

$$\Delta E_{\text{merger}} \approx 0.5 \nu^2 M c^2. \quad (9)$$

To complete the estimate of the merger regime spectrum, we have to estimate the value of Δf in the different cases of interest.

4.2.1. NS–NS Merger

The approach to the merger point, $r = r_{\text{merger}}$, depends on the nature of the binary system. Typically, the merger is assumed to start at the point of maximum GW strain (see, e.g., Bernuzzi et al. 2015, and references therein). However, since the transition from a binary system to a single merged object is not sharply definable, different definitions of the merger point in the literature can be found (see, e.g., Kawaguchi et al. 2015). For our purpose it is sufficient to estimate the frequency at “contact,” namely, the frequency at a binary separation $r_{\text{contact}} \approx r_1 + r_2$, where r_i is the radius of the i -component. This certainly sets a lower limit to the frequency at maximum strain at merger, i.e., $r_{\text{contact}} \gtrsim r_{\text{merger}}$. Thus, we adopt for these systems

$$f_{\text{merger}}^{\text{NS-NS}} \approx f_{\text{contact}}^{\text{NS-NS}} = \frac{1}{\pi} \frac{c^3}{GM} \left[\frac{C_1 C_2 (1+q)}{C_1 + q C_2} \right]^{3/2}, \quad (10)$$

where $q = m_2/m_1$ is the mass ratio, which is related to the symmetric mass-ratio parameter by $\nu = q/(1+q)^2$, and $C_i \equiv Gm_i/c^2 r_i$ is the compactness of the i -component.

For a mass-symmetric NS–NS binary, we have that $f_{\text{contact}}^{\text{NS-NS}} \approx (1/\pi)(c^3/G)C_{\text{NS}}^3/M$, where $C_{\text{NS}} \equiv C_1 = C_2$ is the compactness parameter of the initial NS. For example, for the NL3 EOS, the NS compactness lies in the range $C_{\text{NS}} \approx 0.14\text{--}0.3$ for an NS mass $1.4\text{--}2.8 M_{\odot}$ (see, e.g., Cipolletta et al. 2015). Thus, using the same EOS, we have, for an $M = (1.4 + 1.4) M_{\odot} = 2.8 M_{\odot}$ binary, $f_{\text{contact}}^{\text{NS-NS}} \approx 1.34$ kHz and, for an $M = (2.0 + 2.0) M_{\odot} = 4.0 M_{\odot}$ binary, $f_{\text{contact}}^{\text{NS-NS}} \approx 1.43$ kHz.

In the merger regime either a BH or an MNS can be formed. If the merger does not lead to a BH, the merger frequency is dominated by the frequency of the quasi-normal modes of the MNS formed. This frequency is of the order of

$$f_{\text{qnm}}^{\text{MNS}} \approx \frac{1}{\pi} \left(\frac{GM}{R^3} \right)^{1/2} = \frac{1}{\pi} \left(\frac{c^3}{G} \right) \frac{C_{\text{MNS}}^{3/2}}{M}, \quad (11)$$

where R is the radius of the MNS and $C_{\text{MNS}} \equiv GM/(c^2 R)$ is its compactness. Thus, in the case of S-GRFs the value of Δf is

$$\begin{aligned} \Delta f_{\text{S-GRF}} &\equiv f_{\text{qnm}}^{\text{MNS}} - f_{\text{contact}}^{\text{NS-NS}} \\ &\approx (C_{\text{MNS}}^{3/2} - C_{\text{NS}}^{3/2}) \frac{c^3}{\pi GM}. \end{aligned} \quad (12)$$

If the merger forms a BH, the merger frequency is dominated by the frequency of the quasi-normal modes of the BH formed, namely, the GW-burst spectrum peaks at the frequency (Davis et al. 1971, 1972)

$$f_{\text{qnm}}^{\text{BH}} \approx \frac{0.32}{2\pi} \frac{c^3}{GM}, \quad (13)$$

i.e., $f_{\text{qnm}} \approx 3.4$ kHz for a Schwarzschild BH of $3 M_{\odot}$. In the case of a rotating BH, namely, a Kerr BH, the peak frequency shifts to higher values (Detweiler 1980). Thus, the value of $f_{\text{qnm}}^{\text{BH}}$ given by Equation (13) can be considered as a lower bound to the actual peak frequency. Thus, in the case of

S-GRBs the value of Δf is

$$\begin{aligned} \Delta f_{\text{S-GRB}} &\equiv f_{\text{qnm}}^{\text{BH}} - f_{\text{contact}}^{\text{NS-NS}} \\ &\approx (0.16 - C_{\text{NS}}^{3/2}) \frac{c^3}{\pi GM}. \end{aligned} \quad (14)$$

In either case of BH or MNS formation, $f_{\text{qnm}} > f_{\text{contact}}$ is satisfied. It can be checked that the above frequency estimates are consistent with values obtained from full numerical relativity simulations (see, e.g., Anninos et al. 1995; Bernuzzi et al. 2015).

4.2.2. NS–BH Merger

For an NS–BH merger, the approach to merger is different since general relativistic effects avoid the objects to go all the way to the “contact” point following circular orbits. For example, let us assume $m_1 = m_{\text{BH}} \approx 3 M_{\odot}$ and $m_2 = M_{\text{NS}} \approx 1.5 M_{\odot}$, so that $M = 1.5 + 3.0 M_{\odot} = 4.5 M_{\odot}$. In this case $r_1 = 2Gm_{\text{BH}}/c^2$ (for a Schwarzschild BH) and $r_2 = Gm_2/(c^2 C_2)$, so $r_{\text{contact}} \approx 3.3GM/c^2$. Within the test-particle limit, the LCO around a Schwarzschild BH occurs at $r_{\text{LCO}} = 6Gm_{\text{BH}}/c^2 \approx 6GM/c^2 > r_{\text{contact}}$. Thus, we have that $r_{\text{contact}} < r_{\text{LCO}}$, which suggests that an NS–BH binary, similar to the case of a BH–BH one, can pass from the inspiral regime, to the plunge from $r_{\text{plunge}} = r_{\text{LCO}}$ to merger at $r_{\text{merger}} \approx r_{\text{contact}}$, to the ringing of the newly formed BH. At r_{plunge} , the GW frequency is

$$f_{\text{plunge}}^{\text{NS-BH}} \approx \frac{1}{\pi} \left(\frac{GM}{r_{\text{LCO}}^3} \right)^{1/2} = \frac{1}{\pi 6^{3/2}} \left(\frac{c^3}{GM} \right), \quad (15)$$

and as in the previous case of BH formation from an NS–NS merger, the NS–BH post-merger GW spectrum will be dominated by frequencies given by Equation (13). Namely, for the present example $f_{\text{plunge}}^{\text{NS-BH}} \approx 980$ Hz and $f_{\text{qnm}}^{\text{BH}} \approx 2.3$ kHz.

Thus, in the case of NS–BH merger (U-GRB subclass), the value of Δf is

$$\Delta f_{\text{U-GRB}} \equiv f_{\text{qnm}}^{\text{BH}} - f_{\text{plunge}}^{\text{NS-BH}} \approx 0.092 \frac{c^3}{\pi GM}. \quad (16)$$

In the above analysis we have neglected the possibility that the NS can be tidally disrupted by the BH before it reaches $r = r_{\text{LCO}}$. The NS is disrupted by the BH if $r_{\text{LCO}} < r_{\text{td}}$, where r_{td} is the tidal disruption radius. The value of r_{LCO} and r_{td} for an NS–BH system depends both on the binary mass ratio $q \equiv m_2/m_1 \leq 1$ and on the NS compactness C_{NS} , which depends, in turn, on the NS mass and EOS. Numerical simulations of NS–BH binary mergers adopting a polytropic EOS for the NS matter suggest $r_{\text{td}} \approx 2.4q^{-1/3}R_{\text{NS}}$ and $r_{\text{LCO}} \approx 6GM/c^2[1 - 0.44q^{1/4}(1 - 3.54C_{\text{NS}})^{-2/3}]$ (see Shibata & Taniguchi 2011, and references therein). The ratio $r_{\text{td}}/r_{\text{LCO}}$ is a decreasing function of the BH mass for given NS mass (but always close to unity). If we extrapolate these results to BH masses in the range of 3–10 M_{\odot} and an NS of 1.5 M_{\odot} obeying the NL3 EOS, we have $r_{\text{LCO}} < r_{\text{td}}$ for $m_{\text{BH}} \lesssim 6 M_{\odot}$ and $r_{\text{LCO}} > r_{\text{td}}$ otherwise. It is clear that the specific range of NS and BH masses for which there is tidal disruption is highly sensitive to the compactness of the NS and hence to the nuclear EOS, and thus more simulations using a wide set of updated nuclear EOSs are needed to assess this issue. If tidal disruption

occurs, the inspiral regime will cut off at a GW frequency

$$f_{\text{td}}^{\text{NS-BH}} \approx \frac{1}{\pi} \left(\frac{GM}{r_{\text{td}}^3} \right)^{1/2}. \quad (17)$$

Since r_{td} is near r_{LCO} for our systems, and to not introduce further uncertainties in our estimates, we shall adopt that the inspiral regime of our NS–BH systems ends at the GW frequency given by Equation (15).

5. Characteristic Strain and Detector Sensitivity

From Equations (6) and (8) and with the knowledge of the energy released in GWs (Equation (9)) and the spanned frequencies in the merger regime (see Table 3), we can estimate the characteristic strain given by Equation (4), which can be compared and contrasted with the strain noise of GW detectors.

Figure 1 shows the GW signal ASD produced by S-GRFs, S-GRBs, and U-GRBs, obtained with the aid of Equation (4). In this figure we adopt a (1.4+1.4) M_{\odot} ν NS–NS merger for S-GRFs, a (2.0+2.0) M_{\odot} ν NS–NS merger for S-GRBs, a (1.5+3.0) M_{\odot} ν NS–BH merger for U-GRBs produced by out-states of BdHNe, and a (1.5+10.0) M_{\odot} ν NS–BH merger for U-GRBs produced by out-states of BH–SNe. We have assumed in this plot that these sources are located at the closest luminosity distance d_l at which each subclass has been observed (see Table 3 for details). We show the noise ASD of Advanced LIGO in the current run (O1) and in the expected 2022+ run (Abbott et al. 2016); the expected noise ASD of Advanced Virgo (BNS-optimized; Abbott et al. 2016); the expected noise ASD of the space-based interferometer eLISA for the N2A1, N2A2, and N2A5 configurations (see, e.g., Klein et al. 2016); and the noise ASD of the NAUTILUS bar detector for a 1 ms GW burst (Astone et al. 2006, 2008). Narrowband resonant bar detectors (such as ALLEGRO, AURIGA, EXPLORER, NAUTILUS, and NIOBE) are sensitive within a bandwidth of ~ 1 –10 Hz around the resonant frequency, which is typically $f_0 \sim 1$ kHz (see, e.g., Table 2 in Camp & Cornish 2004, for a summary of the properties of the bar detectors). The bar detector with the wider bandwidth is NAUTILUS, with a minimum strain spectral noise $\sqrt{S_n} = 10^{-21}$ Hz $^{-1/2}$ at $f_0 = 935$ Hz and $\sqrt{S_n} \leq 10^{-20}$ Hz $^{-1/2}$ in a bandwidth of ~ 30 Hz around f_0 (Astone et al. 2008). This implies that a 1 ms GW burst would be detected by this instrument if it has a strain amplitude $h \gtrsim 3 \times 10^{-19}$ (Astone et al. 2006, 2008).

From this figure we can conclude the following for the NS–NS and NS–BH binaries associated with S-GRFs, S-GRBs, and U-GRBs:

1. *Before merging*: they transit, during their inspiral regime which spans the frequency range $f < f_{\text{merger}}/(1+z)$ (see in Table 3 the frequencies and redshift), first the eLISA frequency band and then enter the Advanced LIGO–Virgo ones in the final orbits prior to the merging process (when $P_{\text{orb}} < 0.2$ s). The narrow bandwidth of the bar detectors does not cover these frequencies. For the adopted distances we see that the characteristic strain generated by all these sources is below the sensitivity of eLISA. S-GRFs are below the sensitivity of Advanced LIGO (O1), Advanced Virgo, and NAUTILUS, but inside the sensitivity of Advanced LIGO (2022+). S-GRBs are below the sensitivity of Advanced LIGO (all runs),

Table 3
Properties of the GW Emission of S-GRFs, S-GRBs, and U-GRBs

	ΔE_{insp} (erg)	ΔE_{merger} (erg)	f_{merger} (kHz)	f_{qnm} (kHz)	$z_{\text{min}}^{\text{obs}}$	d_{min} (Mpc)	d_{GW} (Mpc)		
							O1	O2	2022+
S-GRF	7.17×10^{52}	1.60×10^{53}	1.20	3.84	0.111	508.70	90.51–181.02	181.02–271.52	452.54
S-GRB	1.02×10^{53}	2.28×10^{53}	1.43	2.59	0.903	5841.80	121.84–243.67	243.67–365.51	609.18
U-GRB	1.02×10^{53}	2.03×10^{52}	0.98	2.30	0.169	804.57	126.71–253.43	253.43–380.14	633.57
U-GRB (BH–SN)	1.34×10^{53}	1.35×10^{53}	0.38	0.90	0.169	804.57	197.86–395.71	395.71–593.57	989.28

Note. We have made the Drastic simplified assumption that the binary evolution is only driven by GW emission, although it is manifest that the gravitational energy of the system in the merger phase is dominated by the radio, optical, X-ray, gamma-ray, and GeV emission (see Table 1). This assumption is made with the only aim of establishing an absolute upper limit to the GW emission and its detectability under the most optimistic conditions. Column (1): GRB subclass. Column (2): energy emitted in GWs during the inspiral regime ΔE_{insp} given by Equation (7). Column (3): energy emitted in GWs during the merger regime (plunge+merger+ringdown) ΔE_{merger} given by Equation (9). Column (4): GW frequency at merger. Column (5): GW frequency of the ringdown regime. Column (6): lowest cosmological redshift value $z_{\text{min}}^{\text{obs}}$ at which each subclass has been observed. Column (7): luminosity distance corresponding to $z_{\text{min}}^{\text{obs}}$, d_{min} , estimated from Equation (5). Columns (8)–(10): GW horizon calculated with the sensitivity of advanced LIGO during the O1 and O2 runs and with the expected final sensitivity including LIGO-India (2022+), respectively. It can be seen that the current GW horizon is much smaller than the observed distances of GRBs, impeding a positive detection by advanced LIGO. Only in the case of U-GRB (BH–SN) is a possible detection foreseen during the run 2022+. See also Table 4. We have used for S-GRFs $(1.4+1.4) M_{\odot}$, for S-GRBs $(2.0+2.0) M_{\odot}$, and for U-GRBs $(1.5+3.0) M_{\odot}$ and $(1.5+10.0) M_{\odot}$ for the out-states of BdHNe and of BH–SNe, respectively. Even if no U-GRB has yet been identified, we use here the values of $z_{\text{min}}^{\text{obs}}$ and d_{min} corresponding to the closest BdHN observed.

Advanced Virgo, and NAUTILUS. U-GRBs from out-states of BdHNe are below the sensitivity of Advanced LIGO (O1), Advanced Virgo, and NAUTILUS, but inside the sensitivity of Advanced LIGO (2022+). U-GRBs from out-states of BH–SNe are below the sensitivity of Advanced LIGO (O1) and NAUTILUS, inside the sensitivity of Advanced LIGO (2022+), and marginally inside the sensitivity of Advanced Virgo.

- Merging:* the merging regime, which expands frequencies from $f_{\text{contact}}/(1+z)$ to $f_{\text{qnm}}/(1+z)$ (see in Table 3 the frequencies and redshift), is outside the eLISA frequency band but inside the Advanced LIGO-Virgo and bar detector ones. The characteristic strain in this final merger phase $h \sim 10^{-24}$ to 10^{-23} is, unfortunately, well below the sensitivity of all of them (see also Kobayashi & Mészáros 2003, for similar conclusions for Advanced LIGO).

From the above it can be seen that the most interesting instrument for the possible detection of the GW emission from binaries associated with GRBs is Advanced LIGO. Therefore, we estimate in the next section the expected detection rates by Advanced LIGO-Virgo (see Figure 2 and Table 4).

6. GW Detection Rate

We assume a threshold for the Advanced LIGO-Virgo single detector $\rho_0 = 8$ (Abbott et al. 2016). This minimum ρ_0 defines a maximum detection distance or GW horizon distance, which is denoted as d_{GW} . This horizon corresponds to the most optimistic case when the binary is just above the detector and the binary plane is parallel to the detector plane, i.e., $\theta = \phi = \iota = 0$ (Allen et al. 2012):

$$d_{\text{GW}} = \frac{2A}{\rho_0} \left(\int_0^{\infty} \frac{f^{-7/3}}{S_n(f)} df \right)^{1/2}, \quad (18)$$

where $A = 5/(24\pi^{4/3})^{1/2} (GM_c/c^3)^{5/6} c$. Since not all the sources are optimally aligned with the detector, the number of detected sources inside a sphere of radius d_{GW} will be a fraction \mathcal{F}^3 of the total. This fraction determines the so-called “range” of the detector, $\mathcal{R} = \mathcal{F} d_{\text{GW}}$, where $\mathcal{F}^{-1} = 2.2627$ (see

Finn & Chernoff 1993, for details). In order to give an estimate of the annual number of detectable binaries associated with GRBs, we use the *search volume* as computed in Abbott et al. (2016), $\mathcal{V}_s = V_{\text{max}}^{\text{GW}} \mathcal{T}$, where $V_{\text{max}}^{\text{GW}} = (4\pi/3) \mathcal{R}^3$ and \mathcal{T} is the observing time accounting for the detector’s duty cycles. We use here the lower and upper values of \mathcal{R} and \mathcal{V}_s for a $(1.4+1.4) M_{\odot}$ NS binary for the different observational campaigns reported in Abbott et al. (2016): 2015/2016 (O1) with $\mathcal{R} = 40\text{--}80$ Mpc, $\mathcal{T} = 3$ months, $\mathcal{V}_s = (0.5\text{--}(4) \times 10^5 \text{ Mpc}^3 \text{ yr}$; 2016/2017 (O2) with $\mathcal{R} = 80\text{--}120$ Mpc, $\mathcal{T} = 6$ months, $\mathcal{V}_s = (0.6\text{--}2) \times 10^6 \text{ Mpc}^3 \text{ yr}$; 2017/2018 (O3) with $\mathcal{R} = 120\text{--}170$ Mpc, $\mathcal{T} = 9$ months, $\mathcal{V}_s = (3\text{--}10) \times 10^6 \text{ Mpc}^3 \text{ yr}$; and the one by the entire network including LIGO-India at design sensitivity (2022+) with $\mathcal{R} = 200$ Mpc, $\mathcal{T} = 1$ year, $\mathcal{V}_s = 4 \times 10^7 \text{ Mpc}^3 \text{ yr}$. We can use the above information for a $(1.4+1.4) M_{\odot}$ binary and extrapolate it to other binaries with different masses using the property that d_{GW} scales with the chirp mass as $M_c^{5/6}$ (see Equation (18)). We show in Table 3 the GW horizon for a specific value of the binary component masses expected for S-GRFs, S-GRBs, and U-GRBs (see Section 3.2).

From the inferred occurrence rates ρ_{GRB} (not to be confused with signal-to-noise ratio ρ) summarized in Table 1, we show in Figure 2 the expected number of GW detections by Advanced LIGO-Virgo for each observational campaign

$$\dot{N}_{\text{GW}} = \rho_{\text{GRB}} \mathcal{V}_s \quad (19)$$

for S-GRFs, S-GRBs, and U-GRBs as a function of the binary component masses (see Section 3.2).

We compare and contrast the following in Table 4 for the GRB subclasses: the expected GW detection rate by Advanced LIGO-Virgo given by Equation (19), \dot{N}_{GW} ; the inferred occurrence rate of GRBs, \dot{N}_{GRB} ; and the observed GRB rate from γ -ray telescopes (AGILE, BATSE, *BeppoSAX*, *Fermi*, *HETE-II*, *INTEGRAL*, *Konus/WIND*, and *Swift*), simply estimated as $\dot{N}_{\text{GRB}}^{\text{obs}} = N_{\text{GRB}}^{\text{obs}}/T_{\text{obs}}$, where $N_{\text{GRB}}^{\text{obs}}$ is the number of GRBs detected in the observing time T_{obs} . The rate \dot{N}_{GRB} is obtained from the GRB specific rate through the reconstruction of the GRB luminosity function and the study of its evolution with redshift (for details see Ruffini et al. 2016b; Appendix B).

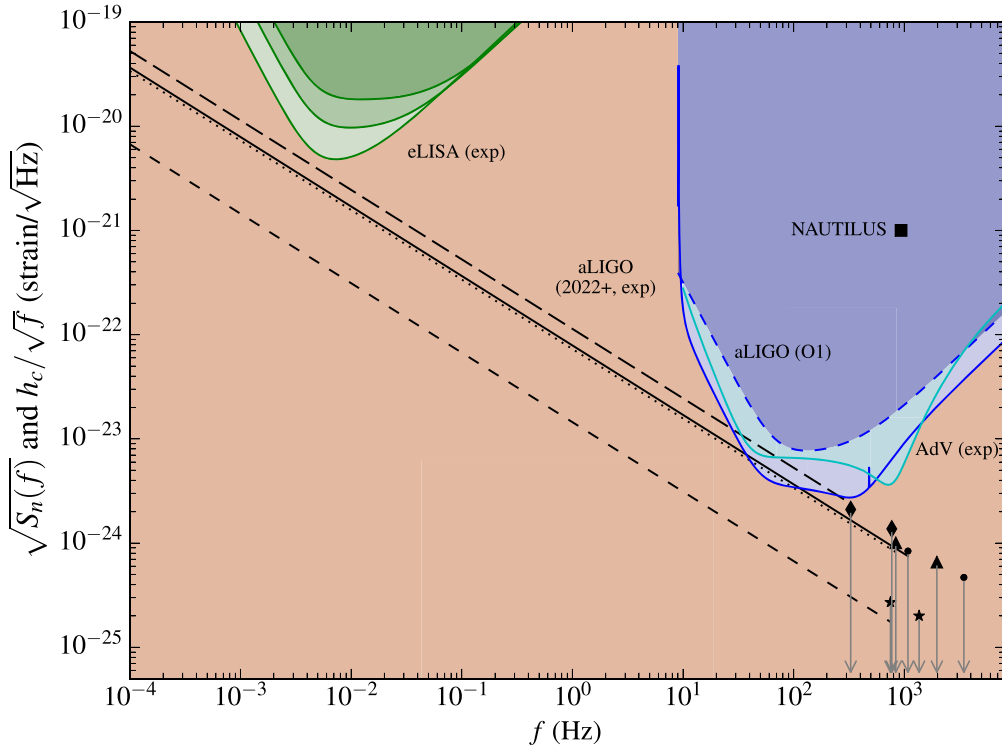


Figure 1. Comparison of the signal’s ASD h_c/\sqrt{f} of S-GRFs, S-GRBs, and U-GRBs with the noise’s ASD $\sqrt{S_n(f)}$, where S_n is the power spectrum density of the detector’s noise of eLISA, of Advanced LIGO (aLIGO), and of the bar detector NAUTILUS. The red lines, from top to bottom, are the expected noise’s ASD of the N2A1, N2A2, and N2A5 configurations of eLISA (Klein et al. 2016). The dashed and solid red lines correspond to the noise’s ASD of the Advanced LIGO O1 run (2015/2016) and of the expected Advanced LIGO 2022+ run (Abbott et al. 2016), respectively, and the cyan line is the expected noise’s ASD of Advanced Virgo (AdV) BNS-optimized (Abbott et al. 2016). The filled square indicates the noise’s ASD of the NAUTILUS resonant bar for a 1 ms GW burst (Astone et al. 2006, 2008). The red filled area indicates the region of undetectability by any of the above instruments. We recall that in this plot the GW frequency is redshifted by a factor of $1+z$ with respect to the source frame value, i.e., $f = f_s/(1+z)$, for which we use the cosmological redshift and corresponding luminosity distance of the closest observed source of each subclass (see Table 3). The following three curves correspond to the inspiral regime of the coalescence: S-GRFs with $(1.4+1.4) M_\odot$ (solid curve), S-GRBs with $(2.0+2.0) M_\odot$ (short-dashed curve), U-GRB with $(1.5+3.0) M_\odot$ (dotted curve) from out-states of BdHNe, and U-GRB with $(1.5+10.0) M_\odot$ (long-dashed curve) from out-states of BH-SNe. The circle, star, triangle, and diamond correspond to h_c in the merger regime for S-GRFs, S-GRBs, U-GRBs from out-states of BdHNe, and U-GRBs from out-states of BH-SNe, respectively. The first point is located at $f_{\text{merger}}/(1+z)$ and the second at $f_{\text{qnm}}/(1+z)$ (see Table 3). The downward-pointing arrows indicate that these estimates have to be considered as upper limits since we have assumed that all the energy released in the system goes in GWs, which clearly overestimates the GW energy output in view of the dominance of the electromagnetic emission (see Table 4). We have also overestimated the GW energy in the merger regime by using Equation (9), which is the expected GW energy emitted in the plunge+merger+ringdown phases of a BH-BH merger. For binary mergers involving NSs, as we have discussed in Section 4, the energy released in GWs must be necessarily lower than this value.

This estimate, therefore, is larger than $\dot{N}_{\text{GRB}}^{\text{obs}}$, which is limited to those events beyond the detector sensitivity threshold, falling inside its field of view and within its operational time.

7. Conclusions

Short and long GRBs have been divided into seven subclasses according to their binary nature (Ruffini et al. 2016b). We summarize in Table 1 their main physical properties characterizing the outcome of X-rays, gamma-rays, and high-energy and ultra-high-energy detectors, as well as their occurrence rate. Particularly important for the present work is the specification of the in-states and out-states of the GRB progenitors.

With the knowledge of the nature of the compact-object binaries associated with each GRB subclass and the relevance of the NS structure and critical mass in Section 2, we introduce in Section 3 the main ingredients for the computation of the GW emission and detectability for such systems. We describe in Section 4 the general properties of the GW emission during the inspiral and merger regimes of these binaries. We argue that S-GRFs, S-GRBs, and U-GRBs are the GRB subclasses relevant

for the GW analysis. It is manifest that the release of the gravitational energy of the system in the merger phase is dominated by the X-rays, gamma-rays, and GeV emission (see Table 1). In order to evaluate the GW emission, we have made in this work the drastic simplified assumption that the binary evolution is only driven by GW emission. This assumption is of interest, with the only aim of establishing an absolute upper limit and checking the detectability of the GW emission under this most optimistic condition. We compare and contrast in Section 5 the GW characteristic strain amplitude produced by the inspiral and merger regimes with the strain noise of the broadband detectors eLISA and Advanced LIGO-Virgo and of the narrowband resonant bar NAUTILUS. In order to do this, we use the cosmological redshift and corresponding luminosity distance of the closest observed source of each subclass (see Table 3). We show that the inspiral regime is possibly detectable only by Advanced LIGO (see Table 3 and Figure 1) and the merger regime is undetectable by any of these instruments.

Therefore, in Section 6 we assess quantitatively the GW detectability of the inspiral regime of S-GRFs, S-GRBs, and U-GRBs only by Advanced LIGO. We recall that, following

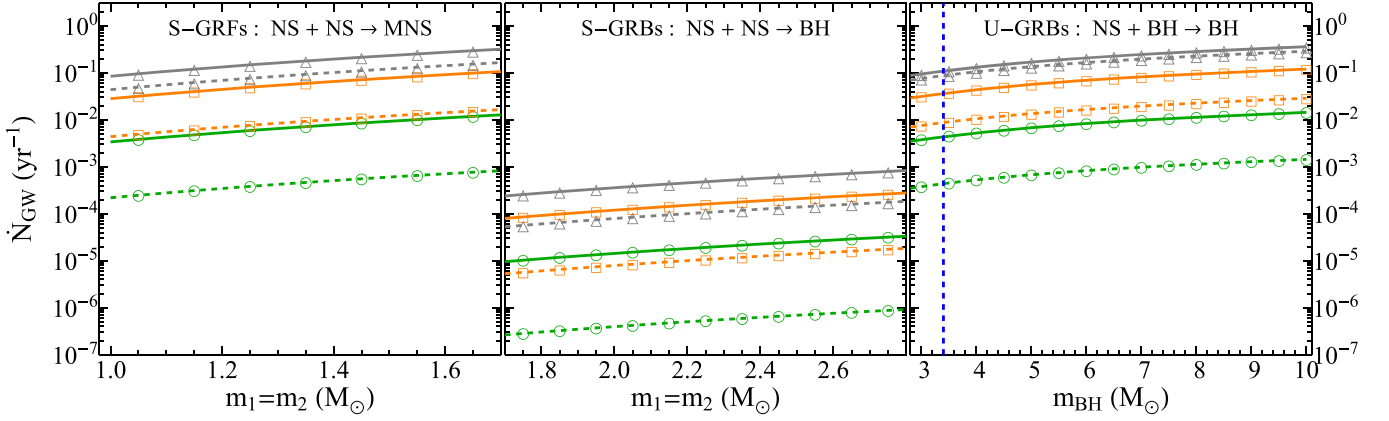


Figure 2. Expected annual GW upper and lower bounds (solid and dashed lines, respectively) for the detections expected from S-GRFs (left panel), S-GRBs (middle panel), and U-GRBs (right panel), for three selected observational campaigns: 2015/2016 (O1; red curves with circles), 2017/2018 (O3; orange curve with squares), and 2022+ (gray curve with triangles). The vertical red dashed line in the plot of U-GRBs separates ν NS–BH binaries produced by BdHNe (BH masses equal to the NS critical mass) and BH–SNe (BH masses larger than the NS critical mass).

Table 4

Inferred and Observed Number of GRBs Per Year, and the Corresponding Expected Rate of GW Detections for Each GRB Subclass

GRB Subclass	\dot{N}_{GRB} (yr^{-1})	$\dot{N}_{\text{GRB}}^{\text{obs}}$ (yr^{-1})	\dot{N}_{GW} (yr^{-1})
XRFs	144–733	1 (1997–2014)	Undetectable
BdHNe	662–1120	14 (1997–2014)	Undetectable
BH–SNe	$\lesssim 662$ –1120	$\lesssim 14$ (1997–2014)	Undetectable
S-GRFs	58–248	3 (2005–2014)	O1: 0.0001–0.002 O2: 0.002–0.01 O3: 0.008–0.05 2022+: 0.1–0.2
S-GRBs	2–8	1 (2006–2014)	O1: $(0.1\text{--}3.1) \times 10^{-6}$ O2: $(0.1\text{--}1.6) \times 10^{-5}$ O3: $(0.6\text{--}7.8) \times 10^{-5}$ 2022+: $(0.78\text{--}3.12) \times 10^{-4}$
U-GRBs	662–1120	...	O1: $(0.9\text{--}9) \times 10^{-4}$ O2: 0.001–0.005 O3: 0.006–0.024 2022+: 0.076–0.094
U-GRBs (BH–SN)	$\lesssim 662$ –1120	...	O1: $\lesssim 0.00036$ –0.0036 O2: $\lesssim 0.004$ –0.018 O3: $\lesssim 0.02$ –0.09 2022+: $\lesssim 0.29$ –0.36
GRFs	29–153	1 (2005–2014)	Undetectable

Note. Column (1): GRB subclass. Column (2): inferred number of GRBs per year in the entire universe, \dot{N}_{GRB} , for each GRB subclass (see also Figure 6 in Ruffini et al. 2016b). Column (3): number of GRBs observed per year, $\dot{N}_{\text{GRB}}^{\text{obs}}$, obtained from the observations of γ -ray telescopes such as AGILE, BATSE, BeppoSAX, Fermi, HETE-II, INTEGRAL, Konus/WIND, and Swift, in the indicated years of observations (see also Tables 2–6 in Ruffini et al. 2016b). Column (4): expected rate of GW detections by advanced LIGO of all the GRB subclasses, computed for three selected observational campaigns, 2015/2016 (O1), 2016/2017 (O2), and 2017/2018 (O3), and the one by the entire network at design sensitivity including LIGO-India (2022+). The binary component masses used here are the same as in Table 3.

Abbott et al. (2016), we adopt as the threshold for detectability a signal-to-noise ratio equal to 8. We present in Figure 2 and Table 4 the expected detection rate of the GW emission. Four observational campaigns of Advanced LIGO are analyzed: O1 (2015/2016), O2 (2016/2017), O3 (2017/2018), and 2022+, namely the one by the entire network at design sensitivity including LIGO-India. In Table 4 we compare and contrast this rate with the occurrence rate of the GRB subclasses and their rate of observations by γ -ray telescopes.

Keeping the above in mind, we conclude the following for each GRB subclass:

- I. XRFs: their ν NS–NS out-states transit, during the inspiral regime, which spans the frequency range $f < f_{\text{merger}}/(1+z)$ (see Table 3), first the eLISA frequency band and then enter the Advanced LIGO–Virgo ones in the final orbits prior to the merging process (i.e., when $P_{\text{orb}} < 0.2$ s). Resonant bar detectors are not sensitive in this inspiral regime frequency range. The characteristic strain generated by these sources in the inspiral regime is below the sensitivity of eLISA. The merger regime, which expands frequencies from $f_{\text{contact}}/(1+z)$ to $f_{\text{qnm}}/(1+z)$ (see Table 3), is outside the eLISA frequency band but inside the frequency band of Advanced LIGO–Virgo and bar detectors. See Figure 1 for details. These ν NS–NS mergers can lead to either S-GRFs or S-GRBs (see in IV and V below the conclusion about their GW detectability).
- II. BdHNe: their ν NS–BH out-states transit, during the inspiral regime, which spans the frequency range $f < f_{\text{merger}}/(1+z)$ (see Table 3), first the eLISA frequency band and then enter the Advanced LIGO–Virgo ones in the final orbits prior to the merging process (i.e., when $P_{\text{orb}} < 0.2$ s). Resonant bar detectors are not sensitive in this inspiral regime frequency range. The characteristic strain generated by these sources in the inspiral regime is below the sensitivity of eLISA. The merger regime, which expands frequencies from $f_{\text{contact}}/(1+z)$ to $f_{\text{qnm}}/(1+z)$ (see Table 3), is outside the eLISA frequency band but inside the frequency band of Advanced LIGO–Virgo and bar detectors. See Figure 1

- for details. These ν NS–BH mergers lead to U-GRBs (see in VI below the conclusion about their GW detectability).
- III. BH–SN: their ν NS–BH out-states transit, during the inspiral regime, which spans the frequency range $f < f_{\text{merger}} / (1 + z)$ (see Table 3), first the eLISA frequency band and then enter the Advanced LIGO–Virgo ones in the final orbits prior to the merging process (i.e., when $P_{\text{orb}} < 0.2$ s). Resonant bar detectors are not sensitive in this inspiral regime frequency range. The characteristic strain generated by these sources in the inspiral regime is below the sensitivity of eLISA. The merger regime, which expands frequencies from $f_{\text{contact}} / (1 + z)$ to $f_{\text{qnm}} / (1 + z)$ (see Table 3), is outside the eLISA frequency band but inside the frequency band of Advanced LIGO–Virgo and bar detectors. See Figure 1 for details. These ν NS–BH mergers lead to U-GRBs (see in VI below the conclusion about their GW detectability).
- IV. S-GRFs: the final orbits of the inspiral regime (when $P_{\text{orb}} < 0.2$ s) fall inside the frequency band of Advanced LIGO–Virgo and bar detectors. However, the GW energy output in the merger regime leads to a characteristic strain that is not sufficient to be detectable either by any of them. See Figure 1 for details. The inspiral regime is detectable for sources located at distances smaller than 181 Mpc for the O1 Advanced LIGO run and smaller than 452 Mpc for the 2022+ run (see Table 3). The closest S-GRF observed up to now is, however, located at 509 Mpc. See Table 4 for the expected GW detection rate.
- V. S-GRBs: the final orbits of the inspiral regime (when $P_{\text{orb}} < 0.2$ s) fall inside the frequency band of Advanced LIGO–Virgo and bar detectors. However, the GW energy output in the merger regime leads to a characteristic strain that is not sufficient to be detectable either by any of them. See Figure 1 for details. The inspiral regime is detectable for sources located at distances smaller than 244 Mpc for the O1 Advanced LIGO run and smaller than 609 Mpc for the 2022+ run (see Table 3). The closest S-GRB observed up to now is, however, located at 5842 Mpc. See Table 4 for the expected GW detection rate.
- VI. U-GRBs: the final orbits of the inspiral regime (when $P_{\text{orb}} < 0.2$ s) fall inside the frequency band of Advanced LIGO–Virgo and bar detectors. However, the GW energy output in the merger regime leads to a characteristic strain that is not sufficient to be detectable either by any of them. See Figure 1 for details. In the case of U-GRBs originating from the BdHN out-states, the inspiral regime is detectable for sources located at distances smaller than 253 Mpc for the O1 Advanced LIGO run and smaller than 634 Mpc for the 2022+ run (see Table 3). In the case of U-GRBs originating from the BH–SN out-states, the inspiral regime is detectable for sources at distances smaller than 396 Mpc for the O1 Advanced LIGO run and smaller than 989 Mpc for the 2022+ run (see Table 3). No U-GRB has yet been electromagnetically identified. The closest distance at which its possible progenitor, namely, a BdHN, is located is 805 Mpc. See Table 4 for the expected GW detection rate.
- VII. GRFs: The tidal disruption of the WD by the NS produces an undetectable GW emission (see, e.g., Paschalidis et al. 2009).

We recalled in the Introduction that the simultaneous detection rates of GWs and GRBs have been estimated up to now in the literature only in the case of S-GRFs, in which no BH is formed but instead the merger of the two NSs leads to an MNS. Indeed, it can be seen that the recent GW detection rate estimated by Patricelli et al. (2016) of short bursts at Advanced LIGO design sensitivity (see Table 1 there), $0.04\text{--}15 \text{ yr}^{-1}$, is consistent with the one of S-GRFs estimated in this work, $\dot{N}_{\text{GW}} = 0.1\text{--}0.2 \text{ yr}^{-1}$ (see Table 4). This represents the most favorable case for the possible GW detection by Advanced LIGO–Virgo of NS–NS merger, which, however, does not lead to a BH formation but to an MNS.

We have given in this article, for the first time, a rate for the formation of BHs in both short and long bursts, and this is of clear astrophysical relevance. Among such bursts producing a BH, the most favorable cases for GW detection are those from U-GRBs from BdHNe with $\dot{N}_{\text{GW}} = 0.08\text{--}0.09 \text{ yr}^{-1}$ and those from BH–SNe with $\dot{N}_{\text{GW}} = 0.3\text{--}0.4 \text{ yr}^{-1}$ (see Table 4). These NS–BH merging binaries were unknown in the literature, and thus their occurrence and GW detection rates are a definite prediction of this work.

Any detection by Advanced LIGO–Virgo of an NS–NS merger or an NS–BH merger will imply a drastic increase of the occurrence rate of events shown here and an examination of the consistency with GRB observations.

We have already given evidence on the unsuitability of the *collapsar* model to explain the GRB observations in Ruffini et al. (2018b). We have published a classification on the ground of the current observations of 480 sources with known redshift (Ruffini et al. 2016b, 2018b), which is both necessary and sufficient, as of today, to cover all GRBs observed. As the number of sources will increase, it is conceivable that the discovery of different systems will be observed, and in that case we will be ready for their inclusion in additional subclasses within our classification scheme.

As we have mentioned, the above are estimates based on the most favorable conditions for GW emission, and realistic \dot{N}_{GW} values will need the assessment of the ratio of GW to electromagnetic energy, which is necessarily smaller than unity from energy conservation.

After the submission of this work, the LIGO–Virgo Collaboration announced the detection of the signal GW 170817 and interpreted it as due to an NS–NS merger (Abbott et al. 2017b). As we have mentioned above, any possible GW detection of an NS–NS merger would imply a revision of its consistency with the inferences from GRB observations. It may then appear that our above conclusions of poor chance of detectability of NS–NS mergers by the Advanced LIGO–Virgo detector network are in tension with the detection of GW 170817 during the O2 run. The association of GW 170817 with GRB 170817A, a weak, short-duration GRB observed by the Gamma-ray Burst Monitor (GBM) on board the *Fermi* satellite (Abbott et al. 2017a; Goldstein et al. 2017) and followed-up in the optical bands (e.g., Cowperthwaite et al. 2017), in the X-rays (e.g., Haggard et al. 2017), and by further gamma-ray facilities (e.g., Savchenko et al. 2017), allows us in the following to make an assessment on this issue.

First, we recall that GRB 170817A, with its isotropic energy emitted in gamma rays of $E_{\text{iso}} \approx 5 \times 10^{46} \text{ erg}$ (Goldstein et al. 2017) and peak luminosity of $(1.7 \pm 0.1) \times 10^{47} \text{ erg s}^{-1}$ (Zhang et al. 2017), would belong to the S-GRF subclass if we assume that it is produced in an NS–NS merger. On the

other hand, we recall that our estimates of the local density rate of the GRB subclasses (see Table 1), obtained from Ruffini et al. (2016b), are reliable for GRBs with luminosities higher than the lowest GRB luminosity in the subclass sample (see Appendix B for details). In the case of S-GRFs, we had identified GRB 050509B as the source with the lowest energetics, $E_{\text{iso}} \approx 8.5 \times 10^{48}$ erg (see Table 4 in Ruffini et al. 2016b), and a peak luminosity of $(1.1 \pm 0.5) \times 10^{51}$ erg s $^{-1}$ (Fox et al. 2005). This implies that our predicted detection rates for the Advanced LIGO-Virgo detectors for S-GRFs are valid for sources with electromagnetic emission over the above values. Even a single observation of a close and underluminous source, such as GRB 170817A, would lead to an increase of the local density rate of this GRB subclass. Indeed, Zhang et al. (2017) have recently estimated the increase in the local density rate when GRB 170817A is included in the sample of short bursts. Following a similar method to the one described in Appendix B, they found that their previously estimated isotropic local density rate of 3.2–5.5 Gpc $^{-3}$ yr $^{-1}$, obtained for sources with peak luminosities above 7×10^{49} erg s $^{-1}$,¹⁰ increases to a lower limit of 30–630 Gpc $^{-3}$ yr $^{-1}$, for sources with peak luminosities above 1.7×10^{47} erg s $^{-1}$, i.e., when GW 170817 is included in the sample. The above range implies an increase of the local density rate by a factor of ~ 10 –100. It is then easy to check, using Table 4, that an increase of such a factor in the S-GRF density rate would imply a detection rate of 0.01–1 yr $^{-1}$ for the O2 observational run, in agreement with the detection of GW 170817.

In fact, the above isotropic density rate inferred by Zhang et al. (2017) is consistent with the NS–NS observed merger rate of 320–4740 Gpc $^{-3}$ yr $^{-1}$, inferred by the LIGO Collaboration with the detection of GW 170817 (see Section 5 in Abbott et al. 2017b, for details). This result implies that S-GRFs (or in general all short bursts) are not beamed or, if a beaming is assumed, the jet half-opening angle should be at least as large as 25°–30°.

We thank the referee for suggestions that improved the presentation of our results. M.K. acknowledges the support given by the International Relativistic Astrophysics Erasmus Mundus Joint Doctorate Program under grants 2013–1471, from EACEA of the European Commission. M.M. and J.A.R. acknowledge the partial support of project no. 3101/GF4 IPC-11 and target program F.0679 of the Ministry of Education and Science of the Republic of Kazakhstan. C.C. and S.F. acknowledge INdAM-GNFM for support.

Appendix A

IGC, Hypercritical Accretion, and Long GRBs

We give in this appendix details of the accretion process within the IGC scenario following Fryer et al. (2014, 2015b) and Becerra et al. (2015, 2016).

There are two main physical conditions for which hypercritical (i.e., highly super-Eddington) accretion onto the NS occurs in XRFs and BdHNe. The first is that the photons are trapped within the inflowing material, and the second is that the shocked atmosphere on top of the NS becomes sufficiently hot ($T \sim 10^{10}$ K) and dense ($\rho \gtrsim 10^6$ g cm $^{-3}$) to produce a very

efficient neutrino–antineutrino ($\nu\bar{\nu}$) cooling emission. In this way the neutrinos become the main source responsible for releasing the energy gained by accretion, allowing hypercritical accretion to continue.

The first IGC simulations were performed in Fryer et al. (2014), including (1) realistic SN explosions of the CO $_{\text{core}}$, (2) the hydrodynamics within the accretion region, and (3) the simulated evolution of the SN ejecta up to their accretion onto the NS. Becerra et al. (2015) then estimated the amount of angular momentum carried by the SN ejecta and how much is transferred to the NS companion by accretion. They showed that the SN ejecta can circularize for a short time and form a disk-like structure surrounding the NS before being accreted. The evolution of the NS central density and rotation angular velocity (the NS is spun up by accretion) was computed from full numerical solutions of the axisymmetric Einstein equations. The unstable limits of the NS are set by the mass-shedding (or Keplerian) limit and the critical point of gravitational collapse given by the secular axisymmetric instability (see, e.g., Becerra et al. 2015, for details).

The accretion rate of the SN ejecta onto the NS is given by

$$\begin{aligned} \dot{M}_B(t) &= \pi \rho_{\text{ej}} R_{\text{cap}}^2 \sqrt{v_{\text{rel}}^2 + c_{\text{s,ej}}^2}, \\ R_{\text{cap}}(t) &= \frac{2GM_{\text{NS}}(t)}{v_{\text{rel}}^2 + c_{\text{s,ej}}^2}, \end{aligned} \quad (20)$$

where G is the gravitational constant, ρ_{ej} and $c_{\text{s,ej}}$ are the density and sound speed of the ejecta, respectively, R_{cap} and M_{NS} are the NS gravitational capture radius (Bondi–Hoyle radius) and gravitational mass, respectively, and v_{rel} is the ejecta velocity relative to the NS, $v_{\text{rel}} = v_{\text{orb}} - v_{\text{ej}}$, where $|v_{\text{orb}}| = \sqrt{G(M_{\text{core}} + M_{\text{NS}})/a}$ and v_{ej} is the velocity of the SN ejecta (see Figure 3).

Numerical simulations of the SN explosions suggest the adopted homologous expansion of the SN, i.e., $v_{\text{ej}}(r, t) = nr/t$, where r is the position of each layer from the SN center and n is the expansion parameter. The density evolves as

$$\rho_{\text{ej}}(r, t) = \rho_{\text{ej}}^0(r/R_{\text{star}}(t), t_0) \frac{M_{\text{env}}(t)}{M_{\text{env}}(0)} \left(\frac{R_{\text{star}}(0)}{R_{\text{star}}(t)} \right)^3, \quad (21)$$

where $M_{\text{env}}(t)$ is the mass of the CO $_{\text{core}}$ envelope, $R_{\text{star}}(t)$ is the radius of the outermost layer, and ρ_{ej}^0 is the pre-SN CO $_{\text{core}}$ density profile, $\rho_{\text{ej}}(r, t_0) = \rho_{\text{core}}(R_{\text{core}}/r)^m$, where ρ_{core} , R_{core} , and m are the profile parameters obtained from numerical simulations. Typical parameters of the CO $_{\text{core}}$ mass are 3.5–9.5 M_{\odot} , corresponding to 15–30 M_{\odot} zero-age main-sequence progenitors (see Fryer et al. 2014; Becerra et al. 2015, for details). The binary period is limited from below by the request of having no Roche lobe overflow by the CO $_{\text{core}}$ before the SN explosion (Fryer et al. 2014). For instance, for a CO $_{\text{core}}$ of 9.5 M_{\odot} forming a binary system with a 2 M_{\odot} NS, the minimum orbital period allowed by this condition is $P_{\text{min}} \approx 5$ minutes. For these typical binary and pre-SN parameters, Equation (20) gives accretion rates of 10^{-4} to 10^{-2} M_{\odot} s $^{-1}$.

We adopt an initially nonrotating NS companion so that its exterior spacetime at time $t = 0$ is described by the Schwarzschild metric. The SN ejecta approach the NS with specific

¹⁰ This rate is consistent with the local density rate $\rho_{\text{S-GRFs}} + \rho_{\text{S-GRBs}} \approx \rho_{\text{S-GRFs}} = (2.6\text{--}5.0)$ Gpc $^{-3}$ yr $^{-1}$ used in the present work; see Table 1 and Ruffini et al. (2016b).

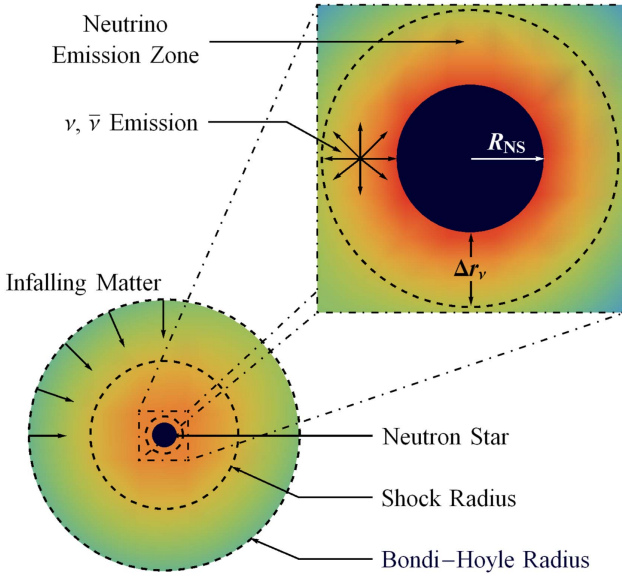


Figure 3. Scheme of the IGC scenario: the CO_{core} undergoes SN explosion, and the NS accretes part of the SN ejecta and then reaches the critical mass for gravitational collapse to a BH, with consequent emission of a GRB. The SN ejecta reach the NS Bondi–Hoyle radius and fall toward the NS surface. The material shocks and decelerates while it piles over the NS surface. At the neutrino emission zone, neutrinos take away most of the gravitational energy gained by the matter infall. The neutrinos are emitted above the NS surface in a region of thickness Δr_ν , about half the NS radius, which allows the material to reduce its entropy to be finally incorporated into the NS. For further details and numerical simulations of the above process see Fryer et al. (2014) and Becerra et al. (2015, 2016).

angular momentum, $l_{\text{acc}} = \dot{L}_{\text{cap}}/\dot{M}_B$, circularizing at a radius $r_{\text{circ}} \geq r_{\text{lco}}$ if $l_{\text{acc}} \geq l_{\text{iso}}$, with r_{lco} the radius of the LCO. For a nonrotating NS $r_{\text{lco}} = 6GM_{\text{NS}}/c^2$ and $l_{\text{lco}} = 2\sqrt{3}GM_{\text{NS}}/c$. For typical parameters, $r_{\text{circ}}/r_{\text{lco}} \sim 10\text{--}10^3$.

The accretion onto the NS proceeds from the radius r_{in} . The NS mass and angular momentum evolve as (Becerra et al. 2015; Cipolletta et al. 2017)

$$\dot{M}_{\text{NS}} = \left(\frac{\partial M_{\text{NS}}}{\partial M_b} \right)_{J_{\text{NS}}} \dot{M}_b + \left(\frac{\partial M_{\text{NS}}}{\partial J_{\text{NS}}} \right)_{M_b} \dot{J}_{\text{NS}}, \quad \dot{J}_{\text{NS}} = \xi l(r_{\text{in}}) \dot{M}_B, \quad (22)$$

where M_b is the NS baryonic mass; $l(r_{\text{in}})$ is the specific angular momentum of the accreted material at r_{in} , which corresponds to the angular momentum of the LCO; and $\xi \leq 1$ is a parameter that measures the efficiency of angular momentum transfer. In this picture we have $\dot{M}_b = \dot{M}_B$.

For the integration of Equations (20) and (22) we have to supply the values of the two partial derivatives in Equation (22). They are obtained from the relation of the NS gravitational mass, M_{NS} , with M_b and J_{NS} , namely, from the knowledge of the NS binding energy. For this we use the general relativistic calculations of rotating NSs presented in Cipolletta et al. (2015). They show that, independent of the nuclear EOS, the following analytical formula represents the numerical results with sufficient accuracy (error $< 2\%$):

$$\frac{M_b}{M_\odot} = \frac{M_{\text{NS}}}{M_\odot} + \frac{13}{200} \left(\frac{M_{\text{NS}}}{M_\odot} \right)^2 \left(1 - \frac{1}{137} j_{\text{NS}}^{1.7} \right), \quad (23)$$

where $j_{\text{NS}} \equiv cJ_{\text{NS}}/(GM_\odot^2)$.

Table 5

Critical NS Mass in the Nonrotating Case and Constants k and p Needed to Compute the NS Critical Mass in the Nonrotating Case Given by Equation (25)

EOS	$M_{\text{crit}}^{J=0} (M_\odot)$	p	k
NL3	2.81	1.68	0.006
GM1	2.39	1.69	0.011
TM1	2.20	1.61	0.017

Note. The values are given for the NL3, GM1, and TM1 EOS.

In the accretion process the NS gains angular momentum and therefore spin-up. To evaluate the amount of angular momentum transferred to the NS at any time, we include the dependence of the LCO specific angular momentum as a function of M_{NS} and J_{NS} . For corotating orbits the following relation is valid for the NL3, TM1, and GM1 EOS (Becerra et al. 2015; Cipolletta et al. 2017):

$$l_{\text{lco}} = \frac{GM_{\text{NS}}}{c} \left[2\sqrt{3} - 0.37 \left(\frac{j_{\text{NS}}}{M_{\text{NS}}/M_\odot} \right)^{0.85} \right]. \quad (24)$$

The NS continues to accrete until an instability limit is reached or up to when all the SN ejecta overcome the NS Bondi–Hoyle region. We take into account the two main instability limits for rotating NSs: the mass-shedding or Keplerian limit and the secular axisymmetric instability limit. The latter defines critical NS mass. For the aforementioned nuclear EOS, the critical mass is approximately given by (Cipolletta et al. 2015)

$$M_{\text{NS}}^{\text{crit}} = M_{\text{NS}}^{J=0} (1 + k j_{\text{NS}}^p), \quad (25)$$

where k and p are EOS-dependent parameters (see Table 5). These formulae fit the numerical results with a maximum error of 0.45%.

A.1. Most Recent Simulations of the IGC Process

Additional details and improvements of the hypercritical accretion process leading to XRFs and BdHNe were presented in Becerra et al. (2016). Specifically:

1. The density profile included finite size/thickness effects, and additional CO_{core} progenitors leading to different SN ejecta masses were considered.
2. In Becerra et al. (2015) the maximum orbital period, P_{max} , over which the accretion onto NS companion is not sufficient to bring it to the critical mass, was inferred. Thus, binaries with $P > P_{\text{max}}$ lead to XRFs, while the ones with $P \lesssim P_{\text{max}}$ lead to BdHNe. Becerra et al. (2016) extended the determination of P_{max} for all the possible initial values of the NS mass. They also examined the outcomes for different values of the angular momentum transfer efficiency parameter.
3. The expected luminosity during the process of hypercritical accretion for a wide range of binary periods covering both XRFs and BdHNe was estimated.
4. It was shown that the presence of the NS companion originates asymmetries in the SN ejecta (see, e.g., Figure 6 in Becerra et al. 2016). The signatures of such asymmetries in the X-ray emission were there shown in the specific example of XRF 060218.

A.2. Hydrodynamics and Neutrino Emission in the Accretion Region

The accretion rate onto the NS can be as high as $\sim 10^{-2}$ to $10^{-1} M_{\odot} \text{ s}^{-1}$. For such accretion rates:

1. The magnetic pressure is much smaller than the random pressure of the infalling material; therefore, the magnetic field effects on the accretion process are negligible (Fryer et al. 1996; Rueda & Ruffini 2012).
2. The photons are trapped within the infalling matter; hence, the Eddington limit does not apply and hypercritical accretion occurs. The trapping radius is defined by Chevalier (1989): $r_{\text{trapping}} = \min\{\dot{M}_B \kappa / (4\pi c), R_{\text{cap}}\}$, where κ is the opacity. Fryer et al. (2014) estimated a Rosseland mean opacity of $\approx 5 \times 10^3 \text{ cm}^2 \text{ g}^{-1}$ for the CO_{cores} . This, together with our typical accretion rates, leads to $\dot{M}_B \kappa / (4\pi c) \sim 10^{13}\text{--}10^{19} \text{ cm}$. This radius is much bigger than the Bondi–Hoyle radius.
3. The above condition, as well as the temperature–density values reached on top of the NS surface, leads to an efficient neutrino cooling that radiates away the gain of gravitational energy of the infalling material (Zel’dovich et al. 1972; Ruffini & Wilson 1973; Fryer et al. 1996, 2014; Rueda & Ruffini 2012).

A.2.1. Convective Instabilities

The accretion shock moves outward as the material piles onto the NS. Since the post-shock entropy is inversely proportional to the shock radius position, the NS atmosphere is unstable with respect to Rayleigh–Taylor convection at the beginning of the accretion process. Such instabilities might drive high-velocity outflows from the accreting NS (Fryer et al. 2006; Fryer 2009). The entropy at the base of the atmosphere is (Fryer et al. 1996)

$$S_{\text{bubble}} \approx 16 \left(\frac{1.4 M_{\odot}}{M_{\text{NS}}} \right)^{-7/8} \left(\frac{M_{\odot} \text{ s}^{-1}}{\dot{M}_B} \right)^{1/4} \times \left(\frac{10^6 \text{ cm}}{r} \right)^{3/8} k_B / \text{nucleon}. \quad (26)$$

The material expands and cools down adiabatically, i.e., $T^3/\rho = \text{constant}$. In the case of a spherically symmetric expansion, $\rho \propto 1/r^3$ and $k_B T_{\text{bubble}} = 195 S_{\text{bubble}}^{-1} (10^6 \text{ cm}/r)$ MeV. In the more likely case that the material expands laterally, we have (Fryer 2009) $\rho \propto 1/r^2$, i.e., $T_{\text{bubble}} = T_0(S_{\text{bubble}})(r_0/r)^{2/3}$, where $T_0(S_{\text{bubble}})$ is obtained from the above equation at $r = r_0 \approx R_{\text{NS}}$. This implies a bolometric blackbody flux at the source from the rising bubbles:

$$F_{\text{bubble}} \approx 2 \times 10^{40} \left(\frac{M_{\text{NS}}}{1.4 M_{\odot}} \right)^{-7/2} \left(\frac{\dot{M}_B}{M_{\odot} \text{ s}^{-1}} \right) \times \left(\frac{R_{\text{NS}}}{10^6 \text{ cm}} \right)^{3/2} \left(\frac{r_0}{r} \right)^{8/3} \text{ erg s}^{-1} \text{ cm}^{-2}, \quad (27)$$

where σ is the Stefan–Boltzmann constant.

The above thermal emission has been shown (Fryer et al. 2014) to be a plausible explanation of the early ($t \lesssim 50$ s) X-ray emission observed in some GRBs. In the specific example of GRB 090618 (Izzo et al. 2012a, 2012b), adopting an accretion rate of $10^{-2} M_{\odot} \text{ s}^{-1}$, the bubble temperature drops

from 50 to 15 keV while expanding from $r \approx 10^9 \text{ cm}$ to $6 \times 10^9 \text{ cm}$.

A.2.2. Neutrino Emission and Effective Accretion Rate

Temperatures $k_B T \sim 1\text{--}10 \text{ MeV}$ and densities $\rho \gtrsim 10^6 \text{ g cm}^{-3}$ develop near the NS surface during the accretion process. Under these conditions, e^+e^- annihilation into $\nu\bar{\nu}$ pairs becomes the dominant neutrino emission process in the accretion region (see Becerra et al. 2016, for details). The effective accretion rate onto the NS can be estimated as (e.g., Fryer et al. 1996) $\dot{M}_{\text{eff}} \approx \Delta M_{\nu} (L_{\nu}/E_{\nu})$, where ΔM_{ν} and L_{ν} are the mass and neutrino luminosity in the emission region, respectively, and E_{ν} is half the gravitational potential energy gained by the material falling from infinity to a distance Δr_{ν} from the NS surface. Δr_{ν} is the thickness of the neutrino emitting region, which is approximately given by the temperature scale height ($\Delta r_{\nu} \approx 0.6 R_{\text{NS}}$). Since $L_{\nu} \approx 2\pi R_{\text{NS}}^2 \Delta r_{\nu} \epsilon_{e^-e^+}$, with $\epsilon_{e^-e^+}$ the e^+e^- pair annihilation process emissivity, and $E_{\nu} = (1/2)GM_{\text{NS}}\Delta M_{\nu}/(R_{\text{NS}} + \Delta r_{\nu})$, for $M_{\text{NS}} = 1.4 M_{\odot}$ one obtains $\dot{M}_{\text{eff}} \approx 10^{-9}$ to $10^{-1} M_{\odot} \text{ s}^{-1}$ for $k_B T = 1\text{--}10 \text{ MeV}$.

A.3. Accretion Luminosity

The energy release in a time interval dt , when an amount of mass dM_b with angular momentum $l\dot{M}_b$ is accreted, is

$$L_{\text{acc}} = (\dot{M}_b - \dot{M}_{\text{NS}})c^2 = \dot{M}_b c^2 \times \left[1 - \left(\frac{\partial M_{\text{NS}}}{\partial J_{\text{NS}}} \right)_{M_b} l - \left(\frac{\partial M_{\text{NS}}}{\partial M_b} \right)_{J_{\text{NS}}} \right]. \quad (28)$$

This is the amount of gravitational energy gained by the matter by infalling to the NS surface that is not spent in NS gravitational binding energy. The total energy release in the time interval from t to $t+dt$, $\Delta E_{\text{acc}} \equiv \int L_{\text{acc}} dt$, is given by the NS binding energy difference between its initial and final state. The typical luminosity is $L_{\text{acc}} \approx \Delta E_{\text{acc}}/\Delta t_{\text{acc}}$, where Δt_{acc} is the duration of the accretion process.

The value of Δt_{acc} is approximately given by the flow time of the slowest layers of the SN ejecta to the NS companion position. If we denote the velocity of these layers by v_{inner} , we have $\Delta t_{\text{acc}} \sim a/v_{\text{inner}}$, where a is the binary separation. For $a \sim 10^{11} \text{ cm}$ and $v_{\text{inner}} \sim 10^8 \text{ cm s}^{-1}$, $\Delta t_{\text{acc}} \sim 10^3 \text{ s}$. For shorter separations, e.g., $a \sim 10^{10} \text{ cm}$ ($P \sim 5$ minutes), $\Delta t_{\text{acc}} \sim 10^2 \text{ s}$. For a binary with $P = 5$ minutes, the NS accretes $\approx 1 M_{\odot}$ in $\Delta t_{\text{acc}} \approx 100 \text{ s}$. From Equation (23) one obtains that the binding energy difference of a $2 M_{\odot}$ and a $3 M_{\odot}$ NS is $\Delta E_{\text{acc}} \approx 13/200(3^2 - 2^2) M_{\odot} c^2 \approx 0.32 M_{\odot} c^2$. This leads to $L_{\text{acc}} \approx 3 \times 10^{-3} M_{\odot} c^2 \approx 0.1 \dot{M}_b c^2$. The accretion power can be as high as $L_{\text{acc}} \sim 0.1 \dot{M}_b c^2 \sim 10^{47}\text{--}10^{51} \text{ erg s}^{-1}$ for accretion rates in the range $\dot{M}_b \sim 10^{-6}$ to $10^{-2} M_{\odot} \text{ s}^{-1}$.

A.4. Possible Evolutionary Scenario for $\text{CO}_{\text{core}}\text{--NS}$ Binary Formation

Two independent communities have introduced a new evolutionary scenario for the formation of compact-object binaries (NS–NS or NS–BH). After the collapse of the primary star forming an NS, the binary undergoes mass-transfer episodes, finally leading to the ejection of both the hydrogen and helium shells of the secondary star. These processes lead naturally to a binary composed of a CO_{core} and an NS companion. In the X-ray binary and SN communities these

systems are called “ultra-stripped” binaries (see, e.g., Tauris et al. 2015b). These systems are expected to compose 0.1%–1% of the total SNe (Tauris et al. 2013).

In the above studies most of the binaries have orbital periods in the range of 3×10^3 – 3×10^5 s, which are longer than the periods expected in the BdHN scenario. The formation of the CO_{core}–NS binaries leading to BdHNe might be a subset of the ultra-stripped binaries. In such a subset the conditions of the initial orbital separation and CO_{core} mass must be such as to lead to final orbital periods in the range of 100–1000 s. Assuming an SN rate of 2×10^4 Gpc^{−3} yr^{−1} (Guetta & Della Valle 2007), the ultra-stripped binaries would have a rate of 20–200 Gpc^{−3} yr^{−1}, and thus BdHNe, with a rate of ~ 1 Gpc^{−3} yr^{−1} (see Table 1 and Ruffini et al. 2016b), might be produced by the 0.5%–5% of the ultra-stripped binary population.

A.5. Post-explosion Orbits and NS–BH Binary Formation

The SN explosion leaves as a central remnant the ν NS, while the NS companion might lead, for sufficient accretion rates, to the formation of a BH. We examined in Fryer et al. (2015b) the question whether BdHNe can indeed form NS–BH binaries or, on the contrary, they are disrupted by the SN explosion.

Most of the typical binaries become unbound during an SN explosion owing to the amount of mass loss and momentum imparted (kick) to the ν NS in the explosion. Assuming an instantaneous explosion, the binary is disrupted if half of the binary mass is lost. For this reason the fraction of massive binaries that can produce double compact-object binaries might be as low as $\sim 0.001\%$ – 1% (Fryer et al. 1999a; Dominik et al. 2012; Postnov & Yungelson 2014). Indeed, this is consistent with our estimated GRB local observed rates: we have shown in Section 3.1 that the NS–NS population leading to short bursts can be explained as being descendant from the CO_{core}–NS if $\sim 1\%$ of them remain bound after the SN explosion.

Assuming instantaneous mass loss, the post-explosion semimajor axis is (Hills 1983)

$$\frac{a}{a_0} = \frac{M_0 - \Delta M}{M_0 - 2a_0 \Delta M / r}, \quad (29)$$

where a_0 and a are the initial and final semimajor axes, respectively, M_0 is the (initial) binary mass, ΔM is the change of mass (in this case the amount of mass loss), and r is the orbital separation before the explosion. For circular orbits, the system is unbound if it loses half of its mass. For the very tight BdHNe, however, additional effects have to be taken into account to determine the fate of the binary.

The shock front in an SN moves at roughly 10^4 km s^{−1}, but the denser, lower-velocity ejecta can move at velocities as low as 10^2 – 10^3 km s^{−1} (Fryer et al. 2014). This implies that the SN ejecta overcomes an NS companion in a time 10–1000 s. For wide binaries this time is a small fraction of the orbital period and the “instantaneous” mass-loss assumption is perfectly valid. BdHNe have instead orbital periods as short as 100–1000 s; hence, the instantaneous mass-loss approximation breaks down.

We recall the specific examples studied in Fryer et al. (2015b): close binaries in an initial circular orbit of radius 7×10^9 cm, CO_{core} radii of $(1\text{--}4) \times 10^9$ cm with a $2.0 M_\odot$ NS companion. The CO_{core} leaves a central $1.5 M_\odot$ NS, ejecting the rest of the core. The NS leads to a BH with a mass equal to the NS critical mass. For these parameters it was there obtained that even if 70% of the mass is lost, the binary remains bound

provided that the explosion time is of the order of the orbital period ($P = 180$ s) with semimajor axes of less than 10^{11} cm.

The tight ν NS–BH binaries produced by BdHNe will, in due time, merge owing to the emission of GWs. For the above typical parameters the merger time is of the order of 10^4 yr, or even less. We expect little baryonic contamination around such a merger site since this region has been cleaned up by the BdHN. These conditions lead to a new family of sources that we have called ultrashort GRBs, U-GRBs.

Appendix B

Local Density Rate of GRB Subclasses

We recall now the method used in Ruffini et al. (2016b) to estimate, for each GRB subclass, the local observed density rates that we use in this work. This is defined by the convolution of the luminosity function, which tells us the fraction of bursts with isotropic equivalent luminosities in the interval $\log L$ and $\log L + d \log L$, and the cosmic GRB occurrence rate, which tells us the number of sources at different redshifts. These functions depend on a priori assumptions, and some investigations have been carried out in the literature: for long bursts (e.g., Soderberg et al. 2006b; Guetta & Della Valle 2007; Liang et al. 2007; Virgili et al. 2009; Rangel Lemos et al. 2010; Wanderman & Piran 2010; Guetta et al. 2011; Kovacevic et al. 2014), for short bursts (e.g., Virgili et al. 2011; Wanderman & Piran 2015), and for both long and short bursts (e.g., Sun et al. 2015). Additional properties that introduce further uncertainties are the instrumental sensitivity threshold, the field of view Ω_i , and the operational time T_i of the i -detector.

Hereafter we neglect the possible redshift evolution of the luminosity function. For ΔN_i events detected by various detectors in a finite logarithmic luminosity bin from $\log L$ to $\log L + \Delta \log L$, the total local event rate density between observed minimum (L_{\min}) and maximum (L_{\max}) luminosities is (e.g., Sun et al. 2015)

$$\rho_0 \simeq \sum_i \sum_{\log L_{\min}}^{\log L_{\max}} \frac{4\pi}{\Omega_i T_i} \frac{1}{\ln 10} \frac{1}{g(L)} \frac{\Delta N_i}{\Delta \log L} \frac{\Delta L}{L}, \quad (30)$$

where

$$g(L) = \int_0^{z_{\max}(L)} \frac{f(z)}{1+z} \frac{dV(z)}{dz} dz, \quad (31)$$

and the comoving volume is

$$\frac{dV(z)}{dz} = \frac{c}{H_0} \frac{4\pi d_L^2}{(1+z)^2 [\Omega_M(1+z)^3 + \Omega_\Lambda]^{1/2}}, \quad (32)$$

where d_L is the luminosity distance. We set $f(z) = 1$, namely, we do not assume any redshift dependence of the GRB cosmic event rate density. The maximum volume within which the event of luminosity L can be detected is defined by the maximum redshift $z_{\max}(L)$. The latter is computed, following Schaefer (2007), from the 1 s bolometric peak luminosity L , k -corrected from the observed detector energy band into the burst cosmological rest-frame energy band $1\text{--}10^4$ keV, and the corresponding 1 s threshold peak flux f_{th} . This is the limiting peak flux for the burst detection (Band 2003). With this, z_{\max} can be defined from

(see, e.g., Zhang et al. 2009; Ruffini et al. 2014)

$$f_{\text{th}} = \frac{L}{4\pi d_L^2(z_{\text{max}})k}. \quad (33)$$

The possible evolution with the redshift of the GRB density rates has been analyzed in Ruffini et al. (2016b) by separating the bursts into several redshift bins, following the method suggested in Sun et al. (2015). In each redshift interval $z_j \leq z \leq z_{j+1}$, the integration limits of Equation (31) are replaced by z_j and $\min[z_{j+1}, z_{\text{max},j}(L)]$, where $z_{\text{max},j}(L)$ is the maximum redshift for the j th redshift bin. Finally, from Equation (30) an event rate ρ_0^z in each redshift bin around z is obtained.

We adopt the fields of view and operational times for the detectors: *BeppoSAX*, $\Omega_{\text{BS}} = 0.25$ sr, $T_{\text{BS}} = 7$ yr; *BATSE*, $\Omega_{\text{B}} = \pi$ sr, $T_{\text{B}} = 10$ yr, *HETE-2*, $\Omega_{\text{H}} = 0.8$ sr, $T_{\text{H}} = 7$ yr; *Swift-BAT*, $\Omega_{\text{S}} = 1.33$ sr, $T_{\text{S}} = 10$ yr; *Fermi-GBM*, $\Omega_{\text{F}} = 9.6$ sr, $T_{\text{F}} = 7$ yr. We adopt no beaming correction.

ORCID iDs

M. Muccino  <https://orcid.org/0000-0002-2234-9225>
 J. A. Rueda  <https://orcid.org/0000-0002-3455-3063>
 C. L. Bianco  <https://orcid.org/0000-0001-7749-4078>
 M. Kovacevic  <https://orcid.org/0000-0003-4928-4510>
 G. B. Pisani  <https://orcid.org/0000-0003-3452-2491>

References

- Abbott, B. P., Abbott, R., Abbott, T. D., et al. 2016, *LRR*, 19, 1
 Abbott, B. P., Abbott, R., Abbott, T. D., et al. 2017a, *ApJL*, 848, L13
 Abbott, B. P., Abbott, R., Abbott, T. D., et al. 2017b, *PhRvL*, 119, 161101
 Aimuratov, Y., Ruffini, R., Muccino, M., et al. 2017a, *ApJ*, 844, 83
 Aimuratov, Y., Ruffini, R., Muccino, M., et al. 2017b, arXiv:1704.08179
 Allen, B., Anderson, W. G., Brady, P. R., Brown, D. A., & Creighton, J. D. E. 2012, *PhRvD*, 85, 122006
 Anninos, P., Hobbil, D., Seidel, E., Smarr, L., & Suen, W.-M. 1995, *PhRvD*, 52, 2044
 Antoniadis, J., Freire, P. C. C., Wex, N., et al. 2013, *Sci*, 340, 448
 Astone, P., Ballantini, R., Babusci, D., et al. 2006, *CQGra*, 23, S57
 Astone, P., Ballantini, R., Babusci, D., et al. 2008, *CQGra*, 25, 114048
 Band, D. L. 2003, *ApJ*, 588, 945
 Becerra, L., Bianco, C. L., Fryer, C. L., Rueda, J. A., & Ruffini, R. 2016, *ApJ*, 833, 107
 Becerra, L., Cipolletta, F., Fryer, C. L., Rueda, J. A., & Ruffini, R. 2015, *ApJ*, 812, 100
 Belczynski, K., Bulik, T., & Bailyn, C. 2011, *ApJL*, 742, L2
 Belczynski, K., Bulik, T., & Rudak, B. 2002, *ApJ*, 571, 394
 Belczynski, K., Repetto, S., Holz, D. E., et al. 2016, *ApJ*, 819, 108
 Belvedere, R., Boshkayev, K., Rueda, J. A., & Ruffini, R. 2014, *NuPhA*, 921, 33
 Berger, E. 2014, *ARA&A*, 52, 43
 Bernuzzi, S., Dietrich, T., & Nagar, A. 2015, *PhRvL*, 115, 091101
 Bildsten, L., & Cutler, C. 1992, *ApJ*, 400, 175
 Cadelano, M., Pallanca, C., Ferraro, F. R., et al. 2015, *ApJ*, 812, 63
 Caito, L., Bernardini, M. G., Bianco, C. L., et al. 2009, *A&A*, 498, 501
 Camp, J. B., & Cornish, N. J. 2004, *ARNPS*, 54, 525
 Chevalier, R. A. 1989, *ApJ*, 346, 847
 Cipolletta, F., Cherubini, C., Filippi, S., Rueda, J. A., & Ruffini, R. 2015, *PhRvD*, 92, 023007
 Cipolletta, F., Cherubini, C., Filippi, S., Rueda, J. A., & Ruffini, R. 2017, *PhRvD*, 96, 024046
 Clark, J. P. A., & Eardley, D. M. 1977, *ApJ*, 215, 311
 Cowperthwaite, P. S., Berger, E., Villar, V. A., et al. 2017, *ApJL*, 848, L17
 Dai, Z. G., & Lu, T. 1998a, *A&A*, 333, L87
 Dai, Z. G., & Lu, T. 1998b, *PhRvL*, 81, 4301
 Davis, M., Ruffini, R., Press, W. H., & Price, R. H. 1971, *PhRvL*, 27, 1466
 Davis, M., Ruffini, R., & Tiomno, J. 1972, *PhRvD*, 5, 2932
 Della Valle, M., Chincarini, G., Panagia, N., et al. 2006, *Natur*, 444, 1050
 Detweiler, S. 1980, *ApJ*, 239, 292
 Detweiler, S. L., & Szedenits, E., Jr. 1979, *ApJ*, 231, 211
 Dominik, M., Belczynski, K., Fryer, C., et al. 2012, *ApJ*, 759, 52
 Dominik, M., Berti, E., O'Shaughnessy, R., et al. 2015, *ApJ*, 806, 263
 Dutra, M., Lourenço, O., Avancini, S. S., et al. 2014, *PhRvC*, 90, 055203
 Dutra, M., Lourenço, O., & Menezes, D. P. 2016, *PhRvC*, 93, 025806
 Eichler, D., Livio, M., Piran, T., & Schramm, D. N. 1989, *Natur*, 340, 126
 Finn, L. S., & Chernoff, D. F. 1993, *PhRvD*, 47, 2198
 Flanagan, É. É., & Hughes, S. A. 1998, *PhRvD*, 57, 4535
 Fong, W., Berger, E., Margutti, R., et al. 2012, *ApJ*, 756, 189
 Fong, W., Berger, E., Margutti, R., & Zauderer, B. A. 2015, *ApJ*, 815, 102
 Fong, W., Berger, E., Metzger, B. D., et al. 2014, *ApJ*, 780, 118
 Fox, D. B., Frail, D. A., Price, P. A., et al. 2005, *Natur*, 437, 845
 Fryer, C. L. 2009, *ApJ*, 699, 409
 Fryer, C. L., Belczynski, K., Ramirez-Ruiz, E., et al. 2015a, *ApJ*, 812, 24
 Fryer, C. L., Benz, W., & Herant, M. 1996, *ApJ*, 460, 801
 Fryer, C. L., Herwig, F., Hungerford, A., & Timmes, F. X. 2006, *ApJL*, 646, L131
 Fryer, C. L., Oliveira, F. G., Rueda, J. A., & Ruffini, R. 2015b, *PhRvL*, 115, 231102
 Fryer, C. L., Rueda, J. A., & Ruffini, R. 2014, *ApJ*, 793, L36
 Fryer, C. L., & Woosley, S. E. 1998, *ApJL*, 502, L9
 Fryer, C. L., Woosley, S. E., & Hartmann, D. H. 1999a, *ApJ*, 526, 152
 Fryer, C. L., Woosley, S. E., Herant, M., & Davies, M. B. 1999b, *ApJ*, 520, 650
 Ghirlanda, G., Salafia, O. S., Pescalli, A., et al. 2016, *A&A*, 594, A84
 Giacconi, R., & Ruffini, R. (ed.) 1978, *Physics and Astrophysics of Neutron Stars and Black Holes* (Amsterdam: North Holland Publishing Co.)
 Goldstein, A., Veres, P., Burns, E., et al. 2017, *ApJL*, 848, L14
 Goodman, J. 1986, *ApJL*, 308, L47
 Guetta, D., & Della Valle, M. 2007, *ApJL*, 657, L73
 Guetta, D., Pian, E., & Waxman, E. 2011, *A&A*, 525, A53
 Haggard, D., Nynka, M., Ruan, J. J., et al. 2017, *ApJL*, 848, L25
 Hills, J. G. 1983, *ApJ*, 267, 322
 Izzo, L., Rueda, J. A., & Ruffini, R. 2012a, *A&A*, 548, L5
 Izzo, L., Ruffini, R., Penacchioni, A. V., et al. 2012b, *A&A*, 543, A10
 Kawaguchi, K., Kyutoku, K., Nakano, H., et al. 2015, *PhRvD*, 92, 024014
 Klein, A., Barausse, E., Sesana, A., et al. 2016, *PhRvD*, 93, 024003
 Kluźniak, W., & Ruderman, M. 1998, *ApJL*, 505, L113
 Kobayashi, S., & Mészáros, P. 2003, *ApJ*, 589, 861
 Kovacevic, M., Izzo, L., Wang, Y., et al. 2014, *A&A*, 569, A108
 Landau, L. D., & Lifshitz, E. M. 1975, *The Classical Theory of Fields*, Vol. 2 (Oxford: Pergamon)
 Lazarus, P., Tauris, T. M., Knispel, B., et al. 2014, *MNRAS*, 437, 1485
 Lee, W. H., Ramirez-Ruiz, E., & Page, D. 2004, *ApJL*, 608, L5
 Liang, E., Zhang, B., Virgili, F., & Dai, Z. G. 2007, *ApJ*, 662, 1111
 LIGO Scientific Collaboration, Aasi, J., Abbott, B. P., et al. 2015, *CQGra*, 32, 074001
 MacFadyen, A. I., & Woosley, S. E. 1999, *ApJ*, 524, 262
 MacFadyen, A. I., Woosley, S. E., & Heger, A. 2001, *ApJ*, 550, 410
 Maggiore, M. 2007, *Gravitational Waves*, Vol 1: Theory and Experiments (Oxford: Oxford Univ. Press)
 Meszaros, P., & Rees, M. J. 1997, *ApJL*, 482, L29
 Mirabel, I. F., & Rodríguez, L. F. 1998, *Natur*, 392, 673
 Muccino, M., Ruffini, R., Bianco, C. L., Izzo, L., & Penacchioni, A. V. 2013, *ApJ*, 763, 125
 Narayan, R., Piran, T., & Shemi, A. 1991, *ApJL*, 379, L17
 Nicuesa Guelbenzu, A., Klose, S., Rossi, A., et al. 2011, *A&A*, 531, L6
 Paczynski, B. 1986, *ApJL*, 308, L43
 Paschalidis, V., MacLeod, M., Baumgarte, T. W., & Shapiro, S. L. 2009, *PhRvD*, 80, 024006
 Patricelli, B., Razzano, M., Cella, G., et al. 2016, *JCAP*, 11, 056
 Peters, P. C. 1964, *PhRv*, 136, 1224
 Peters, P. C., & Mathews, J. 1963, *PhRv*, 131, 435
 Postnov, K. A., & Yungelson, L. R. 2014, *LRR*, 17, 3
 Rangel Lemos, L. J., Bianco, C. L., Mosquera Cuesta, H. J., Rueda, J. A., & Ruffini, R. 2010, in 25th Texas Symp. Relativistic Astrophysics, ed. F. M. Rieger, C. van Eldik, & W. Hofmann (Triste: SISSA), 204
 Rees, M., Ruffini, R., & Wheeler, J. A. 1974, *Black Holes, Gravitational Waves and Cosmology* (New York: Gordon and Breach Science Publishers Inc.)
 Rhoades, C. E., & Ruffini, R. 1974, *PhRvL*, 32, 324
 Rigault, M., Aldering, G., Kowalski, M., et al. 2015, *ApJ*, 802, 20
 Rosswog, S., Ramirez-Ruiz, E., & Davies, M. B. 2003, *MNRAS*, 345, 1077

- Rueda, J. A., & Ruffini, R. 2012, [ApJL](#), **758**, L7
- Ruffini, R., Bernardini, M. G., Bianco, C. L., et al. 2006, in The Tenth Marcel Grossmann Meeting, ed. M. Novello, S. Perez Bergliaffa, & R. Ruffini (Singapore: World Scientific), 369
- Ruffini, R., Bernardini, M. G., Bianco, C. L., et al. 2007, in Proc. of the VI INTEGRAL Workshop, The Obscured Universe, ed. S. Grebenev, R. Sunyaev, & C. Winkler (Noordwijk: ESA), 561
- Ruffini, R., Bernardini, M. G., Bianco, C. L., et al. 2008, in Proc. of the MG11 Meeting on General Relativity, The Eleventh Marcel Grossmann Meeting On Recent Developments in Theoretical and Experimental General Relativity, Gravitation and Relativistic Field Theories, ed. H. Kleinert, R. T. Jantzen, & R. Ruffini (Singapore: World Scientific), 368
- Ruffini, R., Bianco, C. L., Frascetti, F., Xue, S.-S., & Chardonnet, P. 2001, [ApJL](#), **555**, L117
- Ruffini, R., Izzo, L., Muccino, M., et al. 2014, [A&A](#), **569**, A39
- Ruffini, R., Muccino, M., Aimuratov, Y., et al. 2016a, [ApJ](#), **831**, 178
- Ruffini, R., Muccino, M., Aimuratov, Y., et al. 2018a, arXiv:1802.07552
- Ruffini, R., Muccino, M., Kovacevic, M., et al. 2015a, [ApJ](#), **808**, 190
- Ruffini, R., Rueda, J. A., Muccino, M., et al. 2016b, [ApJ](#), **832**, 136
- Ruffini, R., Wang, Y., Aimuratov, Y., et al. 2018b, [ApJ](#), **852**, 53
- Ruffini, R., Wang, Y., Enderli, M., et al. 2015b, [ApJ](#), **798**, 10
- Ruffini, R., & Wilson, J. 1973, [PhRvL](#), **31**, 1362
- Savchenko, V., Ferrigno, C., Kuulkers, E., et al. 2017, [ApJL](#), **848**, L15
- Schaefer, B. E. 2007, [ApJ](#), **660**, 16
- Shibata, M., & Taniguchi, K. 2011, [LRR](#), **14**, 6
- Smartt, S. J. 2009, [ARA&A](#), **47**, 63
- Smartt, S. J. 2015, [PASA](#), **32**, e016
- Soderberg, A. M., Berger, E., Kasliwal, M., et al. 2006a, [ApJ](#), **650**, 261
- Soderberg, A. M., Kulkarni, S. R., Nakar, E., et al. 2006b, [Natur](#), **442**, 1014
- Sun, H., Zhang, B., & Li, Z. 2015, [ApJ](#), **812**, 33
- Tauris, T. M., Kaspi, V. M., Breton, R. P., et al. 2015a, in Proc. of Advancing Astrophysics with the Square Kilometre Array (AASKA14), Understanding the Neutron Star Population with the SKA (Triste: SISSA), 39
- Tauris, T. M., Langer, N., Moriya, T. J., et al. 2013, [ApJL](#), **778**, L23
- Tauris, T. M., Langer, N., & Podsiadlowski, P. 2015b, [MNRAS](#), **451**, 2123
- Tauris, T. M., van den Heuvel, E. P. J., & Savonije, G. J. 2000, [ApJL](#), **530**, L93
- Usov, V. V. 1992, [Natur](#), **357**, 472
- Virgili, F. J., Liang, E.-W., & Zhang, B. 2009, [MNRAS](#), **392**, 91
- Virgili, F. J., Zhang, B., O'Brien, P., & Troja, E. 2011, [ApJ](#), **727**, 109
- Wanderman, D., & Piran, T. 2010, [MNRAS](#), **406**, 1944
- Wanderman, D., & Piran, T. 2015, [MNRAS](#), **448**, 3026
- Woosley, S. E. 1993, [ApJ](#), **405**, 273
- Woosley, S. E., & Bloom, J. S. 2006, [ARA&A](#), **44**, 507
- Yonetoku, D., Nakamura, T., Sawano, T., Takahashi, K., & Toyano, A. 2014, [ApJ](#), **789**, 65
- Zel'dovich, Y. B., Ivanova, L. N., & Nadezhin, D. K. 1972, [SvA](#), **16**, 209
- Zhang, B., & Mészáros, P. 2001, [ApJL](#), **552**, L35
- Zhang, B., Zhang, B., Virgili, F. J., et al. 2009, [ApJ](#), **703**, 1696
- Zhang, B.-B., Zhang, B., Sun, H., et al. 2017, arXiv:1710.05851



The Spin Evolution of Fast-rotating, Magnetized Super-Chandrasekhar White Dwarfs in the Aftermath of White Dwarf Mergers

L. Becerra^{1,2}, J. A. Rueda^{1,2,3} , P. Lorén-Aguilar⁴ , and E. García-Berro^{5,6} 

¹Dipartimento di Fisica, Sapienza Università di Roma, P.le Aldo Moro 5, I-00185 Rome, Italy

²ICRANet, P.zza della Repubblica 10, I-65122 Pescara, Italy

³ICRANet-Rio, Centro Brasileiro de Pesquisas Físicas, Rua Dr. Xavier Sigaud 150, 22290-180 Rio de Janeiro, Brazil

⁴School of Physics, University of Exeter, Stocker Road, Exeter EX4 4QL, UK

⁵Departament de Física, Universitat Politècnica de Catalunya, c/Esteve Terrades, 5, E-08860 Castelldefels, Spain

⁶Institut d'Estudis Espacials de Catalunya, Ed. Nexus-201, c/Gran Capità 2-4, E-08034 Barcelona, Spain

Received 2016 September 1; revised 2018 March 30; accepted 2018 April 3; published 2018 April 25

Abstract

The evolution of the remnant of the merger of two white dwarfs is still an open problem. Furthermore, few studies have addressed the case in which the remnant is a magnetic white dwarf with a mass larger than the Chandrasekhar limiting mass. Angular momentum losses might bring the remnant of the merger to the physical conditions suitable for developing a thermonuclear explosion. Alternatively, the remnant may be prone to gravitational or rotational instabilities, depending on the initial conditions reached after the coalescence. Dipole magnetic braking is one of the mechanisms that can drive such losses of angular momentum. However, the timescale on which these losses occur depends on several parameters, like the strength of the magnetic field. In addition, the coalescence leaves a surrounding Keplerian disk that can be accreted by the newly formed white dwarf. Here we compute the post-merger evolution of a super-Chandrasekhar magnetized white dwarf taking into account all the relevant physical processes. These include magnetic torques acting on the star, accretion from the Keplerian disk, the threading of the magnetic field lines through the disk, and the thermal evolution of the white dwarf core. We find that the central remnant can reach the conditions suitable to develop a thermonuclear explosion before other instabilities (such as the inverse beta-decay instability or the secular axisymmetric instability) are reached, which would instead lead to gravitational collapse of the magnetized remnant.

Key words: accretion, accretion disks – stars: magnetic field – stars: rotation – supernovae: general – white dwarfs

1. Introduction

Type Ia supernovae (SNe Ia) are one of the most energetic explosive events in the cosmos. Since there is a well-established relationship between their intrinsic brightnesses and the shapes of their light curves (Phillips 1993) and, moreover, because they are so luminous that they can be detected at very large distances, SNe Ia can be used as standardizable cosmological candles. This has opened a new era in cosmology and has enabled us to measure the acceleration of the universe (Riess et al. 1998; Perlmutter et al. 1999). Additionally, SNe Ia play an important role in modern cosmology, since they allow us to probe the fundamental physical theories underlying dark energy—see, for instance, Weinberg et al. (2013) for a recent review on this interesting topic.

Nevertheless, despite the importance of SNe Ia, we still do not know the nature of their progenitor systems. Actually, this has remained a long-standing mystery for several decades. We do know that the outburst is driven by the explosion of a carbon–oxygen white dwarf in a binary system, but we do not know the precise mechanism that destabilizes the white dwarf. Several hypotheses have been put forward over the years, and most likely SNe Ia may have a diversity of progenitors. In the following we superficially describe the possible evolutionary channels leading to an SN Ia. In the so-called single-degenerate (SD) channel a white dwarf in a binary system accretes matter from a nondegenerate companion and explodes as it approaches the Chandrasekhar limiting mass—see, for instance, Han & Podsiadlowski (2004) for a recent discussion. In the double-degenerate (DD) scenario two white dwarf

members of a close binary system lose angular momentum and energy through the radiation of gravitational waves, and a merger occurs (Iben & Tutukov 1984; Webbink 1984). Another possible scenario is the core-degenerate (CD) scenario. Within this formation channel a hot core is formed at the end of the common envelope phase of the binary system (Livio & Riess 2003; Kashi & Soker 2011), and the merger of the core of the asymptotic giant branch (AGB) star and a secondary white dwarf powers the explosion—see Aznar-Siguán et al. (2015) for a scroccess. Another recently proposed pathway is the white dwarf–white dwarf collisional scenario, in which two white dwarfs collide—see Aznar-Siguán et al. (2013) for a recent summary of the relevant literature on the subject. Despite some attractive features of this scenario, it has been shown that it can only account for at most a few percent of all SNe Ia (Ilkov & Soker 2013). Each of these formation channels has its own advantages and drawbacks, and in some cases these are severe. Currently, one of the most favored ones is the DD channel, because it provides adequate answers to two important observational facts, namely, the absence of hydrogen in the nebular phase (Leonard 2007) and the delay time distribution (Totani et al. 2008). Consequently, we focus on it.

Smoothed particle hydrodynamics (SPH) simulations of the coalescence of binary white dwarfs show that a prompt explosion is not always the result of the interaction during the dynamical phase of the merger (Yoon et al. 2007; Lorén-Aguilar et al. 2009). Only those binary systems in which both the secondary and primary stars are massive enough lead to an SN Ia outburst. Actually, the parameter space for violent mergers is very narrow (Pakmor et al. 2010; Sato et al. 2015),

and only when two carbon–oxygen white dwarfs of masses larger than $\sim 0.8 M_{\odot}$ merge is the result of the dynamical phase a prompt explosion. Within this theoretical framework, the dynamical phase of the merger is followed by a second phase in which the material of the debris region can be accreted and possibly lead to an SN Ia explosion.

The existing simulations of the coalescence of binary white dwarfs (Benz et al. 1990; Lorén-Aguilar et al. 2009; Raskin et al. 2012; Zhu et al. 2013; Dan et al. 2014) show that the final result of the coalescence consists of a central white dwarf made of the undisrupted primary star and a hot, convective corona made of about half of the mass of the disrupted secondary. This central remnant is surrounded by a heavy Keplerian disk, made of the rest of the mass of the disrupted secondary, since little mass is ejected from the system during the merger episode. The rapidly rotating, hot corona is convective, and an efficient $\alpha\omega$ dynamo can produce magnetic fields of up to $B \approx 10^{10}$ G (García-Berro et al. 2012). Recent two-dimensional magneto-hydrodynamic simulations of post-merger systems confirm the growth of the white dwarf magnetic field after the merger (Ji et al. 2013; Zhu et al. 2015). Thus, the role of magnetic fields in the aftermath of the dynamical merger needs to be explored. This is precisely the aim of the present work, as very few studies (Ji et al. 2013; Külebi et al. 2013; Beloborodov 2014) of the post-merger evolution including magnetism have been done so far. On the other hand, there are few works that explore the evolution of the post-merger systems but without considering the effects of the central remnant magnetic field—see, e.g., Yoon et al. (2007), van Kerkwijk et al. (2010), Shen et al. (2012), and Schwab et al. (2012).

Our paper is organized as follows. In Section 2 we explain the model of the evolution of the post-merger system. In particular, we describe the torques that act on the central remnant (Section 2.1), the structure of the rotating central white dwarf (Section 2.2), and its thermal evolution (Section 2.3). In Section 3 we present the prescriptions adopted to model the accretion rate on the central star. In Section 4 we present our choice of initial conditions. In Section 5 we discuss extensively the results of our simulations for two prescriptions to compute the accretion rate. Specifically, in Section 5.1 we discuss the case in which the accretion rate is obtained employing the cooling timescale, while in Section 5.2 we present the results obtained when it is computed using the viscous timescale. Finally, in Section 6 we compare our results with previous works, and in Section 7 we summarize our major findings, elaborate on their significance, and present our concluding remarks.

2. Numerical Setup for the Post-merger Evolution

Numerical simulations of binary white dwarf mergers indicate that in those cases in which a violent merger does not occur the merged configuration has three distinct regions (Benz et al. 1990; Guerrero et al. 2004; Lorén-Aguilar et al. 2009; Raskin et al. 2012; Zhu et al. 2013; Dan et al. 2014). First, there is the central white dwarf that rotates as a rigid solid. On top of it a hot, differentially rotating, convective corona can be found. This corona is made of matter accreted from the disrupted secondary star. The mass of this region is about half of the mass of the secondary white dwarf. Finally, surrounding these two regions there is a rapidly rotating Keplerian disk, which is made of the rest of the material of the disrupted secondary, since only a small amount

of mass is ejected from the system during the coalescence. The evolution of the post-merger configuration depends, naturally, on the mass of the central remnant, which is made of the primary white dwarf and the hot corona, and on the properties of the surrounding disk.

Before entering into details, it is important to discuss some timescales, which are relevant to adopting a reasonable approximation for the evolution of the system. The post-merger configuration formed in the coalescence has a clear hierarchy of timescales. First comes the dynamical timescale $t_{\text{dyn}} \sim \Omega^{-1}$, with Ω being the rotation velocity. This timescale is typically of the order of a few seconds. Next in order of magnitude is the viscous timescale, t_{visc} , of the Keplerian disk. This timescale governs the transport of disk mass inward and of angular momentum outward. The viscous phase of the evolution is normally followed using the Shakura–Sunyaev α prescription (Shakura & Sunyaev 1973). Adopting typical values, van Kerkwijk et al. (2010) found that t_{visc} ranges between 10^3 and 10^4 s. However, for the merger remnants studied here we find that the viscous timescales could be significantly shorter, typically 1 s—see Section 3.2. These viscous timescales are a little longer than, but of the same order as, the dynamical timescale of the post-merger, super-Chandrasekhar white dwarf studied here ($t_{\text{dyn}} \sim 0.2\text{--}0.3$ s; see Section 2.2). Finally, in this set of characteristic times is the thermal timescale of the merger product, t_{th} , which is typically much longer and will be discussed in detail for every simulation.

In the following we first discuss the interactions between the remnant and the disk in order to identify the torque that acts on the central remnant and model the evolution of its angular momentum. Then we present how we model the structure of the rotating white dwarf central remnant, as well as its thermal evolution. The fate of the white dwarf depends crucially on the accretion rate in the post-merger phase. Thus, we consider two very different physical scenarios to determine the accretion rate onto the central remnant. In the first of them the accretion rate is determined by the viscous timescale, whereas in the second scenario the accretion rate is governed by the thermal timescale. These will be discussed in Section 3.

2.1. Torques on the Central Remnant

The most commonly employed model of disk evolution is that of Ghosh & Lamb (1979). This model was later improved by Wang (1987, 1995). Within this model the magnetic field of the remnant penetrates the disk in a broad transition zone as a result of the Kelvin–Helmholtz instabilities, turbulent diffusion, and magnetic field reconnection. Furthermore, the material of the disk corotates with the star only in a narrow region and reaches its surface channeled by the magnetic field lines. We assume that the magnetic field of the remnant penetrates the disk up to approximately the Alfvén radius (Davidson & Ostriker 1973):

$$R_{\text{mag}} = \left(\frac{\mu_{\text{WD}}^2}{\dot{M}_{\text{disk}} \sqrt{2GM_{\text{WD}}}} \right)^{2/7}, \quad (1)$$

where $\mu_{\text{WD}} = B_{\text{WD}} R_{\text{WD}}^3$ is the magnetic moment of the star, B_{WD} is its magnetic field, and \dot{M}_{disk} is the mass flow through the inner radius of the disk, R_0 .

The angular momentum per unit mass entering into the magnetosphere of the white dwarf through the inner radius is

$l_0 = R_0^2 \Omega_K^0$, where

$$\Omega_K^0 = \left(\frac{GM_{\text{WD}}}{R_0^3} \right)^{1/2} \quad (2)$$

is the Keplerian angular velocity at R_0 . This material is channeled by the magnetic field onto the surface of the remnant. Thus, the resulting spin-up torque on the star due to accretion of disk matter is given by

$$T_{\text{acc}} = \xi_{\text{acc}} \dot{M}_{\text{WD}} R_0^2 \Omega_K(R_0), \quad (3)$$

where $\dot{M}_{\text{WD}} = \varepsilon \dot{M}_{\text{disk}}$ is the mass accretion rate on the white dwarf, ε measures how efficient accretion is, and ξ_{acc} is a parameter that accounts for the deceleration of the accreted matter in the inner region of the disk. The values adopted for these two parameters will be discussed below. If the star rotates faster than the matter at the inner disk radius, the centrifugal barrier blocks this material. Hence, it cannot reach the surface of the newly born white dwarf. This matter is therefore ejected from the system. This happens when the inner edge of the disk moves beyond the corotation radius, which is beyond the distance at which the disk rotates with the same angular velocity of the central object:

$$R_{\text{co}} = \left(\frac{GM_{\text{WD}}}{\Omega_{\text{WD}}^2} \right)^{1/3}. \quad (4)$$

When $R_0 > R_{\text{co}}$, the system enters into the dubbed *propeller regime* (Illarionov & Sunyaev 1975). During this phase, the material reaching the magnetosphere is ejected with higher specific angular momentum than the one it had previously, thus resulting in a spin-down torque acting on the star. This torque is given by (Menou et al. 1999)

$$T_{\text{prop}} = \sqrt{GM_{\text{WD}} R_0} \dot{M}_{\text{disk}} (1 - \omega_f). \quad (5)$$

In this expression we have introduced the so-called *fastness parameter*:

$$\omega_f = \Omega_{\text{WD}} / \Omega_K(R_0) = (R_0 / R_{\text{co}})^{3/2}. \quad (6)$$

The rotating magnetic field of the star originates an induced electric field that results in a wind. The wind fills the magnetosphere and corotates with the star (Goldreich & Julian 1969). At the light cylinder, $R_{\text{lc}} = c / \Omega_{\text{WD}}$, the corotation velocity reaches the speed of light, delimiting the region within which corotation of the magnetosphere is enforced. At larger distances, the field lines become open. For the spin-down torque due to electromagnetic energy losses in a force-free magnetosphere, T_{dip} , we adopt the result of Spitkovsky (2006):

$$T_{\text{dipole}} = k_1 \frac{\mu_{\text{WD}}^2 \Omega_{\text{WD}}^3}{c^3} (1 + k_2 \sin^2 \theta), \quad (7)$$

where $k_1 = 1 \pm 0.05$, $k_2 = 1 \pm 0.1$, and θ is the angle between the magnetic moment and the rotation axis of the star.

Finally, an additional torque, T_{mag} , results from the interaction of the disk with the magnetic field of the white dwarf. According to Ghosh & Lamb (1979), matter of the disk moving in the magnetic field of the white dwarf generates currents that confine the stellar field inside the disk. The magnetic field threading the disk is $\mathbf{B}_{\text{disk}} = \eta \mathbf{B}_{\text{WD}}^{\text{p}}$, where \mathbf{B}_{WD}

is the magnetic field of the white dwarf, $\mathbf{B}_{\text{WD}}^{\text{p}}$ is its projection on the plane of the disk, and $\eta \leq 1$ is the screening coefficient that accounts for the effect of currents in the partially diamagnetic disk induced by the stellar field. In particular, the poloidal field induces an azimuthal current due to the radial motion of the plasma, which partially screens the stellar magnetic field. Also, the relative motion between the disk and the star magnetosphere generates a toroidal field, B_ϕ . In the simulations, we have considered that the growth of B_ϕ is limited by diffusive decay due to turbulent mixing within the disk (Wang 1995). Following the analytical formulation of Wang (1997), the magnetic torque acting on the central star due to its interaction with the disk is given by

$$T_{\text{mag}} = \frac{\Gamma \eta^2 \mu_{\text{WD}}^2}{R_0^3} \times \left[\frac{2h}{R_0} (1 - \omega_f) \sin^2 \theta + \frac{\cos^2 \theta}{3} (1 - 2\omega_f) \right], \quad (8)$$

where $h \ll 1$ is the thickness of the disk and $\Gamma \simeq 1$ is a parameter that characterizes the steepness in the vertical transition from Keplerian rotation inside the disk to corotation with the star at the top of the disk. In the derivation of Equation (8), the magnetic field of the white dwarf has been approximated as a dipole, and it was assumed that the rotating axis of the star is perpendicular to the plane of the disk. Note that this expression generalizes the models of Wang (1987, 1995).

Based on this, the post-merger evolution of the angular momentum of the white dwarf is the result of the combined effect of the dipole radiation torque, T_{dipole} , the accretion torque, T_{acc} , the disk-interaction torque, T_{disk} , and the propeller torque T_{prop} :

$$\dot{J}_{\text{WD}} = \begin{cases} T_{\text{acc}} & R_{\text{WD}} > R_0 \\ T_{\text{acc}} + T_{\text{dipole}} + T_{\text{mag}} & R_{\text{WD}} < R_0 \wedge \omega_f \leq 1. \\ T_{\text{dipole}} + T_{\text{prop}} & R_{\text{WD}} < R_0 \wedge \omega_f > 1 \end{cases} \quad (9)$$

In the simulations presented here we assumed that the inner disk radius is the Alfvén radius.

2.2. Rotating White Dwarf Configurations

We follow the evolution of the spin of the post-merger remnant, calculating at every time step the new stable rotating configuration with mass, $M_{\text{WD}} + \delta M$, and angular momentum, $J_{\text{WD}} + \delta J$, adopting the slow rotation approximation (Hartle 1967; Hartle & Thorne 1968). We also assumed that the central remnant product of the merger rotates as a rigid body, as predicted by detailed SPH simulations (Lorén-Aguilar et al. 2009). The equation of state of the white dwarf is assumed to be that of a zero-temperature degenerate electron gas (Chandrasekhar 1931), to which we add the corresponding contribution of ions.

The region of stability of uniformly rotating white dwarfs is bound by the secular axisymmetric instability limit, the mass shedding or Keplerian limit, and the inverse β -decay instability limit, which for pure carbon is $3.49 \times 10^{10} \text{ g cm}^3$ (Rotondo et al. 2011; Boshkayev et al. 2013).

Figure 1 shows the mass–central density relation for the general relativistic uniformly rotating white dwarfs: the static,

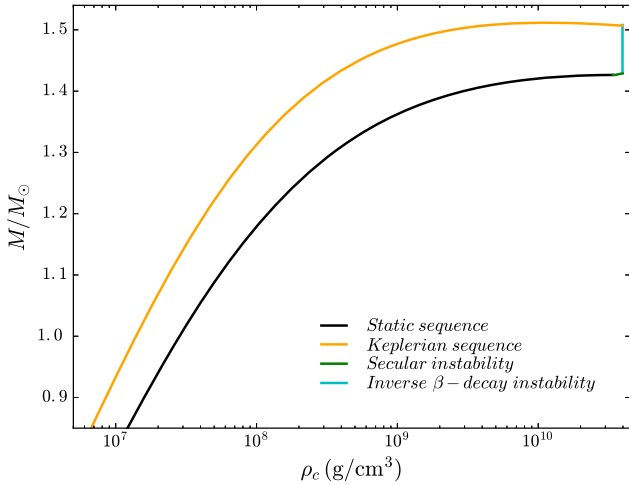


Figure 1. Instability lines of rotating white dwarfs in the diagram of mass vs. central density. The stability region is delimited by the static sequence (black line), the Keplerian sequence (orange line), the line of secular instability (green line), and the inverse β -decay line (blue).

Keplerian, secular axisymmetric instability and inverse β -decay sequences enclose the stability region. The mass-shedding, or Keplerian, limit is reached when the angular velocity of the star equals the Keplerian velocity of a particle orbiting at the equator, namely, when the centrifugal and gravitational forces are balanced. In this situation matter at the surface of the star is marginally bound to it. Hence, small perturbations result in mass loss until the star either becomes stable again or arrives at a dynamical instability point (Shibata et al. 2000; Stergioulas 2003). If the white dwarf crosses the β -decay instability limit, electrons are captured by nuclei. Since the principal contribution to the pressure of the star comes from electrons, electron captures reduce the pressure, leading to an instability (Salpeter 1961). The secular axisymmetric instability arises because the star is unstable with respect to axisymmetric perturbations. In a first phase, the star is expected to evolve quasi-stationarily with the instability growth timescale, which depends on the time required for angular momentum to be redistributed either by viscous dissipation or by the emission of gravitational waves (Chandrasekhar 1970). This timescale is typically long compared to the dynamical timescale (Boshkayev et al. 2013), except in the nonrotating case, where they are equal, because in this case there is no angular momentum to be redistributed. Eventually, when the star crosses the dynamical instability limit, gravitational collapse takes place (Stergioulas 2003). A sufficient (but not necessary) condition for the onset of secular instability can be obtained using the turning-point method (Friedman et al. 1988). This method considers a sequence of uniformly rotating models of a given (constant) angular momentum. The secular axisymmetric instability sets in at the density of the turning point:

$$\left(\frac{\partial M(\rho_c, J)}{\partial \rho_c} \right)_J = 0. \quad (10)$$

Finally, the maximum mass of static configurations is the Chandrasekhar limiting mass $M_{\max} = M_{\text{Ch}} \approx 1.4 M_{\odot}$, while the maximum mass of rotating white dwarfs lies on the Keplerian sequence $M_{\max}^{J=0} = 1.52 M_{\odot}$. The configurations with mass between $M_{\max}^{J=0} < M_{\text{WD}} < M_{\max}^{J \neq 0}$ are called super-Chandrasekhar

white dwarfs and are metastable since they are supported by rotation. As the angular momentum of the star varies, the central white dwarf necessarily evolves toward one of the previously described instability limits (mass-shedding or secular axisymmetric instability).

2.3. Temperature of the Central Remnant

We turn now to the thermal evolution of the central white dwarf remnant. We have seen above in Sections 2.1 and 2.2, and we shall see below from the energy balance and transport equations, that the structure and thermal evolution of the white dwarf depend crucially on the accretion rate, which is set by the disk physics. In Section 3 we analyze the evolution and fate of the post-merger system for two physical prescriptions to set the accretion rate. In the first case the infall rate is driven by the disk angular momentum transport (viscous) timescale, which, owing to its shortness for the present binary parameters, leads to highly super-Eddington rates. It has been argued in the literature that the dissipation required to produce such very short viscous timescales might heat the disk to the point of carbon ignition (see, e.g., Mochkovitch & Livio 1990). Such heating effects are not accounted for in the disk model adopted here. In addition, we also compute the evolution of the system in the case when the matter infall is driven not by the viscous timescale but by the cooling timescale. We show that this assumption leads to accretion rates near the Eddington limit value.

The thermal evolution of an accreting white dwarf has been studied by many authors (Nomoto & Iben 1985; Saio & Nomoto 1985; Yoon et al. 2007). The main goal of most of these works was to establish whether the conditions that may lead to an SN Ia were reached. For instance, in a pioneering work Nomoto & Iben (1985) found that for accretion rates larger than a critical value $\dot{M}_{\text{crit}} \approx 2 \times 10^{-6} M_{\odot} \text{ yr}^{-1}$ the outer layers of the star are heated by mass accretion, while heat conduction and neutrino emission cool it. This results in a thermal inversion near the surface of the star and ultimately leads to an off-center carbon ignition. Saio & Nomoto (1985) followed the subsequent evolution of the star and determined that carbon is burned in the entire white dwarf, being the final outcome of an oxygen–neon white dwarf. However, these works only considered nonrotating configurations and constant accretion rates. More recently, Yoon et al. (2007) studied the viscous evolution of remnants of white dwarf mergers, introducing the effects of rotation, but did not consider the effects of the magnetic field of the white dwarf. The post-merger object was modeled as a differentially rotating white dwarf with a cold core and a hot envelope accreting mass from a surrounding Keplerian disk at a constant rate. This allowed them to compute the conditions under which the off-center ignition can be avoided for the case in which the magnetic field is not taken into account.

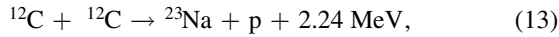
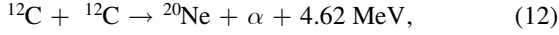
We have explained above (see Section 2.1) how the rotation rate of the merged remnant evolves owing to the interaction of the magnetic field and the disk, which are the equilibrium configurations of the rotating white dwarf. However, during the course of the evolution the temperature of the white dwarf also changes owing to accretion from the disk, which heats the white dwarf interior. This, in turn, may trigger an SN Ia explosion. In order to assess this possibility, we follow the evolution of the interior temperature of the post-merger central white dwarf in an approximate way, which is described next.

The equation of energy conservation reads

$$\frac{dL}{dm} = \epsilon_{\text{nuc}} - \epsilon_{\nu} + T\dot{s}, \quad (11)$$

where m is the mass coordinate (i.e., the mass enclosed within the radial distance r), L is the luminosity, T is the temperature, s is the specific entropy, and ϵ_{nuc} and ϵ_{ν} are the energy release and energy loss per unit mass by nuclear reactions and neutrino emission, respectively.

For carbon–oxygen white dwarfs, thermonuclear energy is essentially released by two nuclear reactions:



with nearly the same probability. We adopted the carbon fusion reaction rates of Gasques et al. (2005), which are valid for all regimes of ρ and T , which is from the thermonuclear regime to the pynuclear regime. For the neutrino energy losses, we used the analytical fits of Itoh et al. (1996), which consider electron–positron pair annihilation ($e^-e^+ \rightarrow \nu\bar{\nu}$), photo-neutrino emission ($e + \gamma \rightarrow e\nu\bar{\nu}$), plasmon decay ($\gamma \rightarrow \nu\bar{\nu}$), and electron–nucleus bremsstrahlung [$e(Z, A) \rightarrow e(Z, A)\nu\bar{\nu}$]. As will be discussed below, the dominant channel for neutrino losses in the central regions is electron–nucleus bremsstrahlung, while in the outer layers emission of neutrinos is dominated by plasmon decay.

The energy flux is given by

$$\frac{dT}{dr} = -\frac{3}{16\sigma} \frac{\kappa\rho}{T^3} \frac{L}{4\pi r^2}, \quad (14)$$

where σ is the Stephan–Boltzmann constant and κ is the opacity, which can be written as

$$\frac{1}{\kappa} = \frac{1}{\kappa_{\text{cond}}} + \frac{1}{\kappa_{\text{rad}}}, \quad (15)$$

with κ_{rad} and κ_{cond} the Rosseland mean radiative opacity and the conductive opacity, respectively. In the white dwarf core degeneracy is so high that the most efficient transport mechanism is conduction. Hence, the opacity is dominated by the first term. We adopted the thermal conductivity of Itoh et al. (1983, 1984), whereas for the radiative opacity we used Kramer’s law, $\kappa_{\text{rad}} = 4.34 \times 10^{24} \rho T^{-3.5} \text{ cm}^2 \text{ g}^{-1}$.

The change of entropy with time can be obtained from

$$T\dot{s} = c_v \dot{T} - \left[\frac{P}{\rho^2} - \left(\frac{\partial u}{\partial \rho} \right)_T \right] \dot{\rho}, \quad (16)$$

where u is the specific internal energy and c_v is the specific heat capacity at constant volume. The first term on the right-hand side of Equation (16) corresponds to the release of the internal energy, while the second term accounts for the change of gravitational potential energy due to the expansion or compression of the configuration.

To evaluate the term in square brackets in Equation (16), we considered a fully ionized nonideal electron–ion plasma, taking into account the ion–ion and the ion–electron Coulomb interactions, as well as the exchange–correlation corrections of electrons. We note that for super-Chandrasekhar white dwarfs both Coulomb corrections and quantum effects are important. The importance of Coulomb corrections is measured by the Coulomb coupling parameter $\Gamma = Z^2 e^2 / (aT)$, where

$a = (3/(4\pi n_i))^{1/3}$ is the mean interaction distance and n_i is the ion number density. At $\Gamma \lesssim 1$ the ions behave as a gas, at $\Gamma > 1$ as a strongly coupled Coulomb liquid, while crystallization occurs at $\Gamma \approx 175$. Quantum effects become important at temperatures smaller than $T_p = \hbar\omega_p/k_B$, where $\omega_p = (4\pi Z^2 e^2 n_i / m_i)^{1/2}$ is the ion plasma frequency. Finally, we used analytical fits to the heat capacity obtained from the free energy computed by Chabrier & Potekhin (1998) and Potekhin & Chabrier (2000).

Following Nomoto (1982), we obtained the density change by adopting the white dwarf mass coordinate, $q_{\text{WD}} \equiv m/M_{\text{WD}}$, as the independent variable:

$$\dot{\rho} = \left[\left(\frac{\partial \rho}{\partial M_{\text{WD}}} \right)_{q_{\text{WD}}} - \frac{q_{\text{WD}}}{M_{\text{WD}}} \left(\frac{\partial \rho}{\partial q_{\text{WD}}} \right)_{M_{\text{WD}}} \right] \dot{M}_{\text{WD}}. \quad (17)$$

This equation explicitly provides the contribution of the global structural changes, as well as the contribution of the internal distribution of density to the thermal evolution during the accretion process.

The post-merger evolution of the system is computed assuming that the central white dwarf evolves in a sequence of stable configurations (see Section 2.2). To calculate the evolution of the temperature, at each time step we integrate Equations (11) and (14) using Equations (16) and (17).

In order to integrate Equations (11) and (14), a set of boundary conditions at the surface of the star must be adopted. We treat the material accreted in each interval time as a thin envelope surrounding the star. Following Townsley & Bildsten (2004), we assume that the accreted material enters on top of the shell and pushes down the existing material deeper into the star. Then, the local heat equation becomes

$$T \left(\frac{\partial}{\partial t} + v_r \frac{\partial}{\partial r} \right) s \approx T v_r \frac{\partial s}{\partial r} = \frac{dL}{dm} - (\epsilon_{\text{nuc}} - \epsilon_{\nu}), \quad (18)$$

where $v_r = \dot{M}_{\text{WD}} / (4\pi r^2 \rho)$ is the velocity of the material given by mass conservation. We constructed static envelopes for each stable configuration with total mass M_{WD} and radius R_{WD} , integrating Equations (14) and (18).

To analyze whether the newly formed white dwarf reaches during its evolution the conditions suitable to produce an SN Ia, we adopted the following procedure. We first require as a necessary condition that the white dwarf crosses the ignition curve, i.e., the curve in the $\log \rho$ – $\log T$ plane where the nuclear energy released becomes larger than the neutrino emissivity, $\epsilon_{\text{nuc}} = \epsilon_{\nu}$. For temperatures and densities beyond this curve nuclear energy production exceeds neutrino losses and the star is heated, possibly leading to an SN outburst. Additionally, we require that burning proceeds in an almost instantaneous way. The characteristic time τ_{CC} of nuclear reactions is

$$\tau_{\text{CC}} = \frac{\epsilon_{\text{nuc}}}{\dot{\epsilon}_{\text{nuc}}} \approx \epsilon_{\text{nuc}} \left(\dot{T} \frac{\partial \epsilon_{\text{nuc}}}{\partial T} \right)^{-1} = c_p \left(\frac{\partial \epsilon_{\text{nuc}}}{\partial T} \right)^{-1}, \quad (19)$$

where c_p is the specific heat at constant pressure. If this characteristic timescale becomes shorter than the dynamical timescale

$$\tau_{\text{dyn}}^{-1} = \sqrt{24\pi G\rho}, \quad (20)$$

the star reaches the thermodynamic conditions necessary to explode as an SN Ia.

3. Mass Accretion Rate on the Central Remnant

As mentioned before, the accretion rate onto the post-merger central remnant can be computed in two different ways. Within the first approximation, the accretion rate is set by the thermal state of the envelope of the white dwarf (Yoon et al. 2007). Within the second one, the central remnant accretes mass from a thin Keplerian disk and its evolution is given by the viscous timescale—see van Kerkwijk et al. (2010), but also Ji et al. (2013). Since, due to the lack of full numerical analyses of this process with realistic physical ingredients, it is not yet clear which one of these treatments is more appropriate, we will calculate the evolution of the central white dwarf remnant adopting both prescriptions, and we will discuss the differences between both sets of calculations. In both cases we are interested in determining the long-term evolution central white dwarf taking into account the interaction between the disk and the magnetic field resulting from the merger. To handle this problem, we adopt a simplified picture of the post-merger system consisting of a magnetized rotating white dwarf surrounded by a thin Keplerian disk.

3.1. Accretion Rate Set by the Thermal Timescale

As discussed by Yoon et al. (2007), the assumption that the accretion timescale is set by the viscous timescale given by the Shakura–Sunyaev α prescription could be inappropriate to estimate the accretion timescale onto the newly formed white dwarf since the structure of the merged system deviates from a central, point-like mass surrounded by a thin disk that is the central assumption adopted within the α -formalism. Yoon et al. (2007) argued that under these conditions the relevant timescale might be the cooling timescale of the low-density envelope between the central object and the disk. If the relevant timescale is the cooling timescale of the envelope of the post-merger white dwarf, the accretion rate will be given by

$$\dot{M}_{\text{WD}} = \frac{M_{\text{disk}}}{\min(\tau_\nu, \tau_{\text{thermal}})}, \quad (21)$$

where M_{disk} is the total mass of the disk, and τ_ν and τ_{thermal} are the neutrino cooling time and the thermal time on the envelope of the white dwarf, respectively. These two timescales are given by

$$\tau_\nu = \frac{c_\nu T_S}{\epsilon_\nu} \Big|_S \quad (22)$$

and

$$\tau_{\text{thermal}} = \frac{3}{64\sigma} \left(\int_{\Delta r} \left(\frac{\kappa c_\nu}{T^3} \right)^{1/2} \rho dr \right)^2 \quad (23)$$

(Heney & L’Ecuyer 1969; Piersanti et al. 2003), where c_ν is the heat capacity at constant volume, κ is the opacity, ϵ_ν is the energy release by the neutrino emission, and Δr delimits the region of interest—see Section 2.3 for a discussion of the thermal properties of the white dwarf.

For the values typical of the post-merger white dwarf ($\rho = 10^6 \text{ g cm}^{-3}$ and $T = 10^8 \text{ K}$), the neutrino luminosity will be $L_\nu \sim 10^2 L_\odot$ and the thermal energy will be $U \sim 10^{48} \text{ erg}$.

At the beginning of the simulations the neutrino cooling timescale is about $\tau_\nu \sim 6 \times 10^5 \text{ yr}$, while the thermal timescale is $\tau_{\text{thermal}} \sim 10^6 \text{ yr}$. Then, the initial accretion rate is about $\dot{M}_{\text{WD}} \sim 10^{-7} M_\odot \text{ yr}^{-1}$, close to the Eddington limit.

3.2. Accretion Rate Set by the Viscous Timescale

Numerical simulations—see, e.g., Benz et al. (1990), Lorén-Aguilar et al. (2009), and Dan et al. (2011)—show that the disk product of the coalescence of two white dwarfs of unequal masses is not thin, although it is not thick either. Specifically, Lorén-Aguilar et al. (2009) found that the thickness of the newly formed disk is $H \sim 5.0 \times 10^{-3} R_\odot$, while the typical size is $R_{\text{disk}} \sim 0.2 R_\odot$ —see their Table 1. Hence, $H/R_{\text{disk}} \simeq 0.025$. Thus, assuming that the disk is thin is not an extreme assumption, and in the worst of the situations, it can be considered as a limiting case. Obviously, the other limiting case is to assume that the disk is thick. Here we assume that the disk is thin, and we postpone the study of a thick disk to a forthcoming publication.

For a thin, Keplerian accretion disk, the evolution of the surface mass density, Σ , is given by the diffusion equation:

$$\frac{\partial \Sigma}{\partial t} = \frac{3}{r} \frac{\partial}{\partial r} \left[r^{1/2} \frac{\partial}{\partial r} (\nu \Sigma r^{1/2}) \right], \quad (24)$$

where ν is the turbulent kinematic viscosity. To describe the time evolution of the disk, we use one of the three self-similar solutions of Equation (24) found by Pringle (1974). These solutions are obtained for an opacity parameterized as $\kappa = \kappa_0 \rho^a T^b$. Within this approximation mass is accreted onto the central white dwarf, but the angular momentum of the disk is conserved, $J_{\text{disk}} = J_0$, because the outer edge of the disk moves outward—see Equation (26). In a general case J_{disk} would not be conserved because there is a trade-off of angular momentum between the disk and the central white dwarf. However, since the angular momentum of the white dwarf, J_{WD} , is much smaller than that of the disk, this solution is accurate enough for the purpose of estimating the accretion rate onto the white dwarf. Actually, we have checked that at all times $J_{\text{WD}}/J_{\text{disk}} < 0.1$ in our simulations.

Within this approximation mass flows at the inner disk boundary at a rate

$$\dot{M}_{\text{disk}} = \frac{(\beta - 1)M_0}{t_{\text{visc}}} \left(1 + \frac{t}{t_{\text{visc}}} \right)^{-\beta}, \quad (25)$$

and the disk outer radius evolves as

$$R_{\text{out}} = r_0 \left(1 + \frac{t}{t_{\text{visc}}} \right)^{2\beta}, \quad (26)$$

where M_0 and J_0 are, respectively, the initial mass and angular momentum of the disk, $j_0 = J_0/M_0$, $r_0 = 3.88 j_0^2 / (GM_0)$, and β is a constant that depends on the opacity regime. Here we have adopted a bound-free opacity ($\beta = 5/4$). The viscous timescale within this model is determined by M_0 and j_0 as follows (Ertan et al. 2009):

$$t_{\text{visc}} = 9.82 \times 10^9 \frac{j_0^{25/7}}{M_{\text{WD}}^{10/7} M_0^{3/7}} \left(\frac{\sigma}{\alpha^8 \kappa_0} \right)^{1/7} \left(\frac{\bar{\mu} m_p}{\kappa_B} \right)^{15/14}, \quad (27)$$

Table 1
Parameters of the Simulations of Post-merger Remnants

Model	M_1 (M_\odot)	M_2 (M_\odot)	M_{WD} (M_\odot)	M_0 (M_\odot)	$R_{\text{eq, WD}}$ (R_\odot)	B_{WD} (G)	Ω_{WD} (rad s $^{-1}$)	J_{WD} (g cm 2 s $^{-1}$)	J_0 (g cm 2 s $^{-1}$)	ε (–)	t_{dyn} (s)	t_{visc} (s)	t_{cool} (yr)
A	1.12	0.78	1.45	0.45	0.0026	10 9	3.00	2.79 \times 10 49	5.86 \times 10 50	0.1	0.3	0.745	2.26 \times 10 4
B	1.12	0.78	1.45	0.45	0.0026	10 6	3.00	2.79 \times 10 49	5.86 \times 10 50	0.1	0.3	0.745	2.26 \times 10 4
C	1.12	0.78	1.45	0.45	0.0026	10 7	3.00	2.79 \times 10 49	5.86 \times 10 50	0.1	0.3	0.745	2.26 \times 10 4
D	1.12	0.78	1.45	0.45	0.0026	10 8	3.00	2.79 \times 10 49	5.86 \times 10 50	0.1	0.3	0.745	2.26 \times 10 4
E	1.12	0.78	1.45	0.45	0.0026	10 9	3.00	2.79 \times 10 49	5.86 \times 10 50	0.1	0.3	0.745	2.26 \times 10 4
F	1.12	0.78	1.45	0.65	0.0026	10 9	3.00	2.79 \times 10 49	5.86 \times 10 50	0.1	0.3	0.253	2.26 \times 10 4
G	1.12	0.78	1.45	0.45	0.0026	10 6	3.00	2.79 \times 10 49	5.86 \times 10 50	0.1	0.3	0.745	2.26 \times 10 4
H	1.12	0.78	1.45	0.45	0.0026	10 9	3.00	2.79 \times 10 49	5.86 \times 10 50	0.5	0.3	0.745	2.26 \times 10 4
I	1.12	0.78	1.45	0.45	0.0039	10 9	2.30	4.56 \times 10 49	5.69 \times 10 50	0.1	0.4	0.668	2.79 \times 10 3
J	1.12	0.78	1.45	0.45	0.0034	10 9	2.50	3.87 \times 10 49	5.76 \times 10 50	0.1	0.4	0.697	5.66 \times 10 3
K	1.12	0.78	1.45	0.45	0.0032	10 9	2.60	3.60 \times 10 49	5.78 \times 10 50	0.1	0.4	0.709	7.79 \times 10 3
L	1.12	0.78	1.45	0.45	0.0030	10 9	2.70	3.35 \times 10 49	5.83 \times 10 50	0.1	0.4	0.719	1.05 \times 10 4
M	1.12	0.78	1.45	0.45	0.0029	10 9	2.80	3.14 \times 10 49	5.68 \times 10 50	0.1	0.4	0.729	1.38 \times 10 4
N	1.12	0.78	1.45	0.45	0.0028	10 9	2.85	2.93 \times 10 49	5.68 \times 10 50	0.1	0.4	0.665	1.57 \times 10 4
O	1.12	0.78	1.45	0.45	0.0028	10 9	2.90	2.93 \times 10 49	5.68 \times 10 50	0.1	0.3	0.737	1.78 \times 10 4
P	1.12	0.78	1.45	0.45	0.0022	10 9	3.50	2.24 \times 10 49	5.86 \times 10 50	0.1	0.3	0.769	5.34 \times 10 4
Q	1.12	0.78	1.45	0.45	0.0017	10 9	4.50	1.75 \times 10 49	5.96 \times 10 50	0.1	0.2	0.793	8.79 \times 10 4

where m_p is the proton mass and μ the mean molecular weight. Adopting $\alpha = 0.1$ for the viscosity parameter (Shakura & Sunyaev 1973) gives

$$t_{\text{visc}} \simeq 10.9 \left(\frac{j_0}{10^{18} \text{ cm}^2 \text{ s}^{-1}} \right)^{25/7} \left(\frac{M_0}{0.1 M_\odot} \right)^{-3/7} \text{ s}. \quad (28)$$

This solution has been employed to describe debris disks around massive black holes formed by tidal disruption of stars (Cannizzo et al. 1990) and in SN fallback disks around young neutron stars (Chatterjee et al. 2000). This formulation was also used in Külebi et al. (2013) to study the long-term evolution of the disk interaction of magnetized white dwarfs resulting from white dwarf mergers that do not develop prompt explosion conditions.

We obtain that the initial conditions of the merged system are such that $t_{\text{visc}} \sim 0.2\text{--}0.8$ s (see Table 1). This, in turn, results in accretion rates at early times $\dot{M}_{\text{WD}} = M_0/t_{\text{visc}} \sim 10^{-1} M_\odot \text{ s}^{-1}$ and an initial disk outer radius $R_{\text{out}} \sim 0.1 R_\odot$. However, for times longer than t_{visc} , the accretion rate drops one order of magnitude, and after 10^2 s, the accretion is $10^{-4} M_\odot \text{ s}^{-1}$.

In the above equations the disk viscous timescale, t_{visc} , is a constant. It is clear from Equation (27) that it is a good approximation for low infall rates because the specific angular momentum would not change appreciably. The above estimate of the accretion rate shows that this is not the present case, so we have checked the effect of the assumption of the constancy of t_{visc} on the evaluation of \dot{M}_{disk} as follows. First, we compute the accretion rate using Equation (25), keeping t_{visc} constant and then allowing it to increase with time owing to the mass loss by the disk. We found that the increase of t_{visc} would lower \dot{M}_{disk} at most by 10% during the evolution. This result assures us about our assumption of a constancy of the viscous timescale on the estimate of the infall rate at the inner disk radius.

4. Initial Conditions

We compute the post-merger initial configuration assuming that both mass and angular momentum are conserved during the merger. This is a reasonable assumption, since SPH simulations show that very little mass is ejected from the system. Moreover, little angular momentum is carried away by the unbound material, since its velocity is mostly radial. A rough estimate of the degree to which mass and angular momentum are conserved is $J_{\text{ej}}/J \sim M_{\text{ej}}/M \sim 10^{-3}$ (Lorén-Aguilar et al. 2009; Dan et al. 2014). Consequently, the orbital angular momentum of the coalescing white dwarfs is invested in spinning up the primary white dwarf and in the angular momentum of the rapidly rotating disk.

If the spin angular momentum of the merging white dwarfs is neglected, the total angular momentum just before the merger is

$$J_{\text{sys}} = q \sqrt{\frac{GM_2^3(R_1 + R_2)}{(1 + q)}}, \quad (29)$$

where (M_1, R_1) and (M_2, R_2) are the masses and radii of the merging stars, respectively, and $q = M_2/M_1$ is the mass ratio of the original binary system. Figure 2 shows the contours of constant angular momentum and of constant total mass in the plane defined by M_1 and M_2 . Given an initial total mass and angular momentum of the remnant ($M_{\text{WD}}, J_{\text{WD}}$) and an initial disk mass M_0 , we computed the initial angular momentum of the disk, J_0 , assuming that the central remnant rotates as a rigid body. To do this, we considered that just before the mass transfer episode the orbital separation was such that the secondary was about to fill its Roche lobe, for which we adopted the expression of Eggleton (1983), which is in all the cases close to $R_1 + R_2$. This is the same as saying that the merger episode begins when both stars are in contact. We also took into account that according to detailed SPH simulations of the merger process roughly half of the mass of the secondary

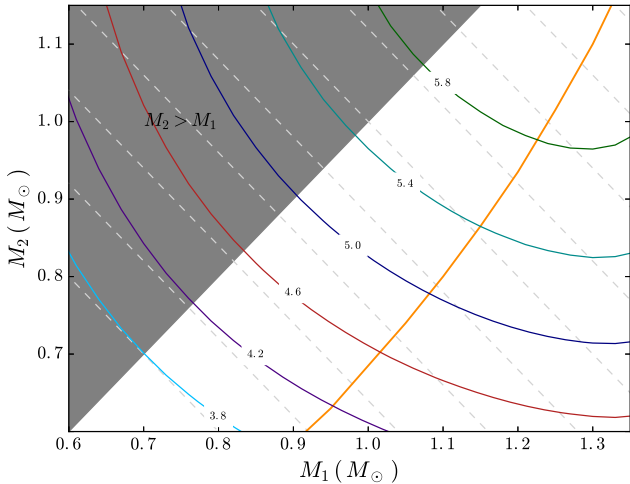


Figure 2. Parameter space of the initial white dwarf binary system. Solid lines are contours of constant total angular momentum, labeled in units of $10^{50} \text{ g cm}^2 \text{ s}^{-1}$. The gray dotted straight lines are contours of constant total mass, from 1.4 to $2.6 M_{\odot}$, in steps of $0.1 M_{\odot}$. The shaded area corresponds to configuration with $q > 1$. The orange line corresponds to the location of the system when the secondary is filling its Roche lobe ($R_2 = R_L$).

star goes to form the disk, whereas the rest of the material is directly accreted onto the primary component of the binary system (Lorén-Aguilar et al. 2009).

Nevertheless, given the exploratory nature of the simulations presented here, we did not constrain ourselves to the values obtained in the SPH simulations, and we adopted different values for the mass of the remnant and for the mass of the disk. Since a rigidly rotating white dwarf can support a maximum angular momentum $\lesssim 10^{50} \text{ g cm}^2 \text{ s}^{-1}$ (Boshkayev et al. 2013), angular momentum conservation implies that a substantial fraction of the angular momentum of the binary system goes to the Keplerian disk.

Also, we mention that detailed SPH simulations of nonsymmetric white dwarf mergers show that as the less massive white dwarf is disrupted and part of its matter is accreted onto the primary star, the accreted mass is compressed and heated. Thus, for all the cases studied here we have assumed an inverse initial temperature profile. Specifically, we adopted initial temperature profiles similar to those resulting from detailed SPH simulations.

In Table 1 we list the initial masses of the stars of the original binary system—Columns (2) and (3), respectively—as well as the initial conditions for the models presented in this work. The top section of this table lists the characteristics of the models for which the accretion rate was computed employing the cooling timescale, while the bottom section summarizes the most relevant information of those models computed employing the accretion rate given by the viscous timescale. Note that the mass of the rapidly rotating central white dwarf M_{WD} of all these simulations (listed in Column (4)) is the same. Since we are modeling white dwarfs as rigidly rotating configurations, only two parameters are needed to determine the remaining characteristics of the merged configuration. Thus, we decided to vary the initial angular velocity Ω_{WD} and the mass of the disk M_0 . These two quantities are listed in Columns (8) and (5), respectively. For a super-Chandrasekhar white dwarf of $1.45 M_{\odot}$, the minimum angular velocity for the gravitational stability to set in is around 2.03 rad s^{-1} . Note that the angular

velocities adopted here are in all cases larger than this value. Once the angular velocity of the white dwarf is known, we determine its total angular momentum, J_{WD} , which is listed in Column (9) of the table, and the equatorial radius of the white dwarf, R_{WD} , listed in Column (6). The adopted magnetic field B_{WD} of the white dwarf is given in Column (7). The rest of the columns of Table 1 list the initial angular momentum J_0 (Column (10)) of the disk and the efficient parameter ε (Column (11)), which is relevant for estimating the mass accretion rate, the dynamical timescale t_{dyn} , the viscous timescale t_{visc} , and the cooling timescale of the disk t_{cool} (Columns (12)–(14)).

In our simulations the magnetic field of the remnant was kept fixed at $B_{\text{WD}} = 10^9 \text{ G}$, a representative value of the magnetic field resulting from the stellar dynamo that originated during the coalescence (García-Berro et al. 2012). For the typical values found in the SPH simulations of merging white dwarfs the magnetic field can be as high as $\sim 10^{10} \text{ G}$, depending on whether the dynamo is saturated. However, we decided to adopt a conservative value as a reference magnetic field, 10^9 G . However, we also computed some models with various magnetic field strengths, ranging from 10^6 to 10^9 G . An important point that is worth emphasizing is that for the simulations presented here we assumed that during the merging process an ordered global dipole field is produced. However, this is not guaranteed—see, for instance, the discussion in the conclusions of Schwab et al. (2012).

5. Results

Since the evolution of the post-merger system depends critically on the adopted prescription for the mass accretion rate onto the central white dwarf resulting from the coalescence of the binary system, we discuss the results obtained using the accretion rates described in Sections 3.2 and 3.1 separately. We first discuss the results obtained using an accretion rate set by the cooling timescale, and subsequently we present the results obtained when the viscous timescale is employed.

5.1. Accretion Rate Set by the Cooling Timescale

To start with, we discuss our reference model. This is model A in Table 1. For this model we adopted a magnetic field $B = 10^9 \text{ G}$. We note that during the early phases of the evolution of the post-merger remnant the dominant cooling mechanism of the external layers of the central white dwarf is neutrino emission. Therefore, the initial relevant timescale to compute the accretion rate is $\dot{M}_{\text{WD}} = M_{\text{WD}}/\tau_{\nu} \sim 10^{20} \text{ g s}^{-1}$. This accretion rate is of the order of the Eddington limit. However, in our calculations the evolution of the model is followed self-consistently. That is, we computed the mass accretion rate with the cooling timescale provided by the evolution—see below.

For this model, the magnetospheric radius is $R_{\text{mag}} = 0.062 R_{\odot}$ and the corotation radius is $R_{\text{co}} = 0.0039 R_{\odot}$. Thus, $R_{\text{mag}} > R_{\text{co}} > R_{\text{WD}}$, so the dipole radiation torque and the propeller torque drive the evolution of the spin of the remnant. Under these conditions the central object does not accrete matter. To illustrate the evolution, Figure 3 shows some temperature profiles at selected times. In particular, we show these profiles at times t_0 (corresponding to the beginning of the evolution; solid line) at a time just before the central white dwarf reaches explosive conditions (time $t = t_3$; long-dashed line) and at two intermediate stages (times t_1 and t_2 ; short-dashed line and dot-dashed line, respectively). As can be seen in this figure, during the entire

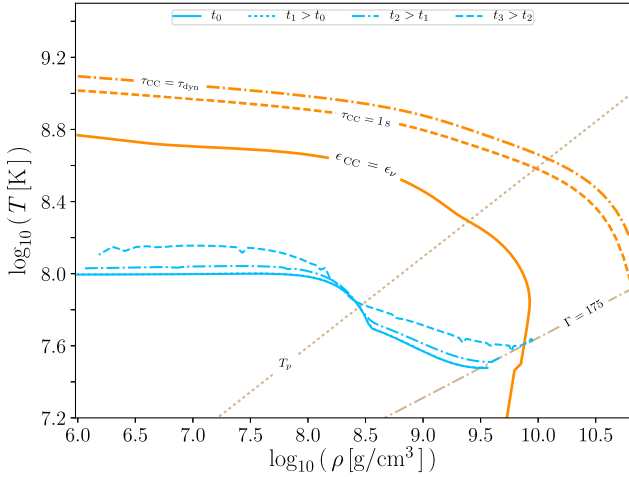


Figure 3. Temperature–density profiles of the central white dwarf at different times of the evolution for model A. This model was computed assuming $B = 10^9$ G and an accretion rate set by the cooling timescale. We also show the carbon ignition line, labeled as $\epsilon_{\text{CC}} = \epsilon_{\nu}$, and two carbon-burning timescales $\tau_{\text{CC}} = \tau_{\text{dyn}}$ and $\tau_{\text{CC}} = 1$ s. In these panels the crystallization curve is labeled as $\Gamma = 175$ and the plasma temperature as T_p . The configuration at t_1 has a temperature profile almost equal to the initial one. At t_2 and t_3 , it heats at the center and at the surface.

evolution both the central regions and the outer layers of the white dwarf are compressed and heated. These two regions of the white dwarf are separated by the line at which the temperature of the nearly isothermal core equals the plasma temperature, T_p . This behavior is a consequence of the torques acting on the white dwarf. The acting torques brake the white dwarf, decreasing its angular velocity. As a consequence, the centrifugal force decreases and the gravitational force dominates. Thus, to balance the enhanced gravity, the density increases, as does the temperature. Ultimately, the center of the star reaches the thermodynamic conditions needed to burn carbon explosively. These conditions are illustrated in this figure by the curves $\epsilon_{\text{nuc}} = \epsilon_{\nu}$, $\tau_{\text{CC}} = \tau_{\text{dyn}}$, and $\tau_{\text{CC}} = 1$ s. This occurs at time 40.8 yr, just before these regions reach the beta-decay instability limit, and when the central regions of the star are already crystallizing. Figure 4 displays the evolution of model A in the mass–central density plane. As can be seen, the evolutionary track corresponds to pure compression, and no matter is accreted. Note as well that carbon in the central regions of the star is ignited before the inverse β -decay instability is reached.

Figure 5 shows the run of the neutrino and thermal timescales in the white dwarf interior of model A at two relevant times, namely, $t = t_0$ and $t = t_3$, as previously defined. As can be seen, for $t = t_0$ neutrinos cool the external layers of the star, while in the internal regions thermal diffusion is the dominant transport mechanism. At time t_3 the relevant cooling timescale in the outer layers of the white dwarf is no longer the neutrino timescale, but the thermal timescale. Actually, it is important to realize that in the dense inner core of the white dwarf the shorter timescale is always the thermal timescale. Thus, Figure 5 clearly shows that the cooling timescale must be computed self-consistently along the evolution of the remnant to obtain physically sound results. We emphasize that although this plot illustrates these timescales for model A, our calculations demonstrate that this is a representative case and that for all the models listed in the top section of Table 1 the run of these timescales is similar.

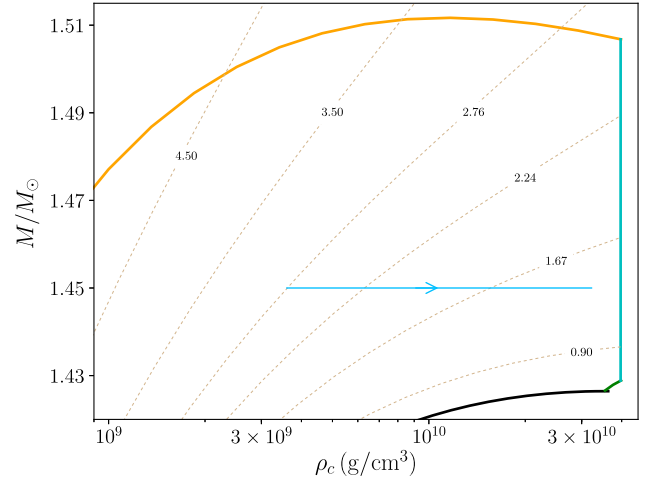


Figure 4. Evolution of model A in the mass–central density plane, at selected times; see text for details. The colors of the lines indicating the regions of the various instabilities discussed here are the same as shown in Figure 1. Also shown are the contours of constant angular momentum (dotted lines).

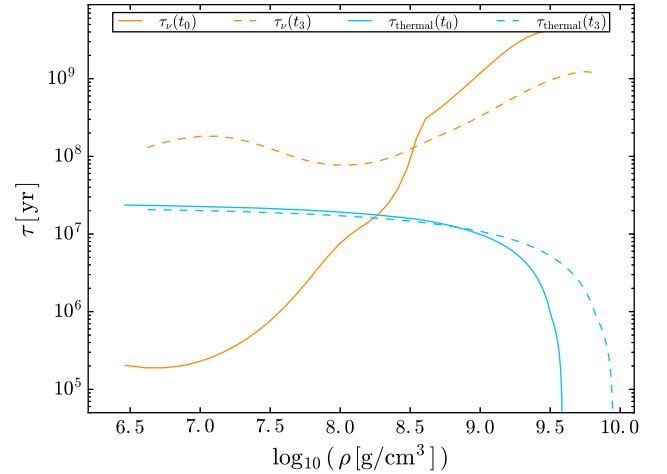


Figure 5. Run of the neutrino and thermal timescales in the interior of model A at selected times; see text for details.

To study the dependence of the evolution of the merged configuration on the magnetic field, we ran a suite of models with varying strengths of the magnetic field. These are models B, C, and D in Table 1, for which we adopted magnetic field strengths $B = 10^6$, 10^7 , and 10^8 G, respectively, keeping unchanged the rest of the parameters of model A. For the sake of conciseness we only discuss model B, which corresponds to the smallest magnetic field strength, 10^6 G.

Figure 6 shows the evolution of the remnant at different times for this model. These times were selected using the same criteria we used previously, and the line coding is the same. In this case $R_{\text{mag}} < R_{\text{WD}}$ and the central white dwarf can accrete matter from the disk. Under these conditions we find that accretion onto the white dwarf heats the outer layers of the star, while the temperature of its core remains almost unchanged. Ultimately the very outer layers of the white dwarf are heated to such an extent that carbon is ignited off-center. However, an inspection of Figure 7, which shows the evolution in the mass–central density plane, reveals that actually the central regions of the star expand slightly. This again is due to the acting torques, which spin up the white dwarf.

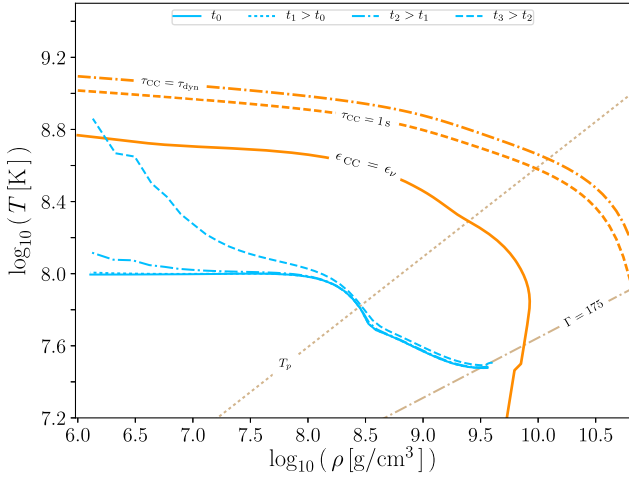


Figure 6. Same as Figure 3, but for the case in which a modest magnetic field, $B = 10^6$ G, is adopted. This is model B in Table 1.

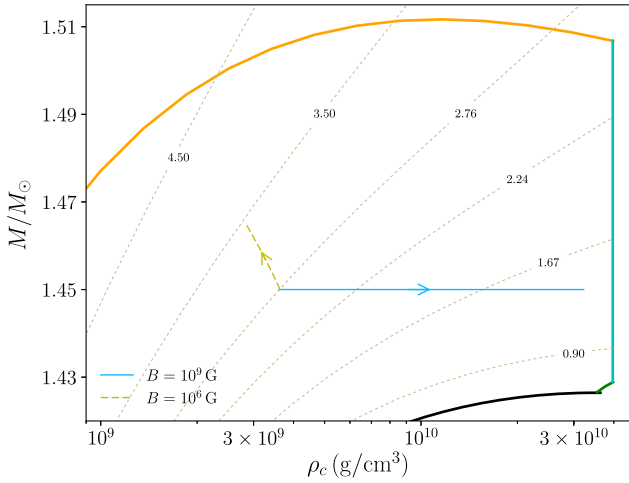


Figure 7. Same as Figure 4, but including the case in which a magnetic field, $B = 10^6$ G, is adopted (yellow line). This is model B in Table 1.

We found that if the magnetic field of the white dwarf is higher than 3.84×10^6 G, the magnetospheric radius is larger than the corotation radius. Thus, in this case the central remnant does not accrete more material after the merger, so the propeller torque and the dipole radiation torque drive the evolution of its spin rate. On the other hand, if the magnetic field is lower than 1.88×10^6 G, the magnetospheric radius is smaller than the white dwarf radius. Hence, the central white dwarf accretes material. Consequently, in this case the evolution of the rotation rate is driven by the accretion torque. Thus, for these initial conditions the magnetic field determines the accretion rate and the evolution of the star.

To further study the dependence of these results on the input parameters, we also analyzed the dependence on the initial angular velocity. In Table 2 we list the times at which the post-merger central star reaches the conditions suitable for an explosion to occur, for several magnetic field strengths (models A to D) and initial angular velocities. Clearly, the duration of this phase and the final outcome depend sensitively on the value of the adopted magnetic field, and to a lesser extent on the initial angular velocity.

5.2. Accretion Rate Set by Viscous Timescale

In the previous section we have assumed that the accretion rate on the white dwarf is given by the shorter timescale of the cooling mechanisms. In this section we present the results for the case in which the white dwarf accretes material at a rate set by the viscous timescale of the Keplerian disk.

For the sake of definiteness, in the following we discuss in detail, with the help of Figures 8 and 9, the time evolution of model E, which is similar to model A, the only difference being that in this case the accretion rate is computed adopting the viscous timescale, while the rest of the initial conditions and assumptions are exactly the same. Furthermore, for this model we study two possibilities for the efficiency parameter ξ_{acc} in Equation (3). The first of these possibilities corresponds to the case in which $\xi_{\text{acc}} = 1.0$, that is, when matter is accreted on the remnant with the Keplerian velocity at the inner disk radius. The second one corresponds to the case in which matter is accreted on the remnant with the Keplerian velocity at the surface of the remnant, which we label as $\xi_{\text{acc}} = \xi_{\text{WD}}$ in the figures discussed below.

Shortly after the merger, due to the high accretion rates, $R_{\text{mag}} < R_{\text{WD}}$ (see the top panel of Figure 8). Hence, the only torque acting on the white dwarf is that resulting from accretion. For the set of parameters of model E, the initial accretion rate onto the white dwarf given by Equation (25) is large, even if an efficiency of $\varepsilon = 0.1$ is adopted, $\dot{M}_{\text{WD}} \sim 0.01 M_{\odot} \text{ s}^{-1}$. Consequently, the mass of the white dwarf rapidly increases during this phase. However, its central density only increases in the case in which matter is accreted with the Keplerian velocity of the remnant (blue line in Figure 9), whereas in the case in which $\xi_{\text{acc}} = 1.0$ (green line in this figure) the central density of the white dwarf decreases.

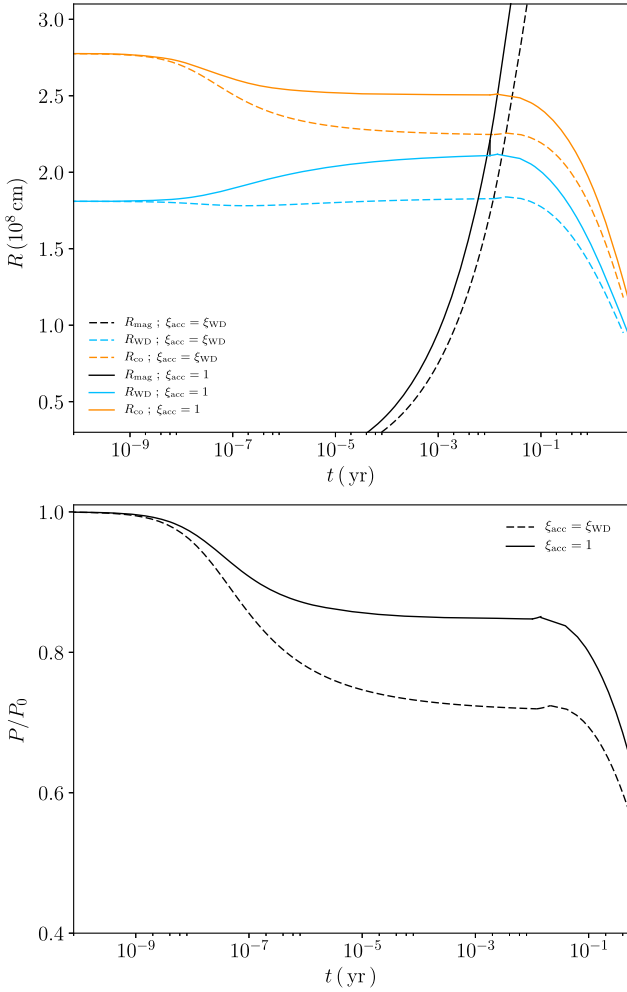
The evolution of the central density of the remnant is the result of an intricate trade-off between the increase in mass, the change in the rotation period due to the acting torque, and the evolution of the moment of inertia of the remnant. The increase in mass of the remnant alone clearly would result in an increase of the central density. The change in the rotation speed due to the acting torque—which tends to increase the angular velocity—would result in a decrease of the central density, as the centrifugal force increases. Finally, since $I \propto M_{\text{WD}} R_{\text{WD}}^2$, as the mass of the white dwarf increases as a result of accretion, the moment of inertia would increase. However, since the mass–radius relationship for rotating white dwarfs depends crucially on the angular velocity, the radius of the remnant, hence I , ultimately depends on the acting torque. Furthermore, for super-Chandrasekhar white dwarfs the slope of the mass–radius relationship is very steep. Consequently, small changes in the mass can induce large variations of the radius of the remnant. The interplay between these factors is rather complex, but in general terms we find that the evolution of the moment of inertia is dominated by the variation of the radius of the remnant.

It is then clear that the crucial parameter that dictates the evolution of the central density of the remnant is ξ_{acc} . Specifically, when $\xi_{\text{acc}} = 1.0$ is adopted, the remnant is spun up very rapidly by the acting torque (as is shown in the bottom panel of Figure 8), its radius increases notably (see the top panel of this figure), the moment of inertia increases markedly, and the central density first decreases. On the contrary, if matter is accreted onto the surface of the white dwarf with the same angular velocity of the remnant, the acting torque is

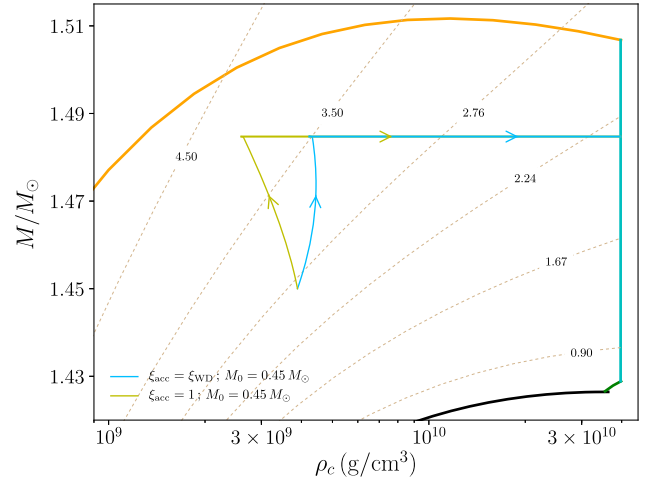
Table 2

Carbon Ignition Location and Evolutionary Times of the Post-merger Remnants for Several Values of the Magnetic Field Strength and Initial Angular Velocity

Model $\Omega_{\text{WD}} \text{ (s}^{-1}\text{)}$	$B_{\text{WD}} \text{ (G)}$	$\Delta t \text{ (yr)}$							Carbon Ignition
		2.3	2.5	2.6	2.7	2.8	2.9	3.0	
A	10^9	5.50×10^1	4.68×10^1	4.33×10^1	4.02×10^1	4.71×10^1	6.95×10^1	4.08×10^1	Center
B	10^6	4.00×10^3	8.81×10^3	6.39×10^3	5.27×10^3	5.63×10^3	3.65×10^3	4.94×10^3	Off-center
C	10^7	2.81×10^4	3.95×10^4	2.09×10^4	1.66×10^4	1.34×10^4	1.59×10^4	1.50×10^4	Center
D	10^8	9.29×10^2	7.96×10^2	7.39×10^2	8.92×10^2	8.31×10^2	7.76×10^2	5.61×10^2	Center


Figure 8. Top panel: evolution of the radius of the remnant R_{WD} , the corotation radius R_{co} , and the magnetospheric radius R_{mag} for model E. Bottom panel: evolution of the rotation period of the central white dwarf.

considerably smaller, the moment of inertia remains approximately constant, the radius of the remnant decreases, and the central density increases steadily. In both cases, once the magnetic radius becomes larger than the radius of the white dwarf ($R_{\text{WD}} < R_{\text{mag}} < R_{\text{co}}$), the dipole and the disk-interaction torques drive the evolution of the remnant—the top panel of Figure 8 clearly depicts this. When this happens, the fastness parameter of the white dwarf is ~ 0.8 . Consequently, shortly after ($\lesssim 0.5$ yr), the remnant reaches a fastness parameter $\omega_f = 1$, and the evolution is driven by the propeller torque. At this point of the evolution, accretion from the disk stops. Consequently, the moment of inertia of the remnant decreases considerably, the rotation period decreases as well, and the


Figure 9. Evolutionary tracks in the mass–density plane for model E for two assumptions about the value of ξ_{acc} and $\varepsilon = 0.1$.

white dwarf contracts. Hence, the central density increases rapidly (see the top panel of Figure 8). This entire sequence of events ultimately leads the remnant to cross the line of inverse β -decay instability. It is interesting to note that the mass of the remnant when it crosses the instability line does not depend on the adopted value of ξ_{acc} . This depends on the mass accretion rate onto the white dwarf, and consequently on the adopted efficiency parameter ξ . The parameter ξ_{acc} is directly related to the change of angular momentum. Thus, ξ_{acc} and ξ play different roles in the evolution of the post-merger configuration, although its effect is combined as shown by Equation (3).

We now address our attention to thermal evolution of the post-merger remnant of model E. Figure 10 shows several temperature–density profiles at selected times after the merger took place. The top panel of this figure shows the case in which $\xi = \xi_{\text{acc}}$ is adopted, whereas the bottom panel corresponds to the case in which $\xi = 1$ is employed. The initial temperature profiles are shown as the solid blue and green lines in Figure 10, respectively. In both cases, during the first evolutionary phases the large accretion rates discussed earlier heat the outer layers of the star. However, neutrino emission also plays a significant role. When $\xi = \xi_{\text{acc}}$ is adopted, compressional work exceeds neutrino emission, and thus an off-center temperature peak rapidly grows. In particular, the temperature profile peaks at $\log \rho \sim 6.54$. As time passes by, the peak temperature increases, and ultimately the outer layers of the white dwarf reach the thermodynamic conditions needed to ignite carbon explosively.

On the contrary, when $\xi = 1.0$ is adopted (bottom panel of Figure 10), the evolution is more complex. In this case accretion first heats the outer layers of the central white dwarf,

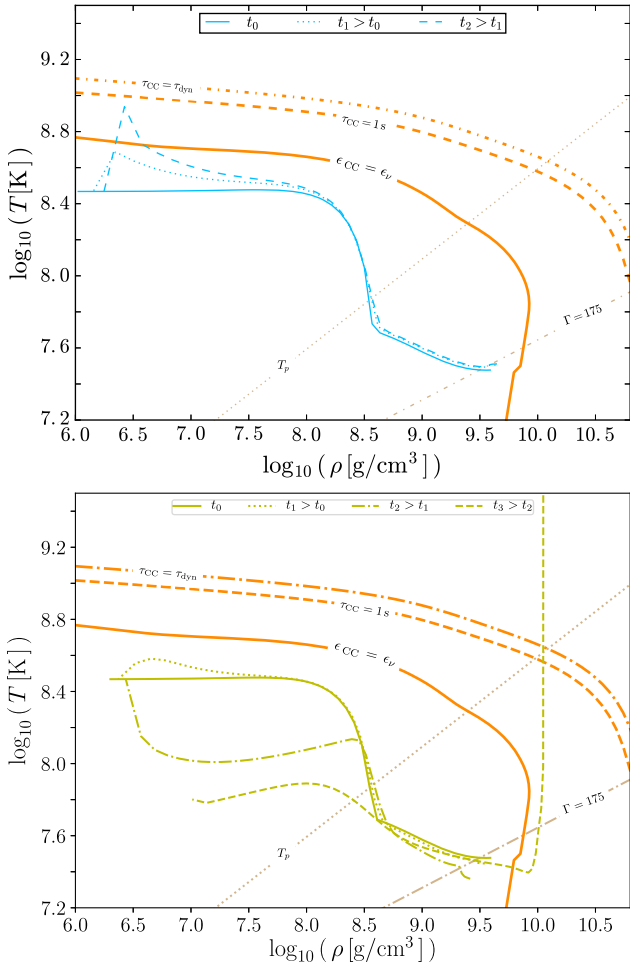


Figure 10. Temperature–density profiles of the central white dwarf at different times of the evolution for model E. The top panel shows the model with $\xi = \xi_{\text{acc}}$, while the bottom panel displays the model for which $\xi = 1$ is adopted. Time t_1 corresponds to a time shortly after accretion from the disk starts (short-dashed line), t_2 is the time at which the merged remnant enters into the propeller phase and accretion stops (dot-dashed line), and t_3 is a time just before the post-merger object crosses the beta-instability limit (long-dashed line).

but neutrino cooling dominates. Hence, after a short time interval the entire central white dwarf cools to a temperature smaller than the initial one. Time t_2 is the time at which accretion stops. Thus, for times longer than t_2 the evolution of the star is driven by angular momentum losses by dipole emission. Eventually, at time t_3 carbon is ignited at the center of the white dwarf.

5.2.1. Sensitivity of the Results to the Free Parameters

We first compare the evolution when different masses of the disk are adopted, keeping the mass of the remnant fixed. With this in mind, in Figure 11 we show the evolutionary tracks of model F and compare them with those of model E. This model corresponds to a final post-merger remnant of mass $1.45 M_{\odot}$ and an initial disk mass of $0.65 M_{\odot}$, whereas the rest of the parameters of the model were not varied—see Table 1. Additionally, as we did for model E, we also studied two possibilities. The first of these corresponds to an accretion efficiency parameter $\xi_{\text{acc}} = 1.0$, whereas for the second one we assumed that at the inner disk radius the accreted material has

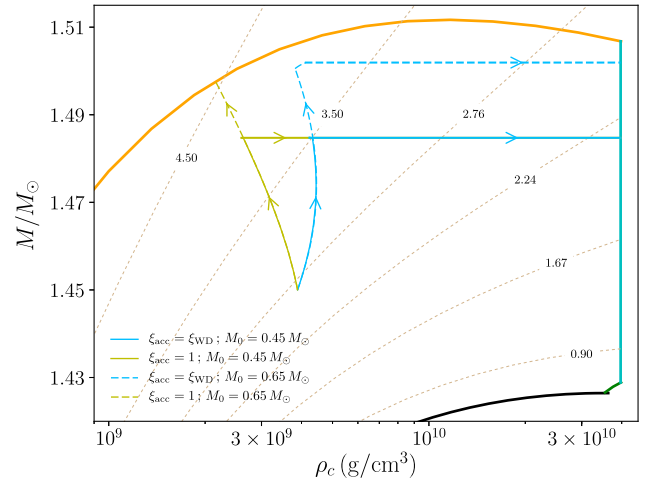


Figure 11. Same as Figure 9, but here we compare models E (solid lines) and F (dashed lines) for two different disk initial masses, 0.45 and $0.65 M_{\odot}$, respectively.

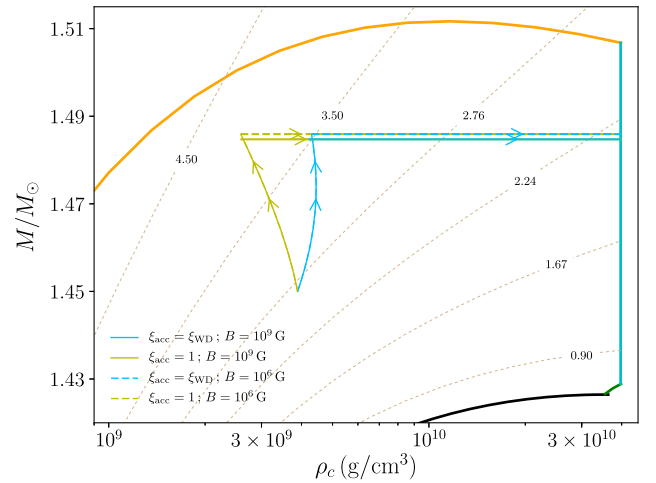


Figure 12. Same as Figure 9, but here we compare models E (solid lines) and G (dashed lines) for two different values of the white dwarf magnetic field, 10^9 and 10^6 G, respectively.

the angular velocity of the white dwarf, $\xi_{\text{acc}} = \xi_{\text{WD}}$. Note that, in the case in which $\xi_{\text{acc}} = 0.1$ is adopted, the evolution of this model is very similar to that of model E, but it arrives at the mass-shedding limit in the accretion phase. When $\xi_{\text{acc}} = \xi_{\text{WD}}$ is chosen, the remnant also crosses the line of inverse β -decay instability. The only difference is that for model F, which has a disk considerably more massive, more mass is accreted before the remnant crosses the instability line. Hence, the remnant has a larger mass in the propeller phase, and the line of β -decay instability is crossed when the white dwarf is more massive.

Next, we analyze the influence on the evolution of the strength of the magnetic field, as we did previously for those models in which the accretion rate is computed using the cooling timescale. We do this comparison adopting a very low value for the magnetic field strength, $B = 10^6$ G (model G in Table 1, the same value adopted in Section 5.1). The results of this analysis are shown in Figure 12. As can be seen, the differences between the evolution of models E and G are minor. Thus, we conclude that for the typical values of the magnetic field strength that originated in the merger of two white dwarfs, the evolution of these models is not significantly

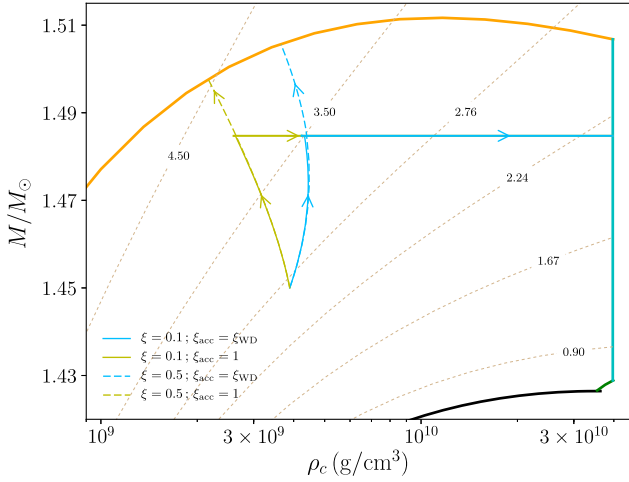


Figure 13. Same as Figure 9, but for two values of the accretion efficiency parameter, $\varepsilon = 0.1$ (solid lines) and 0.5 (dashed lines), for models E and H, respectively.

affected by the adopted magnetic field. This can be explained by the fact that, at early times in the viscous timescale prescription, the mass and angular momentum of the white dwarf post-merger evolution are dominated by the accretion torque and the effect of the magnetic field is neglected until the magnetospheric radius equals the white dwarf one. It is in this initial phase that more significant accretion of mass onto the central star occurs. Since the accretion timescale in this scenario is so short, the evolution of the magnetospheric radius is dominated by the change of the mass accretion rate.

Another free parameter of our formulation is ε , which, we recall, measures how efficient accretion is. All the calculations presented until now have been performed adopting $\varepsilon = 0.1$. However, since the accreted mass depends significantly on the precise value of this free parameter, it is important to assess its impact on the results. We now study the sensitivity of our calculations to the value adopted for it. To this end we conducted an additional set of simulations in which we adopted $\varepsilon = 0.5$. This is model H in Table 1. In Figure 13 we compare the results of these calculations with those of model E. As could be expected, this parameter turns out to be critical, since it controls how efficient accretion is. Consequently, when $\varepsilon = 0.5$ is adopted, the remnant evolves toward the mass-shedding limit instead of crossing the β -instability line. We consider model E as a reasonable guess, although keeping in mind that larger values of ε cannot be discarded “a priori” and therefore could alter the evolution of the remnant.

Naturally, another key ingredient of our approach is the initial angular velocity of the central white dwarf, Ω_{WD} . Figure 14 shows the evolutionary tracks for different values of the initial angular velocity of the post-merger remnant, keeping unchanged the rest of initial conditions of model E (models I to Q in Table 1; dashed lines), and we compare them with the evolutionary sequence of model E, our reference model for this prescription for the accretion rate (solid lines). As can be seen, the model with the smallest initial angular velocity—namely, that with initial angular velocity 2.30 rad s^{-1} , model I—reaches the mass-shedding limit during the accretion phase. Furthermore, for this model the central density decreases, irrespective of the value adopted for ξ_{acc} . Model J, for which we adopted $\Omega_{\text{WD}} = 2.50 \text{ rad s}^{-1}$, only reaches the mass-shedding limit if $\xi_{\text{acc}} = 1.0$; otherwise, it reaches the β instability region. The

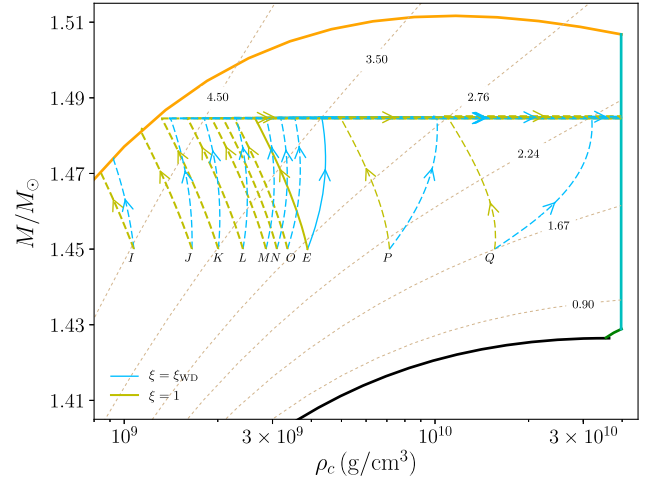


Figure 14. Same as Figure 9, but for several values of the initial angular velocity, models I to P in Table 1, compared to our reference case, for which the initial angular velocity is $\Omega_{\text{WD}} = 3.00$ (model E). From left to right the initial angular velocities of the remnant are $\Omega_{\text{WD}} = 2.30, 2.50, 2.60, 2.70, 2.80, 2.85, 2.90, 3.50$, and 4.50 s^{-1} .

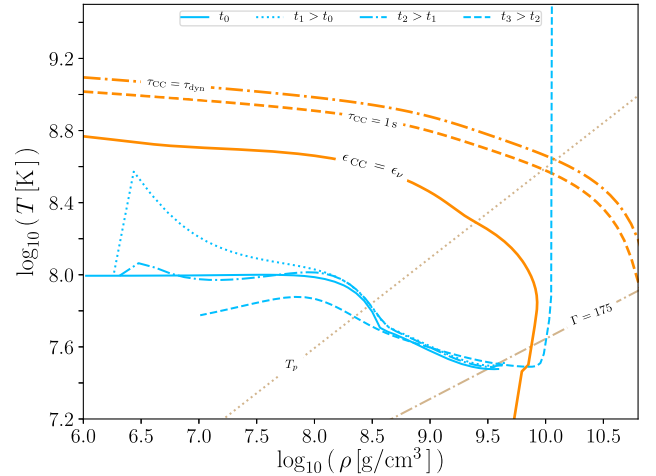


Figure 15. Same as Figure 10, but for the case in which the initial temperature of model E is smaller. For the sake of conciseness we only display the model for which $\xi = 1$ is adopted.

rest of the models do not cross the mass-shedding instability line. Note as well that for model J, as occurs for model I, the central density decreases, independently of the value adopted for ξ_{acc} . For model K the central density decreases if $\xi_{\text{acc}} = 1.0$ and increases otherwise. This is also true for models with even faster rotation rates.

Additionally, to take into account the effects of the initial temperature for the case in which $\xi = \xi_{\text{acc}}$ is adopted, we computed a model in which the initial configuration corresponds to a white dwarf in which the external layers have a temperature sizably smaller (i.e., 10^8 K) than that of our standard case—that is, model E—which was computed adopting a temperature for the external layers of $3 \times 10^8 \text{ K}$. The evolution of this additional model is shown in Figure 15, and it is markedly different from that of model E. Specifically, when the adopted temperature is 10^8 K , the external layers of the white dwarf are initially heated by the accreted material, as happens also for model E. However, in this case neutrino cooling (basically dominated by neutrino bremsstrahlung) is so

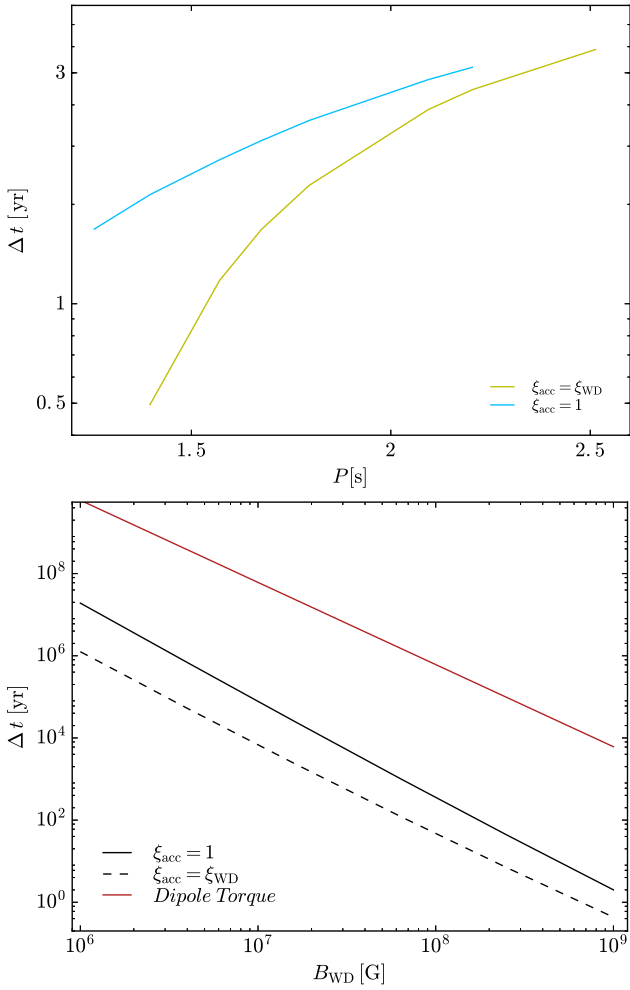


Figure 16. Top panel: time necessary to reach the instability line as a function of the initial period of the remnant. Bottom panel: time necessary to reach the instability line as a function of the magnetic field of the remnant.

strong that the remnant cools rapidly and eventually carbon is ignited at the center of the star, when the central regions have already crystallized.

5.2.2. Evolutionary Times

Finally, we study the time needed to reach the instability lines, Δt . We have shown before that the most important parameter that determines the evolution of the system is the initial period of the system. In the top panel of Figure 16 the dependence of Δt on the initial period of the rotating white dwarf resulting from the merger is displayed, for our two choices for the value of ξ_{acc} . Clearly, the larger the period is, the longer Δt is. This is the natural consequence of the smaller initial centrifugal force.

The second important parameter that determines the duration of this evolutionary phase is the strength of the magnetic field of the remnant. We showed before that the value of B_{WD} has little effect on the outcome of the post-merger system—see Figure 12. Notwithstanding, B_{WD} influences considerably Δt . This occurs because the larger B_{WD} is, the larger is the magnetospheric radius. Thus, we expect that large values of B_{WD} would result in substantially smaller values of Δt . To illustrate this in a quantitative manner, in the bottom panel of

Figure 16 the total time needed to reach the instability region is plotted as a function of the surface magnetic field of the remnant. As can be seen, the evolution of the systems is indeed faster for large magnetic field strengths. This behavior is natural since for large magnetic field strengths the central remnant is more tightly coupled with the surrounding Keplerian disk. Consequently, the accretion phase is shorter. In addition, in this panel we also show (using a solid red line) the time it takes for the remnant to become unstable when only magnetic dipole braking is considered. Since, in this case, there is no accretion, the star evolves in a constant-mass sequence. From Equation (7), we obtained

$$\Delta t = \frac{c^3}{2B_{\text{WD}}^2} \int_{J_{\text{WD},0}}^{J_{\text{WD},f}} \frac{dJ_{\text{WD}}}{\Omega_{\text{WD}}^3 R_{\text{WD}}^6}. \quad (30)$$

It can be seen that Δt is inversely proportional to the square of the magnetic field. Ilkov & Soker (2012) give an analytical expression of Equation (30) in the approximate case when changes in the white dwarf structure due to the configuration rearrangement during the angular momentum loss are neglected. It is important to mention that such changes are very important for the determination of the rotational evolution of super-Chandrasekhar white dwarfs (Boshkayev et al. 2013). Clearly, the evolution of the system is always much faster when all the torques acting on the remnant are correctly taken into account. Furthermore, it is important to realize that the evolution is even faster when matter is accreted onto the surface of the remnant with the Keplerian velocity. Finally, note as well that when $\xi_{\text{acc}} = 1.0$ is adopted, moderately longer durations of the post-merger phase, when compared with the case in which the accreted matter has the Keplerian velocity at the surface of the remnant, are obtained.

6. Comparison with Previous Works

A detailed study of the evolution of the remnant of white dwarf mergers started with the work of Yoon et al. (2007). They mapped the final configuration of the SPH simulations of the merger of a $0.9\text{--}0.6 M_{\odot}$ binary into a 1D stellar evolution hydrodynamic code and followed its forward evolution. Their merger remnant is represented by a cold, slowly rotating rigid core surrounded by a hot, rapid rotating envelope with a Keplerian disk around it. They allowed the accretion from the disk by a constant accretion rate (of the order of the Eddington limit) and included a prescription for the transport of angular momentum with timescales of the order of the thermal timescale. They conclude that an off-center carbon ignition can be avoided if the transport angular momentum timescale is greater than the cooling timescale by neutrino emission and the accretion rate on the star is slow enough, i.e., $\dot{M}_{\text{WD}} < 5 \times 10^{-6}\text{--}10^{-5} M_{\odot} \text{ yr}^{-1}$. We improved this approach by allowing the mass accretion rate to vary with time, consistently with the white dwarf thermal evolution. Additionally, we introduced a framework for evolution of the angular momentum of the post-merger white dwarf including the torque that acts on the star, taking into account the magnetic field effect of the central white dwarf on the evolution of the post-merger configuration. We have found that strong magnetic fields, $B_{\text{WD}} > 10^7$ G, can also avoid an off-center carbon ignition.

Van Kerkwijk et al. (2010) estimated the post-merger evolution based on the results of the SPH simulations of Lorén-Aguilar et al. (2009) and concluded that the accretion occurs in a shorter timescale (~ 10 hr), causing a compression of the white dwarf core, with a consequent increase of its temperature until it reaches the carbon ignition runaway, leading to a delayed explosion. However, they focus on mass-symmetric white dwarf mergers ($0.6\text{--}0.6 M_{\odot}$), in which the two white dwarfs are disrupting and the final remnant configuration has a temperature profile that peaks at the center.

A different approach was presented in Shen et al. (2012) and Schwab et al. (2012, 2016). In these works it was argued that, due to the differential rotation of the system, after the dynamical phase of the merger the magnetorotational instability becomes effective, and that in a viscous timescale of 10^4 s (orders of magnitude shorter than the thermal timescale of $\sim 10^4$ yr) the angular momentum of the tidally disrupted white dwarf can be redistributed in the surface of the central star, leading to a rotating configuration with a hot envelope and with almost all the mass of the secondary star. These works also computed the thermal evolution of the post-merger remnant characterized by a timescale of the order of $10^3\text{--}10^4$ yr. Schwab et al. (2012) studied the merger of a $0.9\text{--}0.6 M_{\odot}$ white dwarf binary, and Schwab et al. (2012, 2016) extended the initial conditions' parameter space, but the evolution of the post-merger configuration in the presence of a magnetic field of the central white dwarf was not considered. These configurations spin down during the viscous evolution, while our super-Chandrasekhar remnants spin up during the entire evolution, even in the case of angular momentum losses.

There are two works considering the effect of the magnetic field during the dynamical timescale of the merger (Zhu et al. 2015) and in the viscous timescale of the post-merger evolution (Ji et al. 2013). In these works, the evolution of the system magnetic field is followed in a different fashion with respect to our approach, since we have adopted a dipole magnetic field with constant magnitude and inclination angle. Assuming as an initial condition the remnant of the merger of a $0.6\text{--}0.6 M_{\odot}$ carbon–oxygen white dwarf binary from the SPH simulation of Lorén-Aguilar et al. (2009), Ji et al. (2013) evolve the system for 3×10^4 s with the FLASH code in a 2D axisymmetric cylindrical Eulerian grid. They introduced a weak poloidal magnetic field and showed that the magnetorotational instability developed in the disk leads to a rapid growth of its magnetic field, the spin-down of the white dwarf remnant, and its magnetization to field strengths around $\sim 2 \times 10^8$ G. They computed an effective magnetic Shakura–Sunyaev parameter of the order of $\langle \alpha_m \rangle \sim 0.01$, a value one order of magnitude smaller than the α we adopted here. They found that the white dwarf magnetic field varies with time, indicating a disordered interior magnetic field. At the end of the simulation the magnetic field toroidal component is 1.5 times bigger than the poloidal one. In our model we have assumed a dipole magnetic field aligned with the white dwarf rotation axis. In this case, the magnetic field has no toroidal component. However, the simulations of Ji et al. (2013) have limited resolution, and the field strengths are affected by numerical resistivity. In addition, in these magnetohydrodynamics simulations the disk lost almost 90% of its initial mass, with 82% of it accreted by the white dwarf remnant and the rest going into outflows of which about $10^{-3} M_{\odot}$ are ejected and unbound to the system. The central white dwarf spins down,

losing angular momentum owing to the development of Maxwell stresses at the white dwarf boundary. A direct comparison is difficult, since we have studied super-Chandrasekhar white dwarfs with initial angular velocity one order of magnitude higher than that studied by Ji et al. (2013) ($\Omega_{\text{WD},0} = 0.03 \text{ s}^{-1}$). However, one difference is that in our model the white dwarf first gains angular momentum owing to the mass accretion and then loses it owing to the magnetic torque.

Zhu et al. (2015) simulated the merger of a $0.625\text{--}0.65 M_{\odot}$ carbon–oxygen white dwarf binary, giving to each white dwarf a dipole seed magnetic field with the moving-mesh code AREPO (Springel 2010). They found that during the merger dynamics the magnetic field was too weak to have an effect on the evolution, obtaining a final remnant composed by a degenerate core with a thermally supported envelope surrounded by a rotationally supported disk. This configuration is similar to the one obtained in the SPH simulations (Zhu et al. 2013). However, the remnant magnetic field has a complex structure with a volume-averaged field strength $> 10^{10}$ G in the core, with both poloidal and toroidal components.

Table 3 summarizes the main features of the post-merger evolution studied in this paper and the comparison with those of the works discussed above. We specified the binary mass of the merger configurations studied, the post-merger configurations after the merger (for the works of Yoon et al. 2007; van Kerkwijk et al. 2010; Zhu et al. 2013) or after the viscous evolutions of the system (for the works of Schwab et al. 2012; Shen et al. 2012; Ji et al. 2013), and the magnitude and configuration of the central remnant magnetic field (if it is considered). In the last column, we specified whether the central remnant developed conditions for an off-center or center carbon ignition.

7. Conclusions

The evolution of the remnant of the merger of a binary white dwarf is still an open problem. Detailed hydrodynamical simulations show that the product of the merger consists of a central white dwarf that rotates as a rigid body, surrounded by a hot, rapidly rotating corona—which has been proven to produce large magnetic fields—and a Keplerian disk. In this paper we studied the evolution of metastable, magnetized super-Chandrasekhar white dwarfs formed in the aftermath of the merger of close binary systems made of two white dwarfs.

Our simulations take into account the magnetic torques acting on the star, accretion from the Keplerian disk, and the threading of the magnetic field lines through the disk—therefore improving previous calculations of this kind. Furthermore, in our computations—at odds with previous efforts—we employ a mass–radius relationship for rotating white dwarfs. Also, our calculations incorporate the thermal evolution of the white dwarf.

Furthermore, our simulations were performed using two different prescriptions for the mass accretion rate on the central white dwarf. In a first set of simulations we adopted an accretion rate set by the cooling timescale of the Keplerian disk, whereas in the second suite of models the adopted accretion rate was computed using the viscous timescale of the disk. These two prescriptions for the accretion rate cover a very large range of values and therefore allow us to investigate the

Table 3
Comparison with Previous Works

Work	Merger Configuration	Post-merger Configurations	Magnetic Field	Magnetic Field Configuration	Carbon Ignition
Yoon et al. (2007)	$0.9 M_{\odot}$ – $0.6 M_{\odot}$, $0.9 M_{\odot}$ – $0.7 M_{\odot}$, $1.0 M_{\odot}$ – $1.0 M_{\odot}$	Slowly rotating cold core ($0.6 M_{\odot}$) with a rapidly rotating hot envelope ($0.5 M_{\odot}$) + a Keplerian disk ($0.4 M_{\odot}$)	Center/off-center ignition
van Kerkwijk et al. (2010)	$0.6 M_{\odot}$ – $0.6 M_{\odot}$, C/O WD	Rapidly rotating WD + thick disk	Center ignition
Shen et al. (2012)	$0.6 M_{\odot}$ – $0.9 M_{\odot}$, C/O WD	WD ($\sim 0.9 M_{\odot}$) with a hot, slowly rotating and radially extended envelope supported by thermal pressure ($\sim 0.6 M_{\odot}$)	Off-center ignition that leads to a high-mass O/Ne WD
Schwab et al. (2012)/ Schwab et al. (2016)	$0.6 M_{\odot}$ – $0.9 M_{\odot}$, $0.9 M_{\odot}$ – $1.2 M_{\odot}$, C/O WD	WD with a thermally supported envelope ($1.5 M_{\odot}$)	Off-center ignition that leads to an O/Ne WD
Ji et al. (2013)	$0.6 M_{\odot}$ – $0.6 M_{\odot}$, C/O WD	Rotating WD ($0.96 M_{\odot}$) surrounded by a hot corona ($0.04 M_{\odot}$) + thick disk ($0.2 M_{\odot}$)	2×10^8 G	$\frac{B_t}{B_p} \sim 1.5$	Center ignition
Zhu et al. (2015)	$0.625 M_{\odot}$ – $0.65 M_{\odot}$, C/O WD	WD ($0.64 M_{\odot}$) surrounded by thermally supported hot envelope ($0.42 M_{\odot}$) + disk ($0.21 M_{\odot}$)	4×10^{10} G	$\frac{E_{Bt}}{E_B} = 0.6$...
This work	$0.78 M_{\odot}$ – $1.12 M_{\odot}$, C/O WD	$1.45 M_{\odot}$ rigidly rotating super-Chandrasekhar WD + $0.45 M_{\odot}$ thin Keplerian disk	$[10^6, 10^9]$ G	Poloidal	Center/off-center ignition

Note. B_t/B_p : ratio of the toroidal to the poloidal field strength. E_{Bt}/E_B : ratio of the toroidal to the total magnetic energy.

possible outcomes of the evolution of these systems in a quite generic way.

Finally, we also explored the effects of the adopted set of initial parameters. These include the mass of the remnant star, its radius, angular velocity, and moment of inertia, as well as the strength of the magnetic field. We showed that the timescale in which the newly formed white dwarf evolves to reach the thermodynamical conditions for carbon to be burned explosively, or to reach the Keplerian mass shedding, secular axisymmetric instability, or inverse beta-decay instability depends crucially on all these parameters.

However, we have made a number of assumptions that might be relaxed in forthcoming works. For instance, we allow a nonzero inclination angle between the spin axis and the orientation of the dipole magnetic field and its evolution with time. Also, the post-merger central remnant rotates differentially between the core and the corona, while we have adopted a totally rigid central remnant. Thus, the model can be improved by implementing a transport mechanism for the angular momentum in the interior of the central white dwarf remnant.

For the accretion rate prescription set by the viscous timescale, we have adopted a geometrically thin disk model. At the early times in the evolution of the post-merger remnant, we obtain a highly super-Eddington accretion rate of up to $10^{-1} M_{\odot} \text{ s}^{-1}$. The dissipation required to produce the needed very short viscous timescales might heat the disk to the point of carbon ignition (Mochkovitch & Livio 1990), but we did not consider these heating effects in the present work. The disk of the post-merger remnant could be best described by a thick-disk model. This might also be studied in a forthcoming work.

On the other hand, we have approximated the white dwarf magnetic field to a perfect dipole configuration, but this is not necessarily the case, as has been shown by the MHD simulations of Ji et al. (2013) and Zhu et al. (2015). This work could be extended in order to introduce additional configurations of the magnetic field and its interaction with the surrounding disk.

We showed that in most of our models carbon reactions are highly efficient in heating the interior of the remnant, with timescales shorter than the dynamical time. This can happen either in the outer layers or at the center of the newly formed white dwarf, depending on the initial conditions of the white dwarf and on the efficiency of mass accretion and angular momentum evolution (see Figure 10). In most cases, the time it takes the star to reach explosive conditions is shorter than that needed to reach the inverse beta-decay instability or the secular instability, which lead to gravitational collapse. Hence, we conclude that the central white dwarf can reach conditions for a delayed explosion for a sufficiently broad set of initial conditions. Whether carbon is ignited at the center or is burned off-center depends crucially on the magnetic field strength and is almost independent of the post-merger WD initial angular velocity. Our simulations show that when the magnetic field is weak, carbon is ignited off-center, while central explosions are the outcome when an ordered global strong dipole magnetic field is produced in the hot, rapidly rotating convective corona formed in the aftermath of white dwarf mergers. Naturally, this depends on whether the stellar dynamo is saturated or not.

In summary, spinning, magnetized, super-Chandrasekhar white dwarfs, resulting from the merger of two less massive white dwarfs that do not produce an SN Ia in a violent merger,

can produce a delayed explosion, provided that the remnant is massive enough and a strong magnetic field is produced during the merger.

During the refereeing process of this work our colleague and dear friend Enrique García-Berro sadly passed away. To him and to his memory, we dedicate this work and express all our gratitude. We thank the referee for the detailed comments and suggestions, which helped improve the presentation of our results. Part of this work was supported by MINECO grant AYA2014-59084-P and by the AGAUR.

ORCID iDs

J. A. Rueda  <https://orcid.org/0000-0003-4904-0014>
 P. Lorén-Aguilar  <https://orcid.org/0000-0001-8627-6478>
 E. García-Berro  <https://orcid.org/0000-0002-1623-5838>

References

- Aznar-Siguán, G., García-Berro, E., Lorén-Aguilar, P., José, J., & Isern, J. 2013, *MNRAS*, **434**, 2539
 Aznar-Siguán, G., García-Berro, E., Lorén-Aguilar, P., Soker, N., & Kashi, A. 2015, *MNRAS*, **450**, 2948
 Beloborodov, A. M. 2014, *MNRAS*, **438**, 169
 Benz, W., Cameron, A. G. W., Press, W. H., & Bowers, R. L. 1990, *ApJ*, **348**, 647
 Boshkayev, K., Rueda, J. A., Ruffini, R., & Siutsou, I. 2013, *ApJ*, **762**, 117
 Cannizzo, J. K., Lee, H. M., & Goodman, J. 1990, *ApJ*, **351**, 38
 Chabrier, G., & Potekhin, A. Y. 1998, *PhRvE*, **58**, 4941
 Chandrasekhar, S. 1931, *ApJ*, **74**, 81
 Chandrasekhar, S. 1970, *ApJ*, **161**, 571
 Chatterjee, P., Hernquist, L., & Narayan, R. 2000, *ApJ*, **534**, 373
 Dan, M., Rosswog, S., Brüggem, M., & Podsiadlowski, P. 2014, *MNRAS*, **438**, 14
 Dan, M., Rosswog, S., Guillochon, J., & Ramirez-Ruiz, E. 2011, *ApJ*, **737**, 89
 Davidson, K., & Ostriker, J. P. 1973, *ApJ*, **179**, 585
 Eggleton, P. P. 1983, *ApJ*, **268**, 368
 Ertan, Ü., Ekşi, K. Y., Erkut, M. H., & Alpar, M. A. 2009, *ApJ*, **702**, 1309
 Friedman, J. L., Ipser, J. R., & Sorkin, R. D. 1988, *ApJ*, **325**, 722
 García-Berro, E., Lorén-Aguilar, P., Aznar-Siguán, G., et al. 2012, *ApJ*, **749**, 25
 Gasques, L. R., Afanasjev, A. V., Aguilera, E. F., et al. 2005, *PhRvC*, **72**, 025806
 Ghosh, P., & Lamb, F. K. 1979, *ApJ*, **232**, 259
 Goldreich, P., & Julian, W. H. 1969, *ApJ*, **157**, 869
 Guerrero, J., García-Berro, E., & Isern, J. 2004, *A&A*, **413**, 257
 Han, Z., & Podsiadlowski, P. 2004, *MNRAS*, **350**, 1301
 Hartle, J. B. 1967, *ApJ*, **150**, 1005
 Hartle, J. B., & Thorne, K. S. 1968, *ApJ*, **153**, 807
 Henyey, L., & L'Ecuyer, J. 1969, *ApJ*, **156**, 549
 Iben, I., Jr., & Tutukov, A. V. 1984, *ApJS*, **54**, 335
 Ilkov, M., & Soker, N. 2012, *MNRAS*, **419**, 1695
 Ilkov, M., & Soker, N. 2013, *MNRAS*, **428**, 579
 Illarionov, A. F., & Sunyaev, R. A. 1975, *A&A*, **39**, 185
 Itoh, N., Hayashi, H., Nishikawa, A., & Kohyama, Y. 1996, *ApJS*, **102**, 411
 Itoh, N., Kohyama, Y., Matsumoto, N., & Seki, M. 1984, *ApJ*, **285**, 758
 Itoh, N., Mitake, S., Iyetomi, H., & Ichimaru, S. 1983, *ApJ*, **273**, 774
 Ji, S., Fisher, R. T., García-Berro, E., et al. 2013, *ApJ*, **773**, 136
 Kashi, A., & Soker, N. 2011, *MNRAS*, **417**, 1466
 Külebi, B., Ekşi, K. Y., Lorén-Aguilar, P., Isern, J., & García-Berro, E. 2013, *MNRAS*, **431**, 2778
 Leonard, D. C. 2007, *ApJ*, **670**, 1275
 Livio, M., & Riess, A. G. 2003, *ApJL*, **594**, L93
 Lorén-Aguilar, P., Isern, J., & García-Berro, E. 2009, *A&A*, **500**, 1193
 Menou, K., Esin, A. A., Narayan, R., et al. 1999, *ApJ*, **520**, 276
 Mochkovitch, R., & Livio, M. 1990, *A&A*, **236**, 378
 Nomoto, K. 1982, *ApJ*, **253**, 798
 Nomoto, K., & Iben, I., Jr. 1985, *ApJ*, **297**, 531
 Pakmor, R., Kromer, M., Röpke, F. K., et al. 2010, *Natur*, **463**, 61
 Perlmutter, S., Aldering, G., Goldhaber, G., et al. 1999, *ApJ*, **517**, 565
 Phillips, M. M. 1993, *ApJL*, **413**, L105
 Piersanti, L., Gagliardi, S., Iben, I., Jr., & Tornambé, A. 2003, *ApJ*, **583**, 885

- Potekhin, A. Y., & Chabrier, G. 2000, *PhRvE*, **62**, 8554
- Pringle, J. E. 1974, PhD thesis, Univ. Cambridge
- Raskin, C., Scannapieco, E., Fryer, C., Rockefeller, G., & Timmes, F. X. 2012, *ApJ*, **746**, 62
- Riess, A. G., Filippenko, A. V., Challis, P., et al. 1998, *AJ*, **116**, 1009
- Rotondo, M., Rueda, J. A., Ruffini, R., & Xue, S.-S. 2011, *PhRvD*, **84**, 084007
- Saio, H., & Nomoto, K. 1985, *A&A*, **150**, L21
- Salpeter, E. E. 1961, *ApJ*, **134**, 669
- Sato, Y., Nakasato, N., Tanikawa, A., et al. 2015, *ApJ*, **807**, 105
- Schwab, J., Quataert, E., & Kasen, D. 2016, *MNRAS*, **463**, 3461
- Schwab, J., Shen, K. J., Quataert, E., Dan, M., & Rosswog, S. 2012, *MNRAS*, **427**, 190
- Shakura, N. I., & Sunyaev, R. A. 1973, *A&A*, **24**, 337
- Shen, K. J., Bildsten, L., Kasen, D., & Quataert, E. 2012, *ApJ*, **748**, 35
- Shibata, M., Baumgarte, T. W., & Shapiro, S. L. 2000, *PhRvD*, **61**, 044012
- Spitkovsky, A. 2006, *ApJL*, **648**, L51
- Springel, V. 2010, *MNRAS*, **401**, 791
- Stergioulas, N. 2003, *LRR*, **6**, 3
- Totani, T., Morokuma, T., Oda, T., Doi, M., & Yasuda, N. 2008, *PASJ*, **60**, 1327
- Townsley, D. M., & Bildsten, L. 2004, *ApJ*, **600**, 390
- van Kerkwijk, M. H., Chang, P., & Justham, S. 2010, *ApJL*, **722**, L157
- Wang, Y.-M. 1987, *A&A*, **183**, 257
- Wang, Y.-M. 1995, *ApJL*, **449**, L153
- Wang, Y.-M. 1997, *ApJL*, **475**, L135
- Webbink, R. F. 1984, *ApJ*, **277**, 355
- Weinberg, D. H., Mortonson, M. J., Eisenstein, D. J., et al. 2013, *PhR*, **530**, 87
- Yoon, S.-C., Podsiadlowski, P., & Rosswog, S. 2007, *MNRAS*, **380**, 933
- Zhu, C., Chang, P., van Kerkwijk, M. H., & Wadsley, J. 2013, *ApJ*, **767**, 164
- Zhu, C., Pakmor, R., van Kerkwijk, M. H., & Chang, P. 2015, *ApJL*, **806**, L1

Comparison and contrast of test-particle and numerical-relativity waveform templates

To cite this article: J.F. Rodríguez *et al* JCAP02(2018)030

View the [article online](#) for updates and enhancements.

Related content

- [Error-analysis and comparison to analytical models of numerical waveforms produced by the NRAR Collaboration](#)
Ian Hinder, Alessandra Buonanno, Michael Boyle et al.
- [Effects of waveform model systematics on the interpretation of GW150914](#)
B P Abbott, R Abbott, T D Abbott et al.
- [Gravitational-wave data analysis using binary black-hole waveforms](#)
P Ajith

Comparison and contrast of test-particle and numerical-relativity waveform templates

J.F. Rodríguez, J.A. Rueda and R. Ruffini

ICRANet, Piazza della Repubblica 10, Pescara, I-65122 Italy
Dipartimento di Fisica and ICRA, Sapienza Università di Roma,
P.le Aldo Moro 5, Rome, I-00185 Italy

E-mail: jose.rodriguez@icranet.org, jorge.rueda@icra.it, ruffini@icra.it

Received September 13, 2017

Revised January 24, 2018

Accepted February 6, 2018

Published February 16, 2018

Abstract. We compare and contrast the emission of gravitational waves and waveforms for the recently established “helical-drifting-sequence” of a test particle around a Kerr black hole with the publicly available waveform templates of numerical-relativity. The merger of two black holes of comparable mass are considered. We outline a final smooth merging of the test particle into the final Kerr black hole. We find a surprising and unexpected agreement between the two treatments if we adopt, for the mass of the particle and the Kerr black hole a Newtonian-center-of-mass description, and for the Kerr black hole spin an effective value whose nature remains to be clarified.

Keywords: gravitational waves / theory, gravitational waves / sources

ArXiv ePrint: [1706.07704](https://arxiv.org/abs/1706.07704)

Contents

1	Introduction	1
2	General considerations of the reduced mass	1
3	Test-particle waveform	2
4	Comparison of the waveforms	3
4.1	Merging black holes of equal-mass and equal, aligned spins	3
4.2	Merging black holes of unequal-mass and spinless	6
5	Mass of the newly-formed black hole	7
6	Conclusions	9

1 Introduction

Following our recent determination of the “helical-drifting-sequence” (hereafter HDS) of a test particle around a Kerr black hole, we attempt to understand the methodology followed in the construction of the waveform templates publicly available from numerical-relativity simulations. For this scope we shall make use of the waveforms of the SXS catalog (see [1] for details), obtained from simulations of binary black-hole coalescences with the Spectral Einstein Code (SpEC).

We adopt the following three steps, which we do not consider to be necessarily valid, adopted only for the sake of a working hypothesis:

1. We adopt the HDS for a test particle following our previous work ([2]).
2. In order to step from a test particle of mass m to a binary black hole of comparable masses m_1 and m_2 , we adopt the Newtonian-center-of-mass description assuming $m = \mu$, where $\mu = m_1 m_2 / M$ is the reduced mass of the binary and $M = m_1 + m_2$ is the total binary mass.
3. We compute the waveform of the HDS all the way up to the passage over the last circular orbit, as originally introduced by [3]. As shown in [2], we do not expect any significant gravitational-wave emission during the final smooth merging of the particle into the Kerr black hole.

2 General considerations of the reduced mass

It is clear already from the Newtonian-center-of-mass approach that the dimensionless spin parameter, a/M , where $a = J/M = \mu\sqrt{r/M}$ is the orbital angular momentum per unit mass and r is the objects interdistance, is typically much larger than unity in any self-gravitating binary system of comparable masses. For equal-masses, it converges from above, namely from $a/M > 1$, to $a/M = 1$ only when $r = 16M$. This implies that only massive neutron stars or black holes can reach black hole formation in their final merger process. Most important,

the condition of $a/M = 1$ under these conditions can only be reached from above, i.e. from $a/M > 1$, and not by accretion. This gives a tangible way to see implemented, by emission of gravitational waves, the no-hair theorem (see, e.g., figure 1 in [4]).

We consider in our previous work ([2]) the gravitational-wave emission of a test particle, initially in circular orbit around a Schwarzschild or a Kerr black hole. We include the gravitational-wave radiation-reaction into the equations of motion to compute the dynamical evolution of the particle, obtaining the HDS of orbits all the way up to the final smooth merger of the particle into the black hole.

Having obtained this result we here proceed, following similar attempts in the literature, to adopt the HDS of the test particle as an effective body to describe the merger of two black holes of comparable mass. We can not refrain from expressing our surprise for the agreement of this treatment with the one of numerical-relativity waveform templates.

3 Test-particle waveform

During the initial phases of the HDS of the particle, the motion is quasi-circular, namely the radial velocity is relatively small with respect to the tangential velocity. Thus, the gravitational waveform can be, in first approximation, constructed from circular-orbit waves. The gravitational wave can be obtained from the scalar ψ_4 as [5]:

$$\frac{1}{2}(h_+ - ih_\times) = -\frac{1}{R} \sum_{l,m} \frac{Z_{lm}^H}{\omega_m^2} {}_{-2}S_{lm}(\Theta) e^{im\Phi} e^{-i\omega_m(t-R^*)}, \quad (3.1)$$

where R is the distance from the Kerr black hole to the observer, Θ is the angle between the axis of rotation and the observer, Φ is the azimuthal coordinate of the orbiting body at $t = 0$; R^* is the Kerr “tortoise” coordinate, and ${}_{-2}S_{lm}$ are the spheroidal harmonics of spin -2 [6]. The complex numbers $Z_{lm\omega}^H$ that depend on $\omega_m = m\omega$, where ω is the orbital angular velocity, were computed in [2] to estimate the gravitational-wave radiation flux, dE/dt , for a particle moving in a circular orbit on the Kerr metric. This radiation has been computed in the Teukolsky’s formalism of curvature perturbations [6, 7] with the aid of the Sasaki-Nakamura radial equation [8, 9].

As the HDS of orbits progresses, the wave frequency changes with time and we evaluate the acquisition of radial momentum. This implies that the complex number $Z_{lm\omega}$ evolves with time, inducing a variable wave amplitude and phase shift. We also replace $\omega_m(t - R^*)$ in the exponential by $m\phi(t - R^*)$ (see, e.g., [10]), where ϕ is the azimuthal coordinate of the test particle along the trajectory. We compute the particle’s trajectory following our previous work ([2]) from the equations of motion associated with the Hamiltonian (see, e.g., [11], and references therein)

$$H = -P_t = -N^i P_i + N \sqrt{m^2 + \gamma^{ij} P_i P_j}, \quad (3.2)$$

where $N = 1/\sqrt{-g^{00}}$, $N^i = -g^{ti}/g^{tt}$ and $\gamma^{ij} = g^{ij} + N^i N^j / N^2 = g^{ij} - g^{ti} g^{tj} / g^{tt}$. The Latin index stands for the spatial coordinates (r, θ, ϕ) and P_i are the spatial momenta. The equations of motion on the equatorial plane $\theta = \pi/2$ are (see [2] for details)

$$\frac{dr}{dt} = \frac{\partial H}{\partial P_r}, \quad \frac{d\phi}{dt} = \frac{\partial H}{\partial P_\phi}, \quad (3.3)$$

$$\frac{dP_r}{dt} = -\frac{\partial H}{\partial r}, \quad \frac{dP_\phi}{dt} = -\frac{1}{\omega} \frac{dE}{dt}. \quad (3.4)$$

As usual we decompose the waveform into the spin-weighted spherical harmonics ${}_sY_{lm}(\theta, \phi)$ as follows [12]:

$$R(h_+ - ih_\times) = \sum_{l,m} h_{lm}(t - R^*) {}_{-2}Y_{lm}(\Theta, \Phi), \quad (3.5)$$

where

$$h_{lm} = -2 \frac{Q_{lm}}{\omega_m^2} e^{-im\phi(t-R^*)}, \quad Q_{lm} = \int d(\cos \Theta) \sum_{l',m'} Z_{l'm'\omega}^H {}_{-2}S_{l'm'\omega}(\Theta) {}_{-2}Y_{lm}(\Theta, 0). \quad (3.6)$$

Near the last circular orbit the radial momentum significantly grows (see figure 2 in [2]). We include the radial motion effects only implicitly through the orbital phase ϕ which is obtained from the numerical integration of eqs. (3.3)–(3.4) which include the effects of both radial drift and radiation-reaction.

4 Comparison of the waveforms

In order to do the comparison of the treatments, we start the HDS at some large distance r_0 at time $t = 0$ and compute the evolution up to the passage over the last circular orbit, at the time $t = t_{\text{plunge}}$. Then, we construct the waveform using the method described in the above section. Since the values of the initial time and phase of the two simulations are arbitrary, we perform a constant change of time and phase which minimizes the overall differences between the two waveforms. Since the comparison is in the waveform at infinity, we assume that the two waveforms are expressed as a function of the same time coordinate.

To quantify the difference between two waveforms one can compute the so-called fitting factor

$$F \equiv (h_1|h_2)/\sqrt{(h_1|h_1)(h_2|h_2)}, \quad (h_1|h_2) \equiv 4\Re \left[\int_0^\infty h_1(f) \tilde{h}_2(f) / S_n(f) df \right], \quad (4.1)$$

where f is the gravitational-wave frequency in the detector's frame, $\tilde{h}_i(f)$ is the Fourier transform of the waveform $h_i(t)$ and $S_n(f)$ is the power-spectrum density of the detector's noise. For the latter we use the Advanced LIGO noise (see, e.g., [13]). Through the fitting factor one can also define the so-called mismatch, $\mathcal{M} \equiv 1 - F$. Since the function $S_n(f)$ is given in physical units (Hertz) then a value for the total mass of the system has to be specified to calculate the fitting factor. For all the examples shown below we set $M = 70 M_\odot$.

Another way to quantify the difference between two waveforms is by the *intrinsic* time-domain phase evolution $Q_\omega = \omega^2 / \dot{\omega}$, where $\omega = d\phi/dt$ and ϕ is the gravitational-wave phase. We did not take into account *the small correction in the phase* from the term Q_{lm} in eq. (3.6) to avoid the noise arising from the interpolation of the radiation flux. To calculate Q_ω we proceed as in ref. [14], although some difficulties were reported there due to the inherent oscillations present in the numerical-relativity data. We prefer here to not perform any fit of the function Q_ω of the numerical-relativity simulation.

4.1 Merging black holes of equal-mass and equal, aligned spins

We turn now to compare and contrast some waveforms of the SXS catalog with the ones obtained from the HDS treatment of the present work. First, we focus on simulations of binaries of merging black-holes with equal-mass and equal, aligned spins.

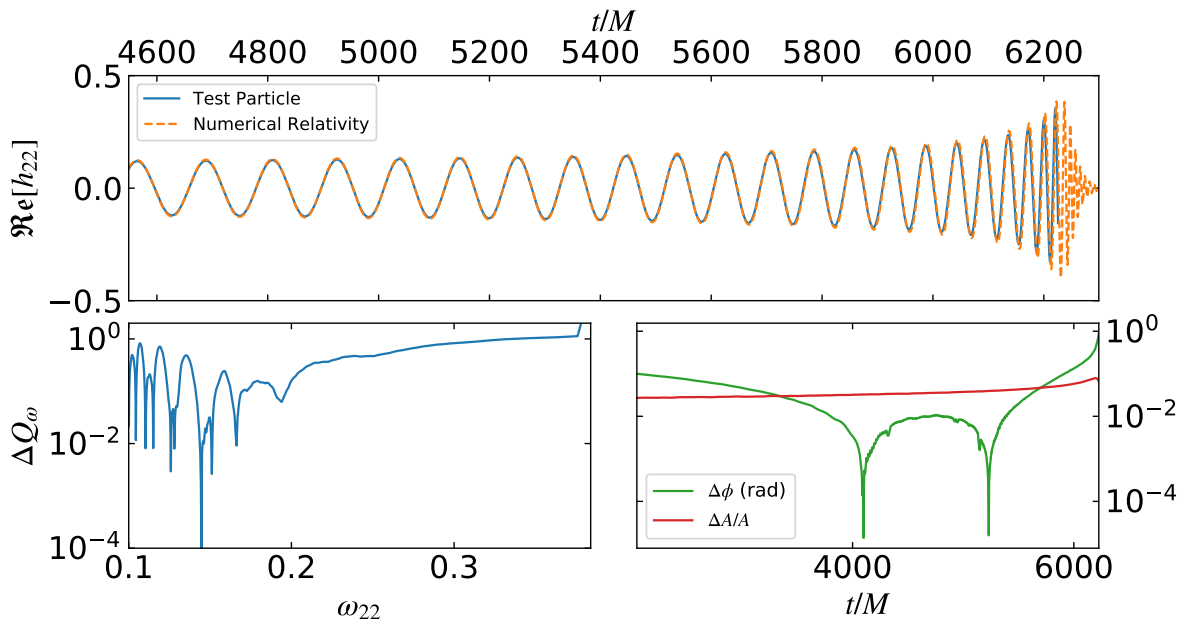


Figure 1. Comparison of the HDS and the numerical-relativity waveforms. Top panel: the dashed orange curve is the numerical-relativity waveform BH:0230 [1, 15] of the coalescence of a binary black-hole with $m_1 = m_2$ and $a_1/m_1 = a_2/m_2 = 0.8$, forming a Kerr black hole with spin parameter $a_f/M_f = 0.907516$. The continuous blue curve is the test-particle waveform during the HDS adopting $m = M/4$ and a dimensionless spin of the Kerr black hole nearly equal to the one of the newly-formed Kerr black hole of the merger simulation, 0.9075. The time is normalized to the total binary mass, M , and the comparison is made up to the instant of passage of the test particle at the location of the last stable circular orbit. For the sake of clarity we show here the waveforms in the last part of the evolution. Left lower panel: intrinsic time-domain phase difference evolution $\Delta Q_\omega = |Q_\omega^{\text{TP}} - Q_\omega^{\text{NR}}|$ as a function of the frequency of the $l = m = 2$ gravitational-wave mode, ω_{22} . We recall that, in this regime of the inspiraling $\omega_{22} \approx 2\omega$, where ω is the orbital angular velocity. Right lower panel: phase difference $\Delta\phi$ (in radians; green curve) and relative difference of the amplitudes of the two waveforms shown in the top panel during the entire time of the comparison.

We start the comparison with the numerical-relativity simulation BH:0230 [1, 15]: the coalescence of two black holes with $m_1 = m_2 = M/2$ and dimensionless spin parameters $a_1/m_1 = a_2/m_2 = 0.8$, forming a Kerr black hole with dimensionless spin parameter $a_f/M_f = 0.907516$. This system is particularly interesting since it is characterized by equal-mass and high-spin components, properties which are in principle different from the non-spinning, test particle domain which we adopt here. No agreement between the two treatments should be a priori expected.

Figure 1 shows the comparison of the two waveforms, the one of numerical-relativity simulations with the one of a test particle during the HDS around a Kerr black hole. We adopt a test particle of mass $m = \mu = m_1 m_2 / M = M/4$ and a Kerr black hole with spin parameter nearly equal to the one of the newly-formed Kerr black hole in the merger, i.e. 0.9075. For completeness of the comparison we also show, for this time-interval, the intrinsic time-domain phase evolution Q_ω , and the difference between the gravitational-wave phases, $\Delta\phi$ (green curve), and the relative difference between the waveform amplitudes, $\Delta A/A$ (red curve).

We obtain for the waveforms of figure 1 a value $F \approx 0.993$, so a mismatch $\mathcal{M} = 0.007$, during the entire time-interval of the comparison, i.e. $t/M \approx 1702.03\text{--}6182.19$, corresponding

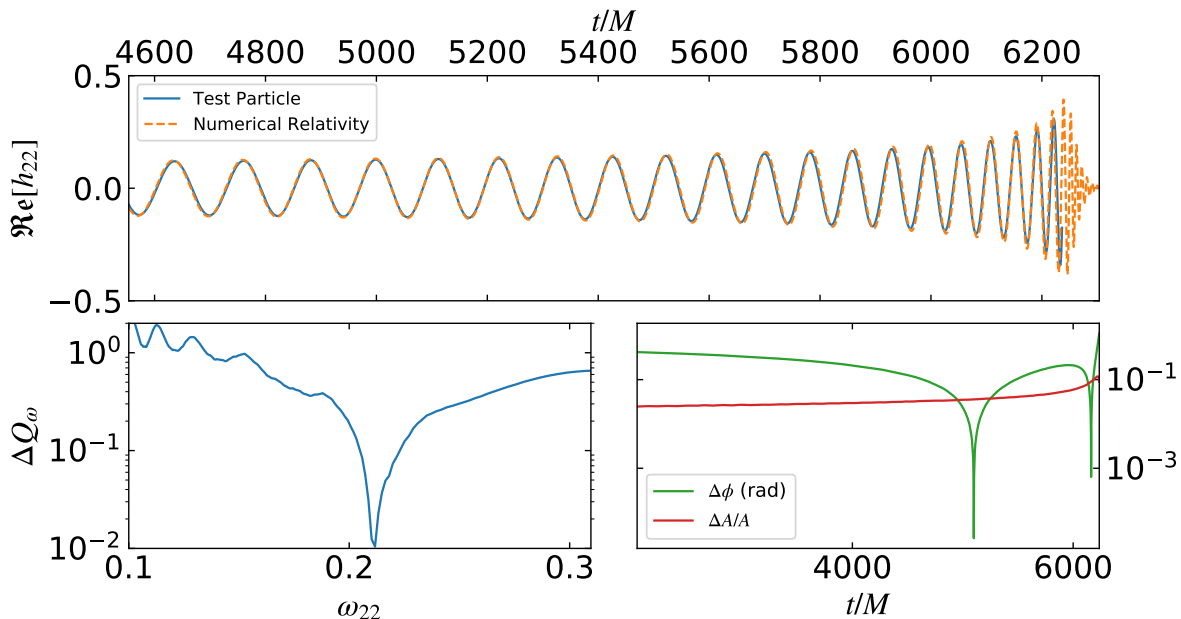


Figure 2. Comparison of the HDS and the numerical-relativity waveforms. Top panel: the dashed orange curve is the numerical-relativity waveform BH:0228 [1, 15] of the coalescence of a binary black-hole with $m_1 = m_2$ and $a_1/m_1 = a_2/m_2 = 0.6$, forming a Kerr black hole with spin parameter $a_f/M_f = 0.857813$. The continuous blue curve is the test-particle waveform during the HDS adopting $m = M/4$ and a dimensionless spin of the Kerr black hole $a_{\text{eff}}/M = 0.8$. We use for the HDS the same mass-ratio of the numerical-relativity simulation. Left lower panel: intrinsic time-domain phase difference evolution $\Delta Q_\omega = |Q_\omega^{\text{TP}} - Q_\omega^{\text{NR}}|$ as a function of the frequency of the $l = m = 2$ gravitational-wave mode, ω_{22} . Right lower panel: phase difference $\Delta\phi$ (in radians; green curve) and relative difference of the amplitudes of the two waveforms.

to an interval of separation distances $r/M = 14.95\text{--}2.27$, where the latter is the location of the last circular orbit. It can be seen that, regardless of the Q_ω oscillations for the numerical-relativity data, $\Delta Q_\omega = |Q_\omega^{\text{TP}} - Q_\omega^{\text{NR}}| \lesssim 1$.

The above agreement between the two waveforms, both in amplitude and in phase, is remarkable and unexpected. We now proceed to the results of additional representative cases. We show in figure 2 the comparison with the numerical-relativity simulation BH:0228 characterized by two black holes with aligned spins $a_1/m_1 = a_2/m_2 = 0.6$ that merge and form a black hole with spin $a_f/M_f = 0.857813$ [1, 15]. We found here a new feature with respect to the previous comparison: the best matching waveform did not correspond to the one generated by the HDS in a Kerr black hole with (nearly) the same spin of the newly-formed black hole. Instead, we found that the agreement is obtained for the HDS in a Kerr black hole with an “effective” spin parameter $a_{\text{eff}}/M = 0.8$. The fitting factor for this case is $F = 0.972$.

The above simulation hinted us the existence of an effective spin parameter for our simulations for which there is a very good matching with the numerical-relativity simulations. Thus, we performed more comparisons with other waveforms of the SXS catalog to confirm it. The results are presented in figure 3 and table 1. We can conclude from this first part of our analysis that, if we adopt for the HDS treatment the same mass ratio as the one of the numerical-relativity simulation, it can be always found an effective spin of the Kerr black hole of the HDS approach for which the waveforms of the two treatments are in excellent

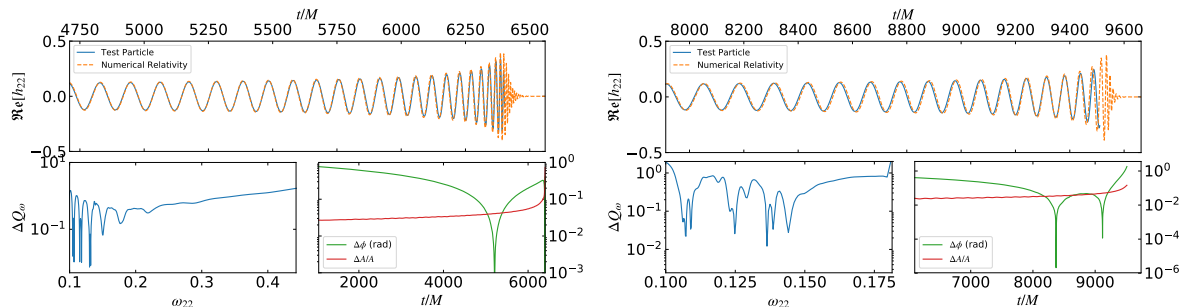


Figure 3. Comparison of numerical-relativity waveform and HDS waveforms. Left panel: BBH:0157, coalescence of a binary black-hole with $m_1 = m_2$ and $a_1/m_1 = a_2/m_2 = 0.949586$, forming a Kerr black hole with spin parameter $a_f/M_f = 0.940851$ [1, 16]. For the HDS treatment we find an effective spin parameter $a_{\text{eff}}/M_f = 0.99$. Right panel: BBH:0001, coalescence of a binary black-hole with $m_1 = m_2$ and $a_1/m_1 = a_2/m_2 = 1.2 \times 10^{-7}$ (i.e. spinless case), forming a Kerr black hole with spin parameter $a_f/M_f = 0.686461$ [1, 17]. For the HDS treatment we find an effective spin parameter $a_{\text{eff}}/M = 0.36$. Again, we found that the effective spin parameter of the Kerr black hole in the HDS treatment is neither the one of the newly-formed black hole nor the one of the merging black holes of the numerical-relativity simulation.

Simulation	a_i/m_i	a_f/M_f	a_{eff}/M_f	F
BBH:0001	1.209309×10^{-7}	0.686461	0.36	0.96
BBH:0157	0.949586	0.940851	0.99	0.93
BBH:0228	0.600000	0.857813	0.80	0.972
BBH:0230	0.800000	0.907516	0.9075	0.993

Table 1. Column 1: code of the numerical-relativity simulation of the SXS catalog [1]. Column 2: spin parameter of the merging black holes, a_i/m_i . Column 3: spin parameter of the newly-formed black hole, a_f/m_f . Column 4: effective spin a_{eff}/M_f of the Kerr black hole in the HDS treatment that gives good agreement with the numerical-relativity simulation. Column 5: fitting factor between the numerical-relativity and HDS waveforms. All the simulations are for equal-mass binaries.

agreement. It can be also seen from ΔQ_ω that, regardless of the oscillations inherent in the numerical-relativity simulations, the two phase evolutions agree each other. Nevertheless, it can be seen that the agreement between the two waveforms decreases in some part of the evolution, suggesting that the effective spin a_{eff} might change with time.

4.2 Merging black holes of unequal-mass and spinless

We also analyzed the case of spinless merging black holes for different mass ratios, $q = m_2/m_1 = 1, 1/2, 1/3, 1/4$, with $m_1 \geq m_2$ (see figure 4). We have found that the effective spin varies proportionally with the binary mass ratio. This also shows that, although the black holes do not spin, there is some spin on the background spacetime even before the formation of the final spinning black hole. The effective spin turned out to be always lower than the spin of the newly-formed black hole.

As we have mentioned, the formation of the Kerr black hole from binaries of black holes of comparable masses occurs from above, namely from $a/M > 1$ at larger distances to $a/M \lesssim 1$ as the objects approach each other. Only in the case of binaries with extreme mass-ratios $\mu/M \ll 1$, the merger leads to a slowly-rotating black hole, and, only when

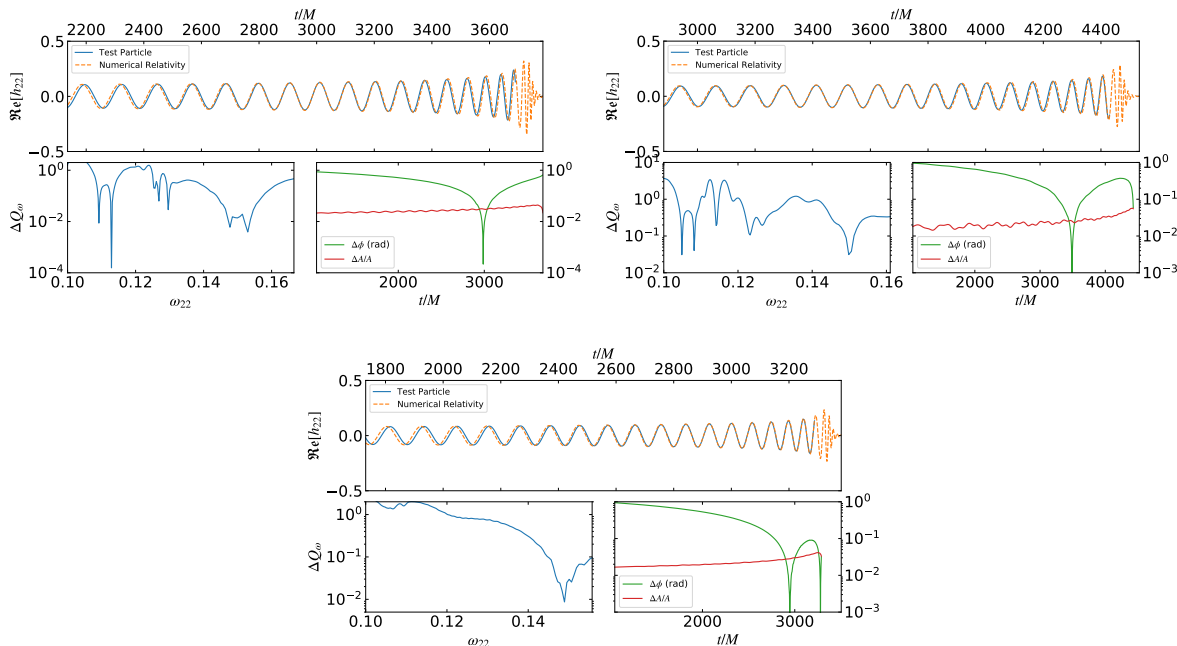


Figure 4. Comparison of three numerical-relativity simulations of spinless merging binary black holes with the current HDS approach. Top left panel: BBH:0169 numerical-relativity waveform of mass ratio $q = 1/2$ [1, 18]. The effective spin for this case is $a_{\text{eff}}/M_f = 0.33$ and the fitting factor between the two waveforms is $F = 0.95$. Top right panel: BBH:0030 numerical-relativity waveform of mass ratio $q = 1/3$ [1, 17]. The effective spin is $a_{\text{eff}}/M_f = 0.29$ and the fitting factor $F = 0.965$. Bottom panel: BBH:0182 numerical-relativity simulation of mass ratio $q = 1/4$ [1, 19]. The effective spin is $a_{\text{eff}}/M_f = 0.25$ and the fitting factor $F = 0.963$.

$\mu/M \rightarrow 0$, the formation of a Schwarzschild black hole can be approached. This is consistent with our results above of an effective spin of the black hole proportional to the mass ratio, so that we expect a vanishing spin, i.e. a Schwarzschild black hole, only in the limiting case of a vanishing mass ratio.

5 Mass of the newly-formed black hole

We have shown in [2] that no significant gravitational radiation is expected after the passage of the test particle over the last circular orbit. Thus, the mass of the newly-formed black hole is expected to be

$$M_{\text{BH}} = M - \Delta E_{\text{rad}}, \quad (5.1)$$

$$\Delta E_{\text{rad}} = m - H_{\text{plunge}}, \quad (5.2)$$

where $H_{\text{plunge}} \equiv H(t = t_{\text{plunge}})$ is the value of the Hamiltonian (energy) of the particle (3.2) during the final smoothly merging into the black hole (see [2] for details). As we have shown in [2] (see section V therein), due to the radial drift and the radiation-reaction effects leading to the HDS, when the particle passes over the location of the last circular orbit H_{plunge} is smaller than the energy of a particle in circular orbit in the Kerr geometry:

$$\frac{E}{m} = \frac{r^2 - 2Mr + aM^{1/2}r^{1/2}}{r(r^2 - 3Mr + 2aM^{1/2}r^{1/2})^{1/2}}, \quad (5.3)$$

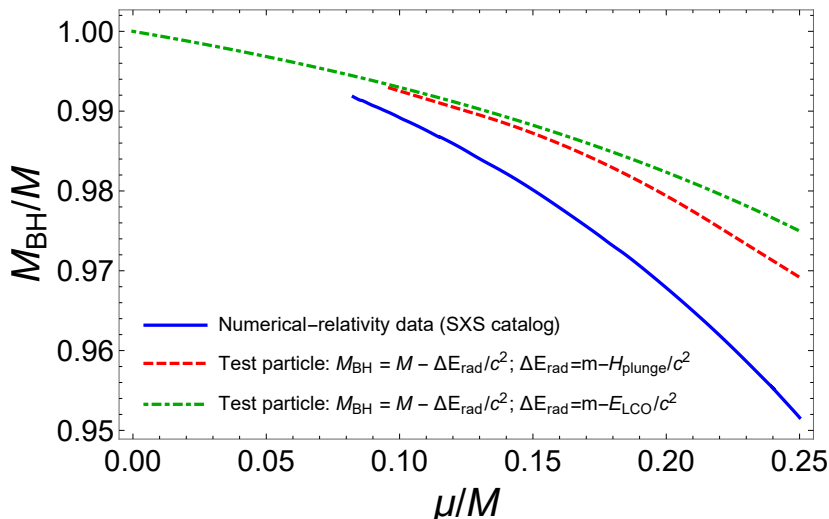


Figure 5. Comparison of the mass of the newly-formed black hole predicted by the HDS of the test particle and numerical-relativity simulations of binary black hole mergers. Blue-solid curve: numerical-relativity simulations ([1]) for coalescences of binary black holes with different values of the mass-ratio $q = m_2/m_1$ (we adopt $m_1 \geq m_2$), thus different values of the ratio $\mu = M = q/(1+q)^2$, and non-spinning, i.e. $a_1/m_1 = a_2/m_2 = 0.0$. Red-dashed curve: test particle prediction by eq. (5.1) adopting $\Delta E_{\text{rad}} = m - H_{\text{plunge}}/c^2$, eq. (5.2). Green-dot-dashed curve: test particle prediction by eq. (5.1) adopting $\Delta E_{\text{rad}} = m - E_{\text{LCO}}/c^2$ with E_{LCO} given by eq. (5.3), evaluated at the last circular orbit of the formed Kerr black hole. In our treatment we adopt the mass of the particle, m , equal to the binary reduced-mass, μ , and the spin of the Kerr black hole equal to spin of the newly-formed black hole in the merger. These simulations range values of spin parameter from ≈ 0.3 in for $\mu/M \approx 0.1$ to ≈ 0.7 for $\mu/M = 0.25$.

evaluated at the last circular orbit, which facilitates the smooth merging of the particle to the Kerr black hole (see [2] for details).

We compare and contrast in figure 5 the mass of the newly-formed black hole predicted by the test particle treatment (5.1) and by the numerical-relativity simulations [1]. The numerical-relativity data in this plot refer to all the available simulations of the waveform catalog of coalescences of binary black holes with non-spinning components. These simulations correspond to different values of the mass-ratio $q = m_2/m_1$ (we adopt $m_1 \geq m_2$), thus different values of the ratio $\mu/M = q/(1+q)^2$. In the case of the above simulations of non-spinning components, the spin parameter of the newly-formed Kerr black hole ranges from ≈ 0.3 (for $\mu/M \approx 0.1$) to ≈ 0.7 (for $\mu/M = 1/4$). We recall that we adopt in the comparison the spin of the Kerr black hole equal to spin of the newly-formed black hole in the numerical-relativity merger simulation.

We find that despite the agreement in the waveforms, the mass of the newly-formed black hole in numerical-relativity simulations is smaller than the one from the HDS of the test particle. It implies the existence in the numerical-relativity simulations of an additional gravitational radiation after the passage of the particle over the last circular orbit, in contrast with the expectations from our results in [2]. At this stage, we do not find any physical reason that explains such an extra loss of gravitational energy at expenses of the black hole mass. We have pointed out in [2] the disagreement between our estimates of the energy radiated with the ones in [20], which also obtain a much larger radiation from their semi-analytic treatment of the final plunge of the particle into the Kerr black hole.

We are currently performing numerical calculations of the gravitational radiation from the Teukolsky equation adopting the actual plunge trajectory into the Kerr black hole after the last circular orbit as described in [2]. The results will be presented elsewhere including a waveform analysis.

6 Conclusions

1. It has been often emphasized in the literature by different groups the necessity of large computing facilities to perform numerical-relativity simulations (see [21] for a recent review, and references therein). However, the results of this article show they can be reproduced with the above theoretical treatment on a single laptop, representing an alternative, more direct, approach.
2. Of course this remarkable agreement does not prove the physical veracity of the assumptions we have made but, on the contrary, requires that more input on the assumptions and details of the numerical-relativity simulations be made publicly available, in order to formulate a diagnosis of this unexpected result and a priori unlikely theoretical event.
3. The agreement between the two treatments, with and without considering the intrinsic spins of the merging black holes, appears to be due to the dominating value of the binary angular momentum over the one of the individual spins of the merging black holes. What clearly stands from this Letter is a call for attention to the non-applicability of relativistic orbits in the Schwarzschild metric and the neglect of the total binary angular momentum which needs to be taken to the general attention.

Acknowledgments

We had the pleasure during the entire development of this work to discuss in our ICRANet headquarter in Pescara with Prof. Roy Kerr. To him, and to the entire ICRANet Faculty and Staff, goes our gratitude.

References

- [1] <http://www.black-holes.org/waveforms>.
- [2] J.F. Rodríguez, J.A. Rueda and R. Ruffini, *Strong-field gravitational-wave emission in Schwarzschild and Kerr geometries: some general considerations*, *EPJ Web Conf.* **168** (2018) 02006 [[arXiv:1706.06440](#)] [[INSPIRE](#)].
- [3] R. Ruffini and J.A. Wheeler, *Relativistic cosmology and space platforms*, A.F. Moore and V. Hardy eds., European Space Research Organization, Neuilly-sur-Seine France (1971), pp. 45–174 [[PRINT-70-2077](#)] [[INSPIRE](#)].
- [4] R. Ruffini and J.A. Wheeler, *Introducing the black hole*, *Phys. Today* **24** (1971) 30 [[INSPIRE](#)].
- [5] S.L. Detweiler, *Black Holes and Gravitational Waves. I. Circular Orbits About a Rotating Hole*, *Astrophys. J.* **225** (1978) 687 [[INSPIRE](#)].
- [6] S.A. Teukolsky, *Perturbations of a rotating black hole. I. Fundamental equations for gravitational electromagnetic and neutrino field perturbations*, *Astrophys. J.* **185** (1973) 635 [[INSPIRE](#)].
- [7] S.A. Teukolsky and W.H. Press, *Perturbations of a rotating black hole. III — Interaction of the hole with gravitational and electromagnetic radiation*, *Astrophys. J.* **193** (1974) 443 [[INSPIRE](#)].

- [8] M. Sasaki and T. Nakamura, *Gravitational Radiation From a Kerr Black Hole. I. Formulation and a Method for Numerical Analysis*, *Prog. Theor. Phys.* **67** (1982) 1788 [INSPIRE].
- [9] M. Sasaki and T. Nakamura, *A Class of New Perturbation Equations for the Kerr Geometry*, *Phys. Lett. A* **89** (1982) 68 [INSPIRE].
- [10] S.A. Hughes, *Evolution of circular, nonequatorial orbits of Kerr black holes due to gravitational wave emission. II. Inspiral trajectories and gravitational wave forms*, *Phys. Rev. D* **64** (2001) 064004 [gr-qc/0104041] [INSPIRE].
- [11] R.T. Jantzen, P. Carini and D. Bini, *The Many faces of gravitoelectromagnetism*, *Annals Phys.* **215** (1992) 1 [gr-qc/0106043] [INSPIRE].
- [12] E.T. Newman and R. Penrose, *Note on the Bondi-Metzner-Sachs group*, *J. Math. Phys.* **7** (1966) 863 [INSPIRE].
- [13] VIRGO and LIGO SCIENTIFIC collaborations, B.P. Abbott et al., *Prospects for Observing and Localizing Gravitational-Wave Transients with Advanced LIGO and Advanced Virgo*, *Living Rev. Relativ.* **19** (2016) 1 [arXiv:1304.0670] [INSPIRE].
- [14] T. Damour, A. Nagar and S. Bernuzzi, *Improved effective-one-body description of coalescing nonspinning black-hole binaries and its numerical-relativity completion*, *Phys. Rev. D* **87** (2013) 084035 [arXiv:1212.4357] [INSPIRE].
- [15] T. Chu et al., *On the accuracy and precision of numerical waveforms: Effect of waveform extraction methodology*, *Class. Quant. Grav.* **33** (2016) 165001 [arXiv:1512.06800] [INSPIRE].
- [16] D.A. Hemberger et al., *Final spin and radiated energy in numerical simulations of binary black holes with equal masses and equal, aligned or anti-aligned spins*, *Phys. Rev. D* **88** (2013) 064014 [arXiv:1305.5991] [INSPIRE].
- [17] A.H. Mroue et al., *Catalog of 174 Binary Black Hole Simulations for Gravitational Wave Astronomy*, *Phys. Rev. Lett.* **111** (2013) 241104 [arXiv:1304.6077] [INSPIRE].
- [18] L.T. Buchman, H.P. Pfeiffer, M.A. Scheel and B. Szilágyi, *Simulations of non-equal mass black hole binaries with spectral methods*, *Phys. Rev. D* **86** (2012) 084033 [arXiv:1206.3015] [INSPIRE].
- [19] J. Blackman et al., *Fast and Accurate Prediction of Numerical Relativity Waveforms from Binary Black Hole Coalescences Using Surrogate Models*, *Phys. Rev. Lett.* **115** (2015) 121102 [arXiv:1502.07758] [INSPIRE].
- [20] A. Ori and K.S. Thorne, *The Transition from inspiral to plunge for a compact body in a circular equatorial orbit around a massive, spinning black hole*, *Phys. Rev. D* **62** (2000) 124022 [gr-qc/0003032] [INSPIRE].
- [21] V. Cardoso, L. Gualtieri, C. Herdeiro and U. Sperhake, *Exploring New Physics Frontiers Through Numerical Relativity*, *Living Rev. Relativity* **18** (2015) 1 [arXiv:1409.0014] [INSPIRE].



Neutrino Oscillations within the Induced Gravitational Collapse Paradigm of Long Gamma-Ray Bursts

L. Becerra^{1,2}, M. M. Guzzo³, F. Rossi-Torres³, J. A. Rueda^{1,2,4} , R. Ruffini^{1,2,4}, and J. D. Uribe^{1,2}

¹Dipartimento di Fisica and ICRA, Sapienza Università di Roma, P.le Aldo Moro 5, I-00185 Rome, Italy

²ICRANet, P.zza della Repubblica 10, I-65122 Pescara, Italy

³Instituto de Física Gleb Wataghin, Universidade Estadual de Campinas, Rua Sérgio Buarque de Holanda 777, 13083-859 Campinas SP Brazil

⁴ICRANet-Rio, i Centro Brasileiro de Pesquisas Físicas, Rua Dr. Xavier Sigaud 150, 22290-180 Rio de Janeiro, Brazil

Received 2017 August 17; revised 2017 November 29; accepted 2017 December 16; published 2018 January 15

Abstract

The induced gravitational collapse paradigm of long gamma-ray bursts associated with supernovae (SNe) predicts a copious neutrino–antineutrino ($\nu\bar{\nu}$) emission owing to the hypercritical accretion process of SN ejecta onto a neutron star (NS) binary companion. The neutrino emission can reach luminosities of up to 10^{57} MeV s⁻¹, mean neutrino energies of 20 MeV, and neutrino densities of 10^{31} cm⁻³. Along their path from the vicinity of the NS surface outward, such neutrinos experience flavor transformations dictated by the neutrino-to-electron-density ratio. We determine the neutrino and electron on the accretion zone and use them to compute the neutrino flavor evolution. For normal and inverted neutrino mass hierarchies and within the two-flavor formalism ($\nu_e\nu_x$), we estimate the final electronic and nonelectronic neutrino content after two oscillation processes: (1) neutrino collective effects due to neutrino self-interactions where the neutrino density dominates, and (2) the Mikheyev–Smirnov–Wolfenstein effect, where the electron density dominates. We find that the final neutrino content is composed by $\sim 55\%$ ($\sim 62\%$) of electronic neutrinos, i.e., $\nu_e + \bar{\nu}_e$, for the normal (inverted) neutrino mass hierarchy. The results of this work are the first step toward the characterization of a novel source of astrophysical MeV neutrinos in addition to core-collapse SNe and, as such, deserve further attention.

Key words: accretion, accretion disks – gamma-ray burst: general – neutrinos – stars: neutron – supernovae: general

1. Introduction

The emergent picture of gamma-ray bursts (GRBs) is that both short-duration and long-duration GRBs originate from binary systems (Ruffini et al. 2016b).

Short bursts originate from neutron star–neutron star (NS–NS) or neutron star–black hole (NS–BH) mergers (see, e.g., Goodman 1986; Paczynski 1986; Eichler et al. 1989; Narayan et al. 1991). For this case Narayan et al. (1992) introduced the role of neutrino–antineutrino ($\nu\bar{\nu}$) annihilation leading to the formation of an electron–positron plasma (e^-e^+) in NS–NS and NS–BH mergers. Such a result triggered many theoretical works, including the general relativistic treatment by Salmonson & Wilson (2002) of the $\nu\bar{\nu}$ annihilation process giving rise to the e^-e^+ plasma in an NS–NS system.

For long bursts we stand on the induced gravitational collapse (IGC) paradigm (Ruffini et al. 2006, 2008, 2015b; Izzo et al. 2012; Rueda & Ruffini 2012; Fryer et al. 2014), based on the hypercritical accretion process of the supernova (SN) ejecta of the explosion of a carbon-oxygen core (CO_{core}) onto an NS binary companion. In the above processes, the emission of neutrinos is a key ingredient.

We focus hereafter on the neutrino emission of long bursts within the IGC scenario. The role of neutrinos in this paradigm has been recently addressed by Fryer et al. (2014, 2015) and Becerra et al. (2015, 2016). The hypercritical accretion of the SN ejecta onto the NS companion can reach very high rates of up to $10^{-2} M_\odot$ s⁻¹, and its duration can be of the order of $10\text{--}10^4$ s depending on the binary parameters. The photons become trapped within the accretion flow and thus do not serve as an energy sink. The high temperature developed on the NS surface leads to e^-e^+ pairs that, via weak interactions,

annihilate into $\nu\bar{\nu}$ pairs with neutrino luminosities of up to 10^{52} erg s⁻¹ for the highest accretion rates. Thus, this process dominates the cooling and gives rise to a very efficient conversion of the gravitational energy gained by accretion into radiation. We refer to Becerra et al. (2016) for further details on this process.

The above hypercritical accretion process can lead the NS to two alternative fates, leading to the existence of two long GRB subclasses (Fryer et al. 2014, 2015; Becerra et al. 2015, 2016; Ruffini et al. 2016b):

- I. The hypercritical accretion leads to a more massive NS companion but not to a BH. These binaries explain the X-ray flashes (XRFs): long bursts with isotropic energy $E_{\text{iso}} \lesssim 10^{52}$ erg and rest-frame spectral peak energy $E_{p,i} \lesssim 200$ keV (see Ruffini et al. 2016b, for further details). The local observed number density rate of this GRB subclass is (Ruffini et al. 2016b) $\rho_{\text{GRB}} = 100^{+45}_{-34}$ Gpc⁻³ yr⁻¹.
- II. The hypercritical accretion is high enough to make the NS reach its critical mass, triggering its gravitational collapse with consequent BH formation. These binaries explain the binary-driven hypernovae (BdHNe): long bursts with $E_{\text{iso}} \gtrsim 10^{52}$ erg and $E_{p,i} \gtrsim 200$ keV (see Ruffini et al. 2016b, for further details). The local observed number density rate of this GRB subclass is (Ruffini et al. 2016b) $\rho_{\text{GRB}} = 0.77^{+0.09}_{-0.08}$ Gpc⁻³ yr⁻¹.

Simulations of the hypercritical accretion process in the above binaries have been presented in Fryer et al. (2014, 2015) and Becerra et al. (2015, 2016). It has been shown how, thanks to the development of a copious neutrino emission near the NS surface, the NS is allowed to accrete matter from the SN at very

high rates. The specific conditions leading to XRFs and BdHNe, as well as a detailed analysis of the neutrino production in these systems, have been presented in Becerra et al. (2016). Neutrino emission can reach luminosities of 10^{52} erg s^{-1} and the mean neutrino energy of the order of 20 MeV. Under these conditions, XRFs and BdHNe become astrophysical laboratories for MeV-neutrino physics additional to core-collapse SNe.

On the other hand, the emission of TeV–PeV neutrinos is relevant for the observations of detectors such as the IceCube (Aartsen et al. 2013). High-energy neutrino emission mechanisms have been proposed within the context of the traditional model of long GRBs. In the traditional “collapsar” scenario (Woosley 1993; Paczyński 1998; MacFadyen & Woosley 1999) the gravitational collapse of a single, fast-rotating, massive star originates a BH surrounded by a massive accretion disk (see, e.g., Piran 2004, for a review), and the GRB dynamics follows the “fireball” model that assumes the existence of an ultrarelativistic collimated jet with Lorentz factor $\Gamma \sim 10^2\text{--}10^3$ (see, e.g., Shemi & Piran 1990; Meszaros et al. 1993; Piran et al. 1993; Mao & Yi 1994). This scenario has been adopted for the explanation of the prompt emission, as well as both the afterglow and the GeV emission of long GRBs. The GRB light-curve structures are there described by (internal or external) shocks (see, e.g., Rees & Meszaros 1992, 1994). The high-energy neutrinos in this context are produced from the interaction of shock-accelerated cosmic rays (e.g., protons) with the interstellar medium (see, e.g., Agostini et al. 2017; Kumar & Zhang 2015, and references therein). A recent analysis of the thermal emission of the X-ray flares observed in the early afterglow of long GRBs (at source rest-frame times $t \sim 10^2$ s) shows that it occurs at radii $\sim 10^{12}$ cm and expands with a mildly relativistic $\Gamma \lesssim 4$ (see Ruffini et al. 2018, for further details). This rules out the ultrarelativistic expansion in the GRB afterglow traditionally adopted in the literature. Interestingly, the aforementioned mechanisms of high-energy neutrino production conceived in the collapsar-fireball model can still be relevant in the context of BdHNe and authentic short GRBs (S-GRBs, NS–NS mergers with $E_{\text{iso}} \gtrsim 10^{52}$ erg leading to BH formation; see Ruffini et al. 2016b, for the classification of long and short bursts in seven different subclasses). The emission in the 0.1–100 GeV energy band observed in these two GRB subclasses has been shown to be well explained by a subsequent accretion process onto the newly born BH (Ruffini et al. 2015a, 2015b, 2016a, 2016b; Aimuratov et al. 2017; see also Aimuratov et al., in preparation). Such GeV emission is not causally connected either with the prompt emission or with the afterglow emission composing the flaring activity (Ruffini et al. 2018). An ultrarelativistic expanding component is therefore expected to occur in BdHNe and S-GRBs, which deserves to be explored in forthcoming studies as a possible source of high-energy neutrinos. Specifically, this motivates the present article to identify the possible additional channels to be explored in the hypercritical accretion not around an NS but around a BH.

The aim of this article is to extend the analysis of the MeV-neutrino emission in the hypercritical accretion process around an NS in the XRFs and BdHNe to assess the possible occurrence of neutrino flavor oscillations.

We shall show in this work that, before escaping to the outer space, i.e., outside the Bondi–Hoyle accretion region, the neutrinos experience an interesting phenomenology. The

neutrino density near the NS surface is so high that the neutrino self-interaction potential, usually negligible in other very well known scenarios such as the Sun, the upper layers of Earth’s atmosphere, and terrestrial reactor and accelerator experiments, becomes more relevant than the matter potential responsible for the famous Mikheyev–Smirnov–Wolfenstein (MSW) effect (Wolfenstein 1978; Mikheev & Smirnov 1986). A number of papers have been dedicated to the consequences of the neutrino self-interaction dominance (Notzold & Raffelt 1988; Pantaleone 1992; Qian & Fuller 1995; Pastor & Raffelt 2002; Sawyer 2005; Duan et al. 2006b, 2007, 2008a, 2008b, 2010; Fuller & Qian 2006; Esteban-Pretel et al. 2007, 2008; Fogli et al. 2007; Raffelt & Sigl 2007; Chakraborty et al. 2008; Dasgupta & Dighe 2008; Dasgupta et al. 2008a; Sawyer 2009; Wu & Qian 2011), most of them focused on SN neutrinos. In these cases, the SN induces the appearance of collective effects such as synchronized and bipolar oscillations leading to an entirely new flavor content of emitted neutrinos when compared with the spectrum created deep inside the star. The density of neutrinos produced in the hypercritical accretion process of XRFs and BdHNe is such that the neutrino self-interactions, as in the case of SNe, dominate the neutrino flavor evolution, giving rise to the aforementioned collective effects. The main neutrino source, in this case, is the $\nu\bar{\nu}$ pair production from e^-e^+ annihilation (Becerra et al. 2016), which leads to an equal number of neutrinos and antineutrinos of each type. This equality does not happen in the SN standard scenario. We will show that bipolar oscillations, inducing very quick flavor pair conversions $\nu_e\bar{\nu}_e \leftrightarrow \nu_\mu\bar{\nu}_\mu \leftrightarrow \nu_\tau\bar{\nu}_\tau$, can occur with oscillation length as small as $O(0.05\text{--}1)$ kilometers. However, the $\nu\text{--}\bar{\nu}$ symmetry characterizing our system leads to the occurrence of kinematic decoherence, making the neutrino flavor content reach equipartition deep inside the accretion zone. In the regions far from the NS surface where the neutrino density is not so high, the matter potential begins to dominate and MSW resonances can take place. As a result, an entirely different neutrino flavor content emerges from the Bondi–Hoyle surface when compared with what was originally created in the bottom of the accretion zone.

This article is organized as follows. In Section 2 we outline the general features of the accretion process onto the NS within the IGC paradigm and present the processes responsible for the neutrino creation. From these features, we obtain the distribution functions that describe the neutrino spectrum near the NS surface. Section 3 shows a derivation of the equations that drive the evolution of neutrino oscillations closely related to the geometrical and physical characteristics of our system. We discuss some details on the neutrino oscillation phenomenology. Since we have to face a nonlinear integro-differential system of equations of motion (EoM), we introduce the single-angle approximation to later recover the full realistic phenomenology after generalizing our results to the multi-angle approach and, consequently, de-coherent picture. In Section 5 the final neutrino emission spectra are presented and compared with those in which neutrinos are created in the accretion zone. Finally, we present in Section 6 the conclusions and some perspectives for future research on this subject.

2. Neutrino Creation during Hypercritical Accretion

The SN material first reaches the gravitational capture region of the NS companion, namely, the Bondi–Hoyle region. The

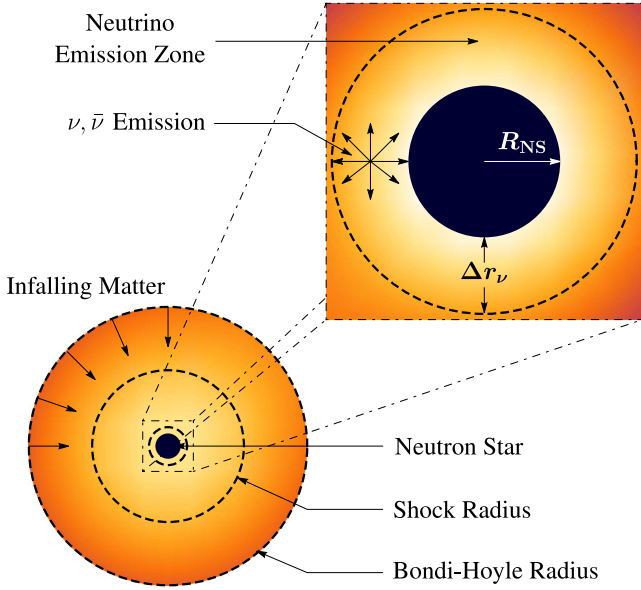


Figure 1. Schematic representation of the accretion process onto the NS and the neutrino emission. The supernova-ejected material reaches the NS Bondi–Hoyle radius and falls onto the NS surface. The material shocks and decelerates as it piles over the NS surface. At the neutrino emission zone, neutrinos take away most of the infalling matter’s energy. The neutrino emission allows the material to reduce its entropy to be incorporated to the NS. The image is not to scale. For a binary system with $M_{\text{NS}} = 2 M_{\odot}$ and $R_{\text{NS}} = 10$ km and an $M_{\text{ZAMS}} = 20 M_{\odot}$ progenitor, at $\dot{M} = 10^{-2} M_{\odot} \text{ s}^{-1}$, the positions of the Bondi–Hoyle and Shock radii are 2.3×10^5 km and 31 km, respectively. The neutrino emission zone’s thickness is $\Delta r_{\nu} = 0.8$ km.

infalling material shocks as it piles up onto the NS surface, forming an accretion zone where it compresses and eventually becomes sufficiently hot to trigger a highly efficient neutrino emission process. Neutrinos take away most of the infalling matter’s gravitational energy gain, letting it reduce its entropy and be incorporated into the NS. Figure 1 shows a sketch of this entire hypercritical accretion process.

It was shown in Becerra et al. (2016) that the matter in the accretion zone near the NS surface develops conditions of temperature and density such that it is in a nondegenerate, relativistic, hot plasma state. The most efficient neutrino emission channel under those conditions becomes the electron–positron pair annihilation process:



The neutrino emissivity produced by this process is proportional to the accretion rate to the 9/4 power (see below). This implies that the higher the accretion rate, the higher the neutrino flux; hence, the largest neutrino flux occurs at the largest accretion rate.

We turn now to estimating the accretion rate and thus the neutrino emissivity we expect in our systems.

2.1. Accretion Rate in XRFs and BdHNe

We first discuss the amount of SN matter per unit time reaching the gravitational capture region of the NS companion, namely, the Bondi–Hoyle accretion rate. It has been shown in Bayless et al. (2015) and Becerra et al. (2016) that the shorter (smaller) the orbital period (separation), the higher the peak accretion rate \dot{M}_{peak} and the shorter the time at which it peaks, t_{peak} .

The Bondi–Hoyle accretion rate is proportional to the density of the accreted matter and inversely proportional to its velocity. Thus, we expect the accretion rate to increase as the denser and slower inner layers of the SN reach the accretion region. Based on these arguments, Becerra et al. (2016) derived simple, analytic formulae for \dot{M}_{peak} and t_{peak} as a function of the orbital period (given all the other binary parameters) that catch both the qualitatively and quantitatively behaviors of these two quantities obtained from full numerical integration. We refer the reader to Appendix A of that article for further details. For the scope of this work these analytic expressions are sufficient to give us an estimate of the hypercritical accretion rates and related timescale developed in these systems:

$$t_{\text{peak}} \approx \left(1 - \frac{2M_{\text{NS}}}{M}\right) \left(\frac{GM}{4\pi^2}\right)^{1/3} \left(\frac{R_{\text{star}}^0}{\eta R_{\text{core}}}\right) \frac{P^{2/3}}{v_{\text{star},0}}, \quad (2a)$$

$$\dot{M}_{\text{peak}} \approx 2\pi^2 \frac{(2M_{\text{NS}}/M)^{5/2}}{(1 - 2M_{\text{NS}}/M)^3} \eta^{3-m} \rho_{\text{core}} \frac{R_{\text{core}}^3}{P}, \quad (2b)$$

where P is the orbital period, m is the index of the power-law density profile of the pre-SN envelope, $v_{\text{star},0}$ is the velocity of the outermost layer of the SN ejecta, $M = M_{\text{CO}} + M_{\text{NS}}$ is the total binary mass, and $M_{\text{CO}} = M_{\text{env}} + M_{\text{NS}}$ is the total mass of the CO_{core} given by the envelope mass and the mass of the central remnant, i.e., the new NS (hereafter νNS) formed from the region of the CO_{core} that undergoes core collapse (i.e., roughly speaking the iron core of density ρ_{core} and radius R_{core}). We here adopt $M_{\nu\text{NS}} = 1.5 M_{\odot}$. The parameter η is given by

$$\eta \equiv \frac{R_{\text{star}}^0}{R_{\text{core}}} \frac{1 + m}{1 + m(R_{\text{star}}^0/\hat{R}_{\text{core}})}, \quad (3)$$

where R_{star}^0 is the total radius of the pre-SN CO_{core} , $\hat{\rho}_{\text{core}}$ and \hat{R}_{core} are parameters of the pre-SN density profile introduced to account of the finite size of the envelope, and m is the power-law index followed by the density profile at radii $r > R_{\text{core}}$ (see Becerra et al. 2016, for further details).

Figure 2 shows the peak accretion rate in Equation (2) as a function of the orbital period. In this example, we consider the following binary parameters (see Becerra et al. 2016, for details): a CO_{core} produced by a zero-age main-sequence (ZAMS) progenitor with $M_{\text{ZAMS}} = 20 M_{\odot}$, i.e., $M_{\text{CO}} = 5.4 M_{\odot}$, an initial NS mass of $2.0 M_{\odot}$, and a velocity of the outermost ejecta layer $v_{\text{star},0} = 2 \times 10^9 \text{ cm s}^{-1}$. For these parameters, $\eta \approx 0.41$.

Becerra et al. (2015, 2016) showed the existence of a maximum orbital period, P_{max} , over which the accretion onto an NS companion is not high enough to bring it to the critical mass for gravitational collapse to a BH. As mentioned in the Introduction, $\text{CO}_{\text{core}}\text{-NS}$ binaries with $P > P_{\text{max}}$ lead to XRFs, while the ones with $P \lesssim P_{\text{max}}$ lead to BdHNe. For the binary parameters of the example in Figure 2, $P_{\text{max}} \approx 127$ minutes (vertical dashed line). We can therefore conclude that BdHNe can have peak accretion rates in the range $\dot{M}_{\text{peak}} \sim 10^{-3}$ –few $10^{-2} M_{\odot} \text{ s}^{-1}$, while XRFs would have $\dot{M}_{\text{peak}} \sim 10^{-4}$ – $10^{-3} M_{\odot} \text{ s}^{-1}$.

2.2. Neutrino Emission at Maximum Accretion

For the accretion rate conditions characteristic of our models at peak $\sim 10^{-4}$ to $10^{-2} M_{\odot} \text{ s}^{-1}$, pair annihilation dominates the

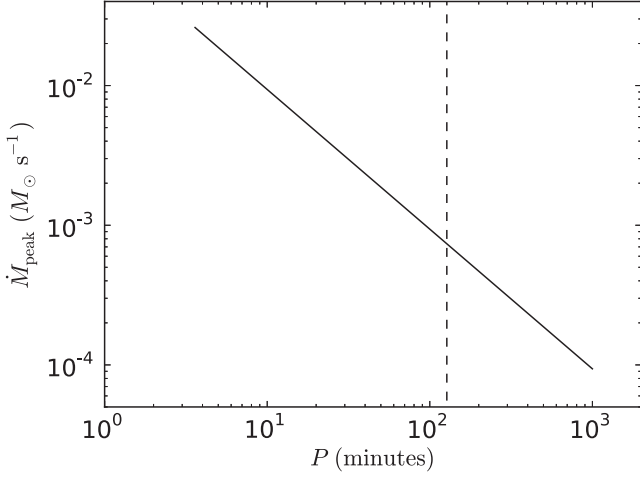


Figure 2. Peak accretion rate, \dot{M}_{peak} , as a function of the binary orbital period, as given by Equation (2). This example corresponds to the following binary parameters: a CO_{core} formed by an $M_{\text{ZAMS}} = 20 M_{\odot}$ progenitor, i.e., $M_{\text{CO}} = 5.4 M_{\odot}$, an initial NS mass of $2.0 M_{\odot}$, $v_{\text{star},0} = 2 \times 10^9 \text{ cm s}^{-1}$, $\eta \approx 0.41$, and index $m = 2.946$ (see Becerra et al. 2016, for further details). For these parameters the largest orbital period for the induced collapse of the NS to a BH by accretion is $P_{\text{max}} \approx 127$ minutes, which is represented by the vertical dashed line.

neutrino emission and electron neutrinos remove the bulk of the energy (Becerra et al. 2016). The e^+e^- pairs producing the neutrinos are thermalized at the matter temperature. This temperature is approximately given by

$$T_{\text{acc}} \approx \left(\frac{3P_{\text{shock}}}{4\sigma/c} \right)^{1/4} = \left(\frac{7 \dot{M}_{\text{acc}} v_{\text{acc}} c}{8 4\pi R_{\text{NS}}^2 \sigma} \right)^{1/4}, \quad (4)$$

where P_{shock} is the pressure of the shock developed on the accretion zone above the NS surface, \dot{M}_{acc} is the accretion rate, v_{acc} is the velocity of the infalling material, σ is the Stefan–Boltzmann constant, and c is the speed of light. It can be checked that, for the above accretion rates, the system develops temperatures and densities ($T \gtrsim 10^{10} \text{ K}$ and $\rho \gtrsim 10^6 \text{ g cm}^{-3}$; see, e.g., Figure 16 in Becerra et al. 2016) for which the neutrino emissivity of the e^+e^- annihilation process can be estimated by the simple formula (Yakovlev et al. 2001)

$$\epsilon_{e^-e^+} \approx 8.69 \times 10^{30} \left(\frac{k_{\text{B}} T}{1 \text{ MeV}} \right)^9 \text{ MeV cm}^{-3} \text{ s}^{-1}, \quad (5)$$

where k_{B} is the Boltzmann constant.

The accretion zone is characterized by a temperature gradient with a typical scale height $\Delta r_{\text{ER}} = T/\nabla T \approx 0.7 R_{\text{NS}}$. Owing to the strong dependence of the neutrino emission on temperature, most of the neutrinos are emitted from a spherical shell around the NS of thickness (see Figure 1)

$$\Delta r_{\nu} = \frac{\epsilon_{e^-e^+}}{\nabla \epsilon_{e^-e^+}} = \frac{\Delta r_{\text{ER}}}{9} \approx 0.08 R_{\text{NS}}. \quad (6)$$

Equations (4) and (5) imply that the neutrino emissivity satisfies $\epsilon_{e^-e^+} \propto \dot{M}_{\text{acc}}^{9/4}$ as we had anticipated. These conditions lead the neutrinos to be efficient in balancing the gravitational potential energy gain, allowing the hypercritical accretion rates.

The effective accretion onto the NS can be estimated as

$$\dot{M}_{\text{eff}} \approx \Delta M_{\nu} \frac{L_{\nu}}{E_g}, \quad (7)$$

where ΔM_{ν} and L_{ν} are, respectively, the mass and neutrino luminosity in the emission region, and $E_g = (1/2)GM_{\text{NS}}\Delta M_{\nu}/(R_{\nu} + \Delta r_{\nu})$ is half the gravitational potential energy gained by the material falling from infinity to the $R_{\text{NS}} + \Delta r_{\nu}$. The neutrino luminosity is

$$L_{\nu} \approx 4\pi R_{\text{NS}}^2 \Delta r_{\nu} \epsilon_{e^-e^+}, \quad (8)$$

with $\epsilon_{e^-e^+}$ being the neutrino emissivity in Equation (5). For $M_{\text{NS}} = 2 M_{\odot}$ and temperatures 1–10 MeV, Equations (7) and (8) give $\dot{M}_{\text{eff}} \approx 10^{-10}$ to $10^{-1} M_{\odot} \text{ s}^{-1}$ and $L_{\nu} \approx 10^{48}$ – $10^{57} \text{ MeV s}^{-1}$.

2.3. Neutrino Spectrum at the NS Surface

After discussing the general features of neutrino emission during the accretion process, it is necessary for our analysis of the neutrino oscillations to determine the neutrino spectrum at the NS surface. Specifically, we need to determine the ratios at which the neutrinos of each flavor are created and their average energy so that we can find a fitting distribution function f_{ν} with these characteristics.

Since the main source of neutrinos is the e^-e^+ pair annihilation process, we can conclude that neutrinos and antineutrinos are created in equal number. Furthermore, the information about the neutrino and antineutrino emission of a given flavor i can be calculated from the integral (Yakovlev et al. 2001)

$$\epsilon_i^m = \frac{2G_{\text{F}}^2(m_e c^2)^4}{3(2\pi\hbar)^7(\hbar c)^3} \int f_e^- f_{e^+} \frac{(E_e^m + E_{e^{\mp}}^m)}{E_e^- E_{e^+}} \sigma_i d^3 p_e^- d^3 p_{e^+}, \quad (9)$$

where $G_{\text{F}} = 8.963 \times 10^{-44} \text{ MeV cm}^3$ is the Fermi constant of weak interactions. Here $m = 0, 1, \dots$ and should not be confused with the index of the power-law density profile of the pre-SN envelope in Section 2.1; $f_{e^{\pm}}$ are the Fermi–Dirac distributions for electron and positrons

$$f_{e^{\mp}} = \frac{1}{1 + \exp\left(\frac{E_{e^{\mp}}}{k_{\text{B}} T} \mp \eta_{e^{\mp}}\right)}, \quad (10)$$

where $\eta_{e^{\mp}}$ is the electron (positron) degeneracy parameter, including its rest mass. The Dicus cross section σ_i is written in terms of the electron and positron four-momenta $p_{e^{\pm}} = (E_{e^{\pm}}/c, \mathbf{p}_{e^{\pm}})$ as (Dicus 1972)

$$\sigma_i = C_{\pm,i}^2 \left(1 + 3 \frac{p_{e^-} \cdot p_{e^+}}{(cm_e)^2} + 2 \frac{(p_{e^-} \cdot p_{e^+})^2}{(cm_e)^4} \right) + 3C_{-,i}^2 \left(1 + \frac{p_{e^-} \cdot p_{e^+}}{(cm_e)^2} \right). \quad (11)$$

The factors $C_{\pm,i}^2$ are written in terms of the weak interaction vector and axial-vector constants: $C_{\pm,i}^2 = C_{V_i}^2 \pm C_{A_i}^2$, where $C_{V_e} = 2 \sin^2 \theta_{\text{W}} + 1/2$, $C_{A_e} = 1/2$, $C_{V_{\mu}} = C_{V_e} = C_{V_{\tau}} - 1$, and $C_{A_{\mu}} = C_{A_{\tau}} = C_{A_e} - 1$, with the numerical value of the Weinberg angle approximated by $\sin^2 \theta_{\text{W}} \approx 0.231$ (Patrignani & the Particle Data Group 2016).

For $m = 0$ and $m = 1$ Equation (9) gives the neutrino and antineutrino number emissivity (neutrino production rate) and the neutrino and antineutrino energy emissivity (energy per unit volume per unit time) for a certain flavor i , respectively. Hence, not only are we able to calculate the total number emissivity with

$$n = \sum_{i \in \{e, \tau, \mu\}} \varepsilon_i^0, \quad (12)$$

but we can also calculate the neutrino or antineutrino energy moments with

$$\langle E_{\nu_i(\bar{\nu}_i)}^m \rangle = \frac{\varepsilon_i^m}{\varepsilon_i^0}, \text{ for } m \geq 1. \quad (13)$$

We wish to construct a Fermi–Dirac-like fitting formula for the neutrino spectrum as is usually done in supernova neutrino emission (Janka & Hillebrandt 1989a, 1989b), that is, a function like Equation (10) in terms of two parameters: the effective neutrino temperature $T_{\nu\bar{\nu}}$ and the effective neutrino degeneracy parameter $\eta_{\nu\bar{\nu}}$, otherwise known as the *pinching* parameter (Raffelt 1996; Keil et al. 2003). To that end, it is enough to calculate the first two moments. In particular, for a relativistic nondegenerate plasma ($k_B T > 2m_e c^2$ and $1 > \eta_{e^\pm}$; see Table 1) Equation (9) can be approximated with a very good accuracy by (Yakovlev et al. 2001)

$$\begin{aligned} \varepsilon_i^m \approx & \frac{2G_F^2 (k_B T)^{8+m}}{9\pi^5 \hbar (\hbar c)^9} C_{+,i}^2 [\mathcal{F}_{m+1}(\eta_{e^+}) \mathcal{F}_1(\eta_{e^-}) \\ & + \mathcal{F}_{m+1}(\eta_{e^-}) \mathcal{F}_1(\eta_{e^+})], \end{aligned} \quad (14)$$

where $\mathcal{F}_k(\eta) = \int_0^\infty dx x^k / [1 + \exp(x - \eta)]$ are the Fermi–Dirac integrals. For $m = 1$, $\eta_{e^\pm} = 0$, and adding over every flavor, this expression reduces to Equation (5). With Equations (13) and (14) we find

$$\langle E_\nu \rangle = \langle E_{\bar{\nu}} \rangle \approx 4.1 k_B T \quad (15a)$$

$$\langle E_\nu^2 \rangle = \langle E_{\bar{\nu}}^2 \rangle \approx 20.8 (k_B T)^2, \quad (15b)$$

regardless of the neutrino flavor. Furthermore, we can calculate the ratio of emission rates between electronic and nonelectronic neutrino flavors in terms of the weak interaction constants

$$\frac{\varepsilon_e^0}{\varepsilon_x^0} = \frac{\varepsilon_e^0}{\varepsilon_\mu^0 + \varepsilon_\tau^0} = \frac{C_{+,e}^2}{C_{+,\mu}^2 + C_{+,\tau}^2} \approx \frac{7}{3}. \quad (16)$$

Some comments must be made about the results we have obtained:

1. It is well known that, within the Standard Model of Particles, there are three neutrino flavors $\nu_e, \bar{\nu}_e, \nu_\mu, \bar{\nu}_\mu$, and $\nu_\tau, \bar{\nu}_\tau$. However, as in Equation (16), we will simplify our description using only two flavors: the electronic neutrinos and antineutrinos $\nu_e, \bar{\nu}_e$, and a superposition of the other flavors $\nu_x, \bar{\nu}_x$ ($x = \mu + \tau$). This can be understood as follows. Since the matter in the accretion zone is composed by protons, neutrons, electrons, and positrons, ν_e and $\bar{\nu}_e$ interact with matter by both charged and neutral currents, while $\nu_\mu, \nu_\tau, \bar{\nu}_\mu$, and $\bar{\nu}_\tau$ interact only by neutral currents. Therefore, the behavior of these states can be clearly divided into electronic and nonelectronic. This distinction will come in handy when studying neutrino oscillations.

2. Representing the neutrino (antineutrino) density and flux in the moment of their creation with $n_{\nu_i(\bar{\nu}_i)}^c$ and $F_{\nu_i(\bar{\nu}_i)}^c$, respectively, and using Equation (16), we can recollect two important facts:

$$n_{\nu_i}^c = n_{\bar{\nu}_i}^c, \quad F_{\nu_i}^c = F_{\bar{\nu}_i}^c \quad \forall i \in \{e, \mu, \tau\} \quad (17a)$$

$$\frac{n_{\nu_e}^c}{n_{\nu_x}^c} = \frac{n_{\bar{\nu}_e}^c}{n_{\bar{\nu}_x}^c} = \frac{F_{\nu_e}^c}{F_{\nu_x}^c} = \frac{F_{\bar{\nu}_e}^c}{F_{\bar{\nu}_x}^c} \approx \frac{7}{3}. \quad (17b)$$

Equation (17) implies that, in the specific environment of our system, of the total number of neutrinos+antineutrinos emitted, $N_\nu + N_{\bar{\nu}}$, 70% are electronic neutrinos ($N_e + N_{\bar{e}}$), 30% are nonelectronic ($N_x + N_{\bar{x}}$), while the total number of neutrinos is equal to the total number of antineutrinos, i.e., $N_\nu = N_{\bar{\nu}}$, where $N_\nu = N_e + N_x$ and $N_{\bar{\nu}} = N_{\bar{e}} + N_{\bar{x}}$.

3. Bearing in mind such high neutrino energies as the ones suggested by Equation (15), from here on out we will use the approximation

$$E_\nu \approx c|\mathbf{p}| \gg m_\nu c^2, \quad (18)$$

where \mathbf{p} is the neutrino momentum.

4. From Equation (13) we obtain the same energy moments for both neutrinos and antineutrinos, but, as Misiaszek et al. (2006) points out, these energies should be different since, in reality, this expression returns the arithmetic mean of the particle and antiparticle energy moments, that is, $(\langle E_\nu^m \rangle + \langle E_{\bar{\nu}}^m \rangle)/2$. However, if we calculate the differences between the energy moments with Equations (41) and (46) in Misiaszek et al. (2006) for the values of T and η_{e^\pm} we are considering, we get $\Delta\langle E \rangle \sim 10^{-2} - 10^{-3}$ MeV and $\Delta\langle E^2 \rangle \sim 10^{-3} - 10^{-4}$ MeV². These differences are small enough that we can use the same effective temperature and pinching parameter for both neutrinos and antineutrinos.

Solving the equations

$$4.1 k_B T = k_B T_{\nu\bar{\nu}} \frac{\mathcal{F}_3(\eta_{\nu\bar{\nu}})}{\mathcal{F}_2(\eta_{\nu\bar{\nu}})} \quad (19a)$$

$$20.8 (k_B T)^2 = (k_B T_{\nu\bar{\nu}})^2 \frac{\mathcal{F}_4(\eta_{\nu\bar{\nu}})}{\mathcal{F}_2(\eta_{\nu\bar{\nu}})} \quad (19b)$$

for any value of T in Table 1, we find $T_{\nu\bar{\nu}} = 1.1331T$ and $\eta_{\nu\bar{\nu}} = 2.0376$. Integrating Equation (10) over the neutrino momentum space using these values should give the neutrino number density. To achieve this, we normalize it with the factor $1/(2\pi^2 (k_B T_{\nu\bar{\nu}})^3 \mathcal{F}_2(\eta_{\nu\bar{\nu}}))$, and then we multiply by

$$n_{\nu_i(\bar{\nu}_i)}^c = w_{\nu_i(\bar{\nu}_i)} \frac{L_\nu}{4\pi R_{\text{NS}}^2 \langle E_\nu \rangle \langle v \rangle} = w_{\nu_i(\bar{\nu}_i)} \frac{\varepsilon_i^0 \Delta r_\nu}{c/2}, \quad (20)$$

where the neutrino's average radial velocity at $r = R_{\text{NS}}$ is $\langle v \rangle = c/2$ (Dasgupta et al. 2008b) and $w_{\nu_e} = w_{\bar{\nu}_e} = 0.35$ and $w_{\nu_x} = w_{\bar{\nu}_x} = 0.15$. To calculate the neutrino fluxes, we use simply $F_{\nu_i(\bar{\nu}_i)}^c = \langle v \rangle n_{\nu_i(\bar{\nu}_i)}^c$. Gathering our results, we can finally write the distribution functions as

$$f_{\nu_e} = f_{\bar{\nu}_e} = \frac{2\pi^2 (\hbar c)^3 n_{\nu_e}^c}{(k_B T_{\nu\bar{\nu}})^3 \mathcal{F}_2(\eta_{\nu\bar{\nu}})} \frac{1}{1 + \exp(E/k_B T_{\nu\bar{\nu}} - \eta_{\nu\bar{\nu}})} \quad (21a)$$

Table 1
 Characteristics inside the Neutrino Emission Zone and the Neutrino Spectrum for Selected Values of the Accretion Rate \dot{M}

\dot{M} ($M_{\odot} \text{ s}^{-1}$)	ρ (g cm^{-3})	$k_{\text{B}}T$ (MeV)	$\eta_{e^{\mp}}$	$n_{e^{-}} - n_{e^{+}}$ (cm^{-3})	$k_{\text{B}}T_{\text{eff}}$ (MeV)	$\langle E_{\nu} \rangle$ (MeV)	$F_{\text{e}^{\pm}}^{\text{C}}$ ($\text{cm}^{-2}\text{s}^{-1}$)	$F_{\text{e}^{\pm}}^{\text{C}}$ ($\text{cm}^{-2}\text{s}^{-1}$)	$n_{\text{e}^{\pm}}^{\text{C}}$ (cm^{-3})	$n_{\text{e}^{\pm}}^{\text{C}}$ (cm^{-3})	$\sum_{\pm} n_{\text{e}^{\pm}}^{\text{C}}$ (cm^{-3})
10^{-8}	1.46×10^6	1.56	∓ 0.325	4.41×10^{29}	1.78	6.39	4.17×10^{36}	1.79×10^{36}	2.78×10^{26}	1.19×10^{26}	3.97×10^{26}
10^{-7}	3.90×10^6	2.01	∓ 0.251	1.25×10^{30}	2.28	8.24	3.16×10^{37}	1.36×10^{37}	2.11×10^{27}	9.00×10^{26}	3.01×10^{27}
10^{-6}	1.12×10^7	2.59	∓ 0.193	3.38×10^{30}	2.93	10.61	2.40×10^{38}	1.03×10^{38}	1.60×10^{28}	6.90×10^{27}	2.29×10^{28}
10^{-5}	3.10×10^7	3.34	∓ 0.147	9.56×10^{30}	3.78	13.69	1.84×10^{39}	7.87×10^{38}	1.23×10^{29}	5.20×10^{28}	1.75×10^{29}
10^{-4}	8.66×10^7	4.30	∓ 0.111	2.61×10^{31}	4.87	17.62	1.39×10^{40}	5.94×10^{39}	9.24×10^{29}	3.96×10^{29}	1.32×10^{30}
10^{-3}	2.48×10^8	5.54	∓ 0.082	7.65×10^{31}	6.28	22.70	1.04×10^{41}	4.51×10^{40}	7.00×10^{30}	3.00×10^{30}	1.00×10^{31}
10^{-2}	7.54×10^8	7.13	∓ 0.057	2.27×10^{32}	8.08	29.22	7.92×10^{41}	3.39×10^{41}	5.28×10^{31}	2.26×10^{31}	7.54×10^{31}

Note. The electron fraction is $Y_e = 0.5$, the pinching parameter for the neutrino spectrum is $\eta_{\text{e}^{\pm}} = 2.0376$.

$$f_{\nu_x} = f_{\bar{\nu}_x} = \frac{2\pi^2(\hbar c)^3 n_{\nu_x}^C}{(k_B T_{\nu\bar{\nu}})^3 \mathcal{F}_2(\eta_{\nu\bar{\nu}})} \frac{1}{1 + \exp(E/k_B T_{\nu\bar{\nu}} - \eta_{\nu\bar{\nu}})}. \quad (21b)$$

It can be checked that these distributions obey

$$\int f_{\nu_i} \frac{d^3\mathbf{p}}{(2\pi\hbar)^3} = n_{\nu_i}^C \quad (22a)$$

$$\int E f_{\nu_i} \frac{d^3\mathbf{p}}{(2\pi\hbar)^3} = \langle E_{\nu} \rangle n_{\nu_i}^C = \varepsilon_i^1, \quad (22b)$$

and with these conditions satisfied we can conclude that Equations (21) are precisely the ones that emulate the neutrino spectrum at the NS surface. In Table 1 we have collected the values of every important quantity used in the calculations within this section for the range of accretion rates in which we are interested.

Considering that the problem we attacked in this section reduces to finding a normalized distribution whose first two moments are fixed, the choice we have made with Equation (21) is not unique. The solution depends on how many moments are used to fit the distribution and what kind of function is used as an ansatz. A different solution based on a Maxwell–Boltzmann distribution can be found in Keil et al. (2003), Fogli et al. (2005), and Misiaszek et al. (2006).

At this stage, we can identify two main differences between neutrino emission in SNe and in the IGC process of XRFs and BdHNe, within the context of neutrino oscillations. The significance of these differences will become clearer in the following sections, but we mention them here to establish a point of comparison between the two systems since SN neutrino oscillations have been extensively studied.

1. Neutrinos of all flavors in XRFs and BdHNe have the same temperature, which leads to equal average energy. The neutrinos produced in SNe are trapped and kept in thermal equilibrium within their respective neutrino sphere. The neutrino spheres have different radii, causing different flavors to have different average energies. This energy difference leads to a phenomenon called *spectral stepwise swap*, which, as we will show below, is not present in our systems (see, e.g., Raffelt 1996; Fogli et al. 2007; Dasgupta & Dighe 2008, and references therein).
2. As we have discussed above, in XRFs and BdHNe neutrinos and antineutrinos are emitted in equal number. Due to this fact, kinematical decoherence occurs (up to a number difference of 30% this statement is valid; see Section 4 for further details). Instead, SN neutrino and antineutrino fluxes differ such that $F_{\nu_e} > F_{\bar{\nu}_e} > F_{\nu_x} = F_{\bar{\nu}_x}$. It has been argued that this difference between neutrinos and antineutrinos is enough to dampen kinematical decoherence, so that bipolar oscillations are a feature present in SN neutrinos (see, e.g., Esteban-Pretel et al. 2007).

In the next section, we will use the results presented here to determine the neutrino flavor evolution in the accretion zone.

3. Neutrino Oscillations

In recent years the picture of neutrino oscillations in dense media, based only on MSW effects, has undergone a change of

paradigm by the insight that the refractive effects of neutrinos on themselves due to the neutrino self-interaction potential are crucial (Notzold & Raffelt 1988; Pantaleone 1992; Qian & Fuller 1995; Pastor & Raffelt 2002; Sawyer 2005; Duan et al. 2006b, 2007, 2008a, 2008b, 2010; Fuller & Qian 2006; Esteban-Pretel et al. 2007, 2008; Fogli et al. 2007; Raffelt & Sigl 2007; Chakraborty et al. 2008; Dasgupta & Dighe 2008; Dasgupta et al. 2008a; Sawyer 2009; Wu & Qian 2011).

As we discussed in Section 2, in our physical system of interest neutrinos are mainly created by electron–positron pair annihilation, and so the number of neutrinos is equal to the number of antineutrinos. Such a fact creates an interesting and unique physical situation, different from, for example, SN neutrinos, for which traditional models predict a predominance of electron neutrinos mainly due to the deleptonization caused by the URCA process (see, e.g., Esteban-Pretel et al. 2007).

The neutrino self-interaction potential decays with the radial distance from the NS faster than the matter potential. This is a direct consequence of the usual $1/r^2$ flux dilution and the collinearity effects due to the neutrino velocity dependence of the potential. Consequently, we identify three different regions along the neutrino trajectory in which the oscillations are dominated by intrinsically different neutrino phenomenology. Figure 3 illustrates the typical situation of the physical system we are analyzing. Just after the neutrino creation in the regions of the accretion zone very close to the surface of the NS, neutrinos undergo kinematic decoherence along the same length scale of a single cycle of the so-called bipolar oscillations. Bipolar oscillations imply very fast flavor conversion between neutrino pairs $\nu_e \bar{\nu}_e \leftrightarrow \nu_\mu \bar{\nu}_\mu \leftrightarrow \nu_\tau \bar{\nu}_\tau$, and, amazingly, the oscillation length in this region can be as small as of the order of tens of meters. Note that kinematic decoherence is just the averaging over flavor neutrino state processes resulting from quick flavor conversion, for which oscillation length depends on the neutrino energy. It does not imply quantum decoherence, and thus, neutrinos are yet able to quantum oscillate if appropriate conditions are satisfied. In fact, as can be observed from Figures 4 and 5, bipolar oscillations preserve the characteristic oscillation pattern, differently from quantum decoherence, which would lead to a monotonous dumping figure.

Kinematic decoherence is relevant when three conditions are met: (i) the self-interaction potential dominates over the vacuum potential, (ii) the matter potential does not fulfill the MSW condition, and (iii) there is a low asymmetry between the neutrino and antineutrino fluxes. We will see that our system satisfies all three conditions.

As the self-interaction potential becomes small and the matter potential becomes important, oscillations are suppressed and we do not expect significant changes in the neutrino flavor content along this region. This situation changes radically when the matter potential is so small that it is comparable to neutrino vacuum frequencies $\Delta m^2/2p$, where Δm^2 is the neutrino squared mass difference and p is the norm of the neutrino momentum \mathbf{p} . In this region, the neutrino self-interaction potential is negligible and the usual MSW resonances can occur. Therefore, we can expect a change in the neutrino spectrum.

We dedicate this section to a detailed derivation of the EoM of flavor evolution. In later sections, we will analyze the neutrino oscillation phenomenology to build the neutrino emission spectrum from a binary hyperaccretion system.

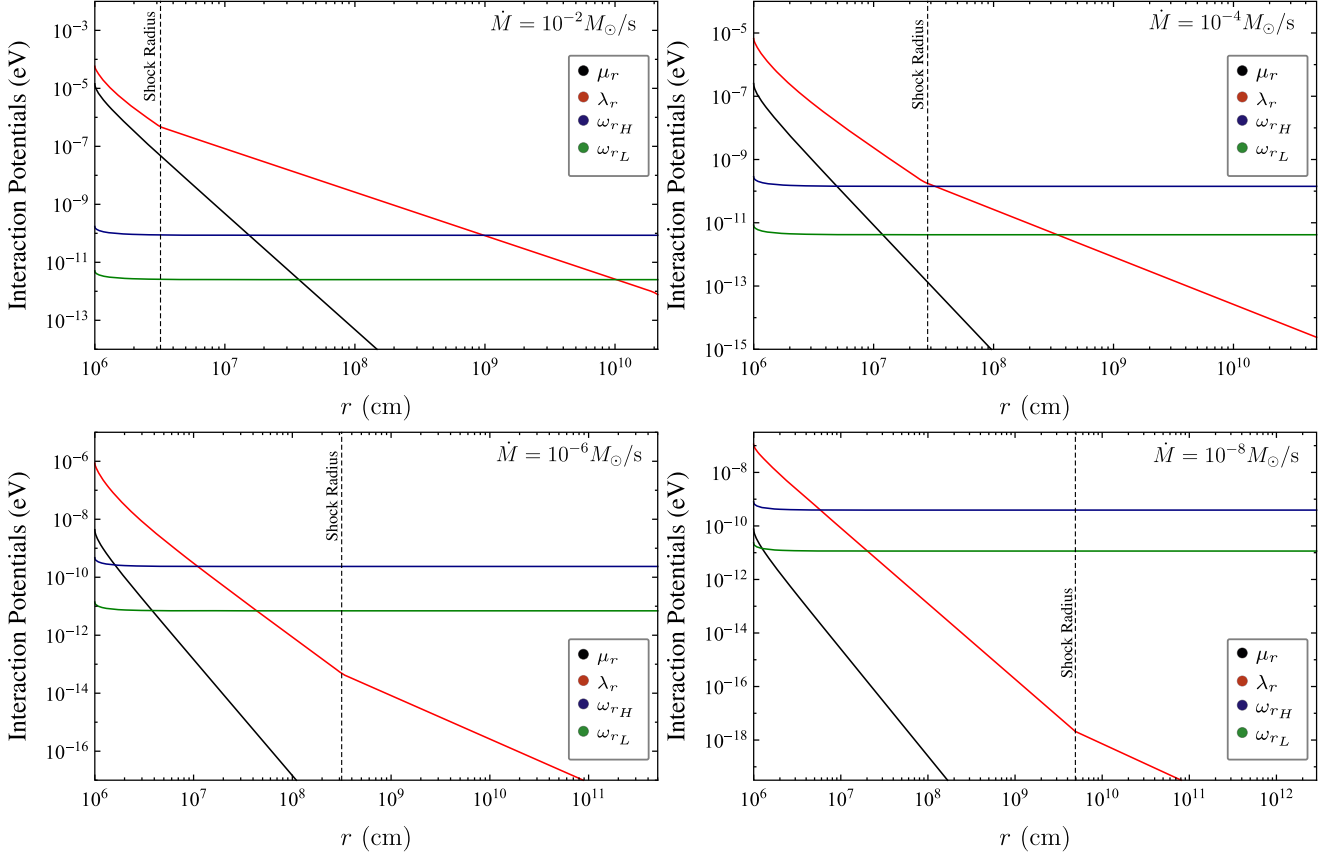


Figure 3. Interaction potentials as functions of the radial distance from the NS center for selected accretion rates \dot{M} (see Table 1). Each plot runs from the NS surface to the Bondi–Hoyle surface. μ_r stands for the self-interaction neutrino potential, λ_r is the matter potential, and ω_H and ω_L are the higher and lower resonances corresponding to the atmospheric and solar neutrino scales, respectively, defined in Equation (59). Outside the Bondi–Hoyle region the neutrino and electron densities depend on the direction of their path relative to the SN and the particular ejecta density profile.

3.1. Equations of Motion

The EoM that govern the evolution of an ensemble of mixed neutrinos are the quantum Liouville equations

$$i\dot{\rho}_p = [H_p, \rho_p] \quad (23a)$$

$$i\dot{\bar{\rho}}_p = [\bar{H}_p, \bar{\rho}_p], \quad (23b)$$

where we have adopted the natural units $c = \hbar = 1$. In these equations ρ_p ($\bar{\rho}_p$) is the matrix of occupation numbers $(\rho_p)_{ij} = \langle a_j^\dagger a_i \rangle_p$ for neutrinos ($(\bar{\rho}_p)_{ij} = \langle \bar{a}_i^\dagger \bar{a}_j \rangle_p$ for antineutrinos), for each momentum \mathbf{p} and flavors i, j . The diagonal elements are the distribution functions $f_{\nu_i(\bar{\nu}_i)}(\mathbf{p})$ such that their integration over the momentum space gives the neutrino number density n_{ν_i} of a determined flavor i . The off-diagonal elements provide information about the *overlapping* between the two neutrino flavors.

Taking into account the current–current nature of the weak interaction in the standard model, the Hamiltonian for each equation is (Dolgov 1981; Sigl & Raffelt 1993; Hannestad et al. 2006)

$$H_p = \Omega_p + \sqrt{2} G_F \int (l_q - \bar{l}_q)(1 - \mathbf{v}_q \cdot \mathbf{v}_p) \frac{d^3 \mathbf{q}}{(2\pi)^3} + \sqrt{2} G_F \int (\rho_q - \bar{\rho}_q)(1 - \mathbf{v}_q \cdot \mathbf{v}_p) \frac{d^3 \mathbf{q}}{(2\pi)^3} \quad (24a)$$

$$\bar{H}_p = -\Omega_p + \sqrt{2} G_F \int (l_q - \bar{l}_q)(1 - \mathbf{v}_q \cdot \mathbf{v}_p) \frac{d^3 \mathbf{q}}{(2\pi)^3} + \sqrt{2} G_F \int (\rho_q - \bar{\rho}_q)(1 - \mathbf{v}_q \cdot \mathbf{v}_p) \frac{d^3 \mathbf{q}}{(2\pi)^3}, \quad (24b)$$

where Ω_p is the matrix of vacuum oscillation frequencies, l_p and \bar{l}_p are matrices of occupation numbers for charged leptons built in a similar way to the neutrino matrices, and $\mathbf{v}_p = \mathbf{p}/p$ is the velocity of a particle with momentum \mathbf{p} (either neutrino or charged lepton).

As in Section 2, we will only consider two neutrino flavors: e and $x = \mu + \tau$. Three-flavor oscillations can be approximated to two-flavor oscillations as a result of the strong hierarchy of the squared mass differences $|\Delta m_{13}^2| \approx |\Delta m_{23}^2| \gg |\Delta m_{12}^2|$ (see Table 2). In this case, only the smallest mixing angle θ_{13} is considered. We will drop the suffix for the rest of the discussion. Consequently, the relevant oscillations are $\nu_e \rightleftharpoons \nu_x$ and $\bar{\nu}_e \rightleftharpoons \bar{\nu}_x$, and each term in the Hamiltonian governing oscillations becomes a 2×2 Hermitian matrix.

Let us first present the relevant equations for neutrinos. Due to the similarity between H_p and \bar{H}_p , the corresponding equations for antineutrinos can be obtained in an analogous manner. In the two-flavor approximation, ρ in Equation (23) can be written in terms of Pauli matrices and the polarization vector \mathbf{P}_p as

Inverted Hierarchy

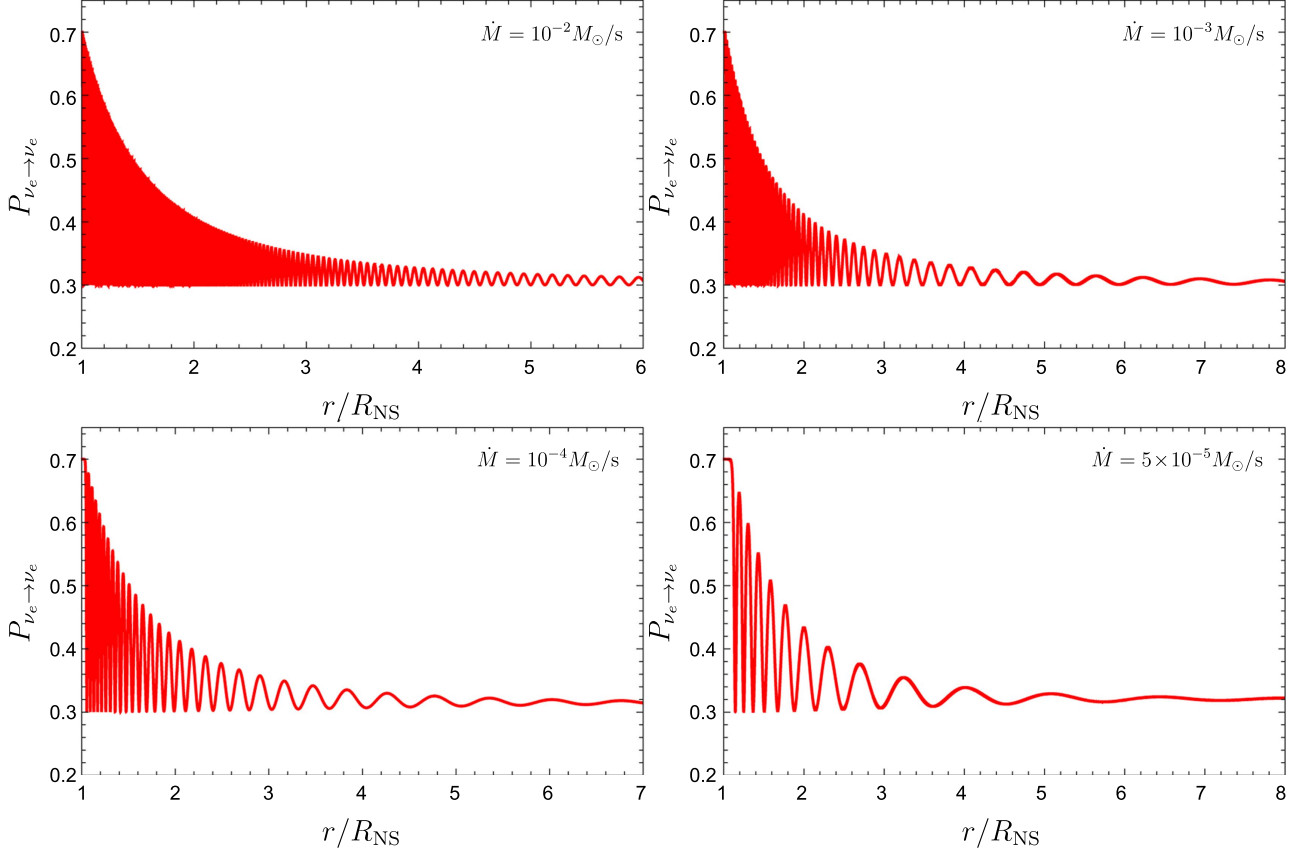


Figure 4. Neutrino flavor evolution for inverted hierarchy. Electron neutrino survival probability is shown as a function of the radial distance from the NS surface. The curves for the electron antineutrino match the ones for electron neutrinos.

$$\rho_p = \begin{pmatrix} \rho_{ee} & \rho_{ex} \\ \rho_{xe} & \rho_{xx} \end{pmatrix}_p = \frac{1}{2}(f_p \mathbf{1} + \mathbf{P}_p \cdot \boldsymbol{\sigma}), \quad (25)$$

where $f_p = \text{Tr}[\rho_p] = f_{\nu_e}(\mathbf{p}) + f_{\nu_x}(\mathbf{p})$ is the sum of the distribution functions for ν_e and ν_x . Note that the z component of the polarization vector obeys

$$\mathbf{P}_p^z = f_{\nu_e}(\mathbf{p}) - f_{\nu_x}(\mathbf{p}). \quad (26)$$

Hence, this component tracks the fractional flavor composition of the system, and appropriately normalizing ρ_p allows us to define a survival and mixing probability

$$P_{\nu_e \leftrightarrow \nu_e} = \frac{1}{2}(1 + \mathbf{P}_p^z), \quad (27a)$$

$$P_{\nu_e \leftrightarrow \nu_x} = \frac{1}{2}(1 - \mathbf{P}_p^z). \quad (27b)$$

On the other hand, the Hamiltonian can be written as a sum of three interaction terms:

$$\mathbf{H} = \mathbf{H}_{\text{vacuum}} + \mathbf{H}_{\text{matter}} + \mathbf{H}_{\nu\nu}. \quad (28)$$

where \mathbf{H} is the two-flavor Hamiltonian. The first term is the Hamiltonian in vacuum (Qian & Fuller 1995):

$$\mathbf{H}_{\text{vacuum}} = \frac{\omega_p}{2} \begin{pmatrix} -\cos 2\theta & \sin 2\theta \\ \sin 2\theta & \cos 2\theta \end{pmatrix} = \frac{\omega_p}{2} \mathbf{B} \cdot \boldsymbol{\sigma}, \quad (29)$$

where $\omega_p = \Delta m^2/2p$, $\mathbf{B} = (\sin 2\theta, 0, -\cos 2\theta)$, and θ is the smallest neutrino mixing angle in vacuum.

The other two terms in Equation (24) are special since they make the evolution equations nonlinear. Even though they are very similar, we are considering that the electrons during the accretion form an isotropic gas; hence, the vector \mathbf{v}_q in the first integral is distributed uniformly on the unit sphere and the factor $\mathbf{v}_q \cdot \mathbf{v}_p$ averages to zero. After integrating, the matter Hamiltonian is given by

$$\mathbf{H}_{\text{matter}} = \frac{\lambda}{2} \begin{pmatrix} 1 & 0 \\ 0 & -1 \end{pmatrix} = \frac{\lambda}{2} \mathbf{L} \cdot \boldsymbol{\sigma}, \quad (30)$$

where $\lambda = \sqrt{2} G_{\text{F}}(n_{e^-} - n_{e^+})$ is the charged current matter potential and $\mathbf{L} = (0, 0, 1)$.

Such simplification cannot be made with the final term. Since neutrinos are responsible for the energy loss of the infalling material during accretion, they must be escaping the accretion zone and the net neutrino and antineutrino flux is nonzero. In this case the factor $\mathbf{v}_q \cdot \mathbf{v}_p$ cannot be averaged to zero. At any rate, we can still use Equation (25) and obtain (Pantaleone 1992; Malkus et al. 2016; Zhu et al. 2016)

$$\mathbf{H}_{\nu\nu} = \sqrt{2} G_{\text{F}} \left[\int (1 - \mathbf{v}_q \cdot \mathbf{v}_p) (\mathbf{P}_q - \bar{\mathbf{P}}_q) \frac{d^3 \mathbf{q}}{(2\pi)^3} \right] \cdot \boldsymbol{\sigma}. \quad (31)$$

Introducing every Hamiltonian term in Equation (23), and using the commutation relations of the Pauli matrices, we find the EoM for neutrinos and antineutrinos for each momentum

Normal Hierarchy

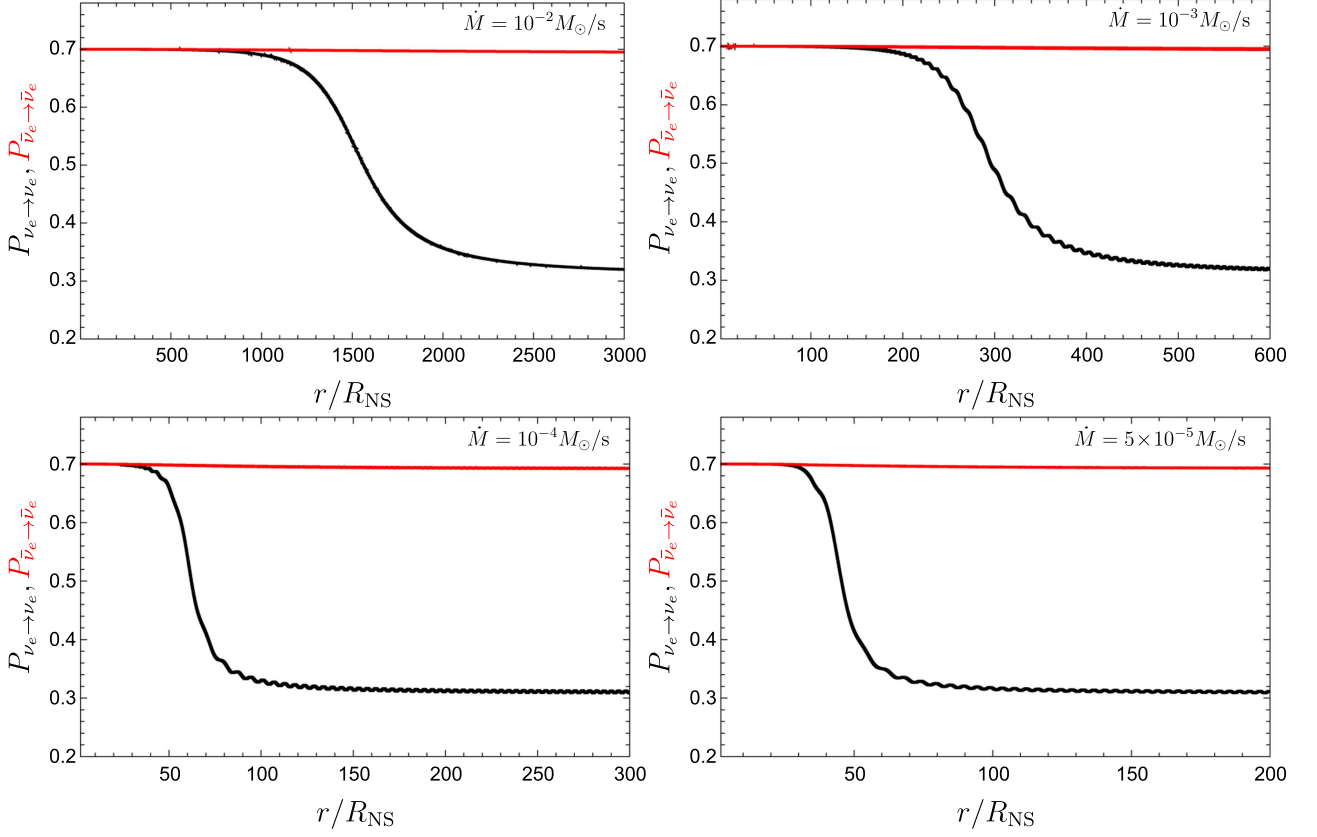


Figure 5. Electron neutrino and antineutrino flavor evolution for normal hierarchy. The survival probability is shown as a function of the radial distance from the NS surface.

Table 2

Mixing and Squared Mass Differences as They Appear
in Patrignani & the Particle Data Group (2016)

$\Delta m_{21}^2 = 7.37(6.93-7.97) \times 10^{-5} \text{ eV}^2$
$ \Delta m^2 = 2.50(2.37-2.63) \times 10^{-3} \text{ eV}^2$ Normal Hierarchy
$ \Delta m^2 = 2.46(2.33-2.60) \times 10^{-3} \text{ eV}^2$ Inverted Hierarchy
$\sin^2 \theta_{12} = 0.297(0.250-0.354)$
$\sin^2 \theta_{23}(\Delta m^2 > 0) = 0.437(0.379-0.616)$
$\sin^2 \theta_{23}(\Delta m^2 < 0) = 0.569(0.383-0.637)$
$\sin^2 \theta_{13}(\Delta m^2 > 0) = 0.0214(0.0185-0.0246)$
$\sin^2 \theta_{13}(\Delta m^2 < 0) = 0.0218(0.0186-0.0248)$

Note. Error values in parentheses are shown in a 3σ interval. The squared mass difference is defined as $\Delta m^2 = m_3^2 - (m_2^2 + m_1^2)/2$.

mode \mathbf{p} :

$$\dot{\mathbf{P}}_p = \left[\omega_p \mathbf{B} + \lambda \mathbf{L} + \sqrt{2} G_{\text{F}} \int (1 - \mathbf{v}_q \cdot \mathbf{v}_p) (\mathbf{P}_q - \bar{\mathbf{P}}_q) \frac{d^3 \mathbf{q}}{(2\pi)^3} \right] \times \mathbf{P}_p \quad (32a)$$

$$\dot{\bar{\mathbf{P}}}_p = \left[-\omega_p \mathbf{B} + \lambda \mathbf{L} + \sqrt{2} G_{\text{F}} \int (1 - \mathbf{v}_q \cdot \mathbf{v}_p) (\mathbf{P}_q - \bar{\mathbf{P}}_q) \frac{d^3 \mathbf{q}}{(2\pi)^3} \right] \times \bar{\mathbf{P}}_p. \quad (32b)$$

Solving the above equations would yield the polarization vectors as a function of time. However, in our specific physical system, both the matter potential λ and the neutrino potential vary with the radial distance from the NS surface, as well as the instant t of the physical process, which can be characterized by the accretion rate \dot{M} . As we will see later, the time dependence can be ignored. This means that Equation (32) must be written in a way that makes explicit the spatial dependence, i.e., in terms of the vector \mathbf{r} . For an isotropic and homogeneous neutrino gas or a collimated ray of neutrinos the expression $dt = dr$ would be good enough, but for radiating extended sources the situation is more complicated. In Equation (23) we must replace the matrices of occupation numbers by the space-dependent Wigner functions $\rho_{p,r}$ (and $\bar{\rho}_{p,r}$) and the total time derivative by the Liouville operator (Cardall 2008; Strack & Burrows 2005)

$$\dot{\rho}_{p,r} = \frac{\partial \rho_{p,r}}{\partial t} + \mathbf{v}_p \cdot \nabla_r \rho_{p,r} + \dot{\mathbf{p}} \cdot \nabla_p \rho_{p,r} \quad (33)$$

We will ignore the third term of the Liouville operator since we would not consider the gravitational deflection of neutrinos. For peak accretion rates $\dot{M} \approx 10^{-8}-10^{-2} M_{\odot} \text{ s}^{-1}$ the characteristic accretion time is $\Delta t_{\text{acc}} = M/\dot{M} \approx M_{\odot}/\dot{M} \approx 10^8-10^2 \text{ s}$. The distances traveled by a neutrino in these times are $r \approx 3 \times 10^{12}-3 \times 10^{18} \text{ cm}$. These distances are much larger than the typical binary separation a . As a consequence,

we can consider the neutrino evolution to be a stationary process. This fact allows us to neglect the first term in Equation (33). Putting together these results, the EoM become

$$i\mathbf{v}_p \cdot \nabla_r \rho_{p,r} = [H_{p,r}, \rho_{p,r}] \quad (34a)$$

$$i\mathbf{v}_p \cdot \nabla_r \bar{\rho}_{p,r} = [\bar{H}_{p,r}, \bar{\rho}_{p,r}], \quad (34b)$$

where $H_{p,r}$ and $\bar{H}_{p,r}$ are the same as in Equation (24) but the matrices of densities (as well as the polarization vectors) depend on the position \mathbf{r} . Note, however, that the electrons in the accretion zone still form an isotropic gas, Equation (30) is still valid, and the matter Hamiltonian depends on \mathbf{r} through $n_e^-(\mathbf{r}) - n_e^+(\mathbf{r})$. The first two terms in the Hamiltonian remain virtually unchanged. On the other hand, projecting the EoM onto the radial distance from the NS and using the axial symmetry of the system, the integral in the neutrino–neutrino interaction term can be written as

$$\frac{\sqrt{2} G_F}{(2\pi)^2} \int (1 - v_{\vartheta'} v_{\vartheta}) (\rho_{q,\vartheta',r} - \bar{\rho}_{q,\vartheta',r}) q^2 dq |d \cos \vartheta'_r|. \quad (35)$$

Since farther from the NS the interacting neutrinos approach a perfect collinearity, the projected velocities v_{ϑ} become decreasing functions of the position. In this particular geometry the diagonal elements of the matrix of densities are written as a product of independent distributions over each variable p , ϑ , ϕ , where the ϕ dependence has been integrated out. The one over p is the normalized Fermi–Dirac distribution, and the one over ϑ is assumed uniform owing to symmetry. The r dependence is obtained through the geometrical flux dilution. Knowing this, the diagonal elements of matrices of densities at the NS surface are

$$(\rho_{p,R_{\text{NS}}})_{ee} = (\bar{\rho}_{p,R_{\text{NS}}})_{ee} = f_{\nu_e}(\mathbf{p}) \quad (36a)$$

$$(\rho_{p,R_{\text{NS}}})_{xx} = (\bar{\rho}_{p,R_{\text{NS}}})_{xx} = f_{\nu_x}(\mathbf{p}), \quad (36b)$$

where the functions f_{ν_i} are given by Equation (21).

3.2. Single-angle Approximations

The integro-differential Equations (32) and (34) are usually numerically solved for the momentum \mathbf{p} and the scalar $v_q \cdot \mathbf{v}_p$. Such simulations are quite time-consuming, and the result is frequently too complicated to allow for a clear interpretation of the underlying physics. For this reason, the analytic approximation called the *single-angle limit* is made. Such an approximation consists of *imposing* a self-maintained coherence in the neutrino system, i.e., it is assumed that the flavor evolution of all neutrinos emitted from an extended source is the same as the flavor evolution of the neutrinos emitted from the source along a particular path. Under this premise, the propagation angle between the test neutrino and the background neutrinos is fixed. In expression (35) this is equivalent to dropping the ϑ' dependence of ρ and replacing the projected velocity v_{ϑ} either by an appropriate average at each r (as in Dasgupta & Dighe 2008) or by a representative angle (usually

0 or $\pi/4$). We will follow the former approach and apply the *bulb model* described in Duan et al. (2006a). Within this model it is shown that the projected velocity at a distance r from the neutrino emission zone is

$$v_r = \sqrt{1 - \left(\frac{R_{\text{NS}}}{r}\right)^2 (1 - v_{R_{\text{NS}}}^2)}, \quad (37)$$

where $v_{R_{\text{NS}}}$ is the projected velocity at the NS surface. By redefining the matrices of density with a change of variable $u = 1 - v_{R_{\text{NS}}}^2$ in the integral (35),

$$\rho_{p,u,r} \frac{p^2}{2(2\pi)^2} \rightarrow \rho_{p,u,r}, \quad (38)$$

and using Equation (25), we can write the full EoM as

$$\frac{\partial}{\partial r} \mathbf{P}_{p,r} = \left[\omega_{p,r} \mathbf{B} + \lambda_r \mathbf{L} + \mu_r \int_0^\infty (\mathbf{P}_{q,r} - \bar{\mathbf{P}}_{q,r}) dq \right] \times \mathbf{P}_{p,r} \quad (39a)$$

$$\frac{\partial}{\partial r} \bar{\mathbf{P}}_{p,r} = \left[-\omega_{p,r} \mathbf{B} + \lambda_r \mathbf{L} + \mu_r \int_0^\infty (\mathbf{P}_{q,r} - \bar{\mathbf{P}}_{q,r}) dq \right] \times \bar{\mathbf{P}}_{p,r}, \quad (39b)$$

where we have replaced v_r by its average value

$$\langle v_r \rangle = \frac{1}{2} \left[1 + \sqrt{1 - \left(\frac{R_{\text{NS}}}{r}\right)^2} \right]. \quad (40)$$

All the interaction potentials now depend on r , and each effective potential strength is parameterized as follows (Dasgupta & Dighe 2008):

$$\omega_{p,r} = \frac{\Delta m^2}{2p \langle v_r \rangle}, \quad (41)$$

$$\lambda_r = \sqrt{2} G_F (n_e^-(r) - n_e^+(r)) \frac{1}{\langle v_r \rangle}, \quad (42)$$

$$\mu_r = \frac{\sqrt{2} G_F}{2} \left(\sum_{i \in \{e,x\}} n_{\nu_i}^C \right) \left(\frac{R_{\text{NS}}}{r} \right)^2 \left(\frac{1 - \langle v_r \rangle^2}{\langle v_r \rangle} \right). \quad (43)$$

It is worth mentioning that all the effective potential strengths are affected by the geometry of the extended source through the projected velocity on the right-hand side of Equation (34). For the neutrino–neutrino interaction potential, we have chosen the total neutrino number density as parameterization. This factor comes from the freedom to renormalize the polarization vectors in the EoM. A different choice has been made in Esteban-Pretel et al. (2007). Of the other two r -dependent factors, one comes from the geometrical flux dilution and the other accounts for collinearity in the single-angle approximation. Overall μ_r decays as $1/r^4$.

In Figure 3 the behavior of the effective potentials within the single-angle formalism is shown for $\dot{M} = 10^{-2}$, 10^{-4} , 10^{-6} , and $10^{-8} M_\odot \text{ s}^{-1}$. In all cases, the neutrino energy is the corresponding average reported in Table 1. Since the oscillatory dynamics of the neutrino flavors are determined by the value of the potentials, and the value of the potentials depends on the data in Table 1, it is important to establish how

sensible this information is to the model we have adopted, in particular, to the pre-SN envelope density profile index m . The reported accretion rates can be seen as different states in the evolution of a binary system or as peak accretion rates of different binary systems. For a given accretion rate, the temperature and density conditions on the NS surface are fixed. This, in turn, fixes the potentials involved in the equations of flavor evolution and the initial neutrino and antineutrino flavor content. To see the consequences of changing the index m , we can estimate the peak accretion rates for new values using Equation (2). Since we are only interested in SNe Ic, we shall restrict these values to the ones reported in Table 1 of Becerra et al. (2016) (that is, $m = 2.771, 2.946, \text{ and } 2.801$), and in each case, we consider the smallest binary separation such that there is no Roche lobe overflow. For these parameters, we find peak accretion rates $\dot{M}_{\text{peak}} \sim 10^{-2}\text{--}10^{-4} M_{\odot} \text{ s}^{-1}$ with peak times at $t_{\text{peak}} \approx 7\text{--}35$ minutes. Because these accretion rates are still within the range in Table 1, the results contained in Section 4 apply also to these cases with different values of the m -index.

The profiles for the electron and positron number densities were adopted from the simulations presented in Becerra et al. (2016). Due to the dynamics of the infalling matter, close to the NS, the behavior of $n_{e^{-}}(r) - n_{e^{+}}(r)$ is similar to μ_r . At the shock radius, the electron density's derivative presents a discontinuity, and its behavior changes, allowing for three distinct regions inside the Bondi–Hoyle radius. The matter potential is always higher than the neutrino potential, yet, in most cases, both are higher than the vacuum potential, so we expect neutrino collective effects (neutrino oscillations) and MSW resonances to play a role in the neutrino flavor evolution inside the Bondi–Hoyle radius. Outside the capture region, as long as the neutrinos are not directed toward the SN, they will be subjected to vacuum oscillations.

4. Single-angle Solutions and Multi-angle Effects

The full dynamics of neutrino oscillations is a rather complex interplay between the three potentials discussed in Section 3, yet the neutrino–antineutrino symmetry allows us to generalize our single-angle calculations for certain accretion rates using some numerical and algebraic results obtained in Hannestad et al. (2006), Fogli et al. (2007), Esteban-Pretel et al. (2007), and references therein. Specifically, we know that if $\mu_r \gg \omega_r$, as long as the MSW condition $\lambda_r \simeq \omega_r$ is not met, collective effects should dominate the neutrino evolution even if $\lambda_r \gg \mu_r$. On the other hand, if $\mu_r \lesssim \omega_r$, the neutrino evolution is driven by the relative values between the matter and vacuum potentials. With this in mind, we identify two different ranges of values for the accretion rate: $\dot{M} \gtrsim 5 \times 10^{-5} M_{\odot} \text{ s}^{-1}$ and $\dot{M} \lesssim 5 \times 10^{-5} M_{\odot} \text{ s}^{-1}$.

4.1. High Accretion Rates

For accretion rates $\dot{M} \gtrsim 5 \times 10^{-5} M_{\odot} \text{ s}^{-1}$ the potentials obey the following hierarchy:

$$\lambda_r \gtrsim \mu_r \gg \omega_r; \quad (44)$$

hence, we expect strong effects of neutrino self-interactions. In order to appreciate the interesting physical processes that happen with the neutrinos along their trajectory in the accretion zone, we begin this analysis with a simplified approach to the EoM for a monochromatic spectrum with the same energy for

both neutrinos and antineutrinos. Let us introduce the following definitions:

$$\mathbf{D} = \bar{P}_r - \bar{P}_r \quad (45)$$

$$\mathbf{Q} = \bar{P}_r + \bar{P}_r - \frac{\omega_r}{\mu_r} \mathbf{B}. \quad (46)$$

The role of the matter potential is to logarithmically extend the period of the bipolar oscillations, so we can ignore it for now. Also, we will restrict our analysis to a small enough region at $R_{\text{NS}} + \Delta r$, so that we can consider $\frac{d}{dr}(\omega_r/\mu_r) \approx 0$ (adiabatic approximation). Then, by summing and subtracting Equation (39) and using definitions (45) and (46), we obtain

$$\frac{d}{dr} \mathbf{Q} = \mu \mathbf{D} \times \mathbf{Q} \quad (47)$$

$$\frac{d}{dr} \mathbf{D} = \omega \mathbf{B} \times \mathbf{Q}. \quad (48)$$

We are now able to build a very useful analogy. The equations above are analogous to the EoM of a simple mechanical pendulum with a vector position given by \mathbf{Q} , precessing around an angular momentum \mathbf{D} , subjected to a force $\omega\mu\mathbf{B}$ with a moment of inertia proportional to the inverse of μ . With Equations (17) and (26) the initial conditions for the polarization vectors are

$$\mathbf{P}(R_{\text{NS}}) = \bar{\mathbf{P}}(R_{\text{NS}}) = (0, 0, 0.4). \quad (49)$$

We can easily show that $|\mathbf{Q}(R_{\text{NS}})| = |\mathbf{P}(R_{\text{NS}}) + \bar{\mathbf{P}}(R_{\text{NS}})| + O(\omega/\mu) \approx 0.8$. Calculating $\frac{d}{dr}(\mathbf{Q} \cdot \mathbf{Q})$, it can be checked that this value is conserved.

The analogous angular momentum is $\mathbf{D}(R_{\text{NS}}) = \mathbf{P}(R_{\text{NS}}) - \bar{\mathbf{P}}(R_{\text{NS}}) = 0$. Thus, the pendulum moves initially in a plane defined by \mathbf{B} and the z -axis, i.e., the plane xz . Then, it is possible to define an angle φ between \mathbf{Q} and the z -axis such that

$$\mathbf{Q} = |\mathbf{Q}|(\sin \varphi, 0, \cos \varphi). \quad (50)$$

Note that the only nonzero component of \mathbf{D} is the y -component, and from Equations (47) and (48) we find

$$\frac{d\varphi}{dr} = \mu |\mathbf{D}| \quad (51)$$

and

$$\frac{d|\mathbf{D}|}{dr} = -\omega |\mathbf{Q}| \cos(2\theta + \varphi). \quad (52)$$

The above equations can be equivalently written as

$$\frac{d^2\varphi}{dr^2} = -k^2 \sin(2\theta + \varphi), \quad (53)$$

where we have introduced the inverse characteristic distance k by

$$k^2 = \omega\mu |\mathbf{Q}|, \quad (54)$$

which is related to the anharmonic oscillations described by the nonlinear EoM (51) and (52). The logarithmic correction to the oscillation length due to matter effects is (Hannestad et al. 2006)

$$\tau_{\dot{M}} = -k^{-1} \ln \left[\left(\frac{\pi}{2} - \theta \right) \frac{k}{(k^2 + \lambda^2)^{1/2}} \left(1 + \frac{\omega}{|\mathbf{Q}|\mu} \right) \right]. \quad (55)$$

The initial conditions (49) imply

$$\varphi(R_{\text{NS}}) = \arcsin\left(\frac{\omega}{|\mathcal{Q}|_l \mu} \sin 2\theta\right). \quad (56)$$

To investigate the physical meaning of the above equation, let us assume for a moment that 2θ is a small angle. In this case $\varphi(R_{\text{NS}})$ is also a small angle. If $k^2 > 0$, which is true for the normal hierarchy $\Delta m^2 > 0$, we expect small oscillations around the initial position since the system begins in a stable position of the potential associated with Equations (51) and (52). No strong flavor oscillations are expected. On the contrary, for the inverted hierarchy $\Delta m^2 < 0$, $k^2 < 0$ and the initial $\varphi(R_{\text{NS}})$ indicates that the system begins in an unstable position, and we expect very large anharmonic oscillations. \mathcal{P}^z (as well as $\bar{\mathcal{P}}^z$) oscillates between two different maxima passing through a minimum $-\mathcal{P}^z$ ($-\bar{\mathcal{P}}^z$) several times. This behavior implies total flavor conversion: all electronic neutrinos (antineutrinos) are converted into nonelectronic neutrinos (antineutrinos) and vice versa. This has been called bipolar oscillations in the literature (Duan et al. 2010).

We solved numerically Equation (39) for both normal and inverted hierarchies using a monochromatic spectrum dominated by the average neutrino energy for $\dot{M} = 10^{-2}$, 10^{-3} , 10^{-4} , and $5 \times 10^{-5} M_{\odot} \text{ s}^{-1}$ and the respective values reported in Table 1 with the initial conditions given by Equations (17) and (36). The behavior of the electronic neutrino survival probability inside the accretion zone is shown in Figures 4 and 5 for inverted hierarchy and normal hierarchy, respectively. For the inverted hierarchy, there is no difference between the neutrino and antineutrino survival probabilities. This should be expected since for these values of r the matter and self-interaction potentials are much larger than the vacuum potential, and there is virtually no difference from Equation (39). Also, note that the antineutrino flavor proportions discussed in Section 2.3 remain virtually unchanged for normal hierarchy, while the neutrino flavor proportions change drastically around the point $\lambda_r \sim \omega_r$. The characteristic oscillation length of the survival probability found on these plots is

$$\tau \approx 0.05 - 1 \text{ km}, \quad (57)$$

which agrees with the ones given by Equation (55) calculated at the NS surface up to a factor of order 1. Such a small value of τ suggests extremely quick $\nu_e \bar{\nu}_e \leftrightarrow \nu_x \bar{\nu}_x$ oscillations.

Clearly, the full EoM are highly nonlinear, so the solution may not reflect the real neutrino flavor evolution. Concerning the single-angle approximation, it is discussed in Hannestad et al. (2006), Raffelt & Sigl (2007), and Fogli et al. (2007) that in the more realistic multi-angle approach, kinematic decoherence happens. And in Esteban-Pretel et al. (2007) the conditions for decoherence as a function of the neutrino flavor asymmetry have been discussed. It is concluded that if the symmetry of neutrinos and antineutrinos is broken beyond the limit of $O(25\%)$, i.e., if the difference between emitted neutrinos and antineutrinos is roughly larger than 25% of the total number of neutrinos in the medium, decoherence becomes a subdominant effect.

As a direct consequence of the peculiar symmetric situation we are dealing with, in which neutrinos and antineutrinos are produced in similar numbers, bipolar oscillations happen, and, as we have already discussed, they present very small oscillation length as shown in Equation (57). Note also that

the bipolar oscillation length depends on the neutrino energy. Therefore, the resulting process is equivalent to an averaging over the neutrino energy spectrum and an equipartition among different neutrino flavors is expected Raffelt & Sigl (2007). Although, for simplicity, we are dealing with the two neutrino hypothesis, this behavior is easily extended to the more realistic three-neutrino situation. We assume, therefore, that at a few kilometers from the emission region neutrino flavor equipartition is a reality:

$$\nu_e : \nu_{\mu} : \nu_{\tau} = 1 : 1 : 1. \quad (58)$$

Note that the multi-angle approach keeps the order of the characteristic length τ of Equation (55) unchanged and kinematics decoherence happens within a few oscillation cycles (Sawyer 2005; Hannestad et al. 2006; Raffelt & Sigl 2007). Therefore, we expect that neutrinos created in regions close to the emission zone will be equally distributed among different flavors in less than a few kilometers after their creation. Once the neutrinos reach this maximally mixed state, no further changes are expected up until the matter potential enters the MSW resonance region. We emphasize that kinematics decoherence does not mean quantum decoherence. Figures 4 and 5 clearly show the typical oscillation pattern, which happens only if quantum coherence is still acting on the neutrino system. Differently from quantum decoherence, which would reveal itself by a monotonous dumping in the oscillation pattern, kinematics decoherence is just the result of averaging over the neutrino energy spectrum resulting from quick flavor conversion, for which oscillation length depends on the neutrino energy. Therefore, neutrinos are yet able to quantum oscillate if appropriate conditions are satisfied.

We discuss now the consequences of the matter potential.

4.1.1. Matter Effects

After leaving the emission region, beyond $r \approx R_{\text{NS}} + \Delta r_{\nu}$, where Δr_{ν} is the width defined in Equation (6), the effective neutrino density quickly falls in an asymptotic behavior $\mu_r \approx 1/r^4$. The decay of λ_r is slower. Hence, very soon the neutrino flavor evolution is determined by the matter potential. Matter suppresses neutrino oscillations, and we do not expect significant changes in the neutrino flavor content along a large region. Nevertheless, the matter potential can be so small that there will be a region along the neutrino trajectory in which it can be compared with the neutrino vacuum frequencies and the higher and lower resonant density conditions will be satisfied, i.e.,

$$\lambda(r_H) = \omega_H = \frac{\Delta m^2}{2\langle E_{\nu} \rangle} \text{ and } \lambda(r_L) = \omega_L = \frac{\Delta m_{21}^2}{2\langle E_{\nu} \rangle}, \quad (59)$$

where Δm^2 and Δm_{21}^2 are, respectively, the squared mass differences found in atmospheric and solar neutrino observations. Table 2 shows the experimental values of mixing angles and mass squared differences taken from Patrignani & the Particle Data Group (2016). The definition of Δm^2 used is $\Delta m^2 = m_3^2 - (m_2^2 + m_1^2)/2$. Thus, $\Delta m^2 = \Delta m_{31}^2 - \Delta m_{21}^2/2 > 0$ if $m_1 < m_2 < m_3$, and $\Delta m^2 = \Delta m_{32}^2 + \Delta m_{21}^2/2 < 0$ for $m_3 < m_1 < m_2$. When the above resonance conditions are satisfied, the MSW effects happen and the flavor content of the flux of electronic neutrinos and antineutrinos will again be modified.

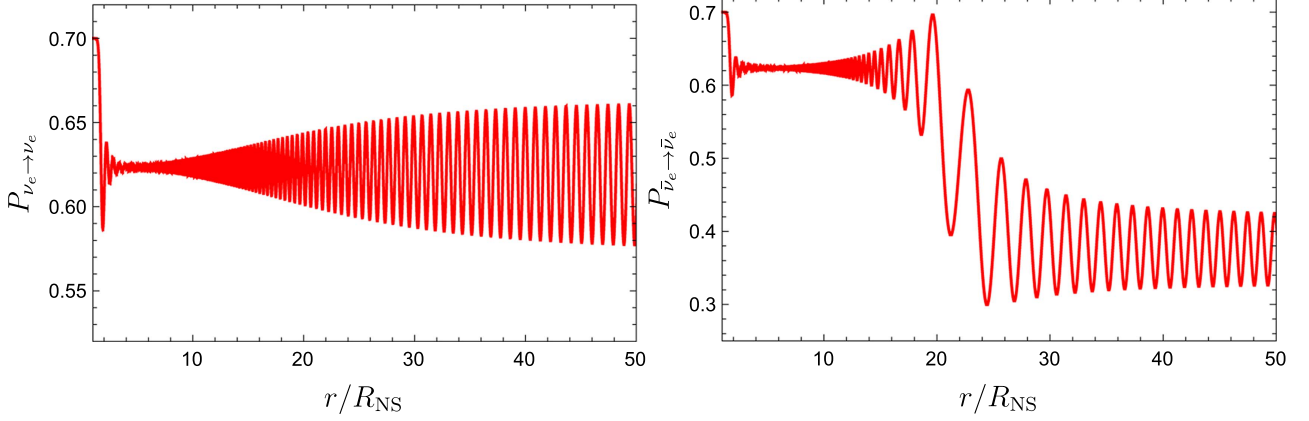


Figure 6. Electron neutrino and antineutrino flavor evolution for inverted hierarchy and $\dot{M} = 10^{-6} M_{\odot} \text{ s}^{-1}$. The survival probability is shown as a function of the radial distance from the NS surface.

Table 3
Fraction of Neutrinos and Antineutrinos for Each Flavor after Decoherence and Matter Effects ($n = 2\sum_i n_{\nu_i}$)

	$n_{\nu_e}^0/n$	$n_{\bar{\nu}_e}^0/n$	$n_{\nu_x}^0/n$	$n_{\bar{\nu}_x}^0/n$	n_{ν_e}/n	$n_{\bar{\nu}_e}/n$	n_{ν_x}/n	$n_{\bar{\nu}_x}/n$
Normal hierarchy	$\frac{1}{6}$	$\frac{1}{6}$	$\frac{1}{3}$	$\frac{1}{3}$	$\frac{1}{3}$	$\frac{1}{6} + \frac{1}{6} \sin^2 \theta_{12}$	$\frac{1}{6}$	$\frac{1}{3} - \frac{1}{6} \sin^2 \theta_{12}$
Inverted hierarchy	$\frac{1}{6}$	$\frac{1}{6}$	$\frac{1}{3}$	$\frac{1}{3}$	$\frac{1}{6} + \frac{1}{6} \cos^2 \theta_{12}$	$\frac{1}{3}$	$\frac{1}{3} - \frac{1}{6} \cos^2 \theta_{12}$	$\frac{1}{6}$

The final fluxes can be written as

$$F_{\nu_e}(E) = P_{\nu_e \rightarrow \nu_e}(E) F_{\nu_e}^0(E) + [1 - P_{\nu_e \rightarrow \nu_e}(E)] F_{\nu_x}^0(E) \quad (60a)$$

$$F_{\bar{\nu}_e}(E) = P_{\bar{\nu}_e \rightarrow \bar{\nu}_e}(E) F_{\bar{\nu}_e}^0(E) + [1 - P_{\bar{\nu}_e \rightarrow \bar{\nu}_e}(E)] F_{\bar{\nu}_x}^0(E), \quad (60b)$$

where $F_{\nu_e}^0(E)$, $F_{\nu_x}^0(E)$, $F_{\bar{\nu}_e}^0(E)$, and $F_{\bar{\nu}_x}^0(E)$ are the fluxes of electronic and nonelectronic neutrinos and antineutrinos after the bipolar oscillations of the emission zone and $P_{\nu_e \rightarrow \nu_e}(E)$ and $P_{\bar{\nu}_e \rightarrow \bar{\nu}_e}(E)$ are the survival probability of electronic neutrinos and antineutrinos during the resonant regions.

In order to evaluate $F_{\nu_e}(E)$ and $F_{\bar{\nu}_e}(E)$ after matter effects, we have to estimate the survival probability at the resonant regions. There are several articles devoted to this issue; for instance, we can adopt the result in Fogli et al. (2003), namely, for normal hierarchy

$$P_{\nu_e \rightarrow \nu_e}(E) = X \sin^2 \theta_{12} \quad (61a)$$

$$P_{\bar{\nu}_e \rightarrow \bar{\nu}_e}(E) = \cos^2 \theta_{12}, \quad (61b)$$

and for inverted hierarchy

$$P_{\nu_e \rightarrow \nu_e}(E) = \sin^2 \theta_{12} \quad (62a)$$

$$P_{\bar{\nu}_e \rightarrow \bar{\nu}_e}(E) = X \cos^2 \theta_{12}. \quad (62b)$$

The factor X , the conversion probability between neutrino physical eigenstates, is given by Petcov (1987), Fogli et al. (2003), and Kneller & McLaughlin (2006):

$$X = \frac{\exp(2r_{\text{res}} k_{\text{res}} \cos 2\theta_{13}) - 1}{\exp(2r_{\text{res}} k_{\text{res}}) - 1}, \quad (63)$$

where $r_{\text{res}} = r_L$ or $r_{\text{res}} = r_H$, defined according to Equation (59) and

$$\frac{1}{k_{\text{res}}} = \left| \frac{d \ln \lambda_r}{dx} \right|_{r=r_{\text{res}}}. \quad (64)$$

The factor X is related to how fast physical environment features relevant for neutrino oscillations change, such as neutrino and matter densities.

For slow and adiabatic changes $X \rightarrow 0$, while for fast and nonadiabatic changes $X \rightarrow 1$. In our specific cases, the MSW resonances occur very far from the accretion zone, where the matter density varies very slow and therefore $X \rightarrow 0$, as can be explicitly calculated from Equation (63). Consequently, it is straightforward to estimate the final fluxes of electronic and nonelectronic neutrinos and antineutrinos.

4.2. Low Accretion Rates

For accretion rates $\dot{M} < 5 \times 10^{-5} M_{\odot} \text{ s}^{-1}$, either the matter potential is close enough to the vacuum potential and the MSW condition is satisfied, or both the self-interaction and matter potentials are so low that the flavor oscillations are only due to the vacuum potential. In both cases, bipolar oscillations are not present. In Figure 6 we show the survival probability for $\dot{M} = 10^{-6} M_{\odot} \text{ s}^{-1}$ as an example. We can see that neutrinos and antineutrinos follow different dynamics. In particular, for antineutrinos there are two decreases. The first one, around $r \approx (1-2) R_{\text{NS}}$, is due to bipolar oscillations that are rapidly damped by the matter potential as discussed in Section 4.1.1. The second one happens around $r \approx (10-20) R_{\text{NS}}$. It can be seen from the bottom left panel of Figure 3 (that one for $\dot{M} = 10^{-6} M_{\odot} \text{ s}^{-1}$) that around $r \approx (1-2) \times 10^7 \text{ cm}$ (or, equivalently, $r \approx (10-20) R_{\text{NS}}$) the higher MSW resonance occurs ($\lambda_r \sim \omega_{r_H}$). For inverted hierarchy, such resonance will affect antineutrinos depleting its number, as can be seen from Equation (60). Without bipolar oscillations, it is not possible to guarantee that decoherence will be complete and Equation (58) is no longer valid. The only way to know the exact flavor proportions is to solve the full Equation (32).

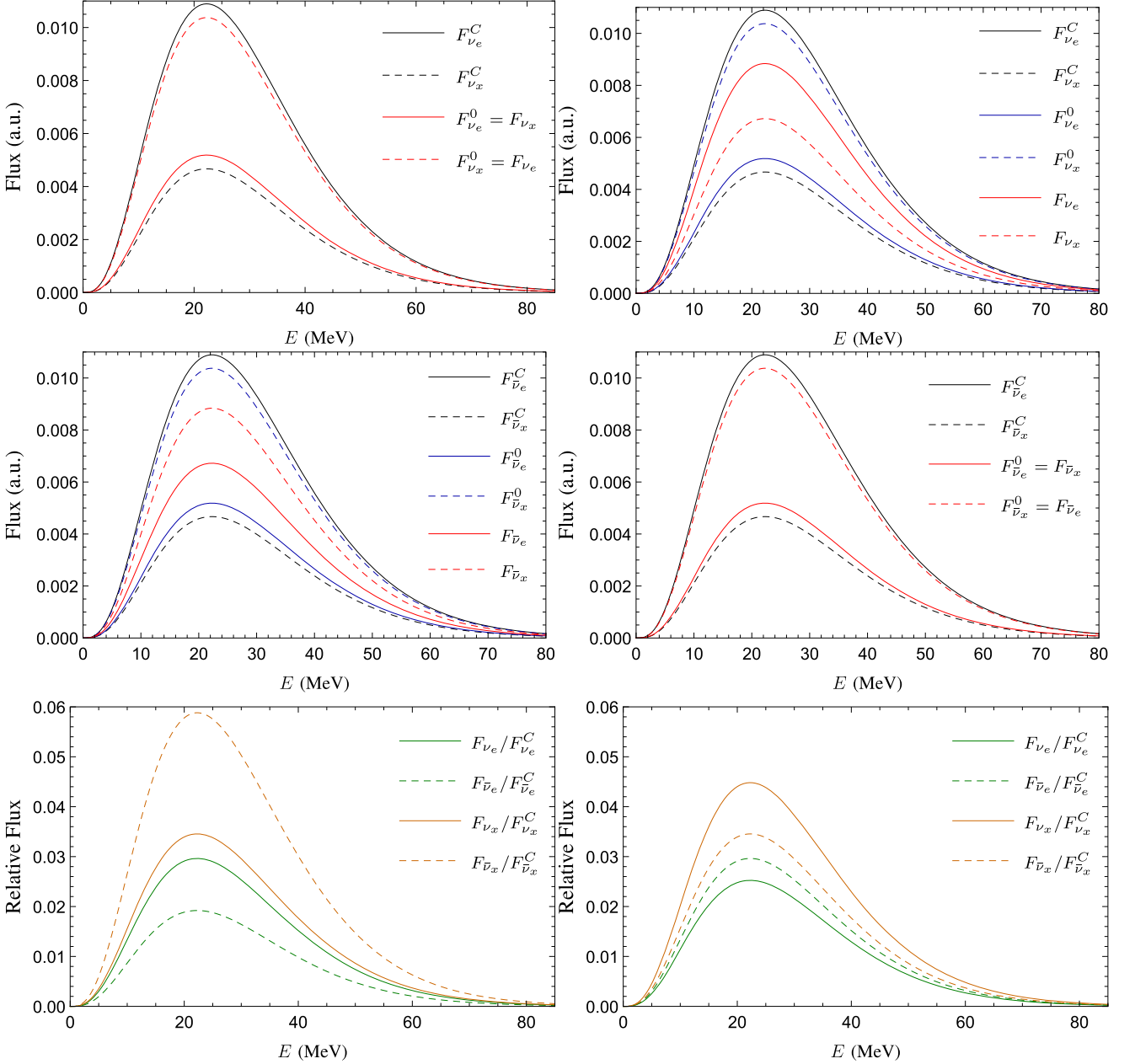


Figure 7. Several neutrino and antineutrino number fluxes for different neutrino flavors are presented for $\dot{M} = 10^{-2} M_{\odot} \text{ s}^{-1}$. Each column corresponds to a neutrino mass hierarchy: normal hierarchy on the left and inverted hierarchy on the right. The first two rows show the number fluxes after each process studied. F_{ν}^C , F_{ν}^0 , and F_{ν} are the creation flux at the bottom accretion zone due to e^+e^- pair annihilation, the flux after the region with dominant neutrino–neutrino potential, and the final emission flux after the region with dominant neutrino–matter potential, respectively. The last row shows the relative fluxes F_{ν}/F_{ν}^C between the creation and emission fluxes.

5. Neutrino Emission Spectra

Using the calculations of the previous section, we can draw a comparison between the creation spectra of neutrinos and antineutrinos at the NS surface (F_{ν}^c , n_{ν}^c), initial spectra after kinematic decoherence (F_{ν}^0 , n_{ν}^0), and emission spectra after the MSW resonances (F_{ν} , n_{ν}). Table 3 contains a summary of the flavor content inside the Bondi–Hoyle radius. With these fractions and Equation (21) it is possible to reproduce the spectrum for each flavor and for accretion rates $\dot{M} \geq 5 \times 10^{-5} M_{\odot} \text{ s}^{-1}$.

The specific cases for $\dot{M} = 10^{-2} M_{\odot} \text{ s}^{-1}$ are shown in Figure 7. In such figures, the left column corresponds to normal hierarchy and the right column corresponds to inverted hierarchy. The first two rows show the number fluxes after each process studied. The last row shows the relative fluxes F_{ν}/F_{ν}^C between the creation and emission fluxes. For the sake of clarity, we have normalized the curves to the total neutrino number at the NS surface

$$n = 2 \sum_{i \in \{e,x\}} n_{\nu_i}, \quad (65)$$

so that each one is a normalized Fermi–Dirac distribution multiplied by the appropriate flavor content fraction. To reproduce any other case, it is enough to use Equation (21) with the appropriate temperature.

At this point two comments have to be made about our results:

1. As we mentioned before, the fractions in Table 3 were obtained by assuming a monochromatic spectrum and using the single-angle approximation. This would imply that the spectrum-dependent phenomenon called the *spectral stepwise swap* of flavors is not present in our analysis even though it has been shown that it can also appear in multi-angle simulations (Fogli et al. 2007). Nevertheless, we know from our calculations in Section 2.3 that neutrinos and antineutrinos of all flavors are created with the exact same spectrum up to a multiplicative constant. Hence, following Raffelt & Smirnov (2007a, 2007b), by solving the equation

$$\int_{E_c}^{\infty} (n_{\nu_e} - n_{\nu_x}) dE = \int_0^{\infty} (n_{\bar{\nu}_e} - n_{\bar{\nu}_x}) dE, \quad (66)$$

we find that the critical (split) energy is $E_c = 0$. This means that the resulting spectrum should still be unimodal and the spectral swap in our system could be approximated by a multiplicative constant that is taken into account in the decoherence analysis of Section 4.

2. The fluxes of electronic neutrinos and antineutrinos shown in these figures and in Equation (60) represent fluxes at different positions up to a geometrical $1/r^2$ factor, r being the distance from the NS radius. Also, since we are considering the fluxes before and after each oscillatory process, the values of r are restricted to $r = R_{\text{NS}}$ for F_{ν}^C , $\tau_M < r < r_H$ for F_{ν}^0 , and $r > r_L$ for F_{ν} . To calculate the number flux at a detector, for example, much higher values of r have to be considered, and it is necessary to study vacuum oscillations in more detail. Such calculations will be presented elsewhere.

From Figure 7 one can observe that the dominance of electronic neutrinos and antineutrinos found at their creation at the bottom of the accretion zone is promptly erased by kinematic decoherence in such a way that the content of the neutrinos and antineutrinos entering the MSW resonant region is dominated by nonelectronic flavors. After the adiabatic transitions provoked by MSW transitions, electronic neutrinos and antineutrinos dominate again the emission spectrum except for nonelectronic antineutrinos in the normal hierarchy. Although no energy spectrum distortion is expected, the flavor content of neutrinos and antineutrinos produced near the NS surface escape to the outer space in completely different spectra when compared with the ones in which they were created, as shown in the last row of Figure 7.

6. Concluding Remarks

We can now proceed to draw the conclusions and some astrophysical consequences of this work:

1. The main neutrino production channel in XRFs and BdHNe in the hypercritical accretion process is pair annihilation: $e^-e^+ \rightarrow \nu\bar{\nu}$. This mechanism produces an initial equal number of neutrinos and antineutrinos and an initial 7/3 relative fraction between electronic and other

flavors. These features lead to a different neutrino phenomenology with respect to the typical core-collapse SN neutrinos produced via the URCA process.

2. The neutrino density is higher than both the electron density and the vacuum oscillation frequencies for the inner layers of the accretion zone, and the self-interaction potential dictates the flavor evolution along this region, as illustrated by Figure 3. This particular system leads to very fast pair conversions $\nu_e\bar{\nu}_e \leftrightarrow \nu_{\mu,\tau}\bar{\nu}_{\mu,\tau}$ induced by bipolar oscillations with oscillation length as small as $O(0.05-1)$ km. However, due to the characteristics of the main neutrino production process, neutrinos and anti-neutrinos have very similar fluxes inside the neutrino emission zone and kinematic decoherence dominates the evolution of the polarization vectors.
3. The kinematic decoherence induces a fast flux equipartition among the different flavors that then enters the matter-dominated regions in which MSW resonances take place.
4. Therefore, the neutrino flavor content emerging from the Bondi–Hoyle surface to the outer space is different from the original one at the bottom of the accretion zone. As shown in Table 3, The initial 70% and 30% distribution of electronic and nonelectronic neutrinos becomes 55% and 45% or 62% and 38% for normal or inverted hierarchy, respectively. Since the $\nu \leftrightarrow \bar{\nu}$ oscillations are negligible (Pontecorvo 1957, 1968; Xing 2013), the total neutrino-to-antineutrino ratio is kept constant.

We have shown that such a rich neutrino phenomenology is uniquely present in the hypercritical accretion process in XRFs and BdHNe. This deserves the appropriate attention since it paves the way for a new arena of neutrino astrophysics besides SN neutrinos. There are a number of issues that still have to be investigated:

1. We have made some assumptions that, albeit being a first approximation to a more detailed picture, have allowed us to set the main framework to analyze the neutrino oscillation phenomenology in these systems. We have shown in Becerra et al. (2015) that the SN ejecta carry enough angular momentum to form a disk-like structure around the NS before being accreted. However, the knowledge of the specific properties of such possible disk-like structure surrounding the NS is still pending more accurate numerical simulations at such distance scales. For instance, it is not clear yet whether such a structure could be modeled via thin-disk or thick-disk models. We have adopted a simplified model assuming isotropic accretion and the structure of the NS accretion region used in Becerra et al. (2016), which accounts for the general physical properties of the system. In order to solve the hydrodynamics equations, the neutrino emission region features, and the neutrino flavor oscillation equations, we have assumed spherically symmetric accretion onto a nonrotating NS, a quasi-steady-state evolution parameterized by the mass accretion rate, a polytropic equation of state, and subsonic velocities inside the shock radius. The matter is described by a perfect gas made of ions, electrons, positrons, and radiation with electrons and positrons obeying a Fermi–Dirac distribution. The electron fraction was fixed and equal to 0.5. We considered pair annihilation,

photo-neutrino process, plasmon decay, and bremsstrahlung to calculate neutrino emissivities. Under the above conditions we have found that the pair annihilation dominates the neutrino emission for the accretion rates involved in XRFs and BdHNe (see Becerra et al. 2016, for further details). The photons are trapped within the infalling material and the neutrinos are transparent, taking away most of the energy from the accretion. We are currently working on the relaxation of some of the above assumptions, e.g., the assumption of spherical symmetry to introduce a disk-like accretion picture, and the results will be presented elsewhere. In this line it is worth mentioning that some works have been done in this direction (see, e.g., Zhang & Dai 2008, 2009), although in a Newtonian framework, for complete dissociated matter, and within the thin-disk approximation. In these models, disk heights H are found to obey the relation $H/r \sim 0.1$ near the NS surface, which suggests that the results might be similar to the ones of a spherical accretion, such as the ones we have adopted. We are currently working on a generalization including general relativistic effects in axial symmetry to account for the fast rotation that the NS acquires during the accretion process. This was already implemented for the computation of the accretion rates at the Bondi–Hoyle radius position in Becerra et al. (2016), but it still needs to be implemented in the computation of the matter and neutrino density–temperature structure near the NS surface. In addition, the description of the equation of state of the infalling matter can be further improved by taking into account beta and nuclear statistical equilibrium.

In forthcoming works we will not only relax the assumptions made on the binary system parameters but also make more detailed calculations on the neutrino oscillations, including general relativistic and multi-angle effects. This paper, besides presenting a comprehensive nonrelativistic account of flavor transformations in spherical accretion, serves as a primer that has allowed us to identify key theoretical and numerical features involved in the study of neutrino oscillations in the IGC scenario of GRBs. From this understanding, we can infer that neutrino oscillations might be markedly different in a disk-like accretion process. First, depending on the value of the neutron star mass, the inner disk radius may be located at an $r_{\text{inner}} > R_{\text{NS}}$ beyond the NS surface (see, e.g., Ruffini et al. 2016b; Cipolletta et al. 2017); hence, the neutrino emission must be located at a distance $r \geq r_{\text{inner}}$. On the other hand, depending on the accretion rate, the density near the inner radius can be higher than in the present case and move the condition for neutrino cooling farther from the inner disk radius, at $r > r_{\text{inner}}$. Both of these conditions would change the geometric setup of the neutrino emission. Furthermore, possible larger values of T and ρ may change the mechanisms involved in neutrino production. For example, electron–positron pair capture, namely, $p + e^- \rightarrow n + \nu_e$, $n + e^+ \rightarrow p + \bar{\nu}_e$ and $n \rightarrow p + e^- + \bar{\nu}_e$, may become as efficient as the electron–positron pair annihilation. This, besides changing the intensity of the neutrino emission, would change the initial neutrino flavor configuration.

2. Having obtained the flux and the total number of neutrinos and antineutrinos of each flavor that leave the binary system during the hypercritical accretion process in XRFs and BdHNe, it raises naturally the question of the possibility for such neutrinos to be detected in current neutrino observatories. For instance, detectors such as Hyper-Kamiokande are more sensitive to the inverse beta decay events produced in the detector, i.e., $\bar{\nu}_e + p \rightarrow e^+ + n$ (see Abe et al. 2011, for more details); consequently, the $\bar{\nu}_e$ are the most plausible neutrinos to be detected. Liu et al. (2016) have pointed out that for a total energy in $\bar{\nu}_e$ of 10^{52} erg and $\langle E_{\bar{\nu}_e} \rangle \sim 20$ MeV, the Hyper-Kamiokande neutrino horizon is of the order of 1 Mpc. In the more energetic case of BdHNe we have typically $\langle E_{\nu, \bar{\nu}} \rangle \sim 20$ MeV (see Table 1) and a total energy carried out $\bar{\nu}_e$ of the order of the gravitational energy gain by accretion, i.e., $E_g \sim 10^{52} - 10^{53}$ erg. Therefore, we expect the BdHN neutrino-horizon distance to be also of the order of 1 Mpc. These order-of-magnitude estimates need to be confirmed by detailed calculations, including the vacuum oscillations experienced by the neutrinos during their travel to the detector, which we are going to present elsewhere.
3. If we adopt the local BdHNe rate $\sim 1 \text{ Gpc}^{-3} \text{ yr}^{-1}$ (Ruffini et al. 2016b) and the data reported above at face value, it seems that the direct detection of this neutrino signal is very unlikely. However, the physics of neutrino oscillations may have consequences on the powering mechanisms of GRBs such as the electron–positron pair production by neutrino-pair annihilation. The energy deposition rate of this process depends on the local energy-momentum distribution of (anti)neutrinos, which, as we have discussed, is affected by the flavor oscillation dynamics. This phenomenon may lead to measurable effects on the GRB emission.
4. An IGC binary leading either to an XRF or to a BdHN is a unique neutrino physics laboratory in which there are at least three neutrino emission channels at the early stages of the GRB emission process: (i) the neutrinos emitted in the explosion of the CO_{core} as SN, (ii) the neutrinos studied in this work created in the hypercritical accretion process triggered by the above SN onto the NS companion, and (iii) the neutrinos from fallback accretion onto the νNS created at the center of the SN explosion. It remains to establish the precise neutrino time sequence, as well as the precise relative neutrino emissivities from all these events. This is relevant to establish both the time delays in the neutrino signals and their fluxes, which will become a unique signature of GRB neutrinos following the IGC paradigm.
5. As discussed in Ruffini et al. (2016b), there are two cases in which there is the possibility of having hypercritical accretion onto a BH. First, in BdHNe there could still be some SN material around the newly born BH that can create a new hypercritical accretion process (Becerra et al. 2016). Second, a $\sim 10 M_{\odot}$ BH could already be formed before the SN explosion, namely, the GRB could be produced in a CO_{core} –BH binary progenitor. The conditions of temperature and density in the vicinity of these BHs might be very different from the ones analyzed here and, therefore, the neutrino emission and its associated phenomenology. We noted in the introduction

that such an accretion process onto the BH can explain the observed 0.1–100 GeV emission in BdHNe (Ruffini et al. 2015a, 2015b, 2016a, 2016b; Aimuratov et al. 2017; see also Aimuratov et al. in preparation). The interaction of such an ultrarelativistic expanding emitter with the interstellar medium could be a possible source of high-energy (e.g., TeV–PeV) neutrinos, following a mechanism similar to the one introduced in the traditional collapsar-fireball model of long GRBs (see, e.g., Kumar & Zhang 2015; Agostini et al. 2017, and references therein).

6. Although the symmetry between the neutrino and antineutrino number densities has allowed us to generalize the results obtained within the single-angle and monochromatic spectrum approximations, to successfully answer the question of detectability, full-scale numerical solutions will be considered in the future to obtain a precise picture of the neutrino emission spectrum. In particular, it would be possible to obtain an r -dependent neutrino spectrum without the restrictions discussed in Section 5.
7. For low accretion rates ($\dot{M} \lesssim 5 \times 10^{-5} M_{\odot} \text{ s}^{-1}$) the matter and self-interaction potentials in Equation (39) decrease and the general picture described in Figure 3 changes. The resonance region could be located around closer to the NS surface, anticipating the MSW condition $\lambda_r \sim \omega_r$ and interfering with the kinematic decoherence. This changes the neutrino flavor evolution and, of course, the emission spectrum. Hence, the signature neutrino emission spectrum associated with the least luminous XRFs might be different from the ones reported here.

We thank the referee for the comments and suggestions that helped to make more clear the presentation of our results. M.M.G. thanks FAPESP (contract no. 2016/00799–7) for the financial support and ICRANet in Pescara and Rome for the hospitality during the realization of this article. R.R. acknowledges the collaboration ICRANet-INFN. J.D.U. thanks COLCIENCIAS for the financial support. J.A.R. acknowledges the partial support of project no. 3101/GF4 IPC-11 and the target program F.0679 of the Ministry of Education and Science of the Republic of Kazakhstan.

ORCID iDs

J. A. Rueda  <https://orcid.org/0000-0003-4904-0014>

References

- Aartsen, M. G., Abbasi, R., Abdou, Y., et al. 2013, *PhRvL*, **111**, 021103
- Abe, K., Abe, T., Aihara, H., et al. 2011, arXiv:1109.3262
- Agostini, M., Altenmüller, K., Appel, S., et al. 2017, *APJ*, **86**, 11
- Aimuratov, Y., Ruffini, R., Muccino, M., et al. 2017, *ApJ*, **844**, 83
- Bayless, A. J., Even, W., Frey, L. H., et al. 2015, *ApJ*, **805**, 98
- Becerra, L., Bianco, C. L., Fryer, C. L., Rueda, J. A., & Ruffini, R. 2016, *ApJ*, **833**, 107
- Becerra, L., Cipolletta, F., Fryer, C. L., Rueda, J. A., & Ruffini, R. 2015, *ApJ*, **812**, 100
- Cardall, C. Y. 2008, *PhRvD*, **78**, 085017
- Chakraborty, S., Choubey, S., Dasgupta, B., & Kar, K. 2008, *JCAP*, **0809**, 013
- Cipolletta, F., Cherubini, C., Filippi, S., Rueda, J. A., & Ruffini, R. 2017, *PhRvD*, **96**, 024046
- Dasgupta, B., & Dighe, A. 2008, *PhRvD*, **77**, 113002
- Dasgupta, B., Dighe, A., & Mirizzi, A. 2008a, *PhRvL*, **101**, 171801
- Dasgupta, B., Dighe, A., Mirizzi, A., & Raffelt, G. G. 2008b, *PhRvD*, **78**, 033014
- Dicus, D. A. 1972, *PhRvD*, **6**, 941
- Dolgov, A. D. 1981, *SvJNP*, **33**, 700
- Duan, H., Fuller, G. M., & Carlson, J. 2008a, *CS&D*, **1**, 015007
- Duan, H., Fuller, G. M., Carlson, J., & Qian, Y.-Z. 2006a, *PhRvD*, **74**, 105014
- Duan, H., Fuller, G. M., Carlson, J., & Qian, Y.-Z. 2008b, *PhRvL*, **100**, 021101
- Duan, H., Fuller, G. M., & Qian, Y.-Z. 2006b, *PhRvD*, **74**, 123004
- Duan, H., Fuller, G. M., & Qian, Y.-Z. 2007, *PhRvD*, **76**, 085013
- Duan, H., Fuller, G. M., & Qian, Y.-Z. 2010, *ARNPS*, **60**, 569
- Eichler, D., Livio, M., Piran, T., & Schramm, D. N. 1989, *Natur*, **340**, 126
- Esteban-Pretel, A., Pastor, S., Tomas, R., Raffelt, G. G., & Sigl, G. 2007, *PhRvD*, **76**, 125018
- Esteban-Pretel, A., Pastor, S., Tomas, R., Raffelt, G. G., & Sigl, G. 2008, *PhRvD*, **77**, 065024
- Fogli, G. L., Lisi, E., Marrone, A., & Mirizzi, A. 2007, *JCAP*, **0712**, 010
- Fogli, G. L., Lisi, E., Mirizzi, A., & Montanino, D. 2005, *JCAP*, **0504**, 002
- Fogli, G. L., Lisi, E., Montanino, D., & Mirizzi, A. 2003, *PhRvD*, **68**, 033005
- Fryer, C. L., Oliveira, F. G., Rueda, J. A., & Ruffini, R. 2015, *PhRvL*, **115**, 231102
- Fryer, C. L., Rueda, J. A., & Ruffini, R. 2014, *ApJL*, **793**, L36
- Fuller, G. M., & Qian, Y.-Z. 2006, *PhRvD*, **73**, 023004
- Goodman, J. 1986, *ApJL*, **308**, L47
- Hannestad, S., Raffelt, G. G., Sigl, G., & Wong, Y. Y. 2006, *PhRvD*, **74**, 105010
- Izzo, L., Rueda, J. A., & Ruffini, R. 2012, *A&A*, **548**, L5
- Janka, H.-T., & Hillebrandt, W. 1989a *A&A*, **224**, 49
- Janka, H.-T., & Hillebrandt, W. 1989b *A&AS*, **78**, 375
- Keil, M. T., Raffelt, G. G., & Janka, H.-T. 2003, *ApJ*, **590**, 971
- Kneller, J. P., & McLaughlin, G. C. 2006, *PhRvD*, **73**, 056003
- Kumar, P., & Zhang, B. 2015, *PhR*, **561**, 1
- Liu, T., Zhang, B., Li, Y., Ma, R.-Y., & Xue, L. 2016, *PhRvD*, **93**, 123004
- MacFadyen, A. I., & Woosley, S. E. 1999, *ApJ*, **524**, 262
- Malkus, A., McLaughlin, G. C., & Surman, R. 2016, *PhRvD*, **93**, 045021
- Mao, S., & Yi, I. 1994, *ApJL*, **424**, L131
- Meszáros, P., Laguna, P., & Rees, M. J. 1993, *ApJ*, **415**, 181
- Mikheev, S. P., & Smirnov, A. Yu. 1986, *NCimC*, **9**, 17
- Misiaszek, M., Odrzywołek, A., & Kutschera, M. 2006, *PhRvD*, **74**, 043006
- Narayan, R., Paczyński, B., & Piran, T. 1992, *ApJL*, **395**, L83
- Narayan, R., Piran, T., & Shemi, A. 1991, *ApJL*, **379**, L17
- Notzold, D., & Raffelt, G. 1988, *NuPhB*, **307**, 924
- Paczynski, B. 1986, *ApJL*, **308**, L43
- Paczynski, B. 1998, *ApJL*, **494**, L45
- Pantaleone, J. 1992, *PhLB*, **287**, 128
- Pastor, S., & Raffelt, G. 2002, *PhRvL*, **89**, 191101
- Patrignani, C., & the Particle Data Group 2016, *ChPhC*, **40**, 100001
- Petcov, S. T. 1987, *PhLB*, **191**, 299
- Piran, T. 2004, *RvMP*, **76**, 1143
- Piran, T., Shemi, A., & Narayan, R. 1993, *MNRAS*, **263**, 861
- Pontecorvo, B. 1957, *JETP*, **6**, 429
- Pontecorvo, B. 1968, *JETP*, **26**, 984
- Qian, Y. Z., & Fuller, G. M. 1995, *PhRvD*, **51**, 1479
- Raffelt, G. G. 1996, *Stars as Laboratories for Fundamental Physics: The Astrophysics of Neutrinos, Axions, and Other Weakly Interacting Particles* (Chicago, IL: Univ. Chicago Press)
- Raffelt, G. G., & Sigl, G. 2007, *PhRvD*, **75**, 083002
- Raffelt, G. G., & Smirnov, A. Yu. 2007a *PhRvD*, **76**, 081301
- Raffelt, G. G., & Smirnov, A. Yu. 2007b *PhRvD*, **76**, 125008
- Rees, M. J., & Meszaros, P. 1992, *MNRAS*, **258**, 41P
- Rees, M. J., & Meszaros, P. 1994, *ApJL*, **430**, L93
- Rueda, J. A., & Ruffini, R. 2012, *ApJL*, **758**, L7
- Ruffini, R., Bernardini, M. G., Bianco, C. L., et al. 2006, in *The Tenth Marcel Grossmann Meeting*, ed. M. Novello, S. Perez Bergliaffa, R. Ruffini et al. (Singapore: World Scientific), 369
- Ruffini, R., Bernardini, M. G., Bianco, C. L., et al. 2008, in *The Eleventh Marcel Grossmann Meeting on Recent Developments*, ed. H. Kleinert, R. T. Jantzen, & R. Ruffini (Singapore: World Scientific), 368
- Ruffini, R., Muccino, M., Aimuratov, Y., et al. 2016a, *ApJ*, **831**, 178
- Ruffini, R., Muccino, M., Kovacevic, M., et al. 2015a, *ApJ*, **808**, 190
- Ruffini, R., Rueda, J. A., Muccino, M., et al. 2016b, *ApJ*, **832**, 136
- Ruffini, R., Wang, Y., Aimuratov, Y., et al. 2018, *ApJ*, **852**, 53
- Ruffini, R., Wang, Y., Enderli, M., et al. 2015b, *ApJ*, **798**, 10
- Salmonson, J. D., & Wilson, J. R. 2002, *ApJ*, **578**, 310
- Sawyer, R. F. 2005, *PhRvD*, **72**, 045003
- Sawyer, R. F. 2009, *PhRvD*, **79**, 105003
- Shemi, A., & Piran, T. 1990, *ApJL*, **365**, L55
- Sigl, G., & Raffelt, G. 1993, *NuPhB*, **406**, 423

Strack, P., & Burrows, A. 2005, [PhRvD](#), **71**, 093004
Wolfenstein, L. 1978, [PhRvD](#), **17**, 2369
Woosley, S. E. 1993, [ApJ](#), **405**, 273
Wu, M.-R., & Qian, Y.-Z. 2011, [PhRvD](#), **84**, 045009
Xing, Z.-Z. 2013, [PhRvD](#), **87**, 053019

Yakovlev, D. G., Kaminker, A. D., Gnedin, O. Y., & Haensel, P. 2001, [PhR](#), **354**, 1
Zhang, D., & Dai, Z. G. 2008, [ApJ](#), **683**, 329
Zhang, D., & Dai, Z. G. 2009, [ApJ](#), **703**, 461
Zhu, Y.-L., Perego, A., & McLaughlin, G. C. 2016, [PhRvD](#), **94**, 105006